ABSTRACT

Title of dissertation: MICROSTRUCTURAL EVOLUTION IN FRICTION STIR
                           WELDING OF TI 5111

                           Jennifer Nguyen Wolk, Doctor of Philosophy, 2010

Dissertation directed by: Professor Lourdes Salamanca-Riba

                              Department of Materials Science & Engineering

Titanium and titanium alloys have shown excellent mechanical, physical, and corrosion properties. To address the needs of future naval combatants, this research examines an alternative joining technology, friction stir welding (FSW). Friction stir welding uses a non-consumable tool to generate frictional heat to plastically deform and mix metal to form a consolidated joint. This work focuses on FSW of Ti-5111 (Ti-5Al-1Sn-1Zr-1V-0.8Mo), a near alpha (α) alloy. This study aims to gain a fundamental understanding of the relationship between processing parameters, microstructure, and mechanical properties of experimental 12.7mm and 6.35mm Ti-5111 friction stir welds.

The resulting weld microstructure shows significant grain refinement within the weld compared to the base metal. The weld microstructures show a fully lamellar colony structure with peak welding temperatures exceeding β transformation temperature. The friction stir weld shows material texture strengthening of the BCC F fiber component before transformation to D_2 shear texture in the stir zone. Transmission electron microscopy results of the base metal and the stir zone show a lath colony-type structure with low dislocation

density and no lath grain substructure. In situ TEM heating experiments of Ti-5111 friction stir welded material show transformation to the high temperature β phase at significantly lower temperatures compared to the base metal.

Thermal and deformation mechanisms within Ti-5111 were examined through the use of thermomechanical simulation. Isothermal constant strain rate tests show evidence of dynamic recrystallization and deformation above β transus when compared with the FSW thermal profile without deformation. Subtransus deformation shows kinking and bending of the existing colony structure without recrystallization. Applying the friction stir thermal profile to constant strain rate deformation successfully reproduced the friction stir microstructure at a peak temperature of 1000ºC and a strain rate of 10/s. These results provide unique insight into the strain, strain rates, and temperatures regime within the process.

Finally, the experimental thermal and deformation fields were compared using ISAIAH, a Eulerian based three-dimensional model of friction stir welding. These results are preliminary but show promise for the ability of the model to compute thermal fields for material flow, model damage prediction, and decouple texture evolution for specific thermomechanical histories in the friction stir process.

MICROSTRUCTURAL EVOLUTION IN FRICTION STIR WELDING OF TI 5111

By

Jennifer Nguyen Wolk

Dissertation submitted to the Faculty of the Graduate School of the
University of Maryland, College Park, in partial fulfillment
of the requirements for the degree of
Doctor of Philosophy
2010

Advisory Committee:
Professor Lourdes Salamanca-Riba, Dept. of Materials Science & Engineering, Chair
Professor Isabel Lloyd, Dept. of Materials Science& Engineering
Professor Manfred Wuttig, Dept. of Materials Science& Engineering
Professor F. Patrick McCluskey, Dept. of Mechanical Engineering
Dr. Mary Juhas, Ohio State University Dept. of Materials Science & Engineering

ACKNOWLEDGEMENTS

not be who I am today. I would like to thank my sisters Lana and Christie for their never ending encouragement.

Finally, I would like to thank my husband Josh for all the love and support he has given me through this process. You are my loudest cheerleader and my very best friend. I could not have done this without you. Our future is just beginning.

Table of Contents

LIST OF TABLES

LIST OF FIGURES

CHAPTER 1: INTRODUCTION

1.1. Background

Titanium and titanium alloys have shown excellent mechanical, physical, and corrosion properties. The high strength to weight ratio for this material is desirable for future weight critical marine, aerospace, and biomedical applications. In particular, the Navy after next is exploring smaller, faster, lightweight ships for rapid response which makes structural weight issues increasingly important for future combatants. To address the needs of future naval combatants, this research examines an alternative joining technology, friction stir welding (FSW). This work focuses on FSW of Ti-5111 (Ti-5Al-1Sn-1Zr-1V-0.8Mo), a near alpha (α) alloy. Developed as a lower cost alternative to Ti-100 (Ti-5Al-2Cb-1Ta-0.8Mo) in the late 1980s by Titanium Metals Corporation (TIMET), Ti-5111 is a naval alloy of interest for high strength structures. During Navy qualification of this alloy, Ti-5111 properties were evaluated on production ingots fabricated into plate, bar, forgings, and welding wire. Welding of Ti-5111 under the Metallic Materials Advanced Development and Certification Project (MMADCP) of Ti-5111 for critical applications [MMADCP] and ONR Programs [Neuberger] focused primarily on gas tungsten arc welding as discussed below in Section 1.1.2. Prior to this study, there was little research or development of alternative joining techniques, such as friction stir welding, for Ti-5111. Under support from the Office of Naval Research, this study aims to use experimental welding, physical simulation, and constitutive modeling to gain a fundamental understanding of the relationship between processing parameters, microstructure, and mechanical properties of experimental Ti-5111 friction stir welds.

1.1.1 Fundamentals of Titanium

The physical metallurgy of titanium alloys is highly dependant on the composition of phase-stabilizing elements and on the processing of the material. Based on the composition and phases present, titanium alloys can be classified into four groups: hexagonal close packed alpha (α), near alpha (near α), alpha-beta ($\alpha+\beta$), and body-centered cubic beta (β). The work discussed in this research focuses on near α titanium alloys, thus this chapter will primarily discuss the general properties and physical metallurgy of titanium and its alloys. A large focus of this work will be placed on near α and $\alpha+\beta$ alloys. A more in depth discussion on the production, microstructure, and mechanical properties of α, $\alpha+\beta$, and β can be found in Lutjering and Williams [Lutjering].

1.1.1.1 Basic Properties of Titanium

Compared to other structural metals, titanium has the highest strength to density ratio with a high melting temperature and high yield strength. The physical properties of titanium compared to other common structural metals are shown in Table 1. However, the high cost has limited the wide spread use of titanium. In addition to the high starting cost of raw material, titanium is highly reactive. An inert atmosphere or vacuum is necessary in titanium production and joining to prevent contamination which leads to high fabrication costs.

Table 1. Physical properties of titanium compared to other structural metals [Luterjing]

	Ti	Fe	Ni	Al
Melting temperature	1670	1538	1455	660
Crystal structure	BCC→HCP	FCC→BCC	FCC	FCC
Room temperature E (GPa)	115	215	200	72
Yield stress (MPa)	1000	1000	1000	500
Density	4.5	7.9	8.9	2.7
Comparative corrosion resistance	Very High	Low	Medium	High
Comparative reactivity with oxygen	Very High	Low	Low	High
Comparative price of metal	Very High	Low	High	Medium

As mentioned in Section 1.1.1, Ti-5111 is a near α alloy. Identified in ASTM B 265 as ASTM Grade 32, Ti-5111 physical properties are given in Table 2. Additionally, representative mechanical properties provided by TiMet are given in Table 3. Ti-5111 undergoes a duplex anneal with rolling of plate in the β phase and a α+β anneal with an air cool. Near α and α+β alloys are qualitatively similar in terms of physical properties, but have distinct differences in the transformation temperatures and kinetics which will be discussed later in this chapter.

Table 2. Ti-5111 Physical Properties [Timet]

Property	At T (°C)	Value (Sl)
Density	22	4.43 g/cm^3
β Transus	980	
Thermal Conductivity	24 146 300	7.5 W/m^{3}K] 8.87 10.7
Specific Heat	24 146 300	0.533 J/gK 0.572 0.613
Electric Resistivity	24 152 301	153 Ohm cm 164 173
Coefficient of Thermal Expansion	50 100 150 200 250 300	8.2 x 10^{-6}m/m/°C 8.7 8.9 9.1 9.3 9.4
Modulus of Elasticity	RT	1.07-1.14 x 10^{5}MPa

Table 3. Ti-5111 Representative Mechanical Properties [Timet]

Direction	Ultimate Tensile Strength, MPa (ksi)	0.2% Yield Strength, MPa(ksi)	Elongation % (4D)	Reduction of Area, %
3/8 plate ß roll plus α/ß anneal (60 min@1745 °F(952 °C), air cool)				
L	814 (118)	710 (103)	15.5	29
T	883 (128)	807 (117)	15	35

1.1.1.2 Phases in Titanium

Upon cooling pure titanium undergoes an allotropic transformation from a body centered cubic (BCC) structure to a hexagonally close-packed (HCP) structure at 882ºC. The BCC structure is known as the β phase and is stable up to the melting temperature of pure titanium (1670 ºC). The HCP structure is known as the α phase. The transformation temperature in β→ α+β is commonly referred to as the β transus. The transformation temperature, α phase, and β phases are highlighted in the Ti-Al phase diagram in Figure 1. The lattice parameters for α (up to 885 ºC) along the a axis is 2.95Å and along the c axis is 4.68 Å. The lattice parameter for β (885 ºC to 1670 ºC) is 3.31 Ấ.
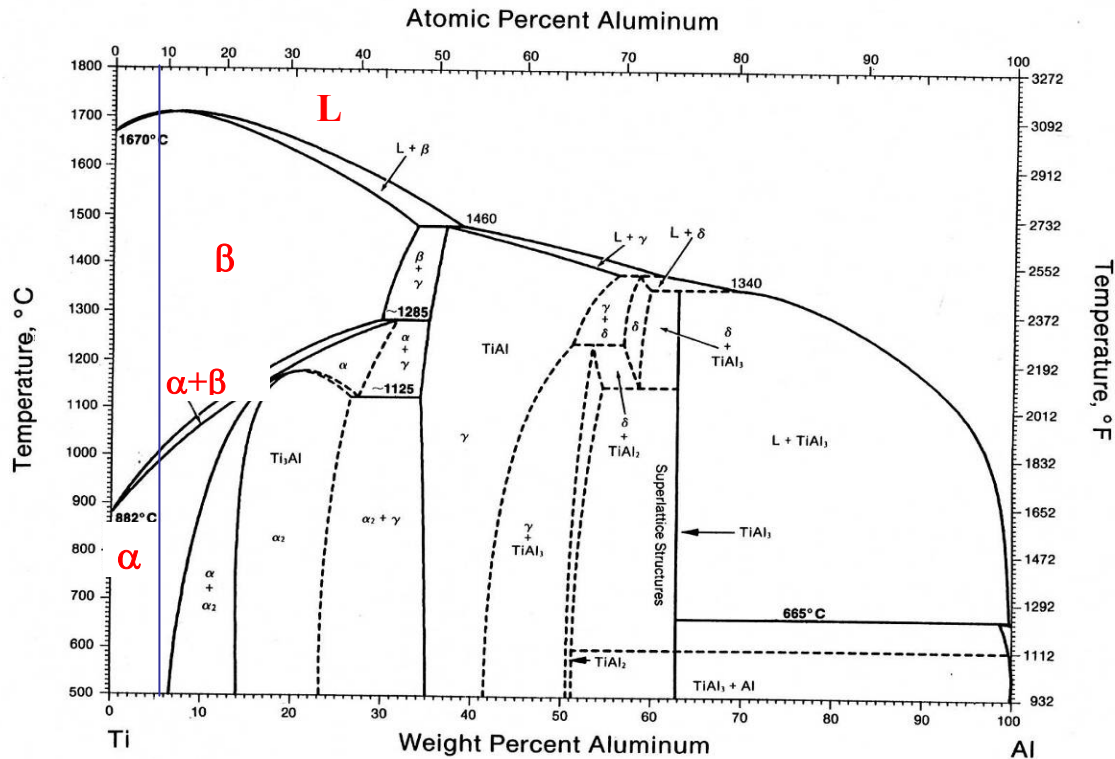
Figure 1. Binary phase diagram for titanium-aluminum. The blue line represents the amount of Al in Ti-5111 [ASM]

While pure titanium is very ductile, it has relatively low strength. Titanium strengthening often occurs through the use of alloying elements. The alloying elements affect the β transus temperature. Elements that raise the β transus are known as α-stabilizers whereas elements that lower the β transus are known as β-stabilizers. Known α-stabilizers such as aluminum (Al), oxygen (O), carbon (C), and nitrogen (N) are soluble in the α phase. Aluminum is widely used as an alloying element for titanium because of solid solution strengthening. However, greater than 8% Al can cause embrittlement. Tin (Sn) and zirconium (Zr) are considered neutral elements because they are soluble in both α and β phases. β stabilizers can be divided into two classifications: β-isomorphous and β-eutectoid elements. A pseudo-binary β isomorphous phase diagram is shown in Figure 2 [ASM].
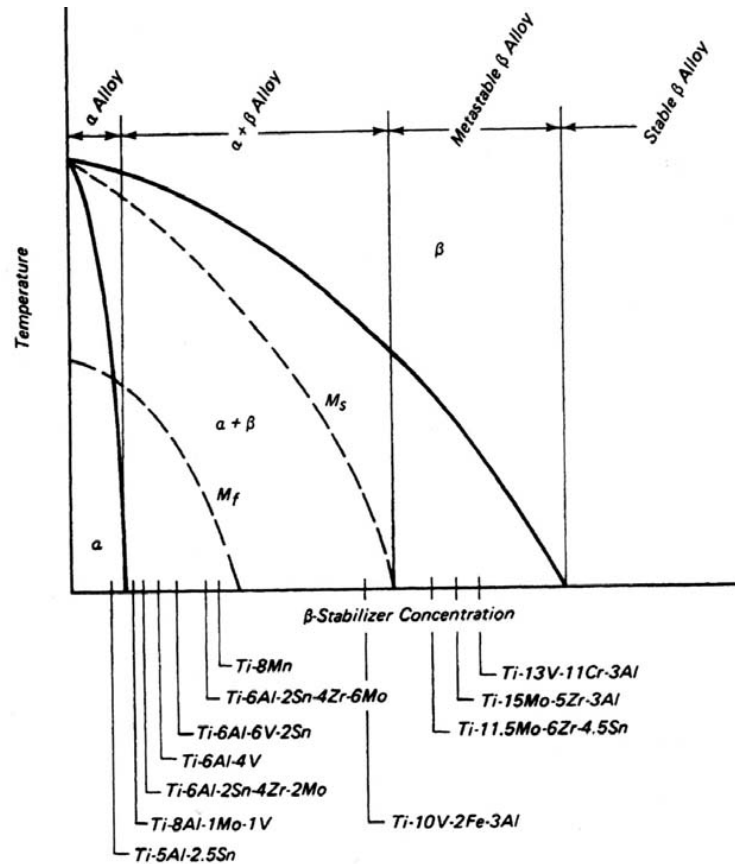
Figure 2. Psuedo-binary β isomorphous phase diagram [ASM titanium]

The ASTM chemistry for Grade 32 Ti-5111 is given in Table 4. (Ti-5Al-1Sn-1Zr-1V-0.8Mo). As discussed above, for Ti-5111 α stabilizers of Al, O, N, C are added for strength. Neutral elements Sn and Zr are also added for strengthening. β-stabilizer silicon (Si) is added for enhanced creep resistance and fracture toughness. Both vanadium (V) and molybdenum (Mo) add strength, but Mo increases fracture toughness.

Table 4. ASTM B 265 Grade 32 Ti-5111 (Ti-5Al-1Sn-1Zr-1V-0.8Mo) [ASTM B 265]

Element	ASTM B 265 Grade 32
Aluminum	4.5-5.5
Tin	0.6-1.4
Vanadium	0.6-1.4
Zirconium	0.6-1.4
Molybdenum	0.6-1.2
Iron	0.25 max
Silicon	0.06-0.14
Oxygen	0.11 max
Carbon	0.08 max
Nitrogen	0.03 max
Hydrogen	0.015 max
Titanium	Remainder

In near α and $\alpha+\beta$ alloys, a fully lamellar microstructure forms upon slowly cooling from above the β transus in near equilibrium conditions. As the alloy cools from the β-phase, metastable β transforms to α through nucleation and growth. The α phase initiates nucleation from the β grain boundary creating a continuous α network known as grain boundary α. During continued cooling, α plates (or lamellae/lath) form either at the prior β grain boundary or from a grain boundary α. The α plates grow into the β grain as parallel plates [Peters, Luterjing] with retained β at the edges of the α plate. The preferred orientation of the α plates belongs to the variant of the Burgers relationship relating the crystallographic orientation for α and β. First identified in zirconium and later confirmed for titanium, the Burgers relationship is defined as:

$$(110)_\beta \parallel (0002)_\alpha$$
$$[1\text{-}11]_\beta \parallel [11\text{-}20]_\alpha$$

A schematic of the crystallographic relationship of the α plates and the retained β is shown in Figure 3. As α plates continue to grow under the Burgers relationship, plates with the same orientation are known as α colonies. As the α colony approaches the interior of the prior β grain, it encounters other α colonies that have nucleated from other prior β grain boundaries

[Lutjering].   This sympathetic nucleation and growth generates the fully lamellar microstructure.
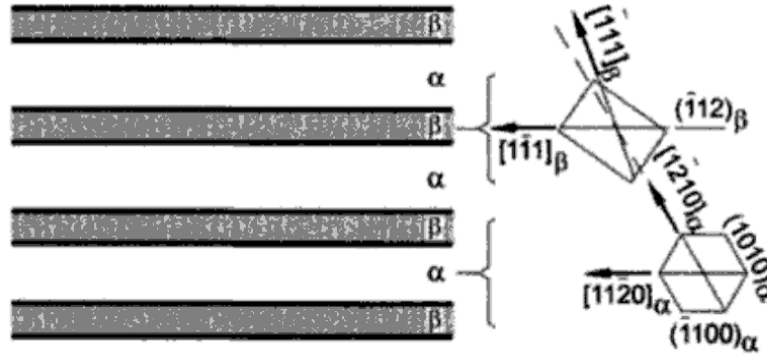
Figure 3. Schematic of the morphology and crystallographic orientation of the α and βphases in Ti. [Luterjing]

With respect to near α and α+b alloys, the cooling rate from β transus plays an important role in the size of the α colonies and α laths. Higher cooling rates cause a reduction in α colony and lath size. This reduction in α colony size causes α lath nucleation to form at the boundaries of other α colonies. The new α lath is almost at a 90 degree angle to the broad face of the original α colony to minimize elastic strain energy and generating a "basketweave" or Widmanstatten structure.

Unlike other near α alloys, Ti-5111 wrought plate processing is unique [Ma]. Typical α+β alloys have a "β-annealed" structure. This microstructure occurs through homogenizing in the β field then deforming in the α+β field. The plate is then recrystallized above β transus and then slow cooled with a α+β stress relief. In contrast, Ti-5111 is deformed beginning in the β field and ending in the α+β field. Ti-5111 is then given an α+β anneal at 954ºC with an air cool.   This processing generates a "β-processed" condition more commonly found in β

alloys. β-processing results in deformed or discontinuous grain boundary α. The typical microstructure of Ti-5111 is shown in Figure 4.
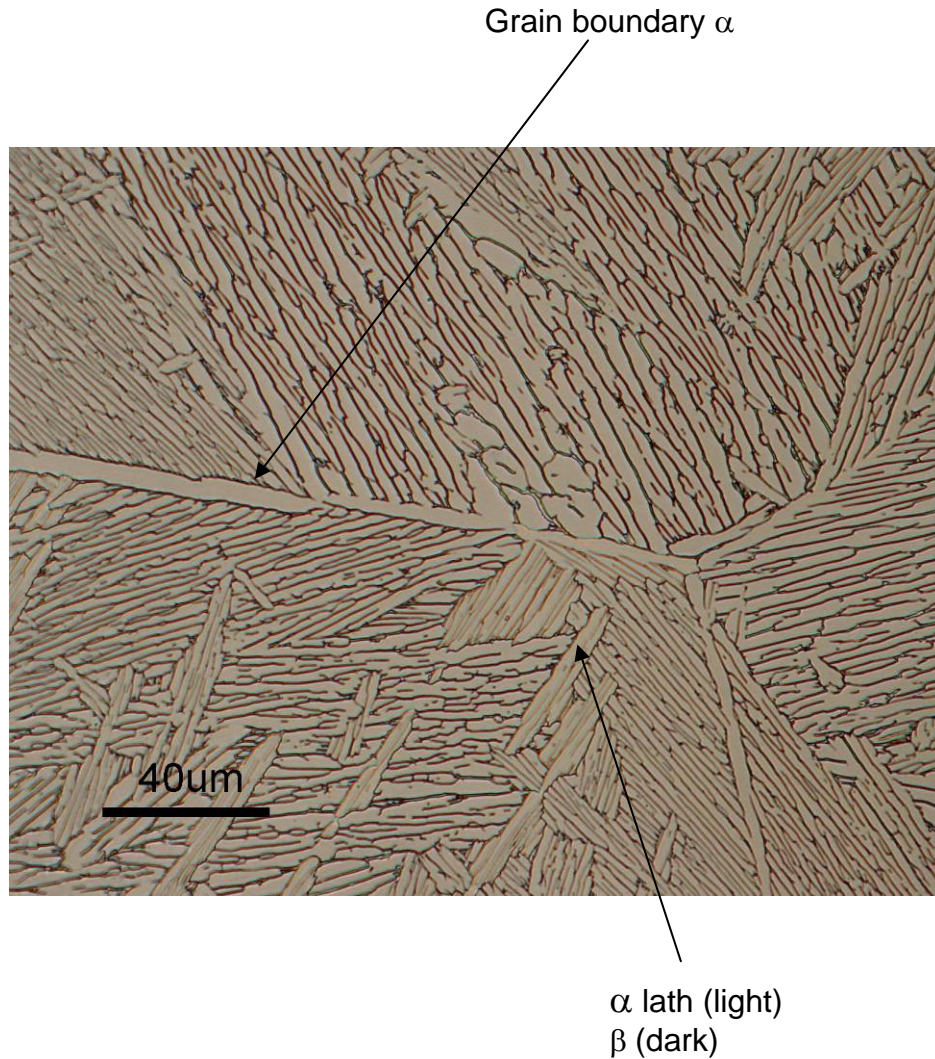
Figure 4. Ti-5111 microstructure (transverse to the rolling direction) showing the typical α+β microstructure in Ti-5111.

1.1.1.3 Deformation Mechanisms in Titanium Alloys

Deformation mechanisms for hexagonally close packed (HCP) materials are more complex than their cubic counterparts. α phase titanium relies on twinning in addition to dislocation

slip. Twinning modes are important for commercially pure (CP) Ti and some α alloys, with

observed twinning modes in CP Ti of $\{10\bar{1}2\}, \{11\bar{2}1\},$ and $\{11\bar{2}2\}$. However, twinning

becomes less important in α+β and β alloys because solute atoms such as aluminum and

oxygen suppress twinning [Luterjing].

In metals, plastic deformation occurs through slip in which the planes of atoms exceed a

critical shear stress and the atoms move along a preferred plane. Slip (or glide) typically

occurs on the plane with the highest density of atoms and in the direction with the closest

packed direction and shortest Burgers vector [Dieter]. For HCP systems, the basal plane

(0002) has the highest packing density along the close-packed direction of $<11\bar{2}0>$. There

are three independent slip systems based on the close packed direction (Equation 1).

$$\text{Burgers vector in HCP crystals:} \, b = \frac{a}{3} <11\bar{2}0> \qquad \textbf{Equation 1}$$

Based on the von Mises criterion, the most likely non-basal Burgers vector for $\vec{c} + \vec{a}$ slip, as

well as the independent slip directions and slip planes are shown in Table 5.

Table 5. Slip systems for HCP α titanium

Slip System Type	Burgers vector type	Slip Direction	Slip Plane
1	$\vec{a}$	$<11\bar{2}0>$	(0002)
2	$\vec{a}$	$<11\bar{2}0>$	$\{10\bar{1}0\}$
3	$\vec{a}$	$<11\bar{2}0>$	$\{10\bar{1}1\}$
4	$\vec{c} + \vec{a}$	$<11\bar{2}3>$	$\{11\bar{2}2\}$

In contrast, for BCC systems, there are three near close packed planes {110}, {112}, and

{123} with the close-packed direction of <111>. Within BCC there are 48 possible slip

systems [Dieter]. Comparing the possible slip systems for α (HCP) to β (BCC), there tends

to be a loss of ductility with extreme orientation dependence in HCP systems.

1.1.2 Traditional Welding Techniques in Titanium

Titanium alloys have been joined through conventional fusion welding techniques such as gas tungsten arc welding (GTAW) and gas metal arc welding (GMAW). Welding is defined as the joining of two or more pieces through the application of heat or pressure, with or without the use of a filler metal [Welding Handbook]. GTAW is a commonly used welding technique for titanium alloys that uses heat generated by an arc between a non-consumable tungsten electrode and the work piece for joining. This is shown schematically in Figure 5. In GTAW, a filler metal can be introduced into the weld pool in a manual, mechanized, or semi-automatic form.
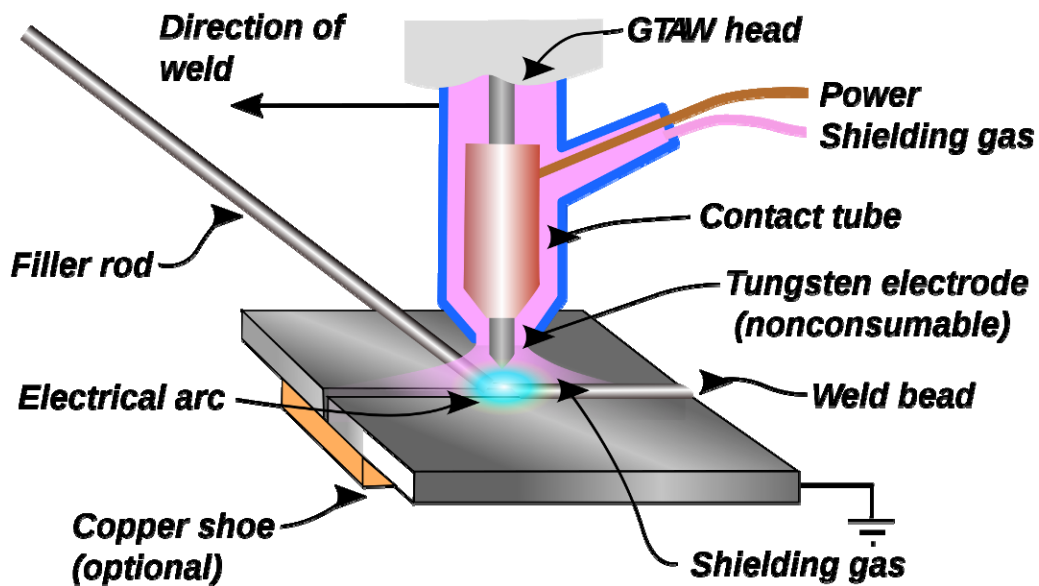
Figure 5. Schematic of gas tungsten arc welding (GTAW) [Welding Handbook]

GTAW is most commonly used for thin materials due to the low deposition rates. In contrast GMAW uses a continuous filler metal electrode to generate an arc with the work piece and is

ideal for automated weld processes in large and/or thick structures. Welding microstructures can be classified as having three regions:

1) Base metal – as received unaffected parent material that has not experienced temperature affecting the microstructure or properties

2) Heat affected zone (HAZ) – this area has experienced temperatures affecting the microstructure and/or mechanical properties

3) Weld – recast microstructure dependant on the weld metal composition. Welds are often described as matching, under-matched, or over-matched weld strength. The weld microstructure is dependent on the weld metal composition and on the cooling rate.

The problems associated with welding of titanium alloys include contamination and weld embrittlement from oxygen, nitrogen, and hydrogen incorporation during welding. Preventing atmospheric weld contamination (oxygen and nitrogen) and moisture contamination (hydrogen) requires the use of inert shielding gas around the weld torch and shielding gas trailing the weld torch at high welding speeds. Shielding protection on the backside of the work piece, or root side may also be required for through thickness welds. Inert shielding with argon or helium is required until the weld has cooled to below 427˚C to prevent contamination [AWS G2]. Other potential techniques for joining titanium include electron beam welding, plasma arc welding, laser welding, or friction welding [Titanium handbook]. A potential welding technique for titanium that has shown promise for joining aluminum and steel is friction stir welding (FSW).

1.1.3 Friction Stir Welding

Developed by TWI in the early 1990s, friction stir welding uses a non-consumable tool to generate frictional heat to plastically deform and mix metal to form a consolidated joint as shown schematically in Figure 6 [Thomas]. A cylindrical tool with a small extended probe is rotated at high rpm and plunged into a material. The rotation of the tool in the material generates frictional heat allowing the material to soften and plastically deform. In the case of a butt joint, the probe is applied to the interface of the two plates. A downward forging force is applied as the tool traverses along the joint interface. Material is physically moved with the tool to create plastic deformation within the joint. The advancing side of the weld is identified by the tangent of tool rotation in the direction that the weld traverses. The retreating side of the weld has the tangent of tool rotation opposing the direction of the weld traverse. The leading edge of the tool is in the direction of the weld traverse and the retreating edge of the tool is located behind the tool.
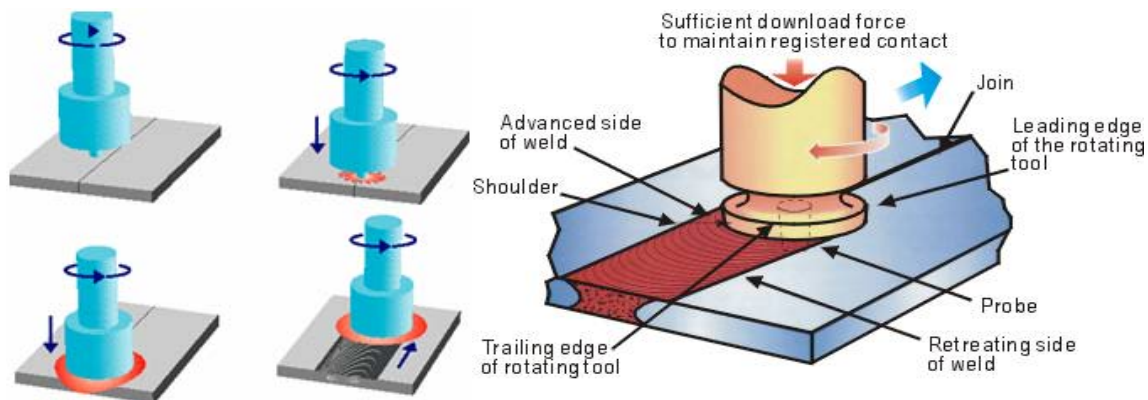
Figure 6. Schematic of the friction stir welding process [TWI]

FSW is a solid-state process that does not reach melting temperatures. This results in reduced distortion from residual stresses and heat due to melting during traditional gas metal

13

arc welding (GMAW). FSW has been widely developed and accepted in the automotive and aerospace industry for aluminum alloys. FSW of steels is under continued development.

1.1.3.1 Friction Stir Welding of Metals

Since the development of friction stir welding in 1991, the majority of research has been focused on aluminum alloys. A review in 2005 by Mishra [Mishra 2005] summarizes the current state of the technology.   In addition to joining aluminum alloys, this joining technology has been applied to higher temperature materials, such as steels, bronzes, and most recently to titanium. Friction stir processing, a variant of friction stir welding, is used to locally modify a microstructure with no joint. This was first used by Mishra et al [Mishra 2000] to change the microstructure for super plastic forming. An in depth review of friction stir welding of metals can be found in ASM's Friction Stir Welding and Processing [Mishra 2007].

1.1.3.2 Friction Stir Welding Microstructures

In a typical friction stir weld, there are distinct regions as schematically defined in Figure 7 as:

A) Base material – unaffected parent material that has not experienced deformation or temperature affecting the microstructure or properties

B) Heat affected zone (HAZ) – similar to arc welding, this area has experienced temperatures affecting the microstructure and/or mechanical properties. This area has not experienced deformation

C) Thermomechanically affected zone (TMAZ) – this region has experienced plastic deformation in addition to heat from the process. This area has not undergone recrystallization.

D) Weld nugget/ Stir Zone (SZ) – this region has experienced temperatures and deformation to become fully recrystallized. This area had immediate interaction with the pin tool.
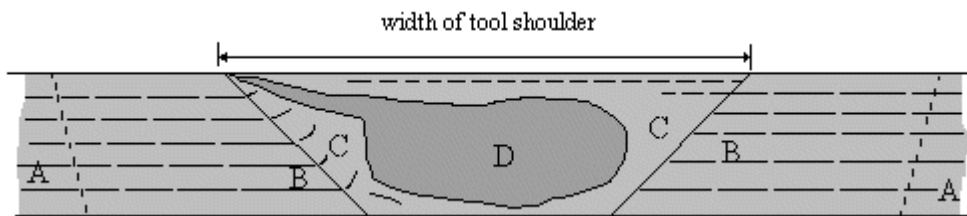
Figure 7. Schematic of friction stir welding. A) Unaffected base material B) Heat affected zone (HAZ) C) Thermo-mechanically affected zone (TMAZ) D) Stir zone [TWI]

In titanium there is no clear difference between the HAZ and TMAZ. A suggested nomenclature for friction stir welding microstructures in titanium combined the HAZ and TMAZ into a transition zone [Pilchak].

1.1.3.3 Friction Stir Welding of Titanium

FSW of titanium has the potential to reduce fabrication costs as well as joint and process simplification compared to conventional joining techniques because it does not require the use of filler material and has the potential for up to ½" depth of penetration in a single pass. Additionally, joining below melting temperature may reduce contamination. A highly automated process, FSW also has the possibility to reduce inspection requirements. Early investigations show promise for friction stir welding of titanium alloys [Mishra 2007, Lienert, Ramirez, Renyolds] such as Timetal-21S (a metastable β-phase alloy), Ti-6-4 (a α/β alloy) and Ti-CP (a single phase α alloy). Friction stir welding of titanium alloys requires

unique fixturing to prevent atmospheric contamination similar to arc welding. Friction stir welding has been described in terms of hot working. Typical hot working temperatures range from 50-60% of the melting temperature. The high melting temperature of titanium requires high temperature tool materials for welding. Unlike aluminum alloys that use common tool steels for friction stir welding, welding of titanium alloys require use of refractory metal based tools, such as tungsten. Lanthanated tungsten (WL10), tungsten, tungsten-25% rhenium (WRe), and tungsten-rhenium with HfC have been used for welding titanium. These tool materials have also been used for welding steel alloys. Unfortunately, due to the reactivity of titanium at high temperatures, polycubic boron nitride (PCBN) tools that have shown success with steels cannot be used with titanium. Welding results for titanium alloy systems will be discussed in the following chapters for comparison to friction stir welding of Ti-5111, a naval alloy of interest.

1.2. Objectives

Friction stir welding is a dynamic system involving high strains, strain rates, and temperatures. The microstructural development and deformation mechanisms involved in friction stir welding of titanium are not well understood due to the inability to isolate the effect of strain, strain rate, and temperature in the FSW process.

The main objectives of this thesis are to investigate the microstructural evolution and texture development of Ti-5111 during friction stir welding through the use of experimental welding, constitutive modeling, and physical simulation and to determine the effect of FSW on the mechanical properties of Ti-5111.

CHAPTER 2: GENERAL PROCEDURES

2.1. Base Metal Properties

Ti-5111 base material was procured from Concurrent Technologies Corporation and supplied to Edison Welding Institute for joining. A base metal specimen (A) and friction stir weld metal (B) was sent to Luvak, INC for wet chemical analysis. Analysis of specimen B focused on the major alloying elements. The chemical analysis techniques and the associated ASTM specification are shown below. The chemistry of the elements below conforms to the specification requirements of ASTM B 265, Grade 32.

Table 6. Chemical analysis of A) base metal and B) friction stir weld metal

Sample Identification	A	B
	%	%
Nitrogen	.003	---
Carbon	.011	---
Hydrogen	.0034	---
Oxygen	.092	---
Iron	.047	---
Aluminum	5.0	4.9
Vanadium	1.0	1.0
Tin	1.1	1.1
Molybdenum	.82	.81
Zirconium	.96	.98
Silicon	.079	---
Titanium	90.8	---

Luvak, inc. Methods: Carbon - Combustion infrared detection - ASTM E 1019-03
Oxygen & Nitrogen - lnert gas fusion - ASTM E 1409-05
Hydrogen - lnert gas fusion - ASTM E 1447-05
All others - Direct current plasma emission spectroscopy in accordance with ASTM E 1097-07

2.2. Scanning Electron Microscopy (SEM) and Optical Microscopy (OM)

2.2.1 Specimen preparation

Areas of interest in the Ti-5111 friction stir weld were sectioned with a SiC abrasive cut-off saw blade. Specimens were mounted in either castable epoxy resin or thermosetting epoxy compound. Specimens were polished on a Struers Abropol 2 automated polisher using an initial grind plane with 120 grit SiC grinding paper. After the initial grinding specimens were ground with 240 and 320 SiC grinding paper for 1 minute each. A fine grind plane was obtained using 600 grit for 30 seconds and another 600 grit paper for an additional 30 seconds. A final polish with 6um MOL polished at 150N of force with a lube of 5 and a suspension of 5 was performed for 4 min. After fine polishing, specimens were etched in Kroll's reagent and returned for a repeat 6um MOL step polish. A final polishing using a mixture of 50 ml Kroll's reagent and 25 ml H_2O_2 to 75 ml of OP-S was used to form a slurry diamond on CHEM for 3 minutes at a polishing force of 150N.

2.2.2 OM Operating Parameters

Optical metallography and images were taken with a LECO Olympus optical microscope and a Nikon digital camera at the magnifications indicated in the image. Polarized light was used to enhance grain boundary α, distinct α colonies, and β plates.

2.2.3 SEM Operating Parameters

Three different SEMs were used for microstructural characterization. A JEOL 6400V with an EDAX electron dispersive x-ray spectroscopy (EDS) detector was used in the early research. Electron backscatter diffraction was performed at both Naval Research Laboratory

and at Naval Surface Warfare Center. Operating parameters for the JEOL and Hitachi SU660 and U70 field emission SEM are indicated within the individual sections.

2.3. Electron Backscatter Diffraction (EBSD)

2.3.1 Specimen preparation

Mounted specimens used in optical microscopy were polished with colloidal silica for 4 hours. Areas of interested were identified with fiduciary markings for further EBSD analysis.

2.3.2 Operating Parameters

Most EBSD was performed in the Hitachi 660 SEM. Electron backscatter diffraction analysis was performed with an EDAX detector with a typical working distance of 21 mm and accelerating voltage of 15-20kV. Automated acquisition and pattern indexing was performed with TSL OIM Acquisition v.5 software. TSL OIM Analysis v.5.3.1 was used for EBSD analysis.

2.4. Transmission Electron Microscopy (TEM)

2.4.1 Sample Preparation

Early experiments used mechanical polishing of 2mm x 2mm x 0.5mm square sections. After mechanical polishing and thinning to 100μm, the specimens were mounted on 3mm copper grids. Further polishing utilized a tripod polishing technique developed by Salamanca-Riba [Li and Salamanca-Riba] to sequentially thin the selected area to 1μm prior

to ion milling. The final TEM sample was obtained by ion milling with Ar2+ ions with 3.3kV and 1.3mA to obtain electron transparency.

2.4.1.1 Cutting TEM samples from welded specimens

Specimens were sectioned from areas of interest using a SiC abrasive cut-off saw blade. Cross-sectional slices of ~0.5mm in thickness were taken from the advancing and retreating sides of the stir zone. After polishing for EBSD analysis, samples were mechanically polished to thin the selected areas using 60μm silicon carbide paper for 15 minutes. 3mm TEM discs were removed from the cross-sectional areas using the South Bay slurry disc cutter with a diamond tool. Cutting burrs were removed with a tripod polishing with 60 μm silicon carbide paper for 5 minutes, 30 μm diamond paper for 5 minutes, and 15 μm diamond paper for 5 minutes.

2.4.1.2 Thinning specimens from selected areas

3mm discs from selected areas of the friction stir weld were jet polished using an Electron Microscopy Science Model 550D vertical jet polisher at a light sensitivity of 3, 65 V, and 400mA. Specimens were jet polished in a solution of 13% HCL 87% methanol at -60°C [Kestel]. After jet polishing, the specimen was ion milled in a Fischione Model 1010 ion mill. Typical parameters for ion milling are given in Table 7. Ion milling times were chosen to prevent specimen damage due to ion milling.

Table 7. Ion milling parameters for TEM sample preparation of Ti-5111

kV	mA	Rotation (°)	Degree	Time (min)
5.0	5.0	360	8	15
2.0	3.0	360	8	10
0.3	3.0	360	8	5

2.4.2. TEM Operating Parameters

All TEM analysis was performed on a JEOL 2100 LaB6 and a JEOL 2100 field emission TEM at the University of Maryland. Specific operating parameters for given experiments are noted in the following chapters. A Gatan heating holder was used for selected TEM experiments and is described in the following chapter.

2.5. Thermomechanical Simulation Gleeble 1500 D

2.5.1 Sample Preparation

A Ti-5111 plate was sectioned in the rolling direction and turned on a lathe to form a 1.25cm diameter titanium rod. The rod was sanded down with emory paper to remove surface grit and dirt.   A silicon carbide cutoff wheel was used to cut the titanium rod into 1.25cm specimens.   Cutting burrs were removed using 60 grit SiC paper. Omega Type R thermocouples were welded to the specimens using an electric discharge mini-arc welder under argon shielding for thermal control. Type R thermocouples are platinum – platinum 10% rhodium wires that can reach temperatures up to 1450ºC. Omega CC thermal cement was applied after thermocouple welding for additional attachment strength. Thermal cement was cured for 24 hours after application.

2.5.2. Gleeble Operating Parameters

Thermomechanical compression experiments were performed on a Gleeble 1500D using Ti-5111 plate material. Specimens were tested in the Gleeble using ISO-t anvils coated with an aerosol spray of boron nitride lubricant. Tantalum sheets were placed at the connection between the anvil and the specimen to protect the anvils. Specimens were tested under Ar

shielding to prevent specimen contamination.   Initial parameter development and experimentation was carried out on commercially pure grade 2 titanium.   Programs were developed in .gsl format and converted .tab for system operation.

CHAPTER 3: MICROSTRUCTURAL EVOLUTION OF FRICTION STIR WELDED TI-5111

3.1. Experimental Welding Procedures

Experimental 12.7mm thick friction stir butt welds of Ti-5111 were fabricated at the Edison Welding Institute (EWI) as a part of collaborative effort with Naval Research Laboratory (NRL) and Naval Surface Warfare Center Carderock Division (NSWCCD). EWI examined two different tool designs using a proprietary tool material. The designs minimized the tool shoulder with a 7.62mm (0.3") pin tip diameter (identified as A) and a 10.16mm (0.4") pin tip diameter (identified as B). A representative pin tool design is shown in Figure 8. Spindle speed varied from 140 to 210 revolutions per minute (rpm) and travel speed varied from 0.84 to 1.48 mm/s (2 to 3.5 inches per minute (ipm)). The weld joint geometry was a butt joint in flat 1G welding position or bead on plate (BOP). All welds were fabricated under argon shielding gas to prevent weld and tool contamination. A summary of the weld development was provided by EWI and is given in Table 8. Wormhole defects were found in welds with high travel speed and high spindle speed. Weld development led to optimized parameters of 200 rpm and 1.48mm/s. Radiographs of welds BJ-11, BJ-12, and BJ-13 are shown in Figure 9. Based on weld quality and steady state behavior, Weld BJ-12 section 8.5-12.5 inches was used for analysis. This weld was fabricated using a 7.62mm pin tip at a travel speed of 1.48mm/s and spindle speed of 200 rpm with 444.5µm advance per revolution.

Figure 8. Representative pin tool design

Table 8. Weld parameter development provided by EWI for FSW of Ti-5111

	Pin Tool Design	Weld Configuration	Spindle Speed (rpm)	Travel speed (ipm)	Weld Length (in)	Notes
BJ-1	A	Butt	190-210	3.5	10	Wormhole
BJ-2	A	Butt	180-200	3.5	14.5	Wormhole
BJ-3	A	Butt	170-150	3.5	12.5	Wormhole; void free @150rpm
BJ-4	A	Butt	150	3.5	25	x-ray voids
BJ-5	A	Butt	150	3.5	25	x-ray voids
BJ-6	A	Butt	140-150	2.5	8.75	Wormhole and voids
BJ-7	A	Butt	150	2	8.75	Wormhole and voids
BJ-8	B	BOP	150	2	9	Faint void at beginning
BJ-9	B	BOP	140	2	10	No void
BJ-11, 12, 13	A	Butt	200	3.5	24	See radiographs
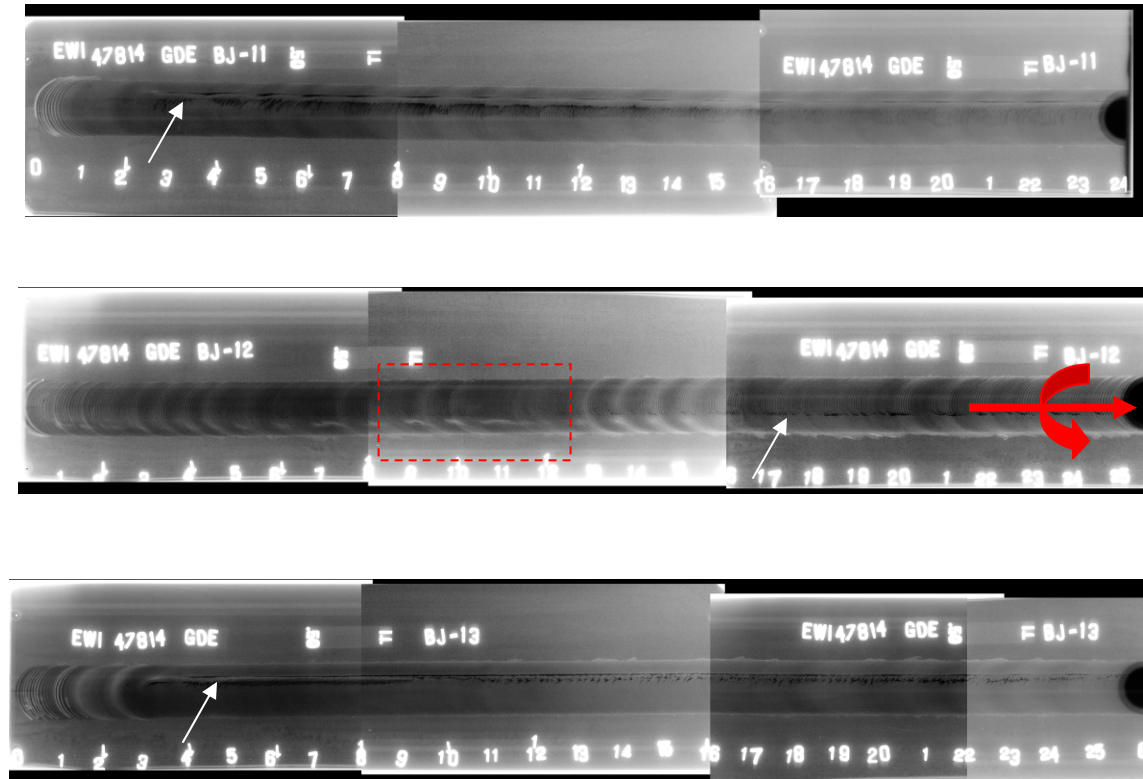
Figure 9. Radiographs of friction stir welds BJ-11, BJ-12, and BJ-13. BJ-12 between 8.5 and 12.5" markers was selected for 12.7mm weld analysis. The selected area is indicated in the radiograph with the red dotted box. Wormhole defects are shown with arrows.

Welds were performed under a position control mechanism. Raw load and torque data for the weld was provided by EWI. Load data taken during welding of BJ-12 shows forging

force loads ranging 4000 to 10000lbs (Figure 10). This large load variation was persistent throughout the weld. In stark contrast, the traverse force remained around 1000 lbs. Sufficient forging force is necessary for weld consolidation. The inability to maintain a consistent forging force is due to the flow stress of the material and can result in defects as shown in Figure 9.

Load for 12.5mm Ti-5111 BG-12 weld
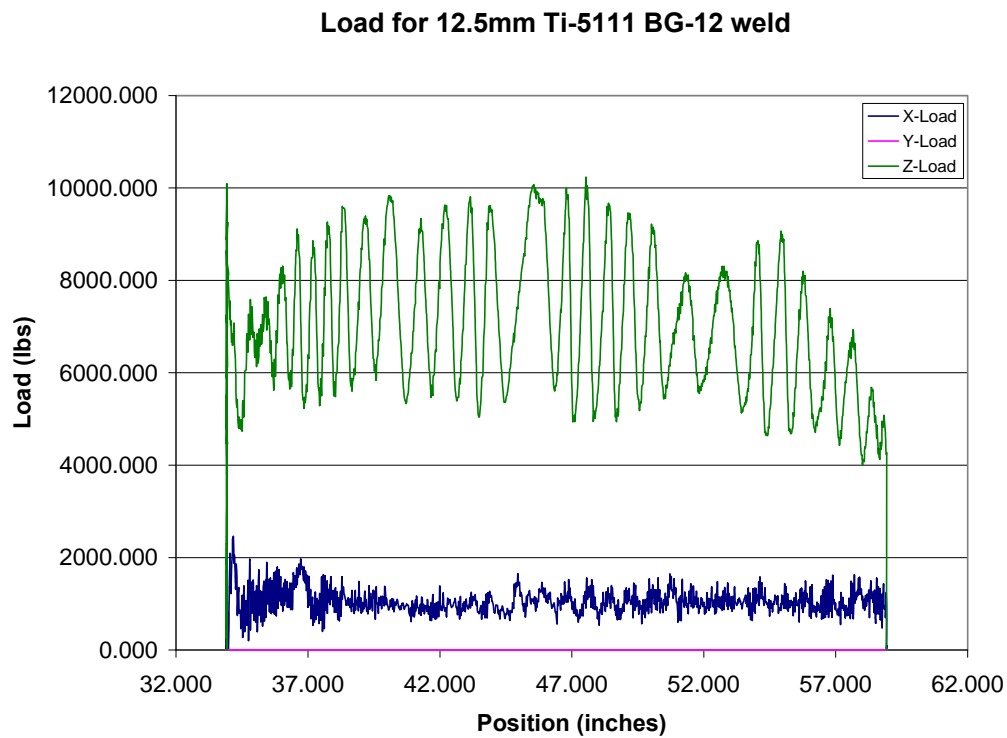
Figure 10. Load data for 12.7mm BJ-12 weld at 1.48mm/s and 200 rpm.

Using optimized parameters of 1.48mm/s and 200 rpm based on metallographic analysis during weld trials, sixteen K type thermocouples were embedded within 12.7mm Ti-5111 to gather temperature data during welding. The thermocouples were located on the surface as well as sub-surface for analysis of thermal gradients and cooling rates. The thermocouple positions are shown in Figure 11. Top surface temperature measurements used thermocouples 1-6, with thermocouples 3 and 4 closest to the weld. Temperature

measurements at the bottom of the weld, closest to the anvil, used thermocouples (TC) 13-16.

Temperature measurements for TC 8-11 are located mid-plane closest to the weld stir zone.

TC 7 and 12 were located at the sides of the plate.
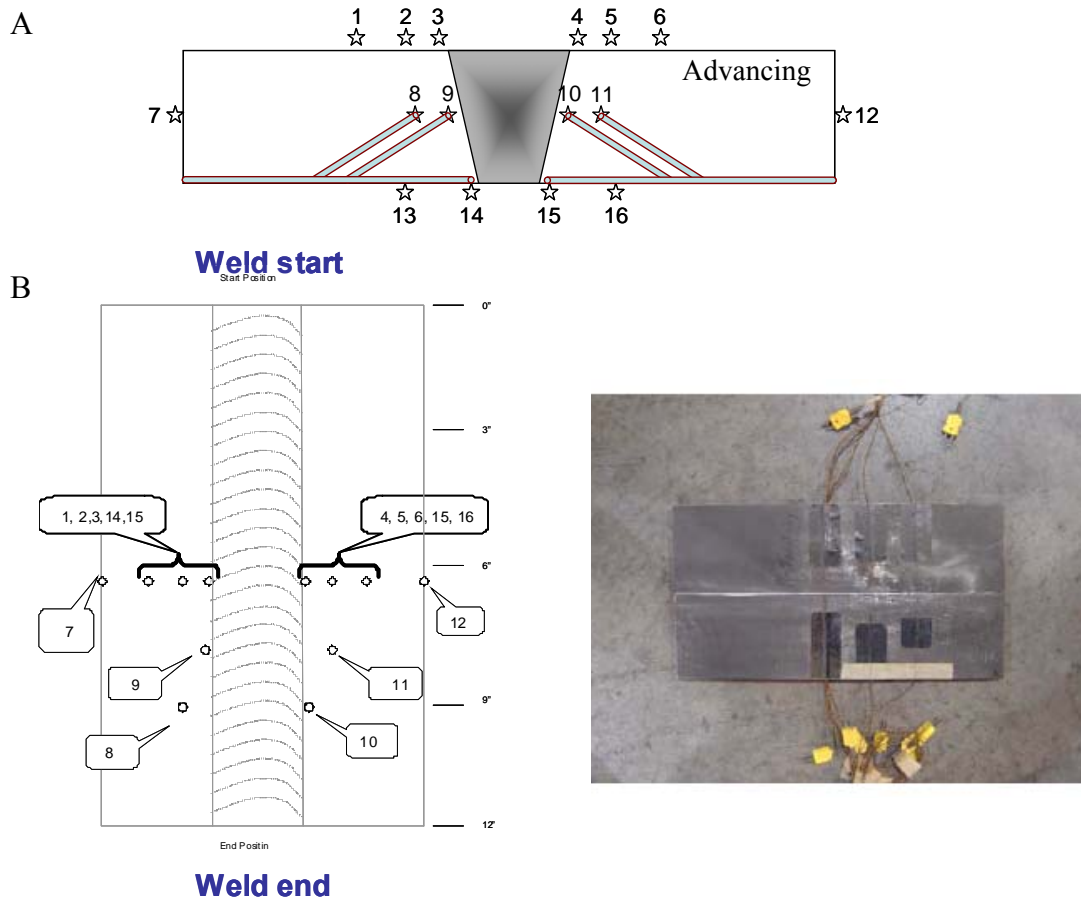
Figure 11. Thermocouple schematics. A) Position with respect to depth B) Position with respect to the weld C) Image of thermocoupled plate.

Thermocouple curves for the experimental data are shown in Figure 12. TC 1 was lost

during temperature collection. A peak temperature of 798 ºC was recorded by TC 3 located

on the advancing side of the weld. This is very close to TC 10 peak temperature of 796 ºC

located on the retreating side and embedded at mid-plane. Embedding thermocouples in

friction stir welding can be difficult due to the inherent nature of the process. Thermocouples

26

require intimate contact with the material for an accurate reading and the connection can be lost during the rotation of the pin tool. An example of this occurred in TC1. The shape of the TC 10 curve shows a truncated peak indicating that the maximum peak temperature experienced by the weld was most likely higher. A cross-section of this weld shows the TC 10 K type thermocouple 2mm from the edge of the weld (Figure 13). A comparison of the peak temperature relative to thermocouple location for all thermocouples is shown in Table 9. The natural asymmetry of the friction stir welding process generates variations between the advancing and retreating side temperatures. Advancing side temperatures are higher than retreating side temperatures at the same distance from the weld as shown in

Table 10. Temperatures closest to the weld on the advancing side were the highest peak temperatures recorded. The sharpest difference in temperature is closest to the tool shoulder on the top surface in TC 3 and 4 with a difference of 282 ºC. The next largest temperature difference can be found at the mid-plane of the plate 2mm away from the weld with a difference of 214ºC. Also at the mid-plane 12mm away from the weld, there is a peak temperature difference of 196ºC. There is a sharper difference between advancing and retreating side temperatures at the top surface of the weld due to the surface boundary condition. The low thermal conductivity of titanium results in poor heat transfer from the weld to the surrounding base material.
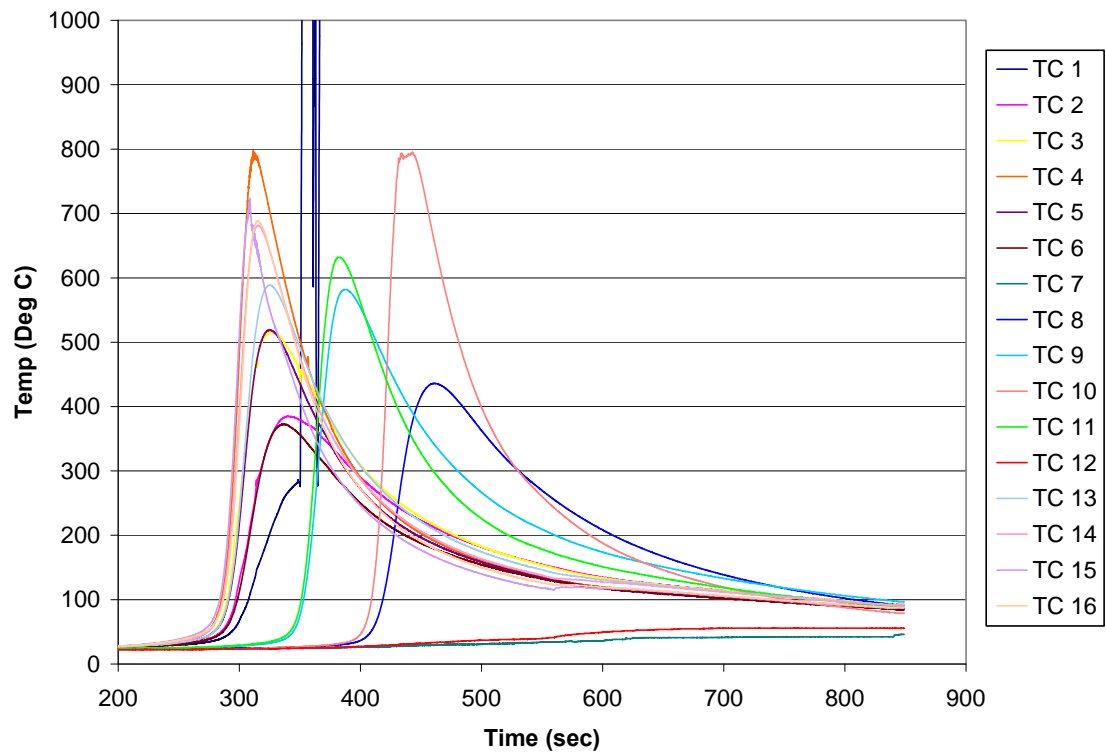
Figure 12. Thermocouple plots based on Figure 10 thermocouple schematics.
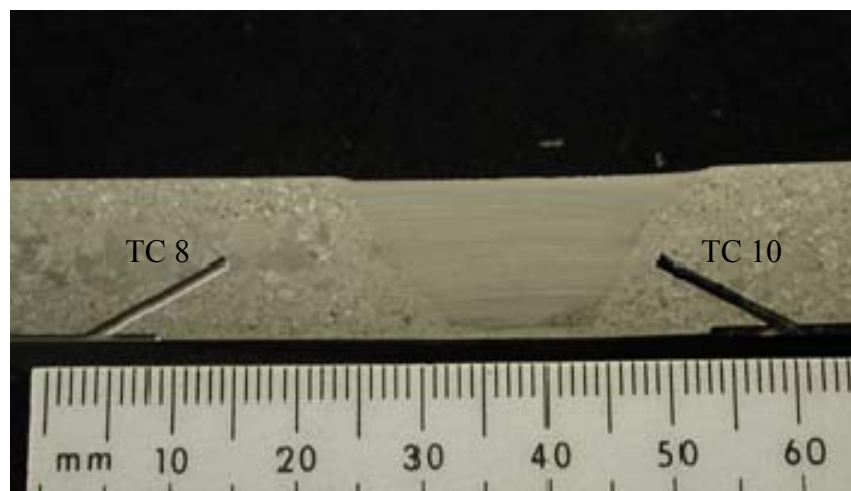
Figure 13. Thermocouple cross-section of TC 8 and 10

Table 9. Peak thermocouple temperatures during FSW of Ti-5111. Values in blue are surface thermocouples. Values in red are anvil thermocouples. Values in green are embedded thermocouples. Values in black are from the edges of the plate.

Location	Thermocouple	Max Value (°C)
Top Retreating	TC 1	NA
Top Retreating	TC 2	385
Top Retreating	TC 3	516
Top Advancing	TC 4	798
Top Advancing	TC 5	519
Top Advancing	TC 6	373
Side Retreating	TC 7	46
Mid-weld Retreating	TC 8	436
Mid-weld Retreating	TC 9	582
Mid-weld Advancing	TC 10	796
Mid-weld Advancing	TC 11	632
Side Advancing	TC 12	56
Bottom Retreating	TC 13	589
Bottom Retreating	TC 14	682
Bottom Advancing	TC 15	723
Bottom Advancing	TC 16	689

Table 10. Retreating/Advancing Side Temperature Comparison

TC Location	Retreating Peak Temperature (°C)	Advancing Peak Temperature (°C)	Δ Temperature (°C)
Top TC 2&5	385	519	134
Top TC 3&4	516	798	282
Side TC 7&12	46	56	10
Mid-plane TC 9&10	582	796	214
Mid-plane TC 8&11	436	632	196
Bottom TC 13&16	589	689	100
Bottom TC 14&15	682	723	41

In addition to 12.7mm welds, 6.35mm thick Ti-5111 welds were fabricated at EWI in an effort to simulate high, low, and nominal heat input conditions. Welding speed was maintained at a constant 225 rpm and varied travel speeds of 0.42mm/s (1ipm), 1.05mm/s (2.5ipm), and 1.69mm/s (4ipm). The weld joint geometry was a butt joint in flat 1G welding position. All welds were fabricated under argon shielding gas to prevent weld and tool contamination. Wormhole defects were found in all welding conditions and will be

discussed later in this chapter. Figure 14-Figure 16 provide forging and traverse loads for all 6.35mm welding conditions. The slowest travel speed shows instability in the forging z-load and traverse load. Unlike the 12.7mm weld, the 6.35mm forging load after initial plunging remained consistent for welding speeds of 1.05mm/s and 1.69mm/s. Loads for both 12.7mm and 6.35mm welds were similar despite the difference in plate thickness. The shallower weld did not result in load reduction, but improved the load consistency for faster welding speeds. The impact of load on microstructure is discussed in Section 3.2.1.
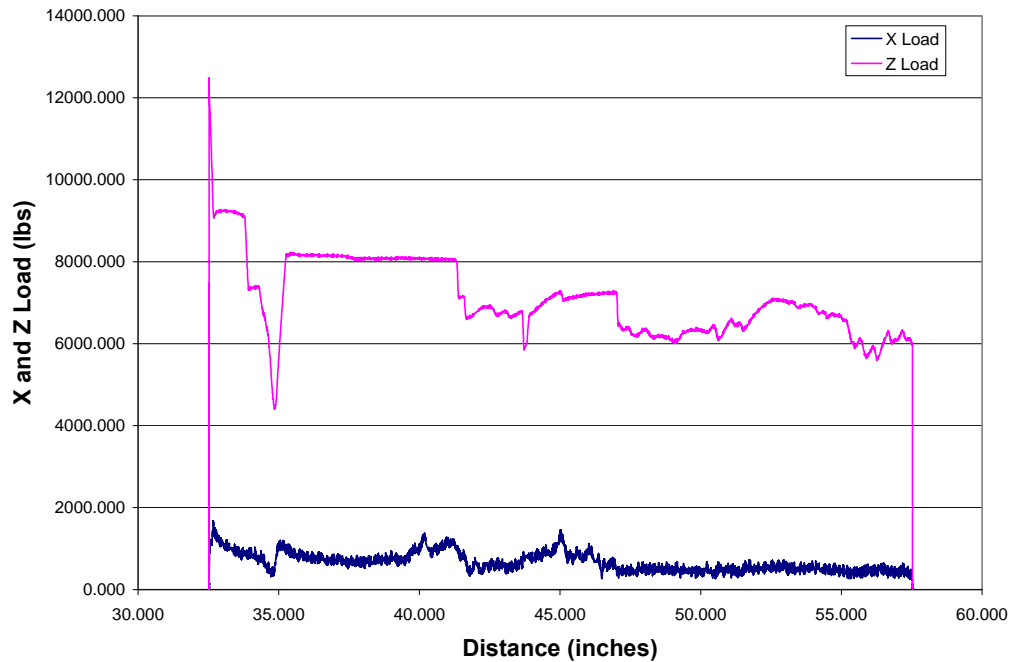
Figure 14. Load data for 6.35mm Ti-5111 weld THP 0.42mm/s and 225 rpm.
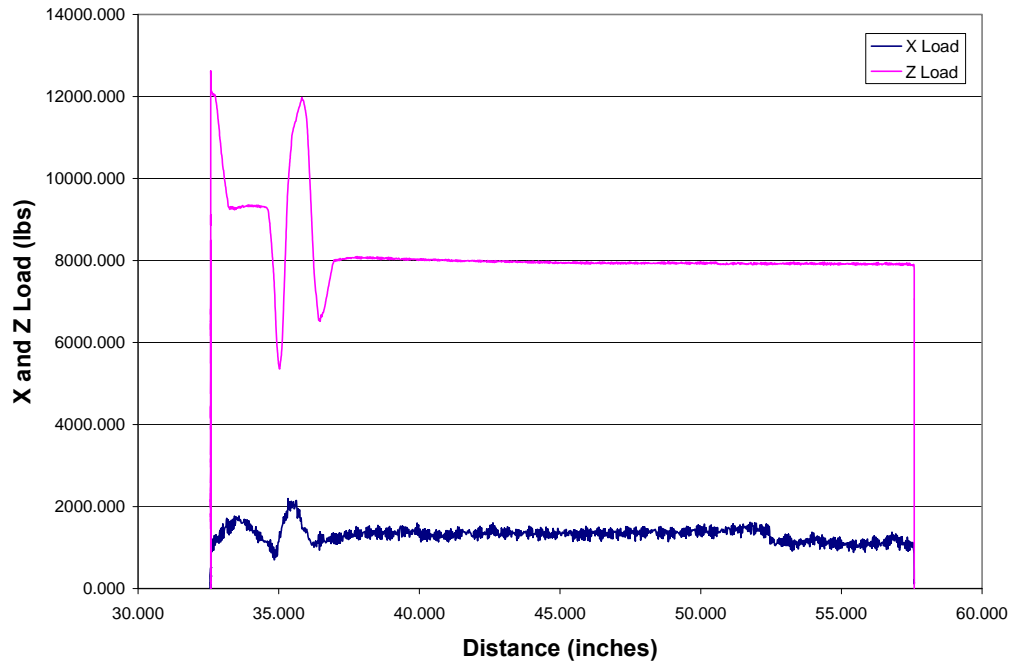
Figure 15. Load data for 6.35mm Ti-5111 weld TNP 1.05mm/s and 225 rpm.
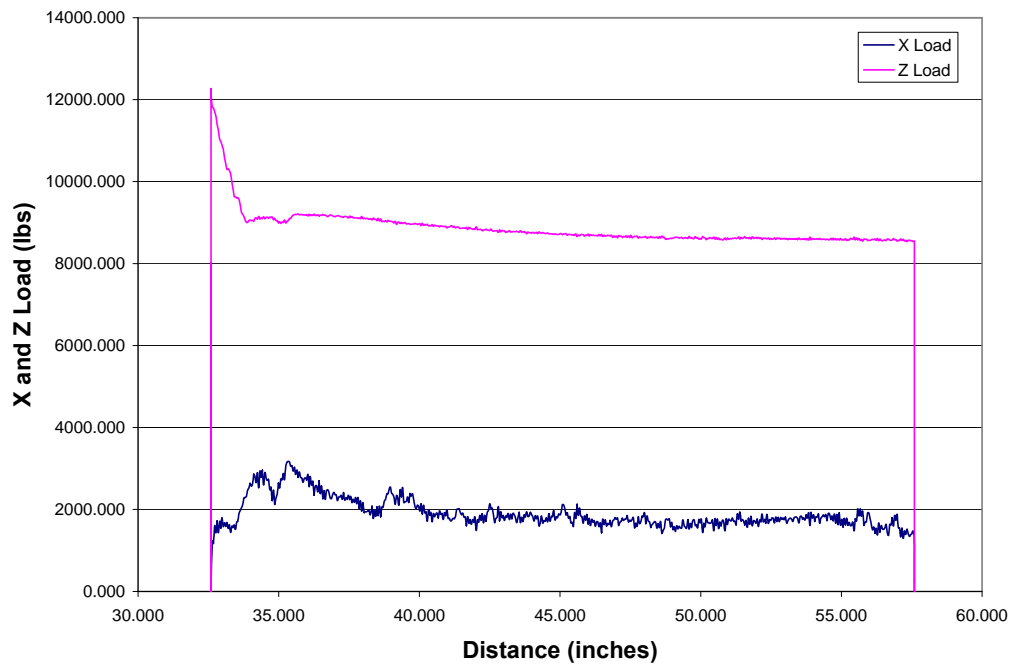
Figure 16. Load data for 6.35mm Ti-5111 weld TCP 1.69mm/s and 225 rpm.

31

Titanium friction stir welds for α, α+β, and β alloys have shown varied results based on tool depth, alloy composition, and phases. β alloys such as Ti-15-3 and β-21s reportedly have the largest welding envelope with the lowest welding loads compared to α+β and α alloys [Mishra 2007]. Comparing welding envelopes and loads for different alloys is challenging due to differences in friction stir welding tool designs, systems, and system configurations. However, temperature comparisons can be made with arc welding of titanium and friction stir welding of other titanium alloys.

Arc welding of titanium, as discussed in Section 1.1.2 is typically performed with gas tungsten arc welding (GTAW). Arc weld strength is determined by weld metal composition, grain size, and martensite formation. Unlike many ferrous and non-ferrous alloys, titanium alloy wire drawing is expensive and difficult; leading to a limited list of recommended filler metals for arc welding [AWS G2]. Heat input and cooling rate are major factors for grain size and martensite formation. Studies have correlated mechanical properties of α-β to α lath thickness. An increase in cooling rate has shown an increase in tensile strength for Ti-64 welds [Yung]. Arc weld heat input is given by:

$$H_{net} = \left(\frac{V \times I \times 60}{S \times 1000} \right) \times Efficiency \qquad \textbf{Equation 2}$$

Where H_{net} = net heat input (kJ/mm), V = volts (V), I = current (A), and S = welding speed (mm/min). Efficiency is dependent on the welding process with GTAW having a weld efficiency of ~0.8. Calculated heat input from actual Ti-5111 GTAW arc welds under the MMADCP program has an average H_{net} of 1.054 kJ/mm (26.78 kJ/in). Cooling rate for thin plates leads to 2-dimensional heat transfer. The cooling rate R (ºC/s) is determined by:

$$R = 2\pi\rho C \left(\frac{t}{H_{net}} \right)^2 (T_P - T_0)^3 \qquad\qquad \textbf{Equation 3}$$

where ρ = density of the material (g/mm^3), C = specific heat (J/(g*°C), t = thickness (mm)

T_P = peak temperature (°C), T_0 = initial temperature of the plate (°C). The calculated cooling

rate for the MMADCP arc welds is 72.167 °C/s (161.9 °F/s) [MMADCP].

In contrast, in friction stir welding the heat input is typically defined through a calculated

power equation.

$$H_{FSW} = \frac{(\tau_{FSW} - \tau_{free}) \times 1.3558 \times \omega}{S_{FSW}} \qquad\qquad \textbf{Equation 4}$$

where H_{FSW} = FSW heat input (kJ/mm), τ_{FSW} = torque during FSW (ft-lbs), τ_{free} = system free

running torque (ft-lbs), ω = rotation rate (rad/s), and S_{FSW} = travel speed (mm/s) and 1.3558

is the conversion for J/ft*lb. For the welds in this study the torque is estimated based on

machine maximum motor load. The calculated friction stir welding heat input is given in

Table 11.

Table 11. Friction stir weld heat input for the experimental welds.

Weld ID	RPM	TS (mm/s)	Torque (ft-lb)	Free Torque (ft-lb)	ω (rad/s)	Power (j/s)	H_{FSW} (kJ/mm)	H_{FSW} (kJ/in)
BJ-12 (12.7mm)	200	1.48	105	65	20.93	1135.26	0.77	19.48
THP (6.35mm)	225	0.42	155	120	23.55	1117.52	2.66	67.58
TNP (6.35mm)	225	1.05	155	120	23.55	1117.52	1.06	27.03
TCP (6.35mm)	225	1.69	155	120	23.55	1117.52	0.66	16.80

Compared to calculated arc welding heat inputs for Ti-5111 of H_{net}=1.054 kJ/mm (26.78

kJ/in), the calculated heat input for friction stir welding is lower for the 12.7mm weld and for

33

6.35mm weld TCP with the highest travel speed of 1.69mm/s. Welding travel speed for TNP (1.05 mm/s) results in a similar heat input as arc welding. As expected the slowest travel speed results in the highest heat input.

Reported temperatures from work performed by Lienert for friction stir welding of Ti-64 0.32cm from the end of the tool shoulder are 990ºC [Lienert 2001]. The extrapolated temperature at the tool shoulder is 1150 ºC. Within the HAZ, 0.32cm from the weld centerline temperatures range from 850-890 ºC. These peak temperatures are higher than temperatures reported in this thesis. Comparing physical properties of Ti-64 to Ti-5111 in Table 12, this difference may be due to the processing parameters and differences in thermal conductivity. The work by Lienert highlights successful processing above β transus temperatures for Ti-64.

Table 12. Physical properties comparison of Ti-5111 and Ti-64 [ASM and Timet]

	Linear thermal expansion coefficient ($10^{-6}K^{-1}$)	Thermal conductivity ($W\,m^{-1}K^{-1}$)	Specific heat capacity ($J\,kg^{-1}K^{-1}$)	β-transus for Ti (˚C)
Ti-5111	8.2	7.5	533	980
Ti-6Al-4V	9.0	7	530	995

3.2. Results and Discussion

3.2.1 Optical Microscopy of Ti-5111 Friction Stir Weld

In a typical friction stir weld, there are four major regions: the unaffected base metal, the heat affected zone (HAZ), the thermo-mechanically affected zone (TMAZ), and the stir zone. In the 12.7mm Ti-5111 friction stir welds, optical images of the transverse weld cross section show a highly defined weld stir zone with an abrupt transition to base material (Figure 17). Similar to other reported titanium welds [Lienert 2001, Ramirez, Fonda 2007, Pilchak] there

is a very narrow HAZ and TMAZ before reaching the stir zone. Grain size analysis in Table 13 using ASTM E112 shows that the base metal grain size was in average 460 μm. After friction stir welding, the grain size in the stir zone ranged from 6 μm at the bottom of the stir zone to 27 μm in the middle of the stir zone. The average base metal grain size consisted of multiple α colonies. Higher magnification images of the base metal (Figure 18) show a fully lamellar β-processed microstructure as described in Section 1.1.1.2. The use of polarized light on the base metal structure highlights the distinct α colonies growing from grain boundary α. The transition from the base metal to the weld shows a sharp contrast in grain size (Figure 19). Under 50x optical magnification, the transition regions show grains with discontinuous grain boundary α and no distinct grain size. Examination of the stir zone shows that it consists of highly refined grains with sharp variation in grain size from the top of the stir zone to the center of the stir zone (Figure 20). A higher magnification image of the stir zone center shows the presence of continuous grain boundary α indicating that the temperature in the region most likely exceeded the β-transus. Based on the microstructure, the stir zone has undergone dynamic recrystallization with deformation above the β phase field. The stir zone remained at such temperature long enough to facilitate growth of a continuous grain boundary α network. Under polarized light in Figure 20B and D, the overall stir zone shows little preferential texture. However, there is texture within the formed alpha colonies. The transverse cross-section of the weld in Figure 17 shows two small defects. One defect is an advancing side wormhole defect. The second defect is a discontinuous lack of consolidation at the bottom of the weld. Further analysis of the defects found in the stir zone is discussed in Section 3.2.7.

Comparing the microstructures with those reported in the literature, Lienert *et al* noted that peak temperatures and microstructural evidence show that friction stir welding temperatures in mill-annealed Ti-64 exceeded β transus [Lienert 2001]. This study also noted the variation of stir zone grain size with respect to location, similar to those observed in the 12.7mm Ti-5111 in the present work. This prior β grain size variation may be due to a combination of strain and temperature. Material near the top weld surface undergoes constant strain due to the rotation of the tool shoulder. Reported temperatures near the tool shoulder in Ti-64 exceeded 990ºC, but heat from the shoulder allows grain growth. Examining the system with regards to heat transfer, the welding configuration and anvil interaction resulted in rapid heat transfer and fast cooling during welding leading to the formation of smaller grains at the bottom of the stir zone.

Table 13. Grain size Analysis (ASTM E112)

Location	Magnification	Grain Size (μm)	Grain size (ASTM)
FSW Top	500	23.365	7.545
FSW Middle	500	26.596	7.171
FSW Bottom	1000	6.1112	11.41
Base Metal	25	460.829	00

Figure 17. Transverse cross-section of 12.7mm Ti-5111 friction stir weld showing the stir zone, transition region and base metal. Worm-hole defects can be seen at the bottom of the stir zone.
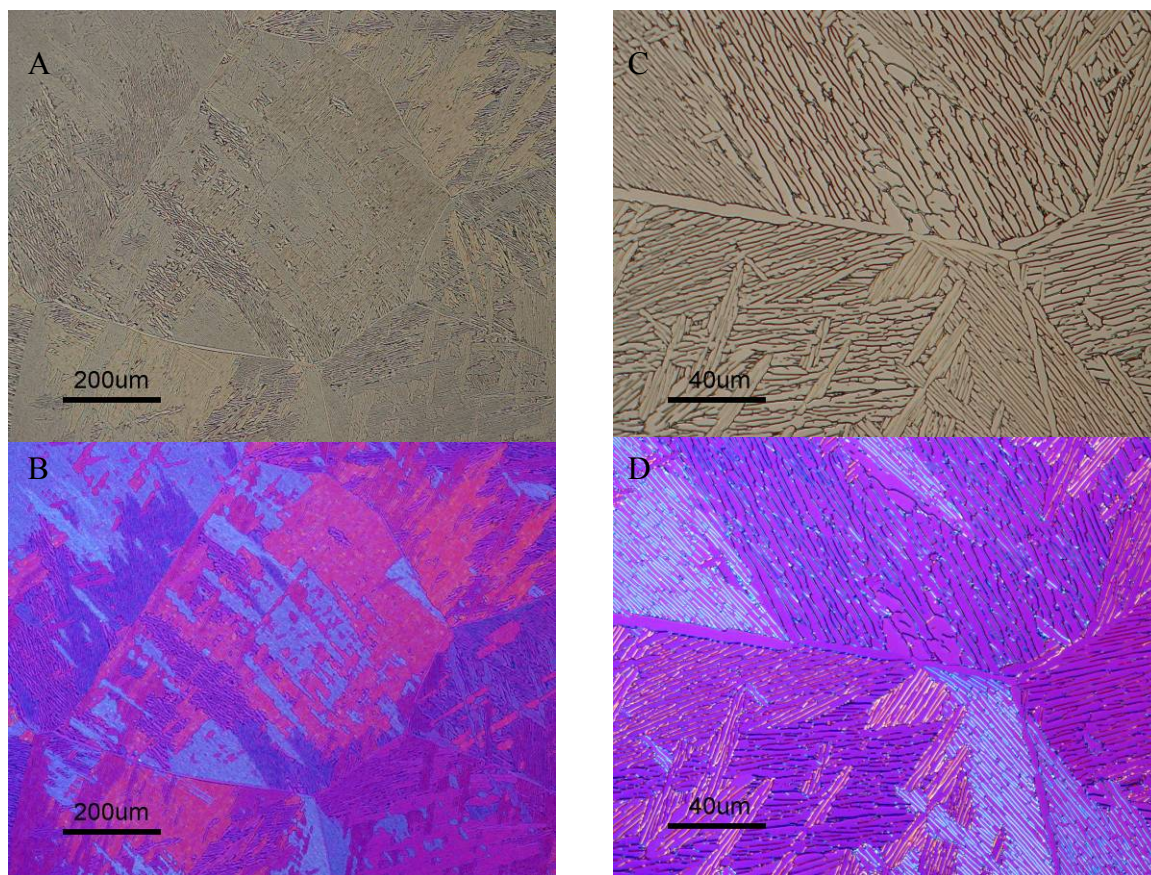
Figure 18. 12.7 mm Base metal optical images. A) 10x magnification of Ti-5111 microstructure consisting of multiple α colonies B) 10x magnification under polarized light C) 50x magnification showing the fully lamellar grain structure D) 50x magnification under polarized light
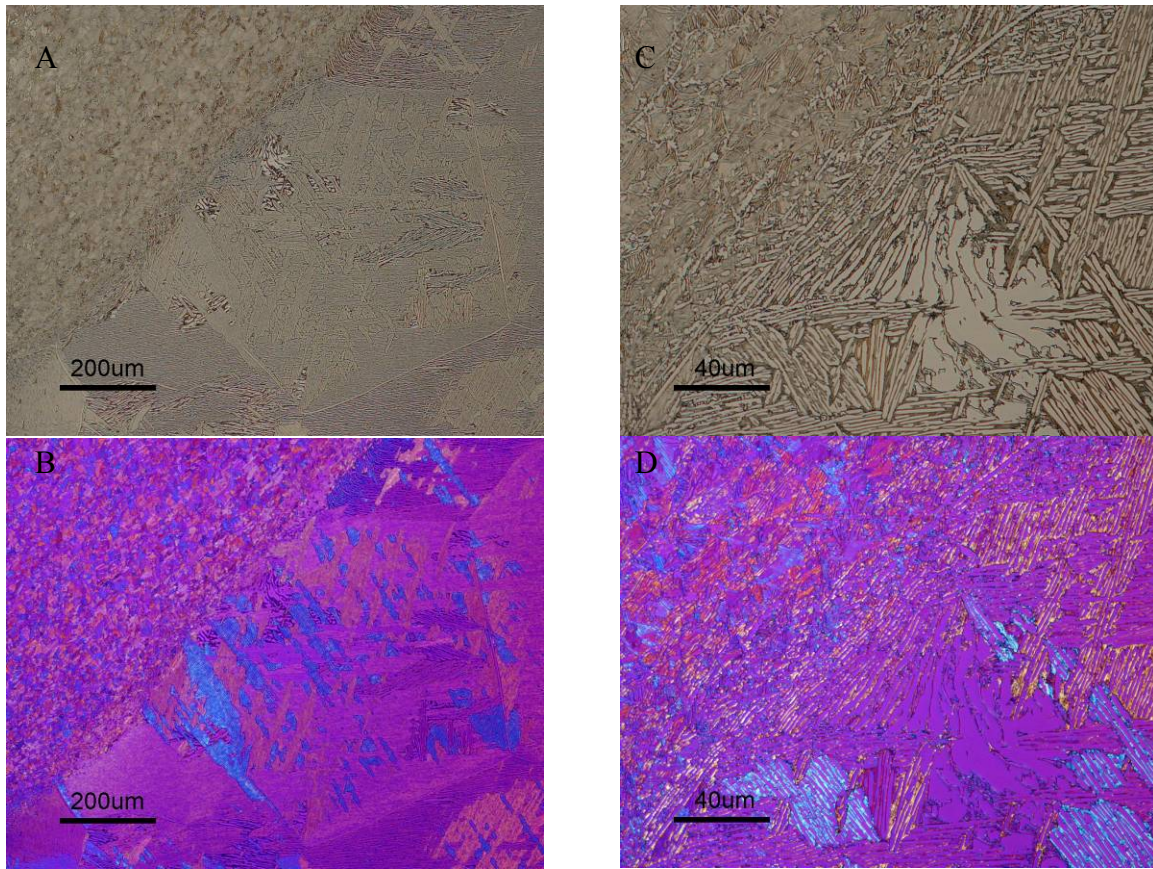
Figure 19. 12.7mm weld transition zone optical images. A) 10x magnification highlighting the transition region from large base metal grains to fine weld metal grains B) 10x magnification under polarized light C) 50x magnification of the transition region showing deformation of the α laths D) 50x magnification under polarized light
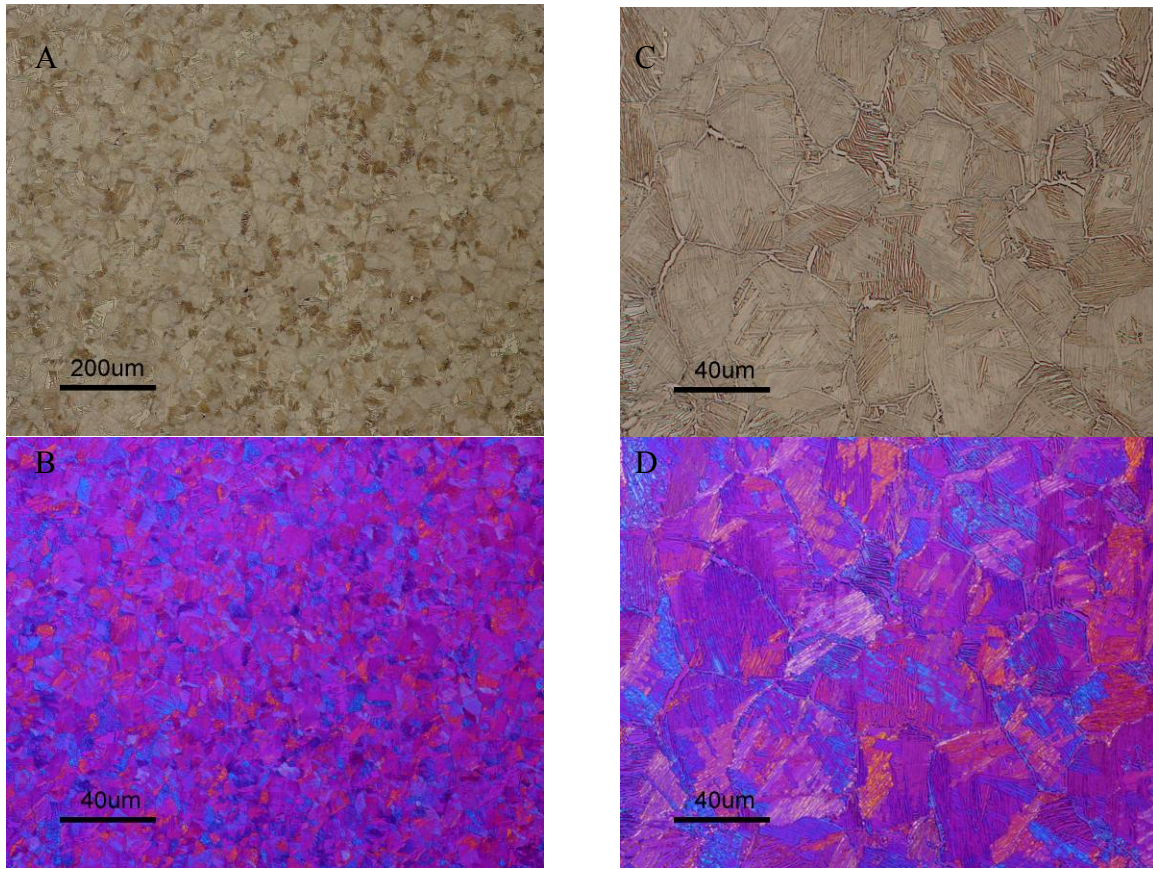
Figure 20. 12.7mm stir zone optical images. A) 10x magnification of the stir zone B) 10x magnification under polarized light C) 50x magnification of the stir zone showing the fully lamellar fine grained microstructure D) 50x magnification under polarized light

Examination of the 12.7mm plan view cross-section and longitudinal cross section gives a detailed view of the defect formation in other dimensions (Figure 21 and Figure 22). Sectioning above the advancing side defect in the plan view shows tungsten debris within the material flow after etching (Figure 21). The longitudinal cross sections shows stir zone defects opening and closing (Figure 22).

Figure 21. Plan view 12.7mm weld cross section highlighting material flow about the defect.

Figure 22. Longitudinal view of 12.7mm cross-section showing defect formation at the bottom of the stir zone. Defects appear to be forming and reconsolidating through the length of the weld.

In comparison to the 12.7mm welds, the 6.35mm transverse cross sections show inconsistent

defect location or size for the different processing parameters and when compared to the

12.7mm weld (Figure 23). All welds were fabricated with the same tool design; however, the

different processing parameters resulted in distinct weld profiles. The slower travel speed (THP - 0.42mm/s) showed severe lack of consolidation compared to the welds fabricated at (N7) 1.05mm/s and (TCP) 1.69mm/s. The faster weld at 1.69mm/s has narrower weld profile with smaller affected weld area and shoulder. A comparison of the stir zone grain size for the different processing parameters is shown in Table 14. Similar to the 12.7mm weld, grain size showed variation from the top, center, and bottom of the stir zone. For the nominal and fast travel speeds, the grain size at the bottom of the stir zone was dramatically smaller than at the center and top of the stir zone. The slowest travel speed has a more even distribution of grain size, most likely due to a more even thermal profile. Higher magnification images of the stir zone center for each set of the parameters show the dependence of the grain boundary alpha network on the processing parameters (Figure 24). With the 6.35mm welds, the faster travel speeds showed a well defined and continuous alpha network compared to the 0.42mm/s travel speed. The slowest travel speed was designed to have the highest weld input, however it resulted in a discontinuous α network. This is most likely due to the severe defect resulting in a variation in the thermal boundary condition preventing formation of the lamellar microstructure. In comparison, the fastest welding travel speed would result in a colder weld heat input. The colder weld input weld generated a more distinct α grain boundary network. As discussed earlier in Section 3.1, the faster welding speed led to more consistent welding loads. Weld consolidation is dependent on both the temperature experienced during welding and the deformation in the process.

Stir zone microstructures for both 12.7mm and 6.35mm friction stir welds at nominal and fast travel speeds show similar characteristics in Figure 24 (bottom images). While there is a

difference in stir zone grain size, 6.35mm welds at the nominal and fast travel speeds have a

well defined grain boundary α with 1-3 α colonies per grain similar to the 12.7mm weld.

Ramirez and Juhas' study on mill annealed and β annealed Ti-64 determined that the

microstructural evolution was dependant on the temperatures and strains experienced in FSW

rather than the starting microstructure [Ramirez]. This suggests that the 12.7mm and

6.35mm weld experienced similar strains and peak temperatures during welding based on the

microstructure.

Table 14. Grain size analysis for 6.35mm stir zone (ASTM E112) THP = 0.42mm/s, N7 = 1.05mm/s, and TCP = 1.69 mm/s

Location	Magnification	Grain Size (µm)	Grain size (ASTM)
TCP 8-10 Top	1000	8.53242	10.45
TCP 8-10 Middle	1000	9.15751	10.25
TCP 8-10 Bottom	1000	3.31565	13.18
N7 7-9 Top	1000	9.22509	10.23
N7 7-9 Middle	1000	9.15751	10.25
N7 7-9 Bottom	1000	4.12541	12.55
THP 65-85 Top	1000	6.03865	11.45
THP 65-85 Middle	1000	7.26744	10.92
THP 65-85 Bottom	1000	7.86164	10.69

Fast

Nominal

Slow

Figure 23. Transverse cross-section in 6.35mm friction stir weld. Fast = 1.69mm/s travel speed. Nominal = 1.05mm/s. Slow =0.42mm/s. Slow travel speed shows a severe lack of consolidation compared to the welds fabricated at Nominal and Fast speed. Faster welding speed resulted in a narrower weld profile with smaller affected weld area and shoulder.
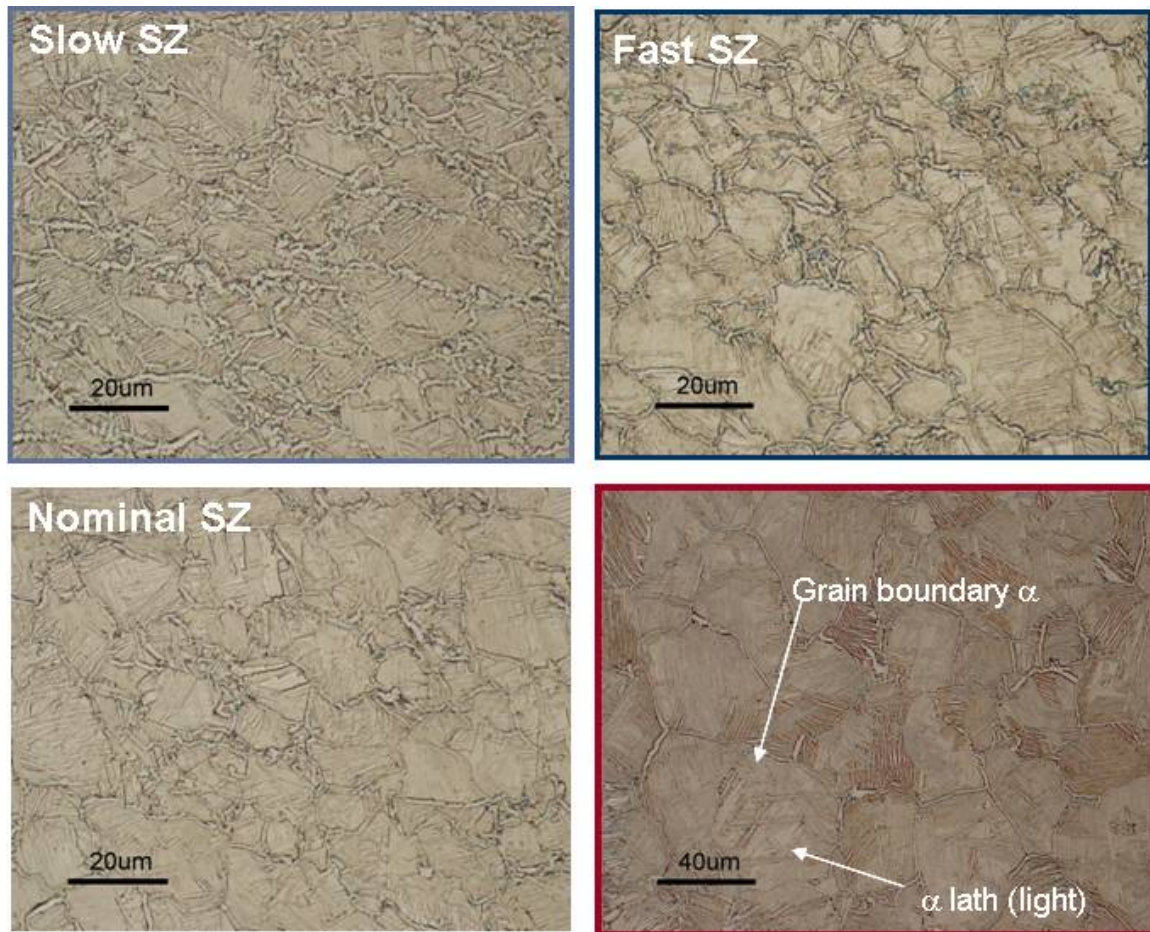
Figure 24. Comparison of 6.35mm weld stir zone center for slow, nominal, and fast travel speeds. There is a dependence of the grain boundary alpha network on the processing parameters. Faster travel speeds show a well defined and continuous alpha network compared to the slower travel speed that resulted in a discontinuous α network. The figure outlined in red is Figure 20C for the 12.7mm weld for comparison with the 6.35mm stir zone.

3.2.2 Vickers Microhardness Mapping

Vickers microhardness mapping on a Mitutoyo hardness system with a 300 gf load of the transverse cross-section resulted in higher hardness (280-300HV) in the stir zone compared to the base metal (260-280HV) as shown in Figure 25. Within the stir zone higher hardness regions (320-340HV) are located at the bottom of the stir zone and at the top of the stir zone. This may be due to the heat transfer at the anvil and top surface. Small patches of higher hardness are dispersed through the stir zone. Higher hardness may also be due to residual

44

oxygen interaction during welding. Unlike friction stir welding of aluminum alloys [Mishra 2005], the hardness mapping of Ti-5111 in this work confirms two distinct regions of hardness of the stir zone and the base metal with no difference in hardness indicating a heat affected zone or a thermomechanically affected zone. This result is consistent with findings for other Ti-5111 welds [Fonda 2007][Knipling][Rubal]. For welds in Ti-64, there has been conflicting data with regards to microhardness profiles. Lienert has shown an increase in HAZ hardness with the weld stir zone approximately the same hardness as the base metal [Lienert 2001]. In contrast, recent results reported by Zhang show a drop in hardness between the parent metal and the weld metal [Zhang 2008]. Stir zone hardness values reported for Ti-5111 and Ti-64 FSW range from 300-340 HV which falls within the range of the stir zone hardness values shown here.
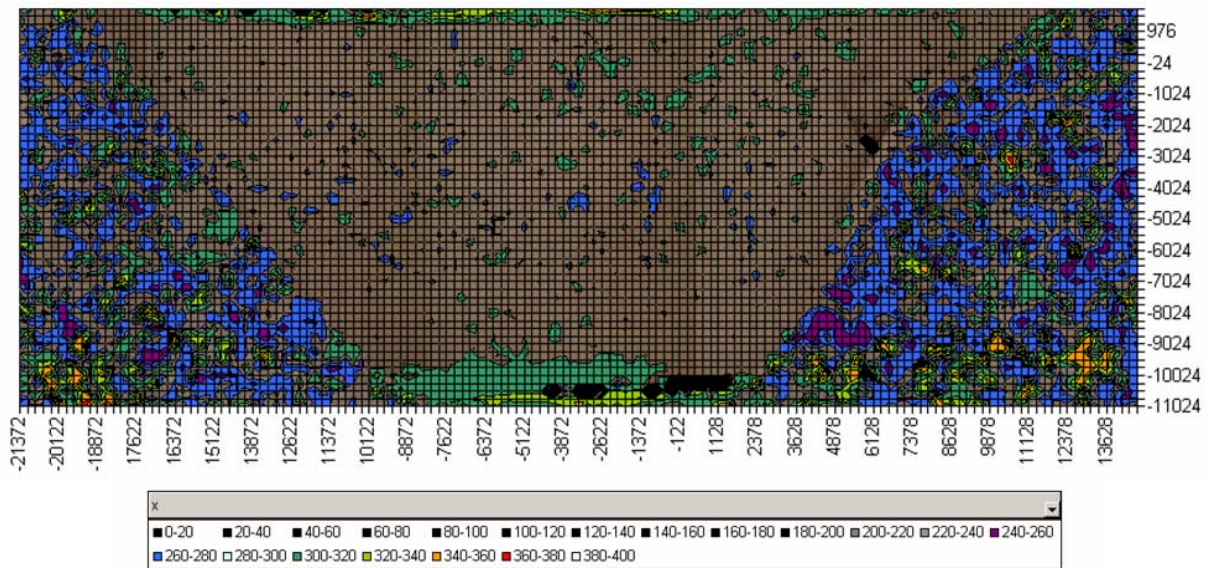
Figure 25. Vickers microhardness mapping of the transverse cross-section. There are regions of high hardness at the top and bottom of the stir zone. Units are in HV.

3.2.3 Localized Mechanical Properties

Bulk mechanical properties of the weld were obtained after weld fabrication at EWI. Transverse tensile tests with the weld centered in the gage length were performed in accordance with ASTM E08 at room temperature (23°C). The tests showed the welded material exhibited a reduction in ultimate tensile strength, slightly higher yield strength, and a reduction in elongation relative to the base metal (Figure 26). However, these values are within the reported range of GTAW all weld metal tensile specimens [MMADCP] shown in Table 15 and close to reported values of base metal properties in Table 3. The loss of strength and elongation in the transverse tensile tests can be attributed to the defects found in the transverse cross-section. This is especially apparent in sample T2 that failed at the heat affected zone. Comparative bulk transverse tensile tests from Ti-64 show failure within the base metal with higher elongation values [Lienert 2001]. A study examining transverse tensile properties with respect to rotational speed showed failure outside the weld stir zone in Ti-64 [Zhang 2008]. This work showed a reduction in yield and tensile strength with increasing rotational rate.

Bulk transverse testing allows testing of the weld system by including the base metal, heat affected zone, and weld. Transverse tensile tests show that the likely point of failure within the weld system, in this instance is within the base metal and HAZ. For more localized study of the mechanical properties, a collaborative work with the University of Maryland Baltimore County (UMBC) utilized microtensile specimens.

46

TENSION TEST RESULTS - ASTM E8

Project Number: 46104GDE-01   **Weld Number:** TCP   **Specification:**

Job Number: 2007-109772   **Customer:** Chris Conrardy

Address:

Test Machine: UK18   **Technician:** Steve O'Mara   **Test Date:** December 8, 2006

Specimen Orientation: Transverse   **Material:** 5111 Ti

Specimen Type: Flat

Nominal Gage Length: 50.80 (mm)   2.000 (in)

Test Rate: 1.27 (mm/min)   0.05 (in./min)

Specimen Identification	Specimen Width	Specimen Thickness	Test Temperature		Ultimate Strength		0.2% Yield Strength		Elongation	Reduction of Area	Failure Location
	(in)	(in)	(°C)	(°F)	(MPa)	(ksi)	(MPa)	(ksi)	(%)	(%)	
T1	0.751	0.463	23	73	864.8	125.4	717.2	104.0	8.8	14.9	Base metal
T2	0.751	0.465	23	73	731.7	106.1	727.6	105.5	1.8	0.8	HAZ

Test Conducted By _____

Title: Technician

Reviewed By _____

Title: Senior Engineer

Figure 26. Bulk mechanical test report on transverse weld tensile tests. The tests showed the welded material exhibited a reduction in ultimate tensile strength, slighter higher yield strength, and a reduction in elongation relative to the base metal.

Table 15. All-weld metal (AWM) tensiles from Ti-5111 GTAW arc weld. Tensile testing data from the MMADCP program. [MMACP]

AWM Tensile

SpecimenNo	Diameter (in)	Area (in)	Load(ksi)	Stress (ksi)	Yield (ksi)	Reduction Area (%)	Elongation (%)	Failure Type
1-HLPX1 (AWM)	0.5007	0.1969	24.207	122.94	113.7	15.5	8.5	Ductile
1-HLPX6 (Transverse)	0.5008	0.197	23.952	121.58	111.4	18.6	9.0	Ductile
1-HLPX7 (Transverse)	0.4997	0.1961	23.764	121.18	111.7	19.7	8.5	Ductile

Micro-tensile specimens of approximately 3mm x 1mm were successfully fabricated and tested by UMBC [Savage] [Zupan 1998, 2001, and 2003]. Micro-tensile experiments measured the Young's modulus, yield strength, work hardening, ultimate stress and failure strain for three regions of the 12.7mm Ti-5111 friction stir weld. Testing at the weld, transition zone, and base metal showed measureable differences in mechanical properties (Figure 27). The weld localized properties exhibit higher ultimate tensile strength compared to the bulk ultimate tensile strength. Similarly, the yield strength in the localized properties was higher than the bulk mechanical yield strength [Cheng]. Correlation of the mechanical properties to localized texture is discussed in Section 3.2.5.3.

	E (GPa)	σ_Y (MPa)	UTS (MPa)
Base	158	830	-
Interface	119	767	802
Weld	135	808	~969
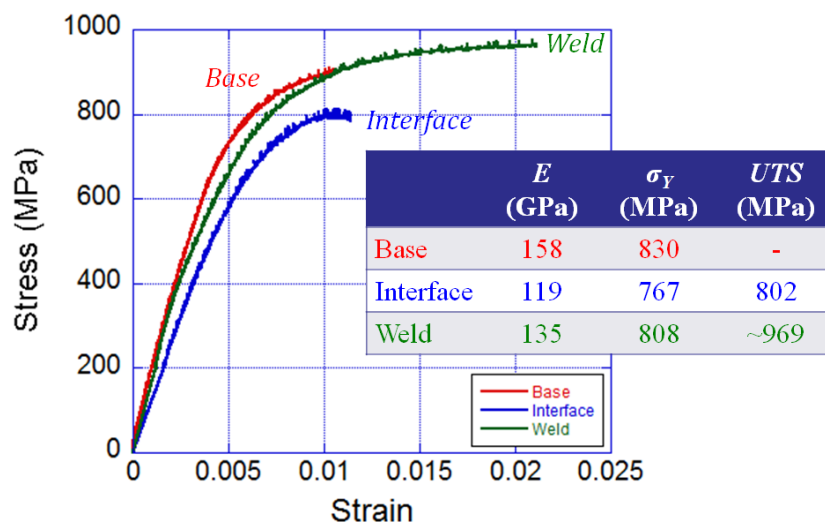
Figure 27. Microtensile test results for the FSW region, base metal, and transition zone.

3.2.4 Scanning Electron Microscopy (SEM)

Scanning electron microscopy images were taken on a JEOL 6400V operated at 15kV. Images were taken in both secondary electron mode and in backscatter mode when indicated. As with the optical metallography images, the SEM images show significant grain refinement in the stir zone compared to the base metal (Figure 28). β is shown in relief in all SEM images. Examination of the fusion line of weld shows the presence of small particles distributed in the stir zone (Figure 29 and Figure 30). Higher magnification images (Figure 31) and energy dispersive x-ray (EDS) spectroscopy identified the particles as tungsten. Tungsten is the primary alloying element in the friction stir welding tool material. Tool wear is the likely cause of tungsten particles within the weld.
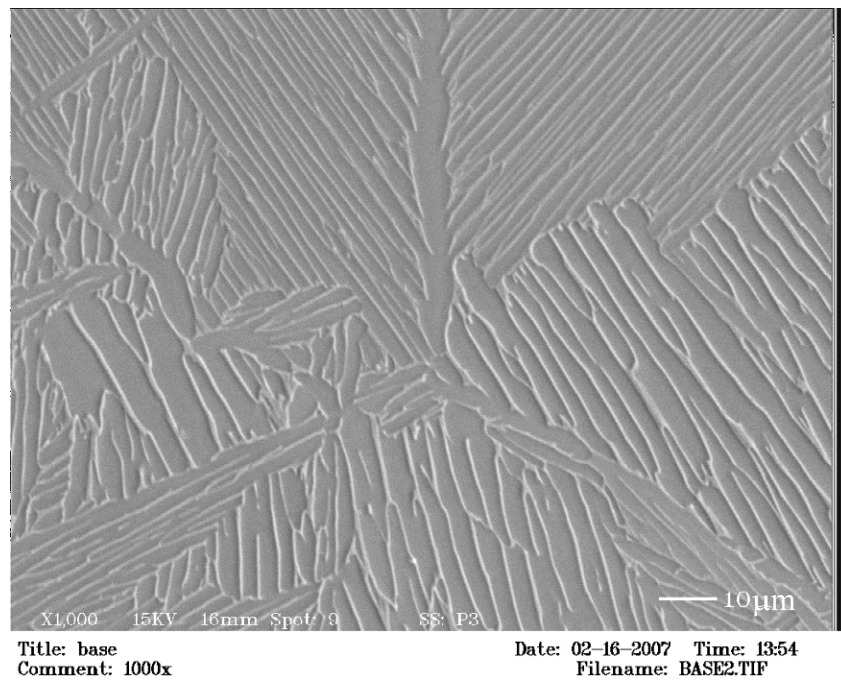
Figure 28. Secondary electron image of Ti-5111 base metal showing the α lath structure with β (shown in relief) regions.
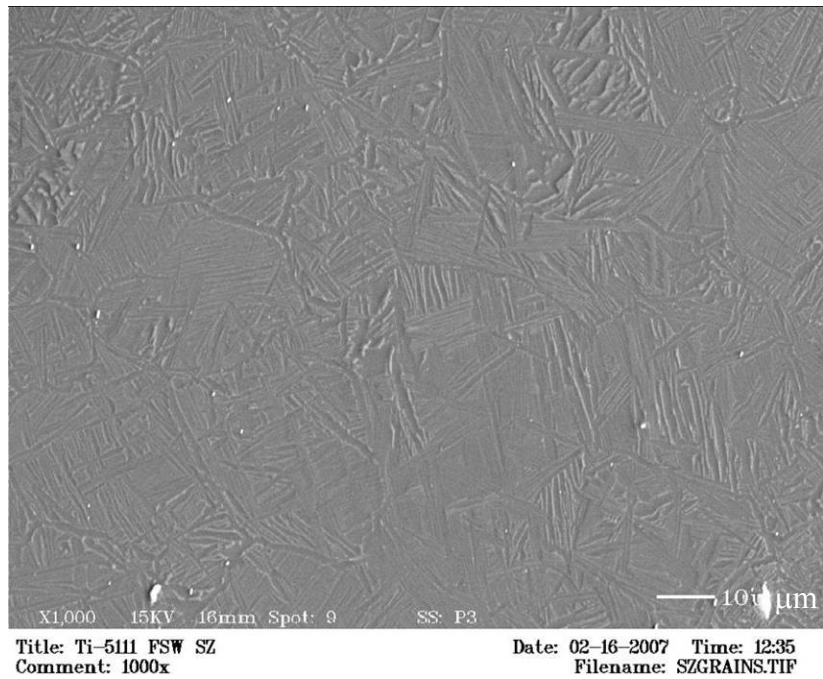
Figure 29. Secondary electron image of Ti-5111 friction stir weld showing tool debris and grain refinement
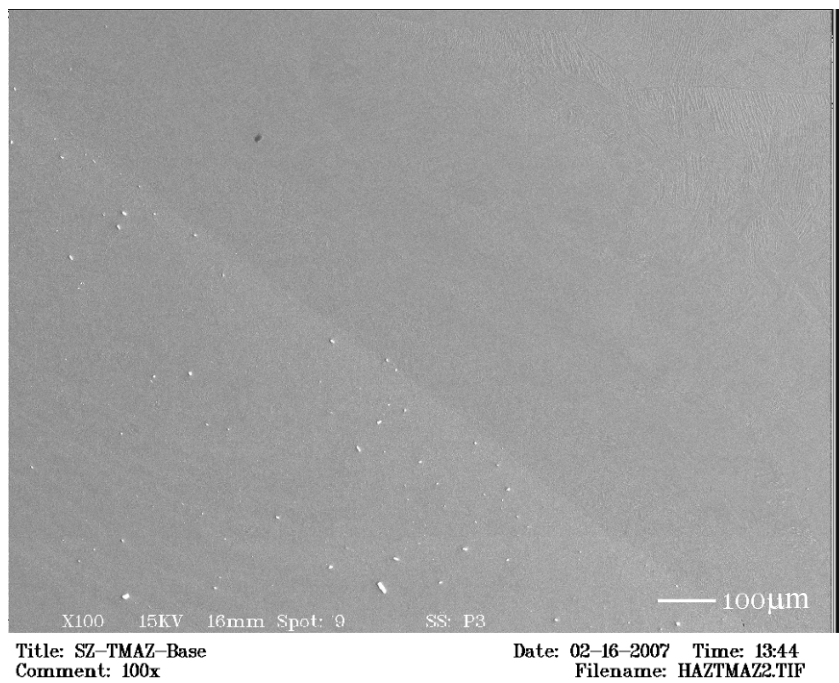
Figure 30. Secondary electron image of Ti-5111 transition region

Title: Ti-5111 FSW HAZ TMAZ   Date: 02-16-2007   Time: 12:45
Comment: 1000x   Filename: HAZTMAZDEFECT
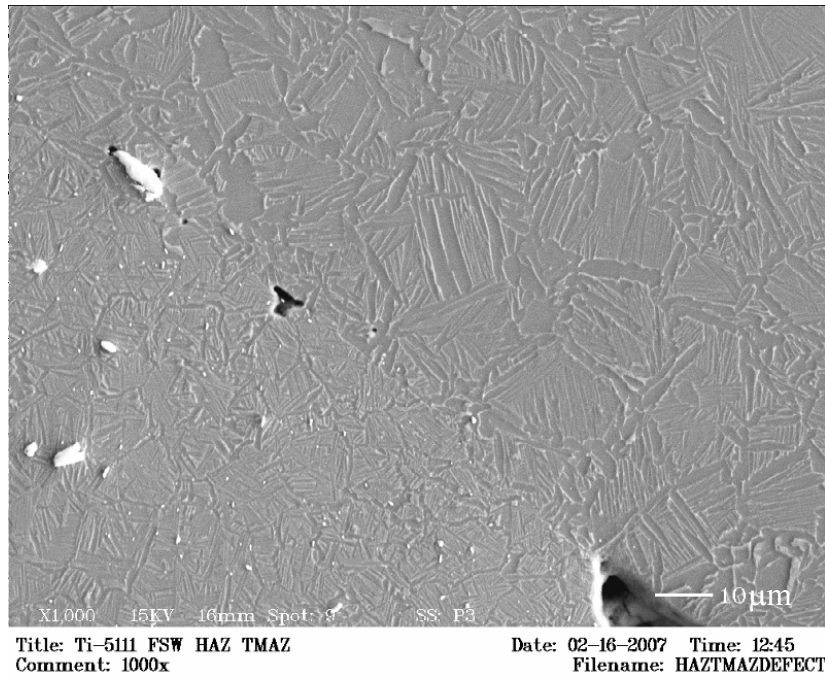
Figure 31. Higher magnification SEM image at the transition from base metal (upper right) to stir zone (lower left) shows the presence of tungsten based debris, most likely from to tool wear.

3.2.5 Electron Backscatter Diffraction (EBSD)

Electron backscatter diffraction (EBSD) was first observed by Kikuchi in 1928 through scattering of the incident beam within a specimen. Use of this technique expanded to scanning electron microscopy by applying Kossel x-ray diffraction to determine the diffraction pattern center and to measure lattice parameters from the Kikuchi lines. Automated EBSD and the development of orientation imaging microscopy led to widespread use in determining crystallographic orientation and phase identification in polycrystalline materials [Schwartz]. This thesis utilized EBSD to examine the evolution of texture as a result of friction stir welding and the impact of texture on the mechanical properties in Ti-5111.

Electron backscatter diffraction analysis was performed on friction stir welds of Ti-5111 using a Hitatchi 660 SEM equipped with an EDAX EBSD detector. The following

51

crystallographic analysis of these welds was performed using TSL, an orientation imaging microscopy (OIM) software developed by EDAX. Texture analysis allows us to determine the preferred crystallographic orientations to better understand the influence of friction stir welding on mechanical properties. Electron backscatter diffraction analysis was performed at various sections of the 12.7mm friction stir weld as well as at selected microtensile sections. The selected locations are shown in the schematic in Figure 32.
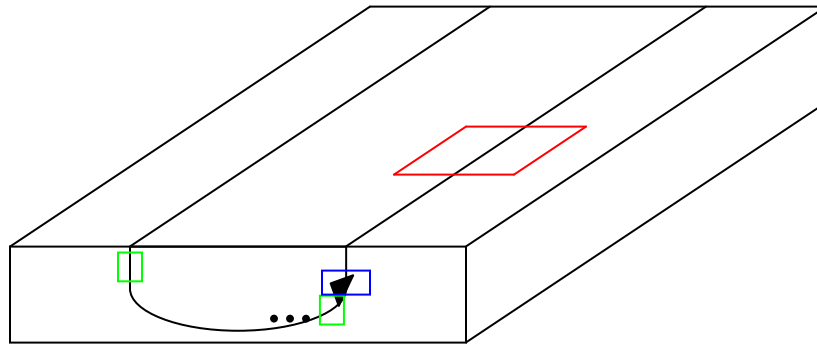
Figure 32. EBSD scan schematic. EBSD and OIM images were taken from the regions marked. The dots indicated positions of defects. The red box is the plan view orientation. The green boxes are locations of the transverse view. The blue box is the advancing side defect.

Merging two plan view scans across the base metal to the friction stir weld on the advancing side shows a distinct transition region. The inverse pole figure (IPF) and image quality map of the merged scan are shown in Figure 33. The alpha colony structure undergoes significant alpha lath refinement at the transition from base metal to the friction stir weld. Within the friction stir welded region the alpha lath shows refinement of the alpha lath structure compared to the base metal. Based on the overall IPF, there does not appear to be any distinct preferred crystallographic orientation in the transition region. Overlaying an image quality map with grain boundary misorientation angles shows that over 91% of the grain boundaries across the plan view are considered high angle grain boundaries (Figure 34). The

distribution of grain boundary misorientation is given in Figure 35 with the average misorientation angle of 56.77°. The phase map in Figure 36 across this region shows primarily α phase. Further orientation analysis sectioned the scan into weld metal and base metal. The results of the sectioning are given below.
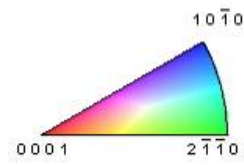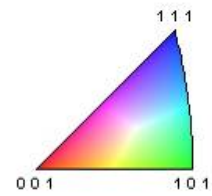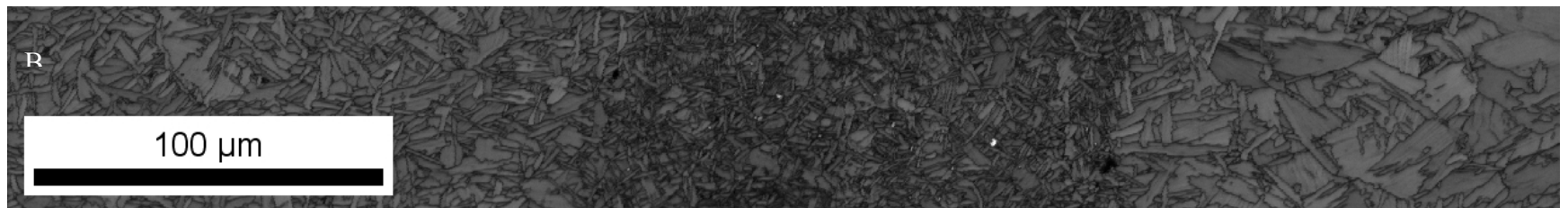
Figure 33. A) Inverse pole figure of the plan view transition region highlighting α colony refinement. The schematic below shows orientations for Ti alpha and Ti beta. B) Image quality map.
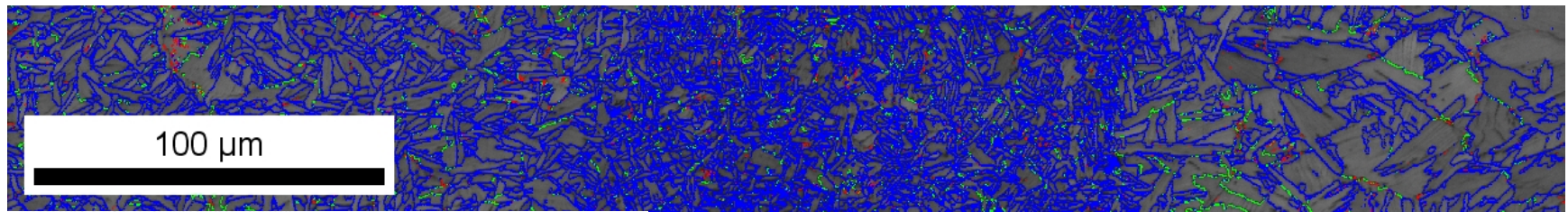
Boundaries: Rotation Angle

	Min	Max	Fraction	Number	Length
▬ (red)	2°	5°	0.027	6813	983.37 microns
▬ (green)	5°	15°	0.061	15343	2.21 mm
▬ (blue)	15°	180°	0.912	229872	3.32 cm

*For statistics - any point pair with misorientation
exceeding 2° is considered a boundary
total number = 252028, total length = 3.64 cm)

Figure 34. Image quality map overlaid with grain boundary misorientation angle. 91% of the grain boundaries across the plan view are considered high angle grain boundaries.
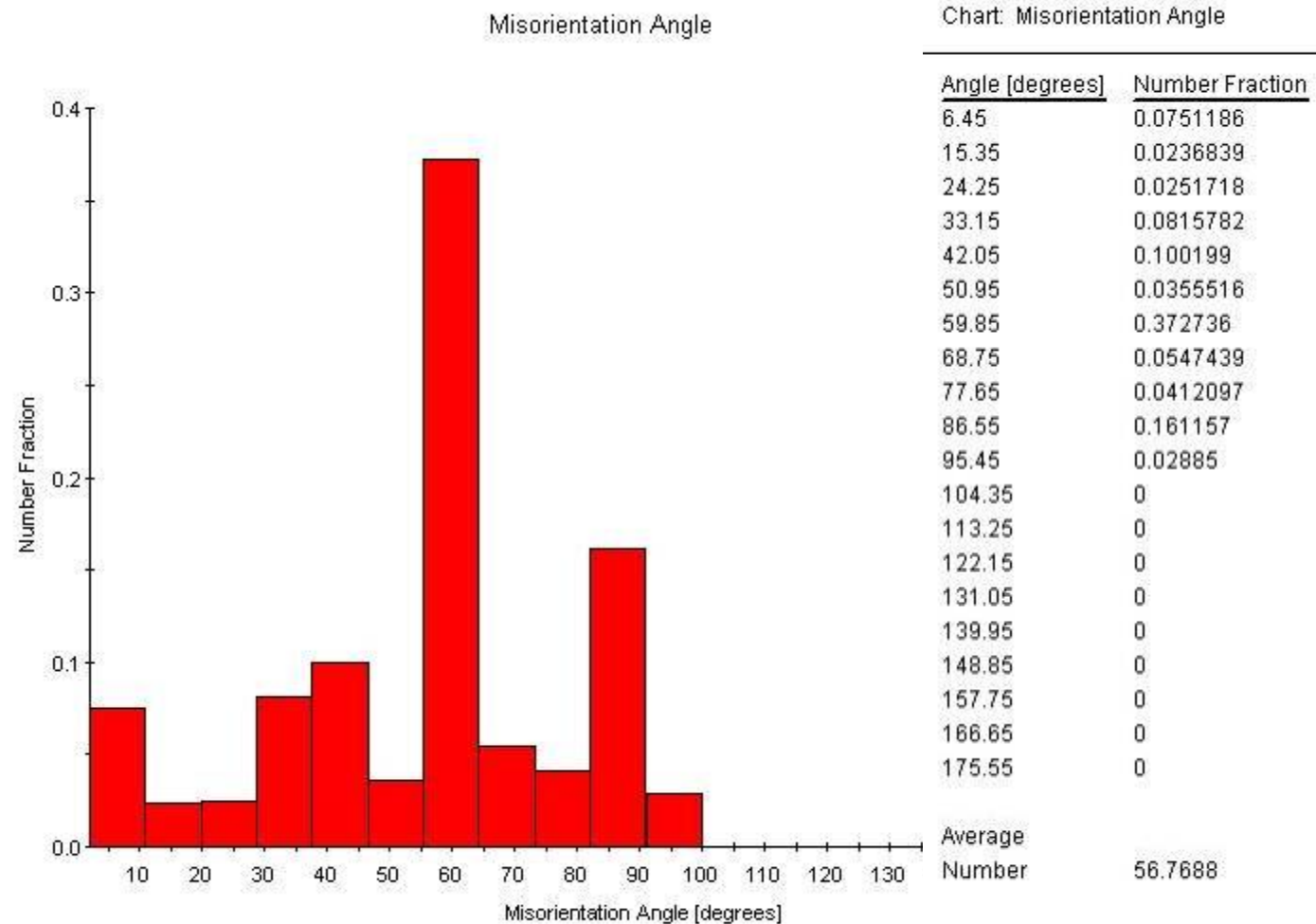
Figure 35. Chart of misorientation angle across the plan view of the weld in Figure 34.

Phase	Total Fraction	Partition Fraction
Titanium (Alpha)	0.983	0.983
Titanium - Beta	0.003	0.003
Tungsten	0.004	0.004
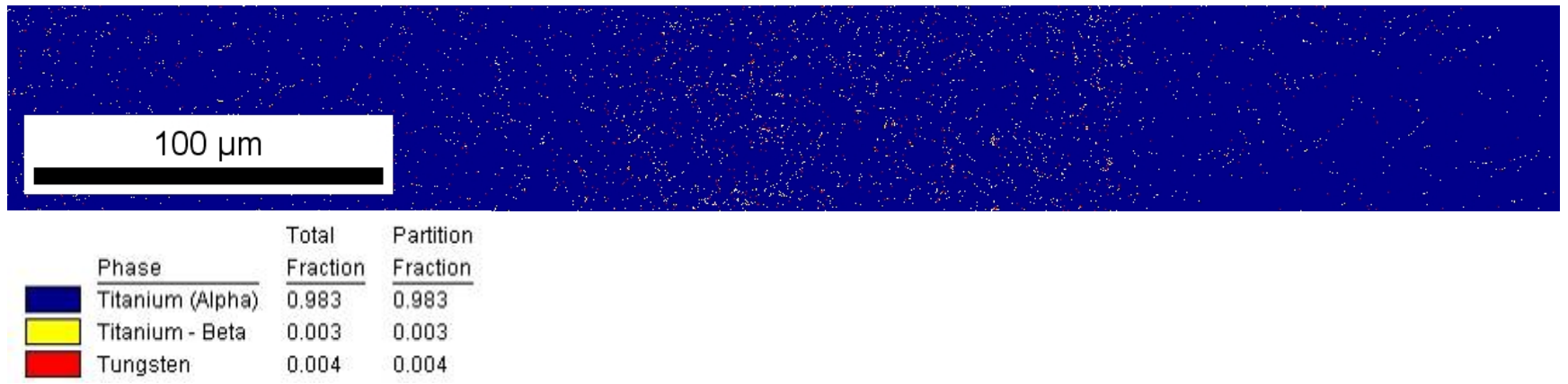
Figure 36. Phase map showing primarily α phase.

Examination of a second area along the plan view shows isolated defects at the interface between the base metal and the stir zone in Figure 37. The phase distribution for α and β shows an increased concentration of β surrounding the voids. Tool wear was noted earlier in this chapter with the presence of tungsten debris. Tool wear during welding can lead to defect formation with the inability to consolidate material. Tungsten, a known β stabilizer, can lead to β phase stabilization around voids as shown in the phase map in Figure 37B.

Tool material wear has also been observed by Zhang and Pilchak [Zhang 2008] [Pilchak 2007]. In friction stir welding of Ti-CP with polycubic boron nitride (PCBN) tool, Zhang noted that the reaction between the Ti matrix with PCBN tool debris lead to a TiB_2 layer around the debris. This occurred near the top surface of the stir zone, suggesting tool wear is most notable at the surface of the weld. Similarly, within Ti-64 processed material Pilchak noted tool wear within two major regions: 1 mm below the surface of the weld and near the surface of the stir zone. Unlike earlier published results noting increased tool wear on the advancing side, Pilchak observed higher tool wear on the retreating side. The low diffusivity of tungsten combined with the short time at peak temperature resulted in partial dissolution of tungsten. These results are in agreement with the observed tool debris behavior with the Ti-5111 friction stir weld in this thesis. Both the microstructural behavior and the thermocouple data support that temperatures within the weld exceeded β transus. While peak temperatures dwell for a short period of time, partial dissolution of tungsten could explain β phase stabilization around the defects in the EBSD phase map.
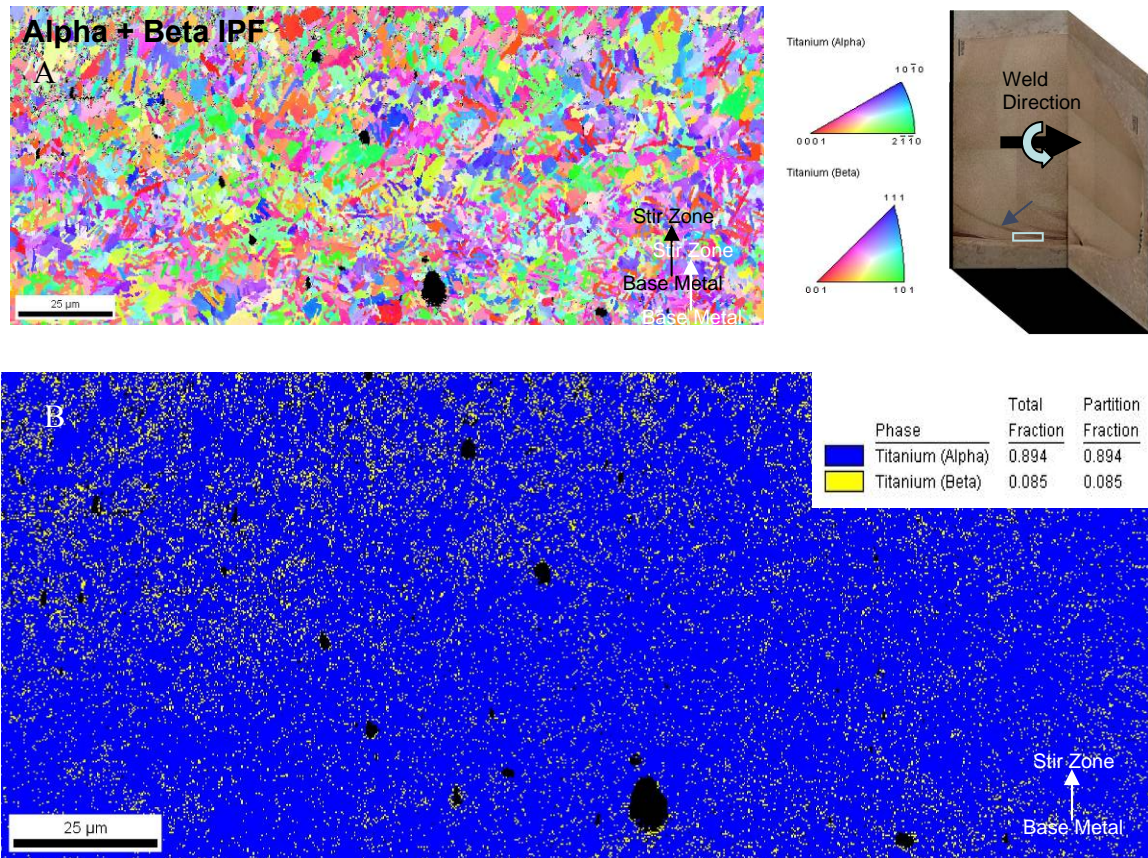
Figure 37. Plan view of 12.7mm Ti-511 FSW. A) Inverse pole figure of the plan view B) Phase map showing β phase surrounding voids shown in black.

In comparison with the plan view, the EBSD from the transverse cross-section in the retreating side shows a reduction in the image quality map of the area (Figure 38). The highest number fraction of misorientation angles was under 10° (Figure 39). The results indicate that the retreating side shows more grain refinement with a higher fraction of low angle misorientation compared to the plan view.
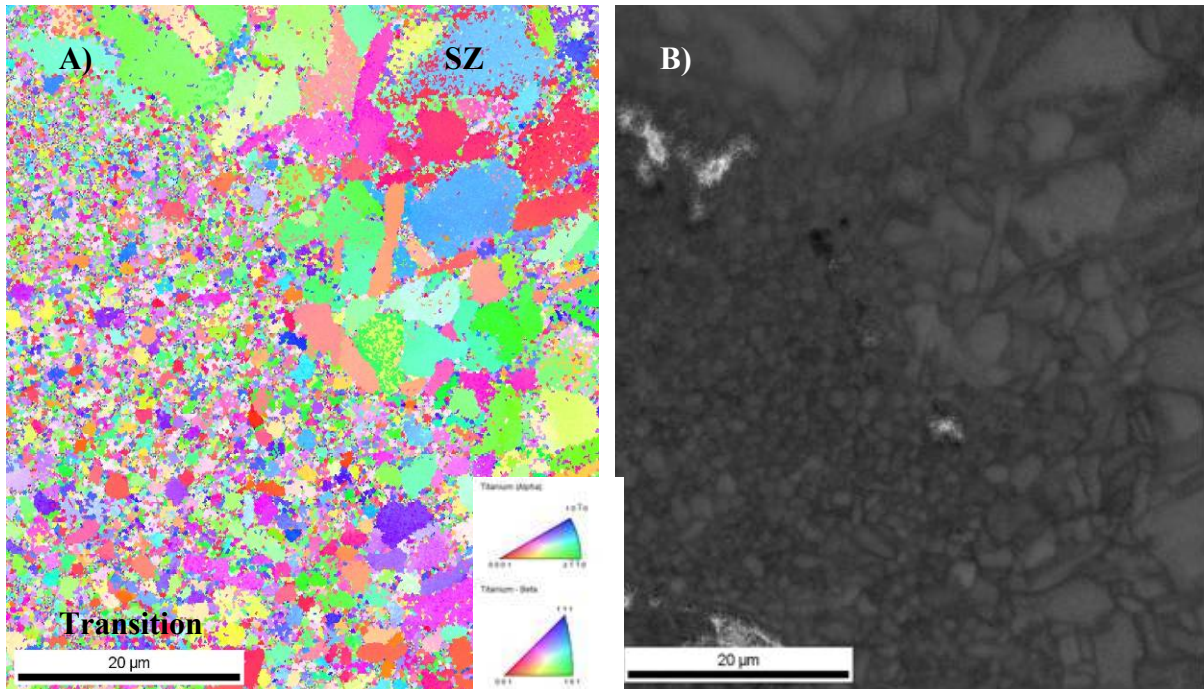
Figure 38. EBSD of transverse cross-section in the retreating side. A) Inverse pole figure B) Image quality map shows a reduction in image quality compared to the plan view Figure 33.
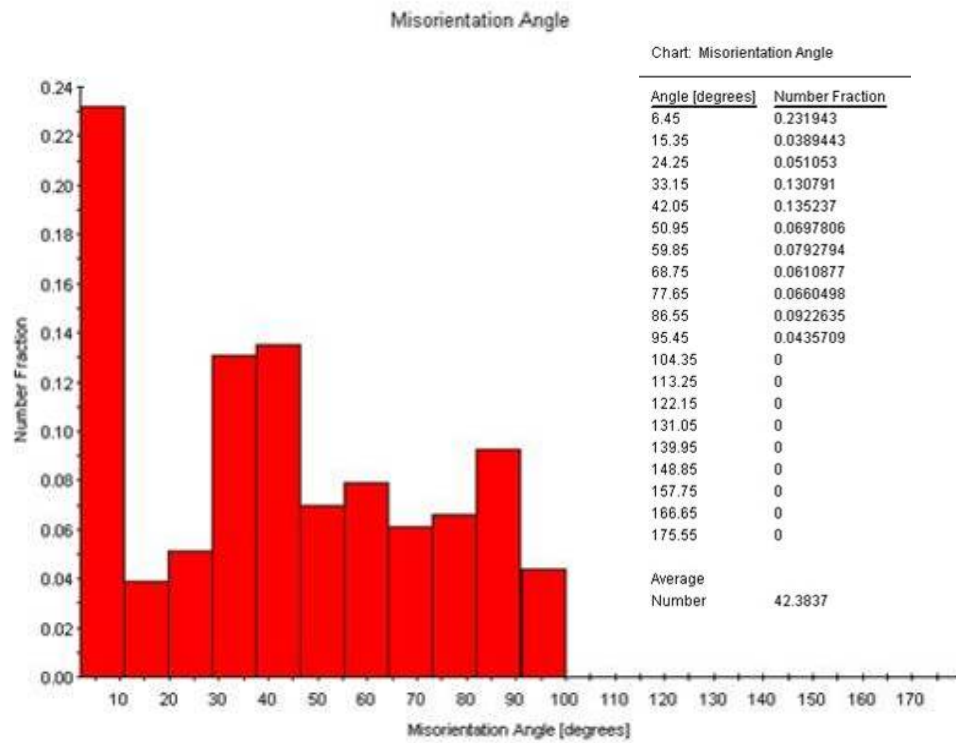
Figure 39. Misorientation angle for transverse cross-section shown in Figure 38. The highest number fraction of misorientation angles was under 10°.

3.2.5.1 Texture within the friction stir weld

Texture is defined as a preferred crystallographic orientation of the grains in a polycrystalline material. Application of large plastic strains can lead to material anisotropy. This is especially strong in hexagonally close packed materials, such as titanium. This section focuses on the experimental analysis of texture within a titanium friction stir weld to known deformation paths, such as extrusions and rolling.

Kocks, et al has defined two stress states in simple shear and pure shear [Kocks 1998]. Pure shear is considered a balanced stress state at all surfaces. Simple shear is considered an unbalanced stress state where the average effect at the surfaces can be described by Equation 5 for dislocation glide as:

$$\delta\gamma = \frac{b\,\delta A}{V}$$ **Equation 5**

where δA is the change in area, b is the magnitude of the Burgers vector, and V is the volume of the specimen. Dislocation glide and twinning are considered simple shear stress states. Simple shear induces lattice rotations to form the basis of texture during deformation [Kocks 1998].
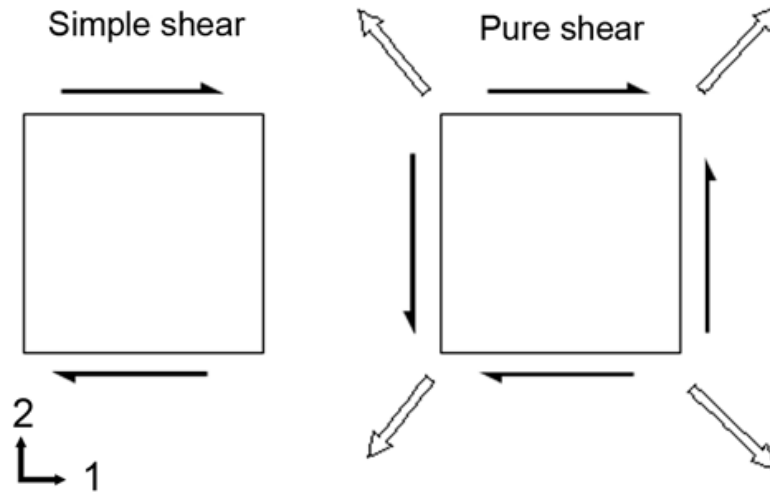
Figure 40. Stress states defined in simple shear and pure shear [Kocks 1998].

Texture is often represented through the use of pole figures. Pole figures are stereographic projections of normal crystallographic plane directions. The crystallographic pole intersects with the surface of a sphere and is projected in two dimensions on the equatorial plane to visualize the relationships of crystallographic directions when viewed in a given direction [Kocks]. An example of orientations for a hexagonal unit cell with the respective pole projection is given in Figure 41. If there is a preferred orientation, pole projections will cluster in certain areas of the stereographic projection. Orientation density functions (ODFs) help provide a quantitative assessment of preferred crystallographic orientations. The density of poles can be explained as a Fourier series with harmonic solutions based on Euler angles. The pole density is plotted with respect to the fraction of grains in a given orientation [Schwartz].
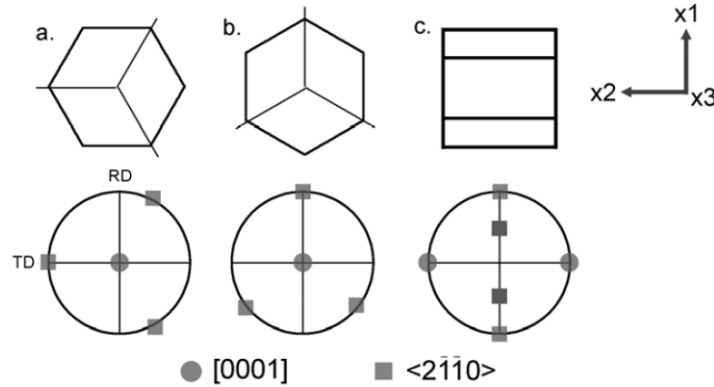
Figure 41. Representative pole figure projection based on crystal location orientation in the HCP crystal structure. [Pilchak]

Titanium alloys also exhibit a transformation texture with the BCC β phase transformation to HCP α. Based on the symmetry of the Burgers relationship and the phases, there are 12 distinct α variants that can form from a β orientation, resulting in 60 unique orientations of the α phase from the β→α transformation. Zeng and Bieler examined this relationship in Ti-64 through variant selection in accordance with the Burgers relationship [Zeng]. This work showed retention of the original texture or alignment of the $<11\overline{2}0>$ with the $(0001)_\alpha$ through a 90° rotation. The authors propose that variant selection is due to transformation of α grains mimicking shear on the $\{110\}_\beta$ of transformation through the Burgers relationship. Gey *et al* show that prior deformation and defects favor the most active slip system for transformation [Gey 1996, 1997, and 2002].

Ideal orientations and texture for HCP systems in simple shear conditions were reported by Beausir in 2007. Five ideal fiber textures were identified: B, P, Y, and C_1-C_2 and are shown schematically in Figure 42. Fiber textures refer to the stability of an orientation with respect to the strain rate sensitivity and the reference stresses. Within the HCP system, the fibers are defined as:

- B fiber: basal plane is along the shear plane

- P fiber: <a> direction is parallel to the shear direction.

- Y fiber: the fiber axis is parallel to the *c*-axis and is rotated 30º towards the shear plane

- C_1 and C_2 fiber: the fiber axis is parallel to the *c*-axis. These fibers are rotated 90º towards the shear direction and $\pm$30º in the shear plane.

While this work was performed in magnesium, Beausir provides insight into development of the fiber textures relative to slip activity. If basal slip is preferred in the crystal the B fiber is the only important fiber. This is in contrast with the other four fibers that have all active slip families. P and Y fibers have only <a> type dislocations while C_1-C_2 have <c+a> type directions.
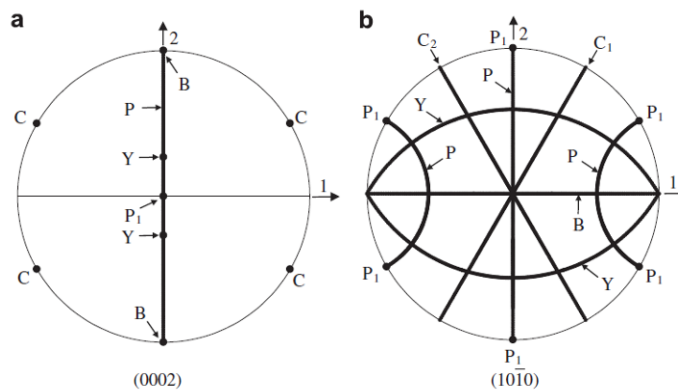
Figure 42. Ideal orientations for HCP magnesium under simple shear for the A) (0002) and B) (10-10) orientations [Beausir].

Ideal orientations and texture for BCC systems in simple shear conditions were reported by Li in 2005 and are given in Table 16 [Li].

64

Table 16. Ideal orientations for BCC under simple shear

Texture Component	{hkl}	<uvw>
D_1	$(\bar{1}\bar{1}2)$	[111]
D_2	$(11\bar{2})$	[111]
E	(110)	$[1\bar{1}1]$
$\bar{E}$	$(\bar{1}\bar{1}0)$	$[\bar{1}11]$
J	(110)	$[1\bar{1}2]$
$\bar{J}$	$(\bar{1}\bar{1}0)$	$[\bar{1}1\bar{2}]$
F	{110}	<001>
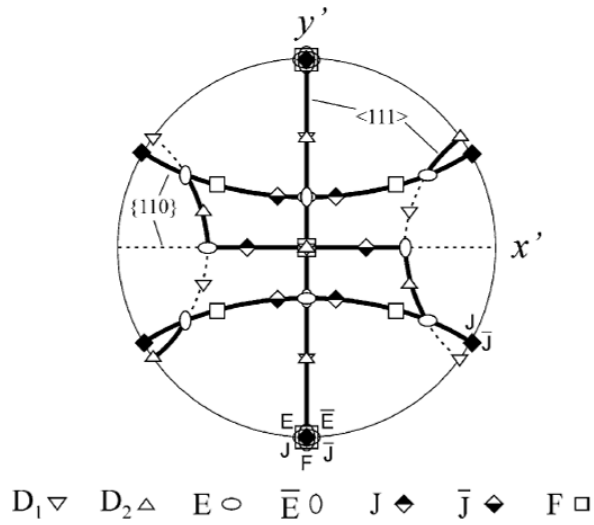
Figure 43. Ideal orientations for BCC simple shear (110) pole figure

Because of the close relationship between the BCC and HCP phases, it is important to visualize the Burgers orientation relationship. This is illustrated in Figure 44.

Figure 44. Combined stereographic image of BCC and HCP in accordance with the Burgers orientation relationship. Open circles are BCC and closed circles are HCP. [Wang]

Texture development within titanium alloys is complex and dependent on a number of factors. To correlate the texture within the friction stir weld to known deformation paths, 50μm scans were selected from Figure 33 for analysis. The selected areas are shown in Figure 45-Figure 48. These figures highlight the texture evolution from base metal to the stir zone. In the associated figures, (A) represents the image quality map generated during the EBSD overlaid with specific crystallographic orientations. (B) shows the symmetric pole figures based on the identified crystallographic directions for the hexagonally close-packed system. The colors associated with the crystallographic direction in (A) correspond to points identified on the pole figures in (B). The selected normal directions for the pole figures correspond to the (0001) basal plane, the $(10\bar{1}0)$ prism plane, and the $(11\bar{2}0)$ plane related to the slip systems for HCP structures. The $<11\bar{2}0>$ direction also relates to the Burger's orientation relationship for transformation from the HCP crystal structure to the BCC crystal structure as discussed in Chapter 1. In (C), the orientation density functions (ODFs) gives a quantitative assessment of crystallographic orientations within the selected area. Similar to

66

(B) the selected normal directions for the pole figures corresponds to the (0001) basal plane, the $(10\bar{1}0)$ prism plane, and the $(11\bar{2}0)$ plane for HCP structures.

Analysis of the base metal (Figure 45) shows distinct orientations on the pole figure in the idealized symmetric pole figure. In particular, orientations associated with the <0001> (highlighted in blue), the $<10\bar{1}0>$ prism (highlighted in red), and the $<11\bar{2}0>$ (highlighted in green) are shown in both the symmetric pole figure and the ODF. There appears to be a strong correlation of the symmetric pole figure and the ODF in the $(11\bar{2}0)$ plane, though a hexagonal variant shows higher texture strength in the ODF. The Ti-5111 weld was fabricated using rolled plate with the welding direction parallel with the rolling direction. Because these scans were obtained in the plan view, there is no distinct base metal texture associated with the rolling process. Moving from the base metal to the transition region in Figure 46 and Figure 47 shows a reduction of texture strength in the $(11\bar{2}0)$ and $(10\bar{1}0)$ planes. Adjacent to the base metal in Figure 46 we see a rotation of (0001) and $(11\bar{2}0)$ texture compared to the base metal. Further in the transition region in Figure 47 we see a reduction of texture strength in all the planes. There appears to be a rotation of $(11\bar{2}0)$ texture with a loss of distinct (0001) HCP texture variants and $(10\bar{1}0)$ texture. These texture rotations result in distinct orientations present in both the idealized symmetric pole figure and in the ODF within the FSW region in Figure 48. However, little texture in the FSW is associated with the (10-10) plane compared to the base metal. Variants from the base metal and transition region appear in the FSW texture ODF for (0001) and $(11\bar{2}0)$. The FSW ODFs show a strong correlation of the symmetric pole figure with the ODF. The FSW

($11\bar{2}0$) ODF appears to be a rotation of the ($11\bar{2}0$) base metal ODF; which signifies that within the friction stir weld the crystallographic orientations in the texture ODF are rotated from the base metal. Based on experimentally determined temperatures during welding, this result indicates that as the material is being welded it transforms from α to β and back to α and the crystallographic orientations in the base metal and weld are related through a rotation in the texture ODF. The resulting texture indicates the associated texture relationship to mechanical properties in the FSW should be similar to the base metal relationship.
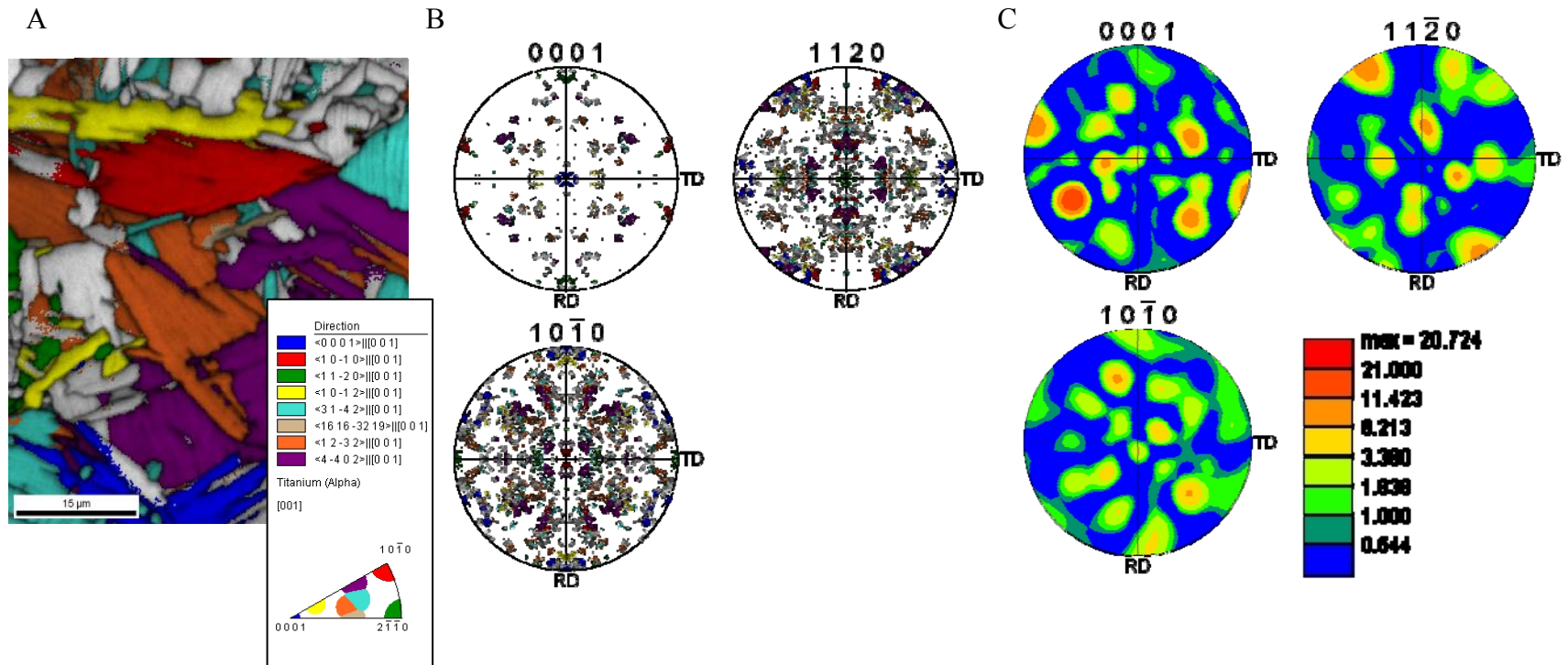
Figure 45. A) Image quality map B) Symmetric pole figures and C) Orientation density functions obtained from the base metal. The colors associated with the crystallographic direction in (A) correspond to points identified on the pole figures in (B). The selected normal directions for the pole figures correspond to the (0001) basal plane, the ($10\bar{1}0$) prism plane, and the ($11\bar{2}0$) plane related to the slip direction for HCP structures. In (C), the orientation density functions (ODFs) gives a quantitative assessment of crystallographic orientations within the selected area. (C) Base metal ODF: Distinct orientations are present in both the idealized symmetric pole figure and in the ODF. No distinct base metal texture in the plan view related to the rolling process is observed.
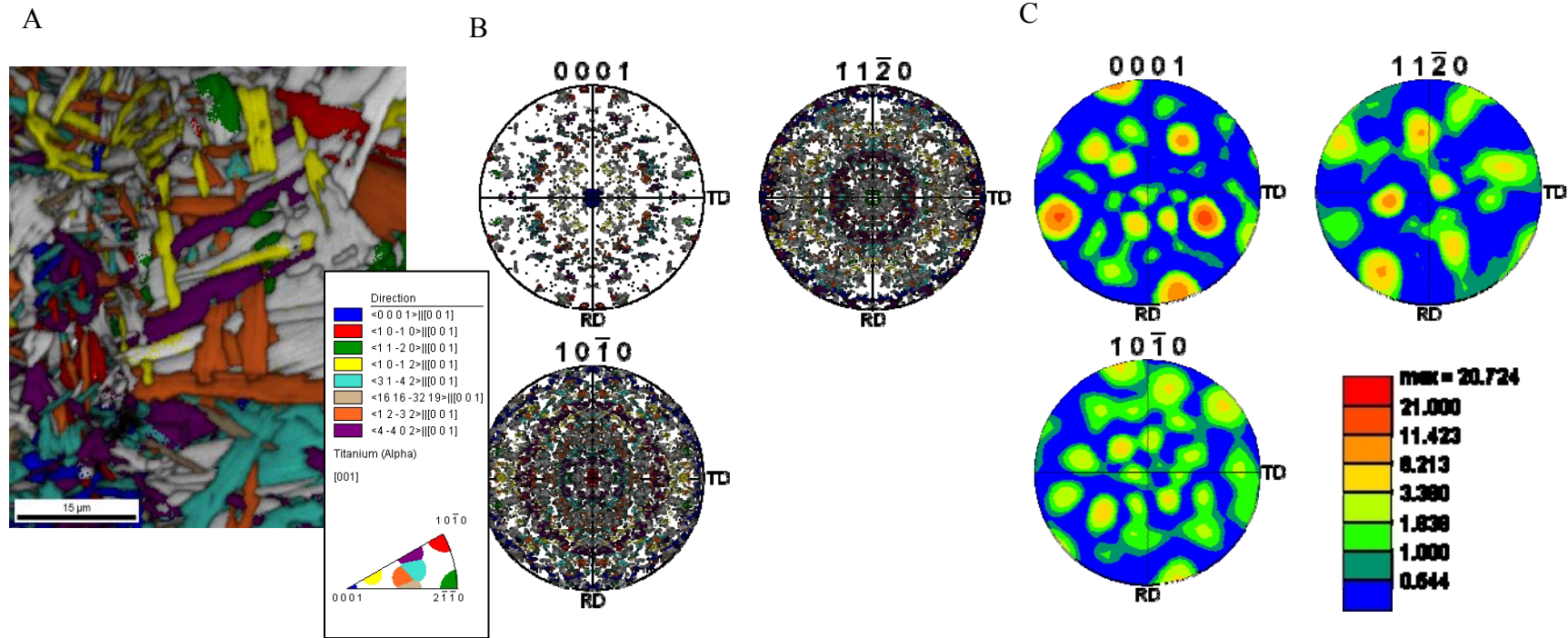
Figure 46. A) Image quality map B) Symmetic pole figures and C) Orientation density functions obtained from the transition region. The colors associated with the crystallographic direction in (A) correspond to points identified on the pole figures in (B). (C) Transition Region (near the base metal) ODF shows a reduction of texture strength in the ($11\bar{2}0$) and ($10\bar{1}0$) planes and a rotation of (0001) and ($11\bar{2}0$) texture compared to the base metal.
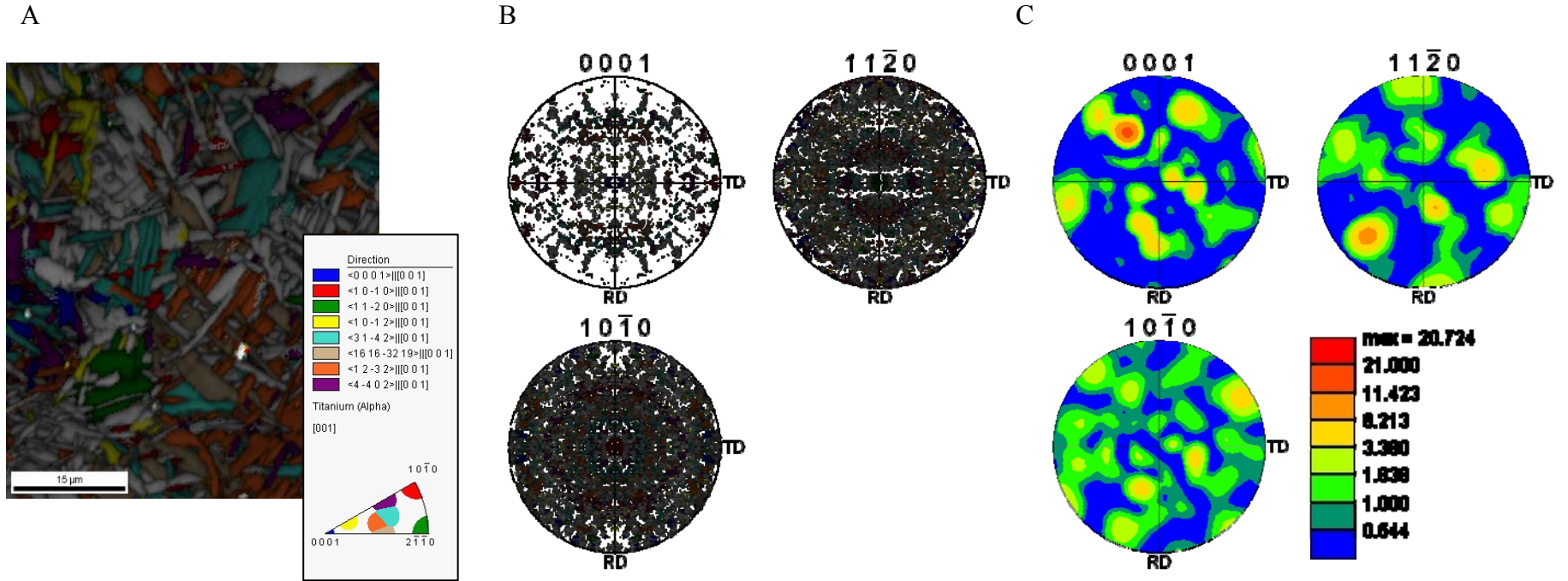
Figure 47. A) Image quality map B) Symmetic pole figures and C) Orientation density functions obtained from the transition region. The colors associated with the crystallographic direction in (A) correspond to points identified on the pole figures in (B). (C) Transition Region (near the stir zone) ODF shows a reduction of texture strength in all planes. There is a rotation of the $(11\bar{2}0)$ texture and a loss of distinct (0001) HCP texture variant and $(10\bar{1}0)$ texture.
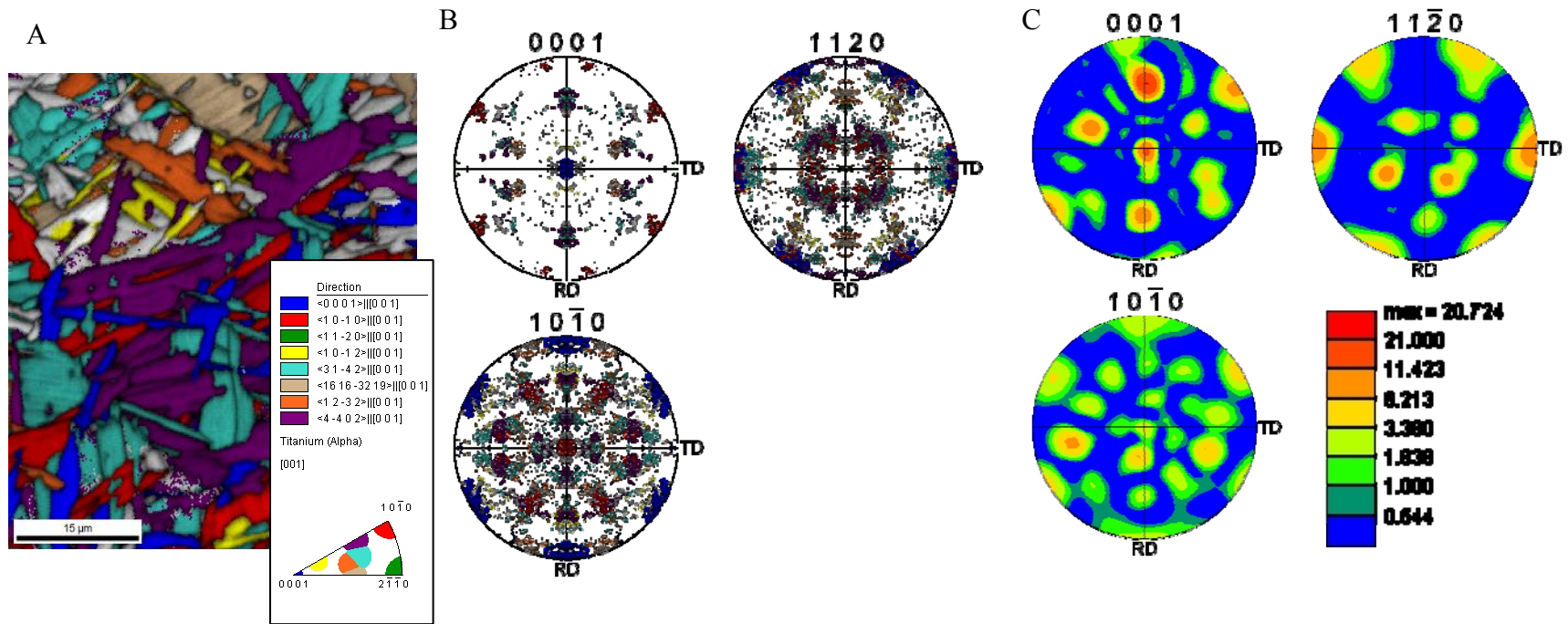
Figure 48. A) Image quality map B) Symmetic pole figures and C) Orientation density functions obtained from the stir zone. The colors associated with the crystallographic direction in (A) correspond to points identified on the pole figures in (B). (C) FSW Region ODF Distinct orientations present in both the idealized symmetric pole figure (B) and in the ODF (C) with a strong correlation between the two. There is little texture associated with the ($10\bar{1}0$).

3.2.5.2 Texture development and grain refinement mechanisms

Reported literature for texture analysis in friction stir welding of metals primarily show simple shear texture developed during the process. For friction stir welds in aluminum alloys, Fonda *et al* used a "stop action" technique to abruptly stop the welding tool and quench in microstructure around the tool in Al 2195, an aluminum lithium alloy [Fonda 2007b]. Adjacent to the tool, the texture was shown to be primarily the B fiber texture associated with simple shear. Based on EBSD within Fonda's work, development of subgrain misorientation around the tool indicates a continuous dynamic recrystallization mechanism with rapid recovery from strain and migration of grain/subgrain boundaries [Fonda 2007]. Certain regions also exhibit geometric dynamic recrystallization with grain elongation and thinning [Fonda 2007a]. Similarly, Reynolds noted the development of shear texture for friction stir welding of β21s and related the developed texture to BCC torsion texture [Reynolds]. Research performed by Mironov showed $\beta \rightarrow \alpha$ phase transformation for friction stir welding of Ti-64. Reconstruction of the prior β grain shows an ideal BCC simple shear texture [Mironov 2008a]. The texture most likely resulted from the {110}<111> slip just before the material transformed in β during welding. Transformation back from β to α shows limited variant selection [Mironov 2008b]. In contrast to the β and $\alpha+\beta$ textures developed through friction stir welding, FSW of pure titanium resulted in a strong P fiber texture [Mironov 2009].

Recently, work published by Knipling and Fonda examining a "stop action" weld in Ti-5111 used locations on the (0001) and $(11\bar{2}0)$ orientations to determine the β texture relationship. Similar to Reynolds work, a rotation of ~35º was needed to align the α hcp texture with

($1\overline{1}2$)[111] BCC shear transformed through the Burgers orientation relationship [Knipling]. β phase reconstruction by Pilchak shows that the β phase exhibits a cube component with the Goss orientation {110}<001> in the reconstructed prior β grain but resulted in a nearly random α phase texture in the stir zone [Pilchak 2009]. Within this thesis, the texture analysis performed is consistent with the reported literature for texture development of titanium alloys during friction stir welding in the stir zone. Analysis across the plan view from the base metal to the weld allows for analysis of the steady state transition region that has not been reported in the literature. Comparing the (0001) texture of the transition zone in Figure 46 and Figure 47 to that of the BCC{110} idealized texture components, shows strengthening of the F fiber component through the transition region before transformation to D_2 shear texture in the stir zone with a rotation of the pole figure by approximately 28.4° about the center of the pole figure. This is illustrated in Figure 49. This work uniquely highlights the development of texture within the transition zone.
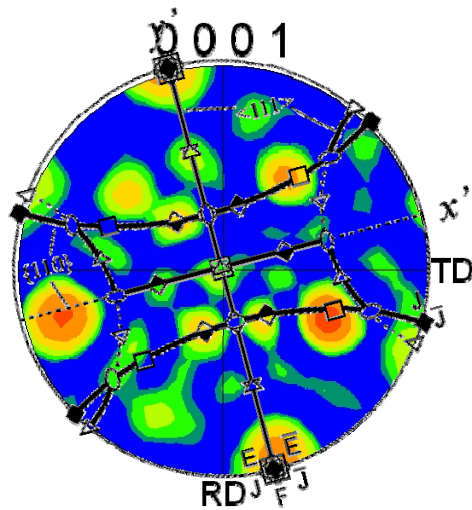
Figure 49. Ideal BCC (110) shear orientation overlaid on the (0001) pole figure from the transition region. Maximum intensity of ODF aligns with strengthening of the F fiber component from BCC simple shear with a rotation of the pole figure by approximately 28.4° about the center of the pole figure.

3.2.5.3 EBSD of localized tensile properties

As discussed in Section 3.2.3, electron backscatter diffraction was applied to microtensiles prior to deformation and after deformation [Cheng]. For the weld microtensile illustrated in Figure 50, shows alignment with the [0$\bar{1}\bar{1}$] BCC and [0$\bar{1}$11] HCP. In contrast at the interface of the weld and the base metal in Figure 51, there is strengthening of the [1$\bar{1}$0]BCC and [0001] HCP texture. This work clearly illustrates the texture dependence and strengthening of preferred textures after mechanical testing.

Figure 50. Pre and post microtensile testing texture analysis of all stir zone Ti-5111. Post-testing shows a preference in the [0$\bar{1}\bar{1}$] **BCC and** [0$\bar{1}$11] **HCP.**
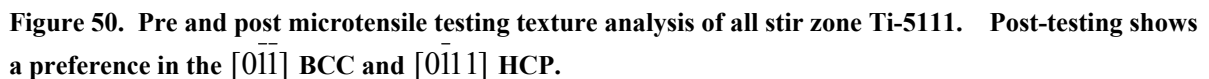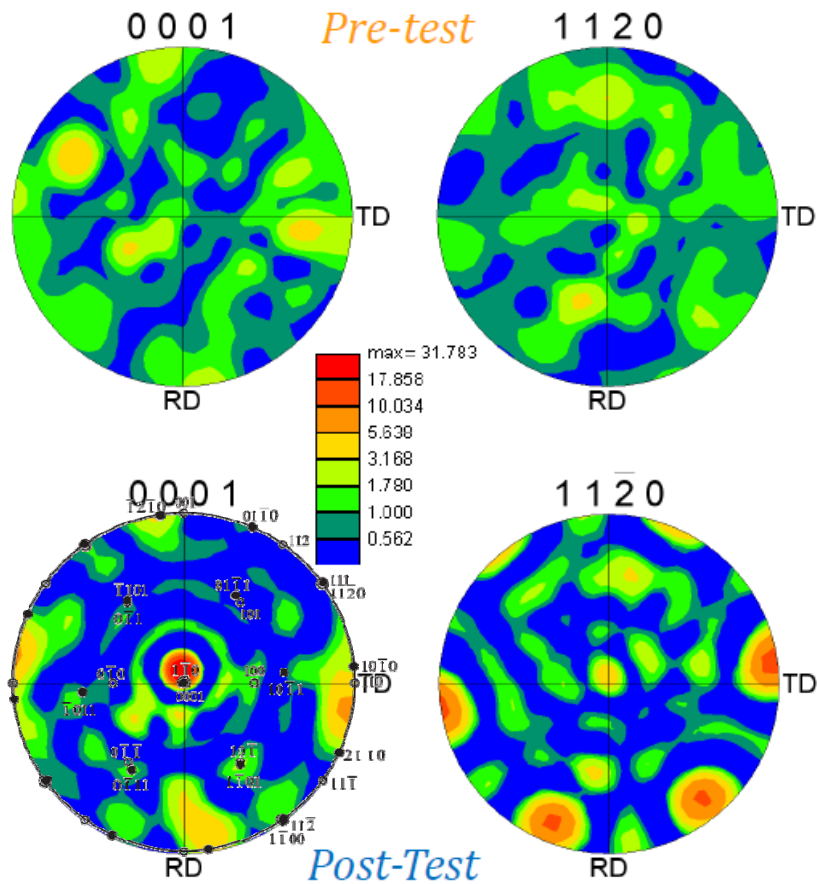
Figure 51. Pre and post microtensile testing texture analysis of all stir zone interface with base metal in Ti-5111. Post-testing shows strengthening in the basal plane texture.

3.2.6 Transmission Electron Microscopy

Transmission electron microscopy (TEM) allows for high magnification materials characterization through the use of an electron beam transmitted through an electron transparent specimen. An in depth explanation of the technique and fundamental principles can be found in Williams and Carter [Williams]. Specimens were prepared for TEM characterization using the techniques described in Section 2.4.1.

Diffraction patterns for both the base metal and stir zone within this section were indexed by determining the experimental *d*-spacing, or interplanar spacing, and comparing it to the

theoretical *d*-spacing of Ti.   The experimental *d*-spacing is measured directly from the

unindexed diffraction pattern. The theoretical *d*-spacing is given by:

$$d_{theoreticalHCP} = \left(\frac{4}{3a^2}(h^2 + hk + k^2) + \frac{l^2}{c^2} \right)^{-1/2} \text{ and } d_{theoreticalBCC} = \frac{a}{\sqrt{h^2 + k^2 + l^2}} \qquad \textbf{Equation 6}$$

where a_{BCC}= the lattice constant of the BCC phase is 3.31Å, a_{HCP} = 2.95 Å for the HCP

phase and c_{HCP} = 4.68 Å for the HCP phase and *h, k, l* are the reflection indices.

An HCP structure has two atoms in the basis of the rhombohedral unit cell. The coordinates

of the atoms are (x, y, z) = (0, 0, 0) and (1/3, 2/3, 1/2). Substituting these values in the

structure factor equation to define the unit cell scattering amplitude gives:

$$F = f\{1 + e^{2\pi i \left(\frac{h}{3} + \frac{2k}{3} + \frac{l}{2} \right)}\} \qquad \textbf{Equation 7}$$

where *f* is the atomic form factor for Ti. Simplifying this equation with *h*/3 + 2*k*/3 + *l*/2 =X

gives:

$$|F|^2 = f^2(2 + 2\cos2\pi X) = f^2(4\cos^2\pi X) \qquad \textbf{Equation 8}$$

meaning that the rules for diffraction for an HCP structure relies on whether or not *h*+2*k* = a

multiple of 3:

- $|F|^2 = 0$ if *h*+2*k* =3*m* and *l* is odd
- $|F|^2 = 4f^2$ if *h*+2*k* =3*m* and *l* is even
- $|F|^2 = 3f^2$ if *h*+2*k* =3*m* +1 and *l* is odd
- $|F|^2 = f^2$ if *h*+2*k* =3*m* +1 and *l* is even

Indexing a BCC diffraction pattern uses two lattice points at (0, 0, 0) and (1/2, 1/2, 1/2) and:

$$F = f\{1 + e^{\pi i(h+k+l)}\}$$
<div align="right">**Equation 9**</div>

Giving the rules of diffraction for a BCC structure as:

- $F = 2f$ if $h + k + l$ is even
- $F = 0$ if $h + k + l$ is odd

A detailed explanation of the derivation of the structure factor and rules for diffraction can be found in Williams and Carter [Williams].

3.2.6.1 Comparison of Selected FSW regions

TEM analysis comparing base metal to the all-stir zone utilized specimen preparation through jet polishing and ion milling as described in Section 2.4.1. With jet polishing and ion milling the resulting bright field and dark field images showed a clearly defined α and β structure. Early TEM experiments using mechanical polishing contained Moiré fringes and polycrystalline precipitates that obscured microstructural details. Bend contour bands were identified within the specimens examined here.

The bright field image for the Ti-5111 base metal lath structure is given in Figure 52. The indexed diffraction pattern from the area is shown in the inset of Figure 52 and gives a [0001] HCP zone axis. Dark field images were taken for $\bar{g} = (\bar{2}1\bar{1}0), (\bar{1}100), (1\bar{2}10), (\bar{1}010)$ and are shown in Figure 53-Figure 56.   Selected dislocations labeled A, B, C were chosen for analysis and are shown in red in the dark field images.

In order to characterize the dislocations, visibility conditions using $\bar{g} \bullet \bar{b}$ where b is the Burger's vector must be evaluated.   In dark field images a dislocation is visible when

$\overline{g} \bullet \overline{b} \neq 0$ and invisible when $\overline{g} \bullet \overline{b} = 0$. Visibility conditions for the selected dislocations are summarized in Table 17. Within the base metal possible Burger's vectors based on visibility conditions using $\overline{g} \bullet \overline{b}$ for dislocation A are $\overline{b} = \frac{1}{3}[11\overline{2}0]$ and $\frac{1}{3}[2\overline{1}\overline{1}0]$. Possible Burger's vectors for dislocation B are $\overline{b} = \frac{1}{3}[11\overline{2}0]$. Possible Burger's vectors for dislocation C are

$$\overline{b} = \frac{1}{3}[0\overline{2}11] \text{ and } \frac{1}{3}[01\overline{1}2].$$
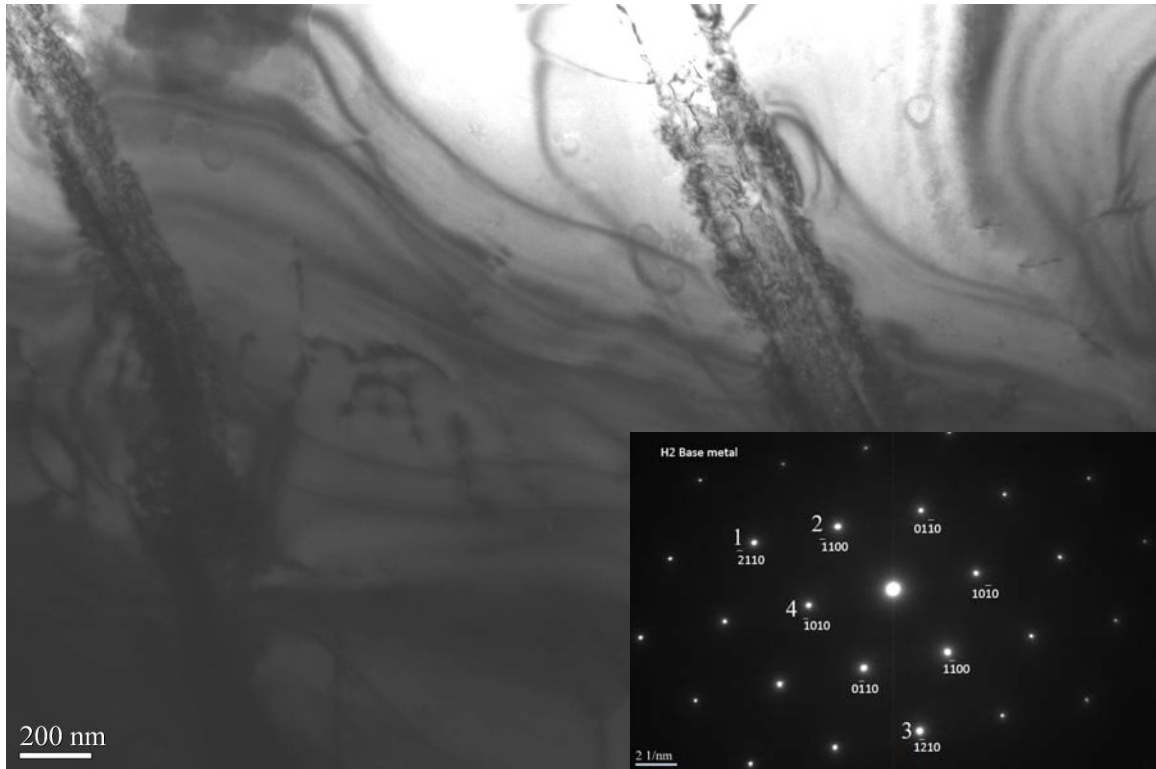
Figure 52. Bright field image of lath base metal microstructure. The indexed diffraction pattern is given in the inset with a [0001] HCP zone axis.
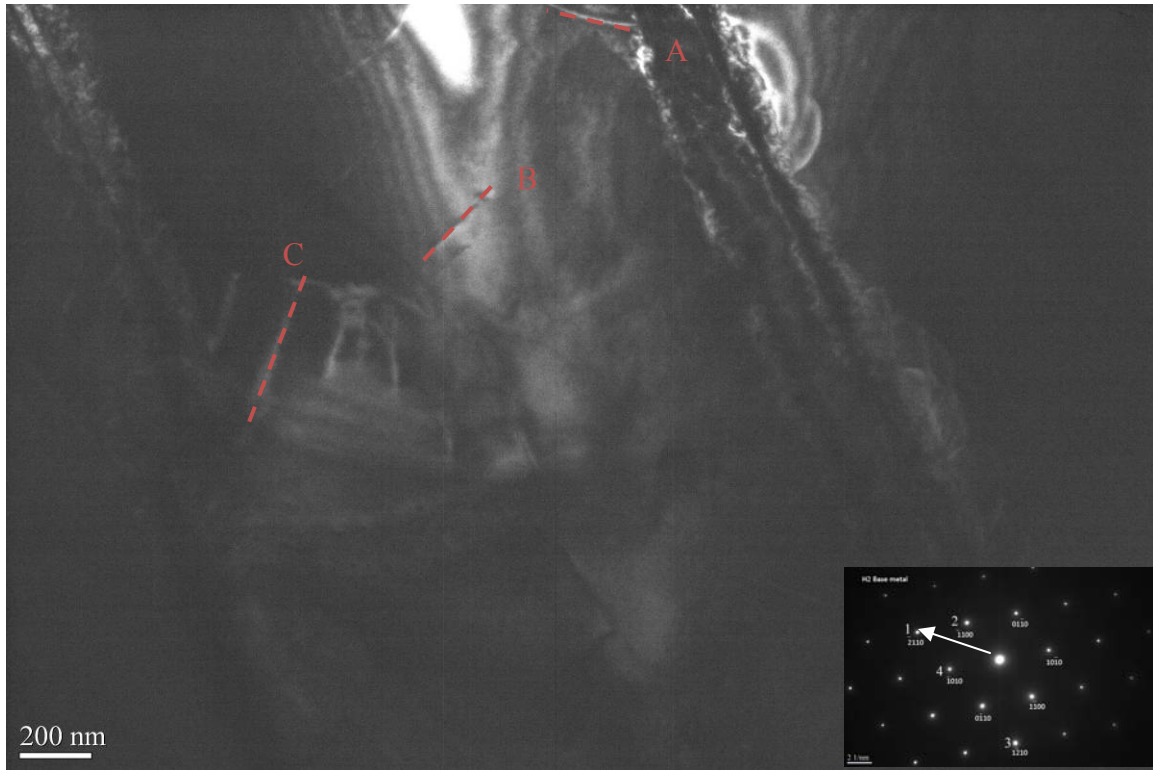
Figure 53. Dark field image from the base metal for $\overline{g} = (\overline{2}110)$
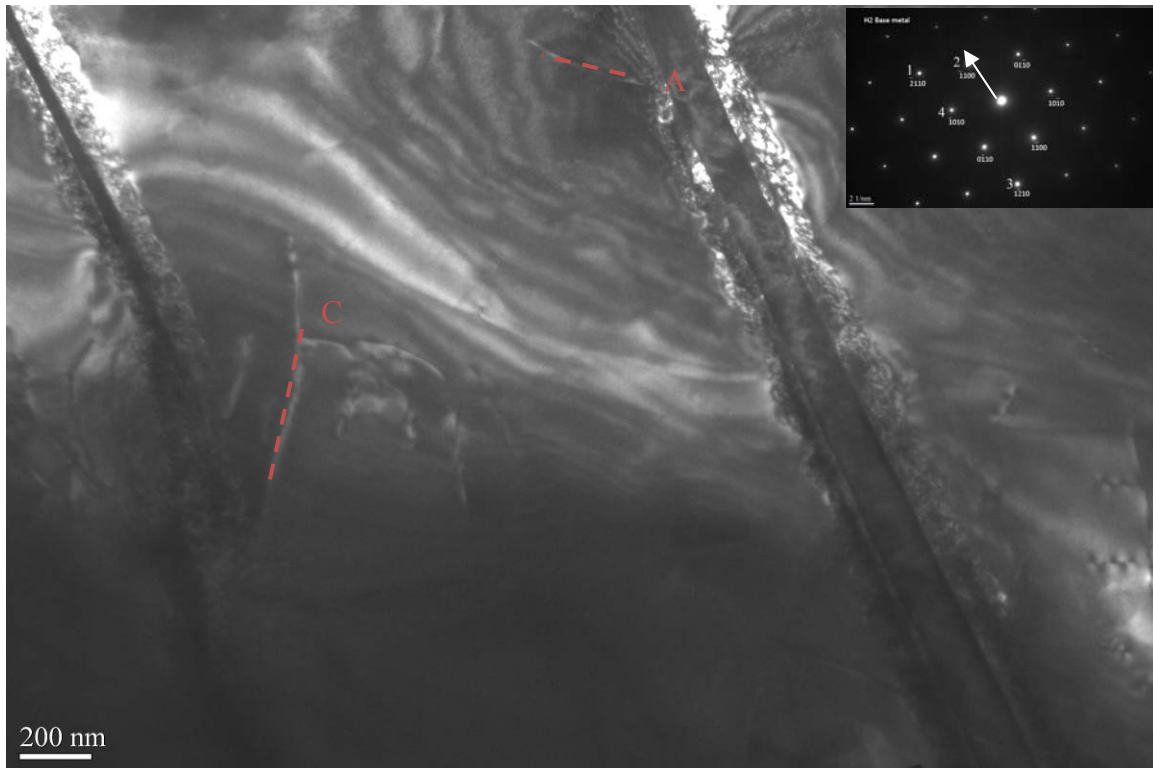
Figure 54. Dark field image from the base metal for $\overline{g} = (\overline{1}100)$
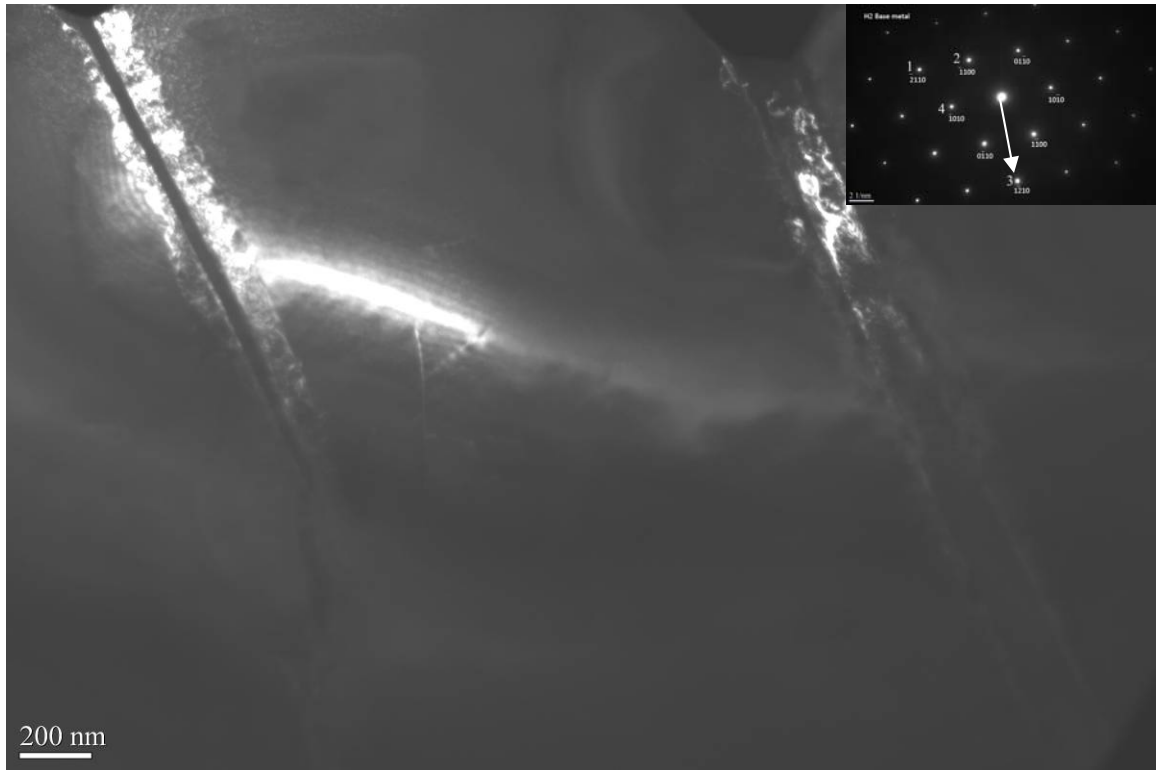
Figure 55. Dark field image from the base metal for $\overline{g} = (1\overline{2}10)$
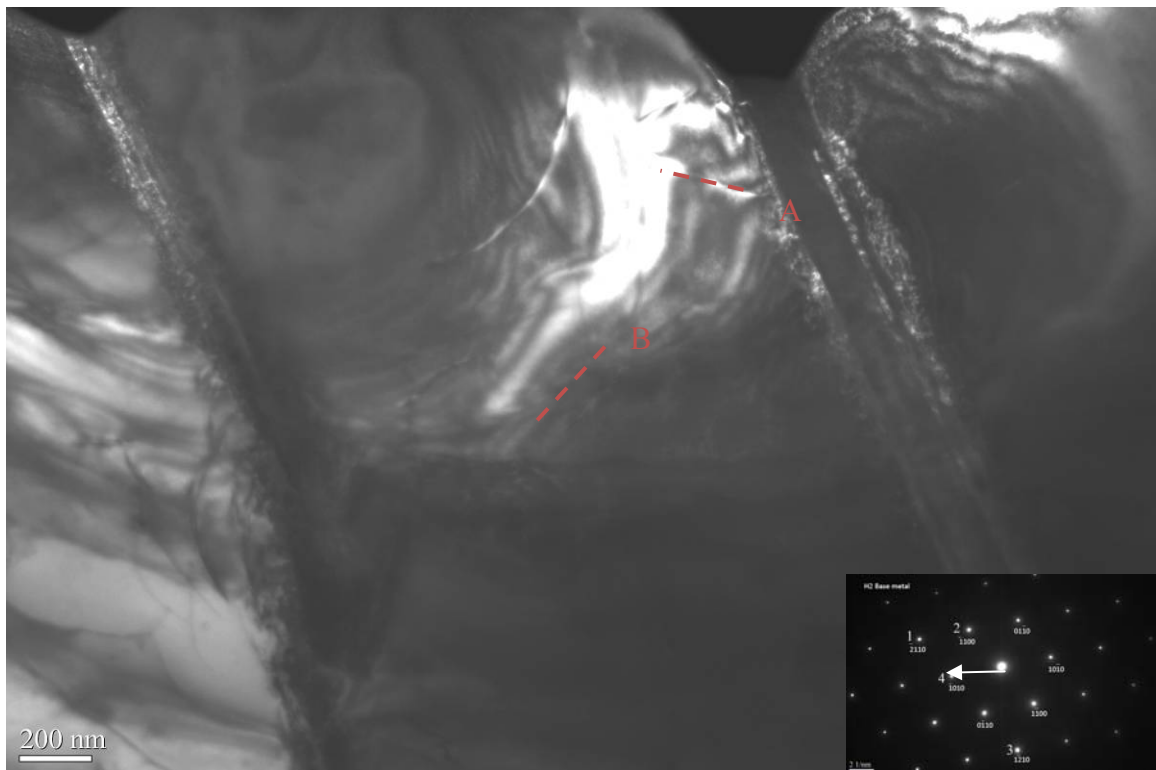
Figure 56. Dark field image from the base metal for $\overline{g} = (\overline{1}010)$

Table 17. Visibility conditions for base metal dislocations A, B, C

Dislocation	$\bar{g} = (\bar{2}1\bar{1}0)$	$\bar{g} = (\bar{1}1\bar{1}0)$	$\bar{g} = (\bar{1}0\bar{1}0)$
A	Visible	Visible	Visible
B	Visible	Invisible	Visible
C	Visible	Visible	Invisible

The bright field image for the Ti-5111 stir zone lath structure is given in Figure 57. The indexed base metal diffraction pattern is shown in the inset of Figure 57 and gives a [0001] HCP zone axis. Dark field images were taken for $\bar{g} = (2\bar{1}\,\overline{1}0), (10\overline{1}0)$ and are shown in Figure 58 and Figure 59. Selected dislocations labeled A, B, and C were chosen for analysis and are shown in red in the dark field images. Visibility conditions for these dislocations are summarized in Table 18. Within the stir zone possible Burger's vectors based on visibility conditions using $\bar{g} \bullet \bar{b}$ for dislocation A are $\bar{b} = \frac{1}{3}[11\bar{2}0], \frac{1}{3}[2\bar{1}\,\overline{1}0]$. Possible Burger's vectors for dislocation B are $\bar{b} = \frac{1}{3}[01\bar{1}2]$. Possible Burger's vectors for dislocation C are $\bar{b} = \frac{1}{3}[01\bar{1}2]$.
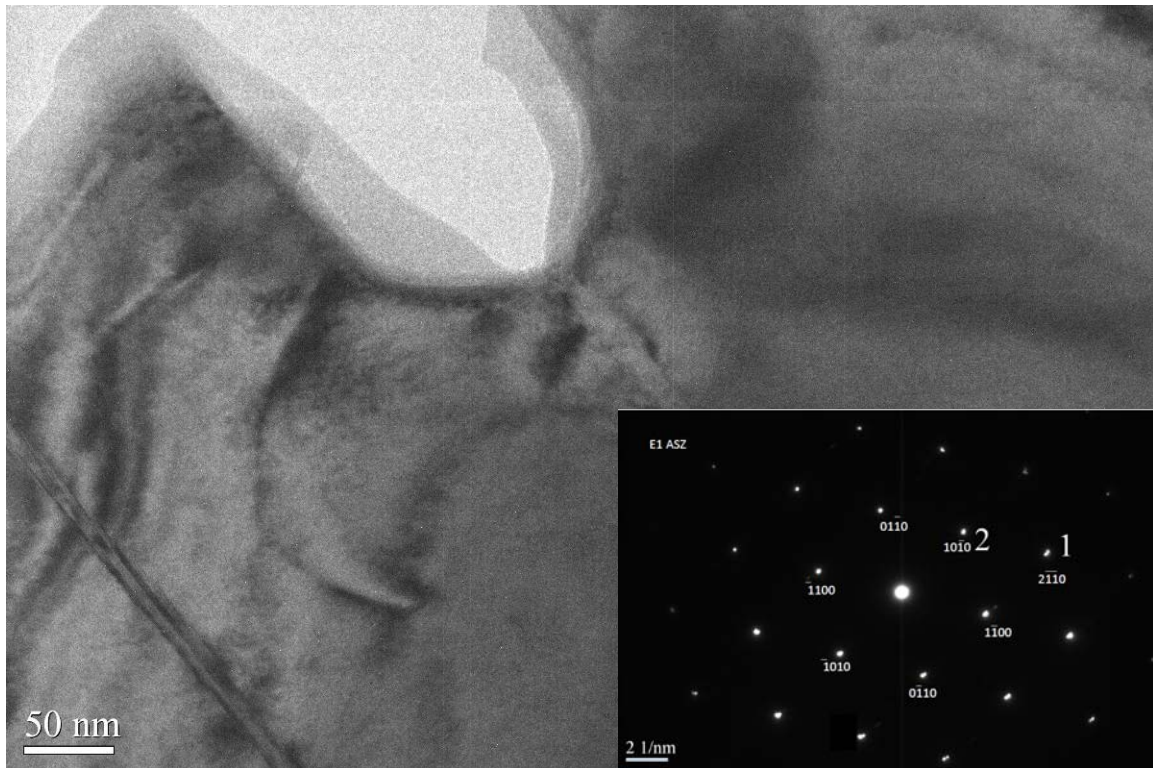
Figure 57. Bright field image of lath stir zone microstructure. The indexed diffraction pattern is given in the inset with a [0001] HCP zone axis.
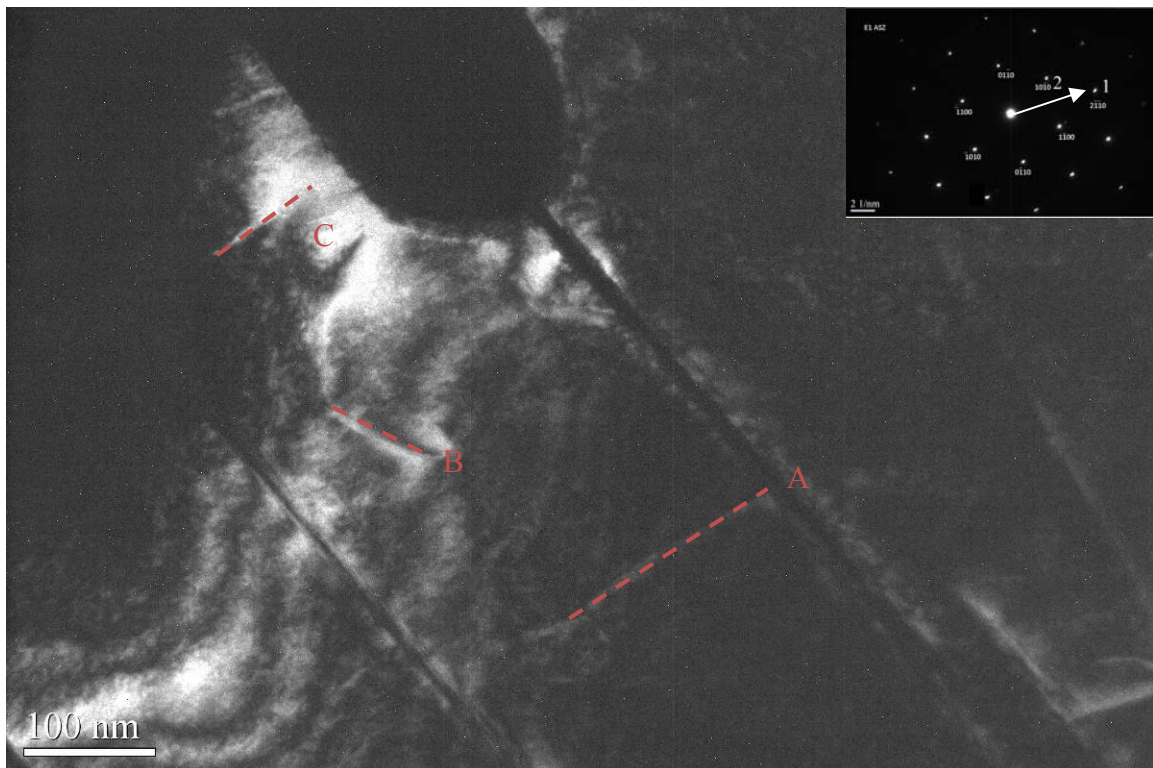
Figure 58. Dark field image from the stir zone for $\bar{g} = (2\bar{1}\bar{1}0)$
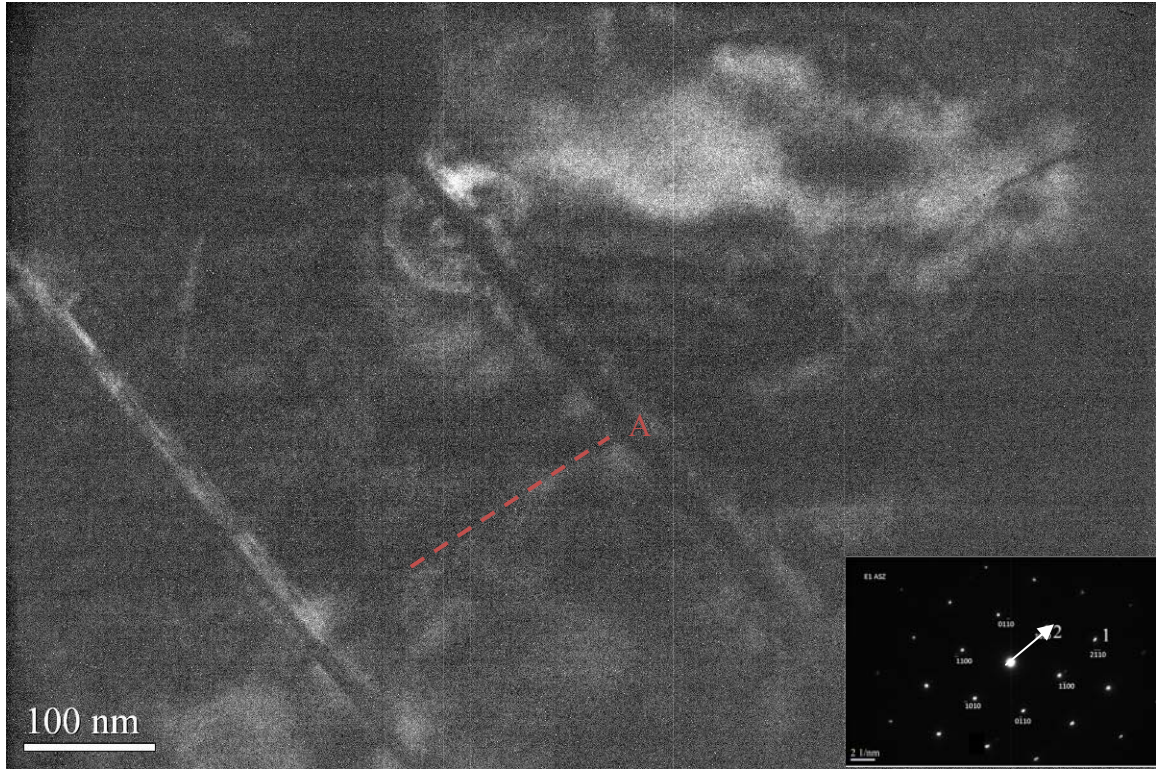
Figure 59. Dark field image from the stir zone for $\bar{g} = (10\bar{1}0)$

Table 18. Visibility conditions for friction stir zone dislocations A, B, C

Dislocation	$\bar{g} = (\bar{2}110)$	$\bar{g} = (10\bar{1}0)$
A	Visible	Visible
B	Visible	Invisible
C	Visible	Invisible

Comparing the electron microscopy images between the base metal and the stir zone shows a similar lath structure with low dislocation density and no lath grain substructure, such as dislocation tangles. Reported TEM results for titanium friction stir welds have also shown dislocation free α within a bimodal lamellar α+β microstructure indicative of dynamic recrystallization of α [Zhou] [Zhou 2010]. Ramirez, Juhas, and Pilchak noted equiaxed α in the stir zone of mill-annealed Ti-64 and acicular α in the TMAZ [Ramirez][Pilchak 2009]. Examining TEM results for friction stir welding of pure titanium shows high dislocation density with dislocation walls which is indicative of incomplete recovery [Lee]. Within this

work, TEM analysis of the stir zone of Ti-5111 friction stir welds shows evidence of recrystallization with low dislocation density and little substructure within the α lamellae.

3.2.6.2 Role of α-β interface

The fully lamellar colony type microstructure has shown Hall-Petch type strengthening associated with the α-β interface and is dependent on α lath thickness [Semiatin 2001]. The authors show that Hall-Petch type strengthening at the α-β interface in a colony structure is analogous to grain boundaries in single phase materials. Further examination of the interface in a fully lamellar colony type structure shows intergranular failure in Ti-64 subtransus hot rolling with a Widmenstatten microstructure [Matsumoto]. Examination of the underlying microstructure shows strain concentration within β and crack propagation along the grain boundary α. At the α and β phase interface, the phase orientation results in strain localization [Semiatin]. This section examines the α-β interface through the use of high resolution TEM on the JEOL 2100 Field Emission TEM in both Ti-5111 base metal and in the stir zone. A comparison of α lath thickness between base metal and the stir zone is also discussed.

Results discussed in Section 3.2.1 have highlighted the dramatic grain refinement within the friction stir welded Ti-5111. The grain refinement leads to a significant difference in α lath thickness which plays a role in Hall-Petch type strengthening [Semiatin 2001]. To measure the α lath thickness, a Clemex Vision software was used. This method is a variation of the linear intercept method from ASTM E112. Base metal images were captured with a 1000x magnification to delineate laths. Stir zone images were taken on the SEM at 4500x due to the fine lath size. A threshold procedure to highlight α and β and then a series of concentric

85

ovals were overlaid on the image as shown in Figure 60. When an oval intersected a lath edge, the segment of the line was removed (Figure 61). For specimens in which the lath orientation was almost vertical, a horizontal grid pattern with the same principles was applied to determine the α lath thickness. The remaining line segments were then measured. Each specimen had 5-13 fields of view and the views were randomly chosen, though care was taken to avoid grain boundary α. For the base metal, the average α lath thickness obtained with this method was 1.99μm. For the stir zone, the average α lath thickness was 0.58μm. This lath thickness is in agreement with the approximate lath thickness measured from the TEM images. The refined α lath thickness within the stir zone likely plays a parallel role in the higher hardness and tensile strength shown in Sectiosn 3.2.2 and 3.2.3 as has been previously reported [Semiatin].
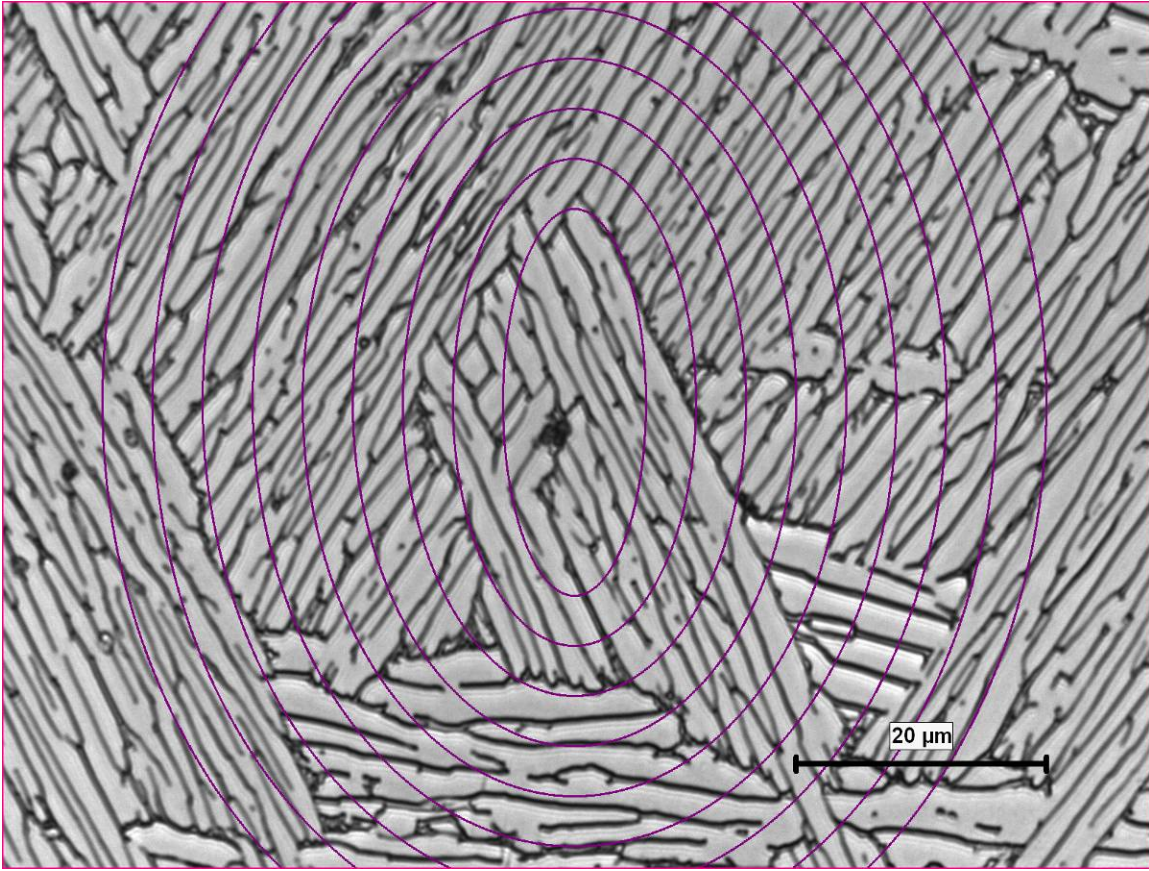
Figure 60. Optical micrograph of α laths with overlaid concentric ovals. This method is a variation of the linear intercept method from ASTM E112.
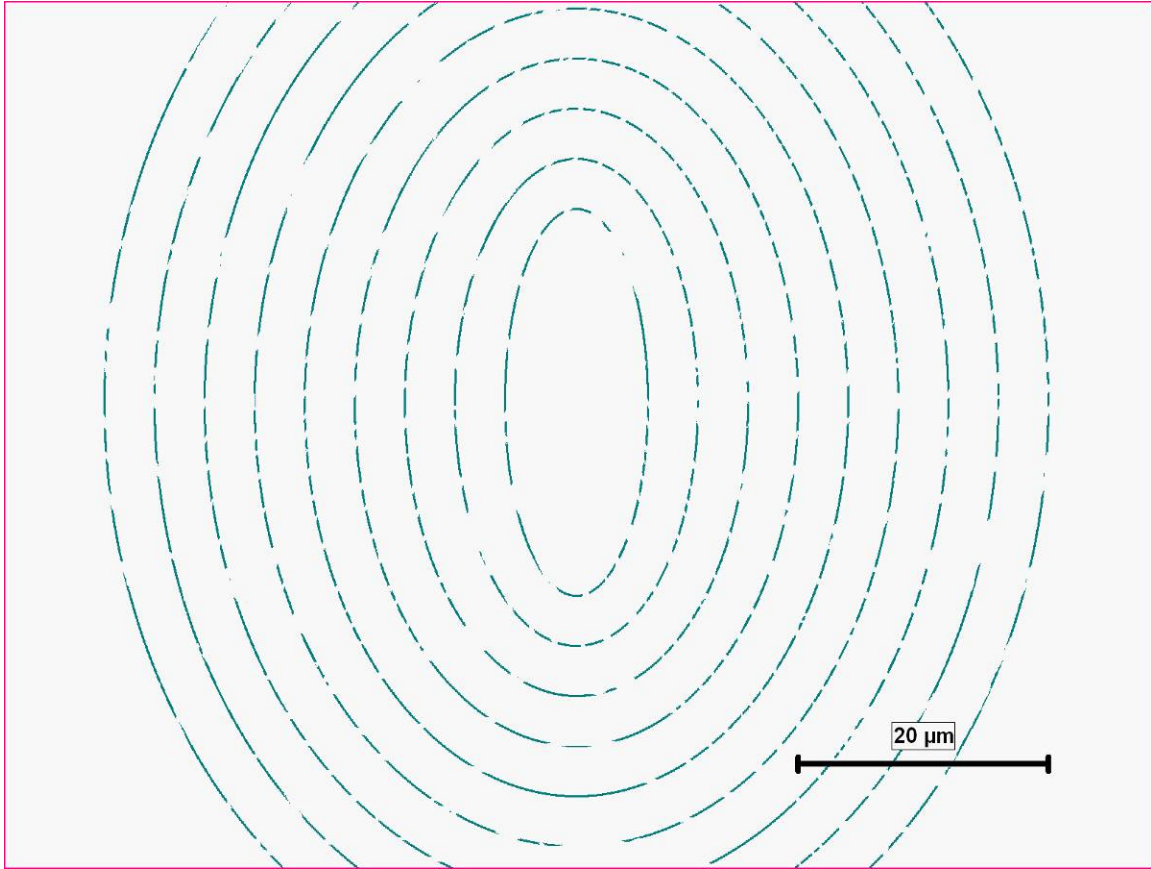
Figure 61. Line segment removal due to the intersection of the pattern with the α lath edge.

A closer examination of the α lath structure can be described schematically as having three sides: an edge face, a side face, and a broad face containing structural ledges. This is shown schematically in Figure 62a and b. Contrary to other reported literature suggesting easy dislocation transfer across the α/β interface, Suri, *et al* suggests that the α/β interface can result in dislocation pileup at the interface [Suri]. A TEM image of the Ti-5111 base metal in Figure 63 with a selected area diffraction pattern shows that the α lath is oriented along the [0001] direction. The structural ledge for the interface is outlined in red. High resolution TEM in Figure 64 shows the difference in atomic structure that is confirmed with a fast Fourier transform of each region (shown in the insets). Smaller ledges are visible in a magnified image in Figure 64b. This area does not show evidence of visible dislocations

within the high resolution TEM image. Figure 65 shows the α-β interface in the Ti-5111 stir

zone. The dashed red line is the interface region with FFT insets showing the difference in

structure. The FFT for α shows a strong [0001] zone axis, but the upper left region shows

distortion of points for the β FFT. The schematic in Figure 62b shows the $[0001]_\alpha \| [101]_\beta$.

The β FFT in Figure 65 may the result of microtwins distorting the $[101]_\beta$ FFT.
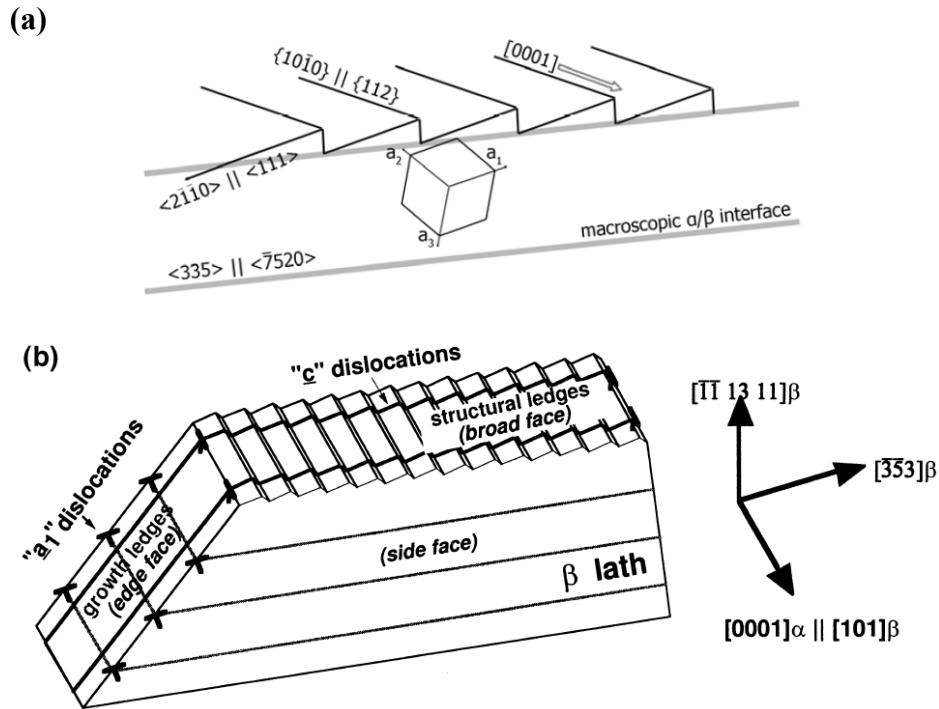
Figure 62. a) Schematic of the α and β phase interface. [Pilchak 2009] b) interface structure describing ledges and side face [Suri].
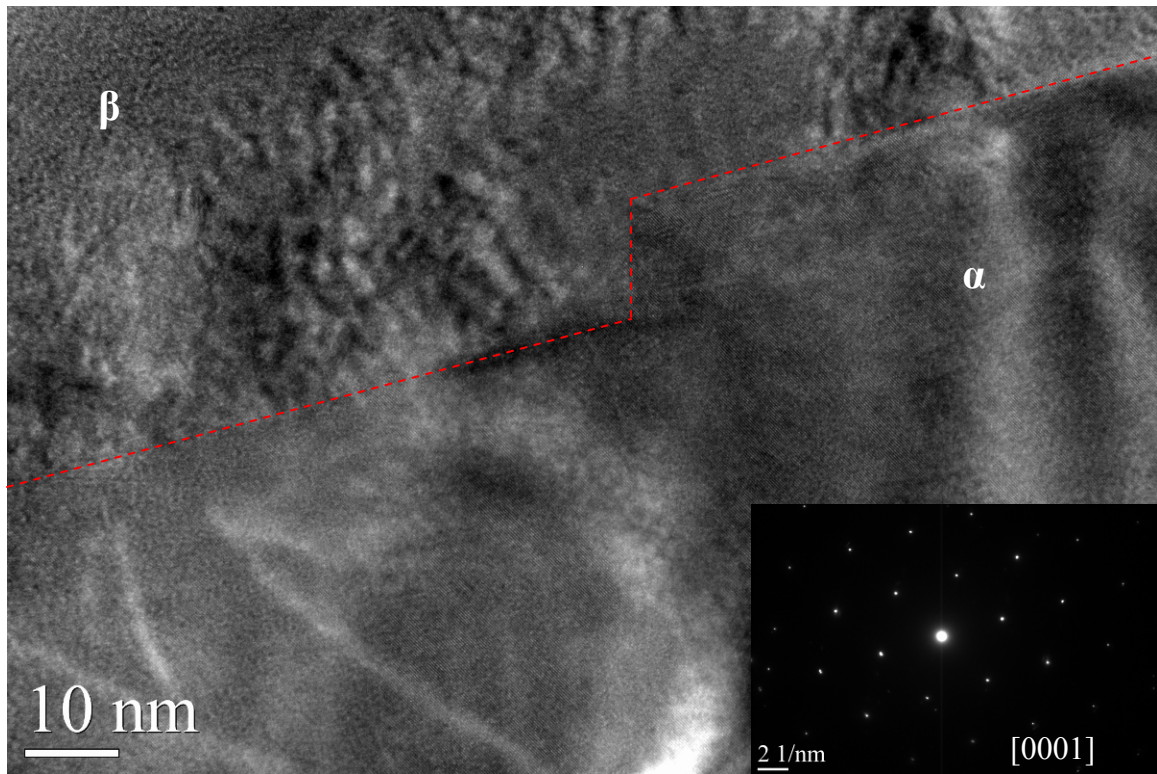
Figure 63. TEM image of the α and β interface in base material showing a structural ledge marked with the red line. The selected area diffraction pattern shown in the inset shows that the α lath is oriented along the [0001] direction.
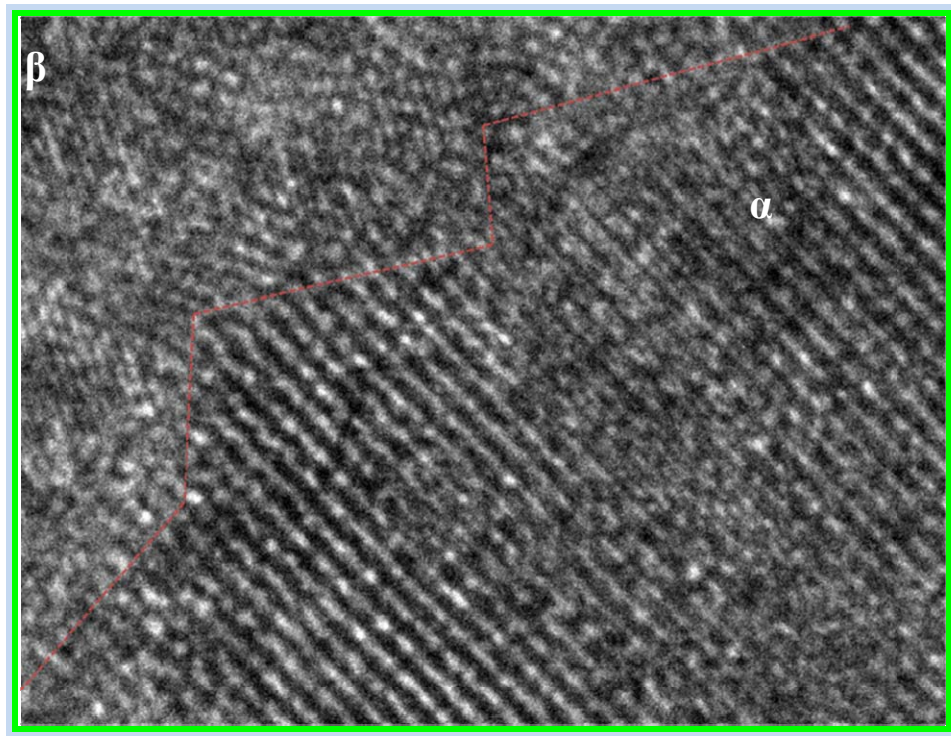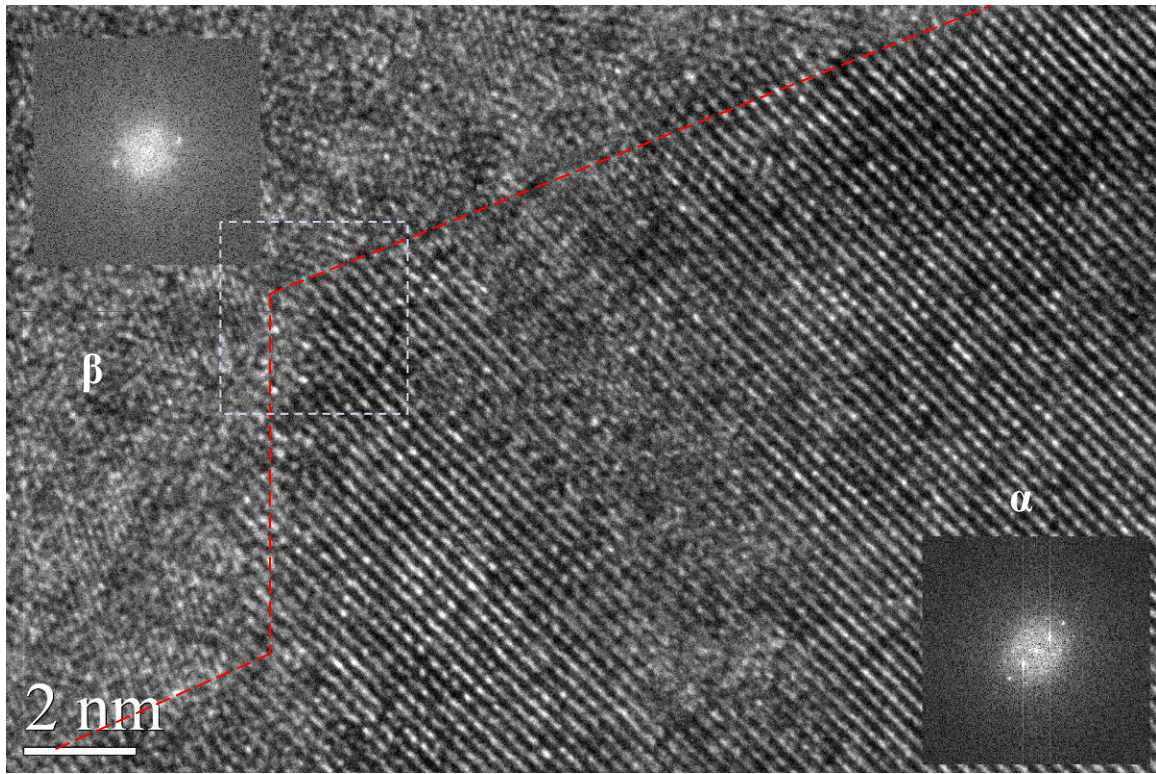
Figure 64. A) High resolution TEM of the α and β interface in the base material B) Magnified step of blue box in A. This image shows the atomic level ledges between α and β atoms marked by the red dashed line.
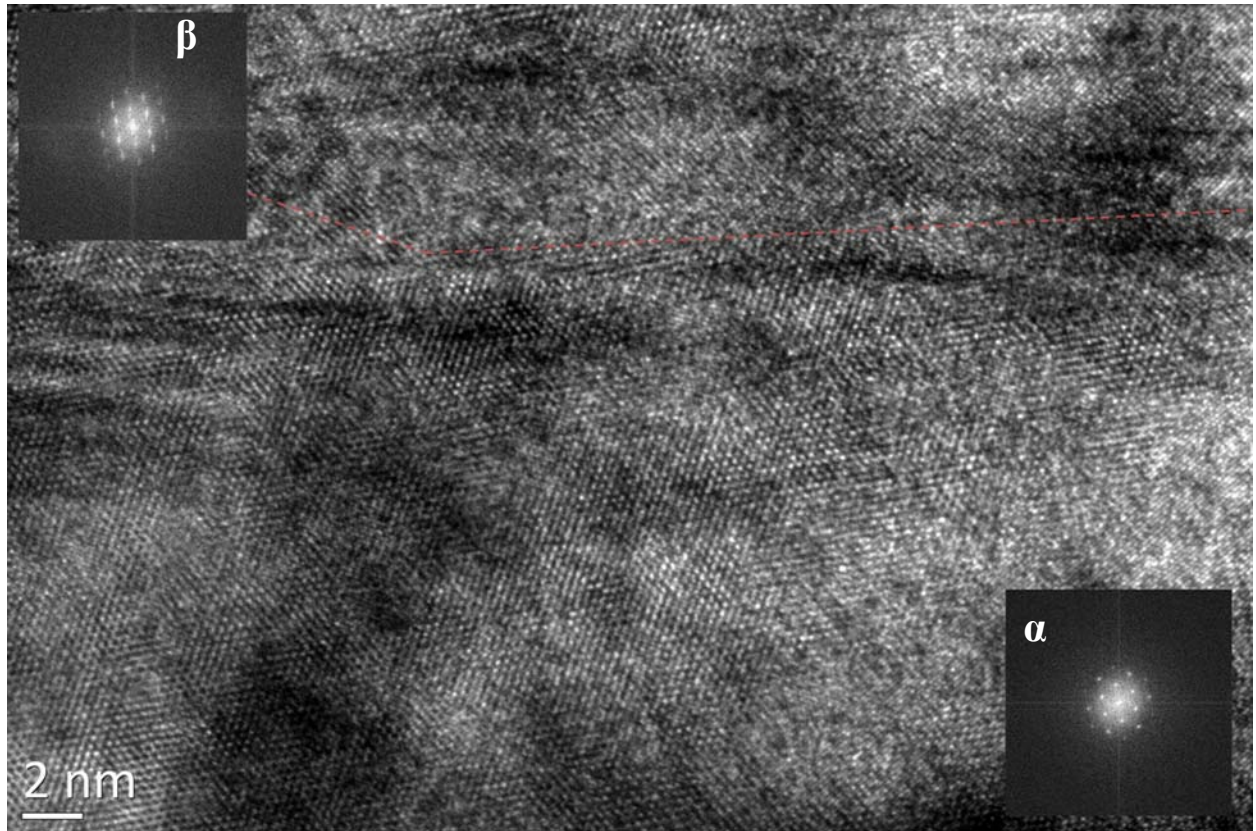
Figure 65. High resolution TEM of the α and β interface in the stir zone. The dashed red line is the interface region with FFT insets showing the difference in structure. The FFT for α shows a strong [0001] zone axis, but the upper left region shows distortion of points for the β FFT. The β FFT may the result of microtwins distorting the [101] $_β$ FFT.

3.2.6.3 High temperature TEM

In situ high temperature TEM was utilized to determine the kinetics of phase transformation from α to β for Ti-5111 and to gain increased understanding of the material as it transforms ahead of the pin tool during friction stir welding. A Gatan Model 901 SmartSet Hot Stage Controller was used in the JEOL LaB6 TEM for all experiments. The SmartSet controller is a water cooled double-tilt holder that uses resistive heating for the specimen. Microstructural analysis combined with thermocouple curves presented in Section 3.1 indicates that the friction stir welding temperature exceeds β transus. Experiments were performed controlling

both heating rate (1000ºC/min) and controlling current to achieve intermediate temperatures for analysis. Both photographic images of the intermediates temperatures and video were recorded during the experiment. The analysis performed within this section focuses on specimen heating. Analysis on specimen cooling was inconclusive because cooling the specimen resulted in a quenched microstructure. Annealing the TEM specimen below the transformation temperature within the holder did not result in a fully lamellar structure.

Base metal specimens were prepared through the use of jet polishing and ion milling. The resulting electron transparent specimens show a fully lamellar microstructure with a diffraction pattern showing both the α and β phase Figure 66. This specimen was heated by controlling the current allowing for sequential heating in between obtaining images and diffraction patterns. Images of the base metal specimen during heating are shown in Figure 67-Figure 69. At 949ºC the diffraction patterns show evidence of polycrystalline rings, but no evidence of transformation (Figure 68). At 1012º, the lamellar structure has evidence of polycrystalline particles which is concurrent with the diffraction pattern. Even at the maximum heating holder temperature of 1025ºC there was no indication of phase transformation from α to β. Further analysis of the specimen shows the presence of aluminum-copper based contaminants on the surface of the specimen (Figure 70). Energy dispersive spectroscopy (EDS) analysis shows 29.75wt% Al and 4.06wt% Cu. At the temperatures reached within the experiment, it is likely that there was aluminum diffusion into the Ti-5111 matrix leading to the formation of a Ti-Al compound. The contamination of Al, a known α phase stabilizer, explains the inability to transform the microstructure to β even at 1025 ºC. At this point it is not clear how the Al and Cu contamination occurred.

This experiment was repeated for a different Ti-5111 base metal TEM specimen using current control for heating. A room temperature bright field TEM image shows the intersection of two α colonies in Figure 71. The specimen was heated up to 940ºC, but still had an α lath microstructure (Figure 72). The diffraction pattern inset in Figure 72 shows less defined spots than those in Figure 71 indicative that transformation is ready to begin. The TEM specimen was then heated past the expected transformation temperature. Transformation initiation began at 949ºC, but transformation finish temperatures could not be determined. Prior to the peak holder temperature of 1006ºC the specimen was lost and no post transformation images or diffraction patterns could be taken. Video still images in Figure 73 show the change in microstructure with the α→β transformation. Transformation initiation temperature for this base metal sample was close to the expected equilibrium transformation temperature.
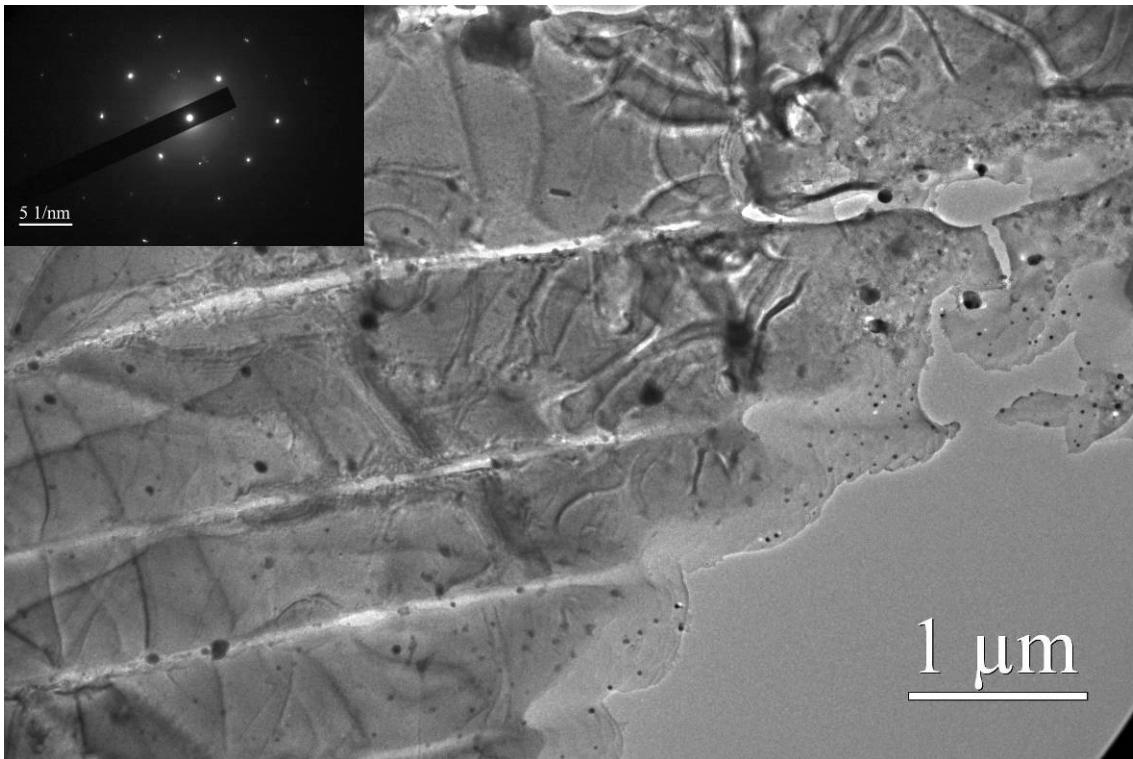
Figure 66. Base metal specimen with defined α and β at room temperature and prior to heating.
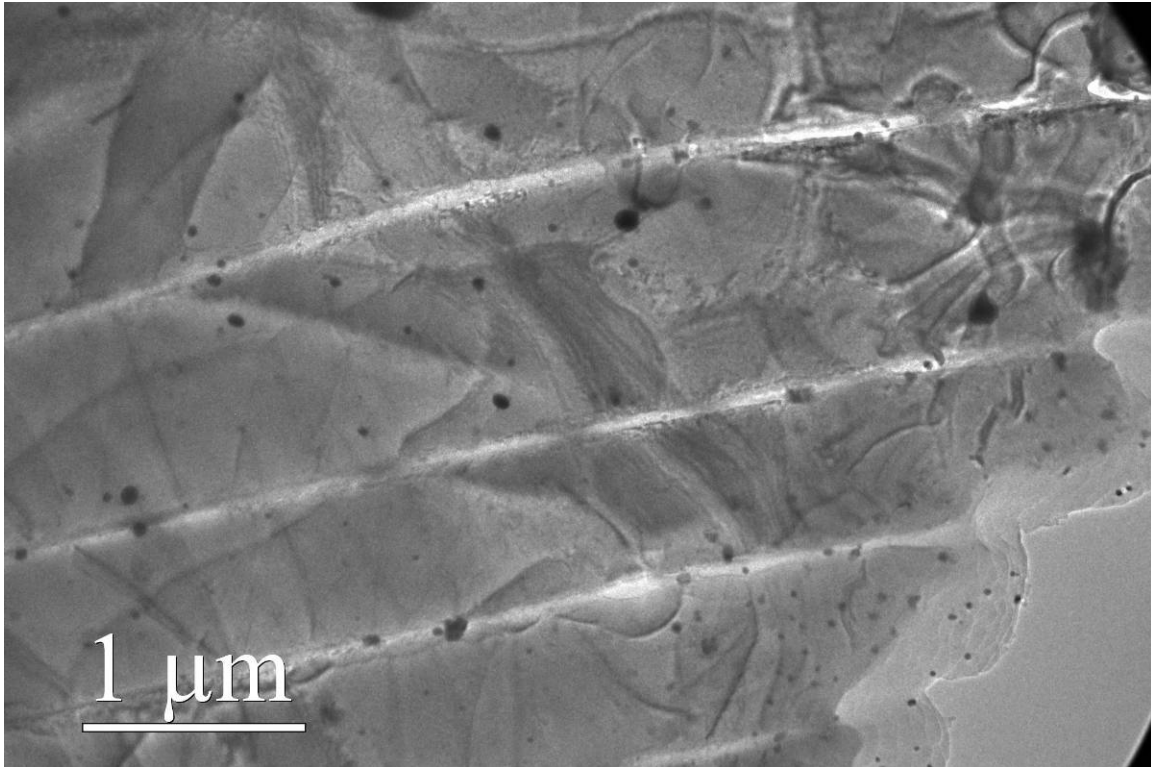
Figure 67. Base metal specimen with defined α and β at 640ºC.

5 1/nm
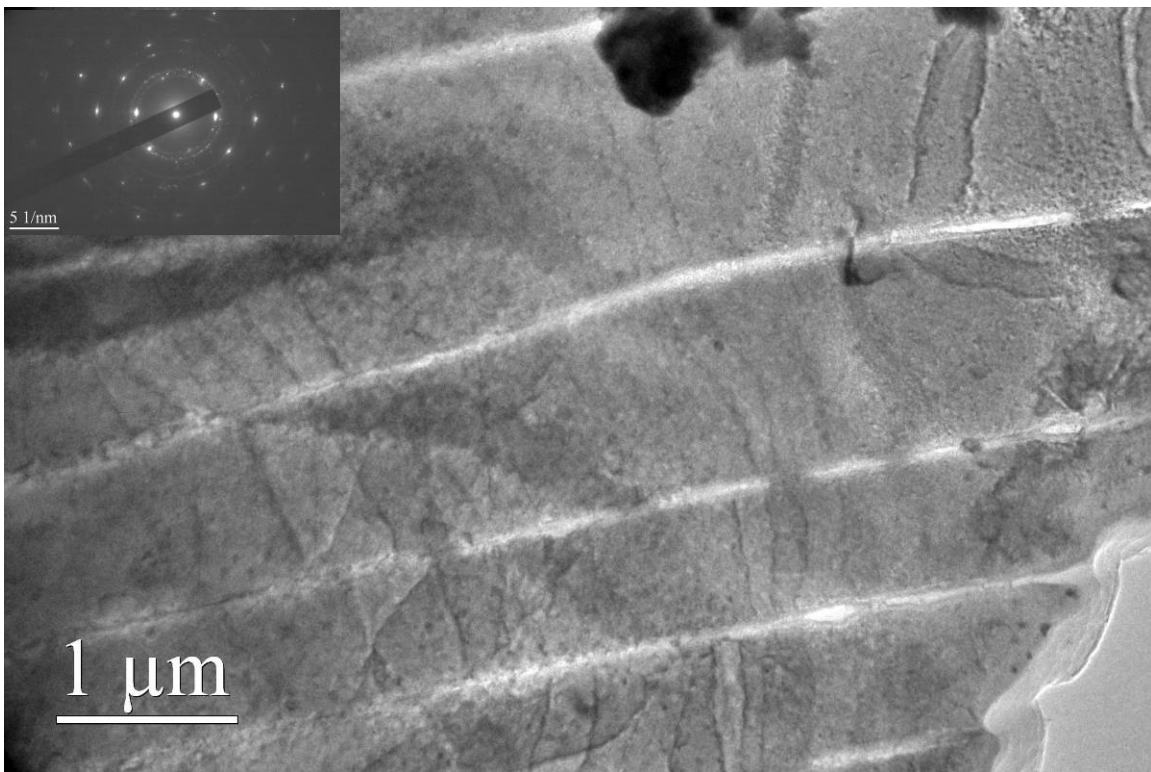
Figure 68. Base metal specimen with defined α and β at 949ºC. Rings are noticeable around the diffraction pattern indicating a polycrystalline structure in addition to the large single crystal pattern.
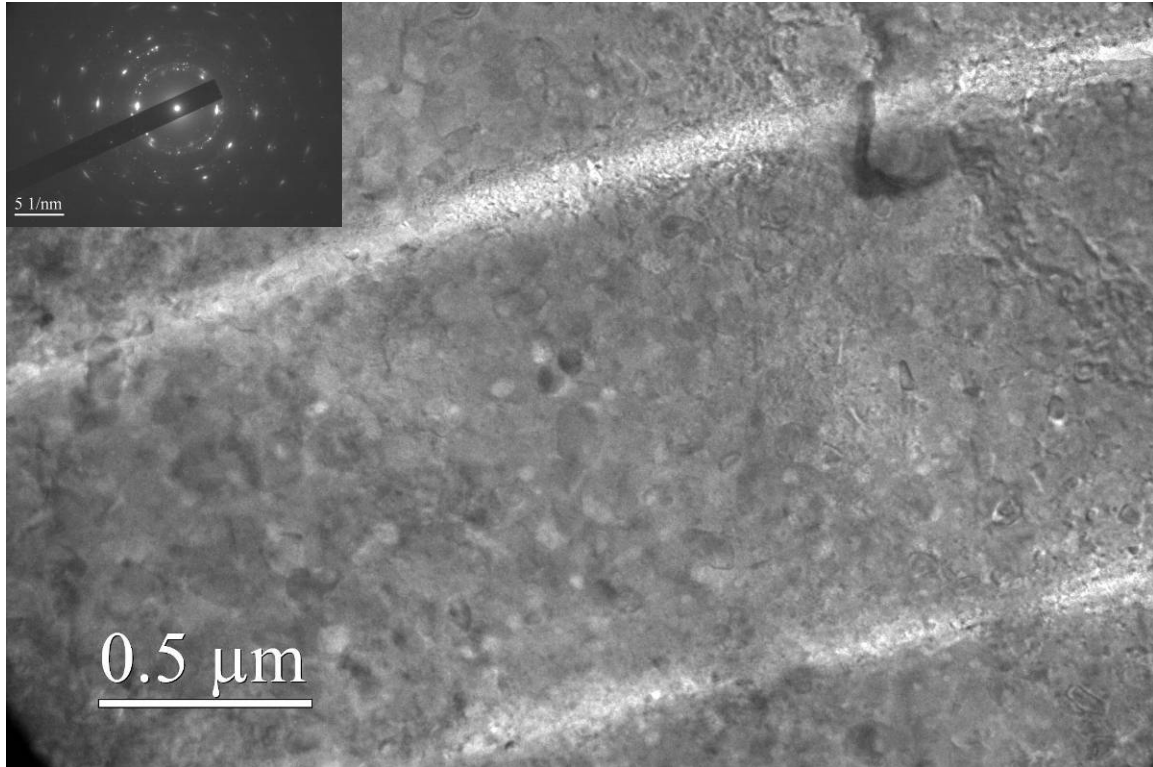
Figure 69. Base metal specimen with defined α and β at 1012ºC. The specimen is untransformed past the equilibrium transformation temperature. Rings are noticeable around the diffraction pattern indicating a polycrystalline structure. The image also shows small crystals within the α and β phases.

Element	Weight%	Atomic%
C K	9.06	24.03
Al K	29.75	35.13
Si K	1.26	1.42
Ca K	1.65	1.31
Ti K	54.23	36.07
Cu K	4.06	2.03
Totals	100.00	
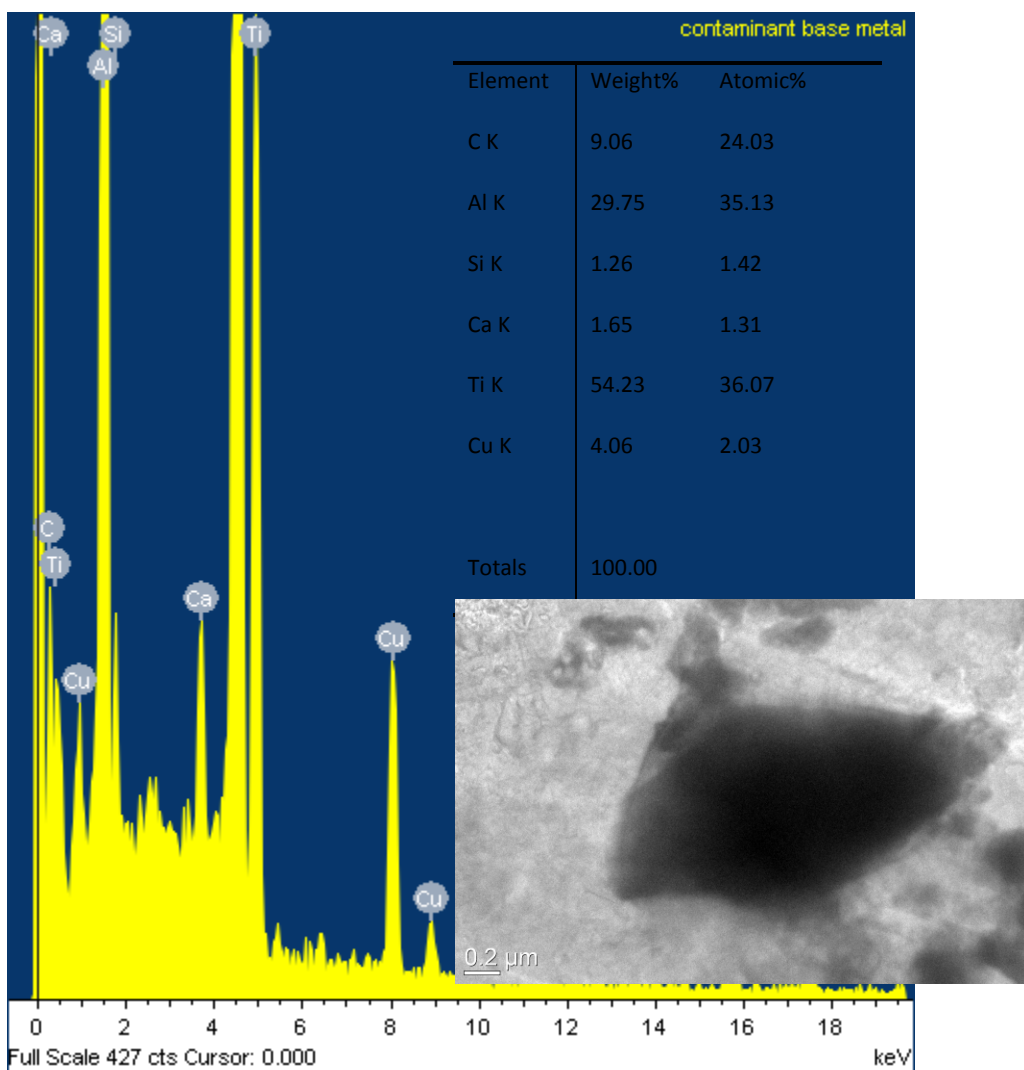
Figure 70. Contamination within the base metal specimen. EDS showing 29.75wt% Al and 4.06wt% Cu. The inset shows a large contaminant in the sample.
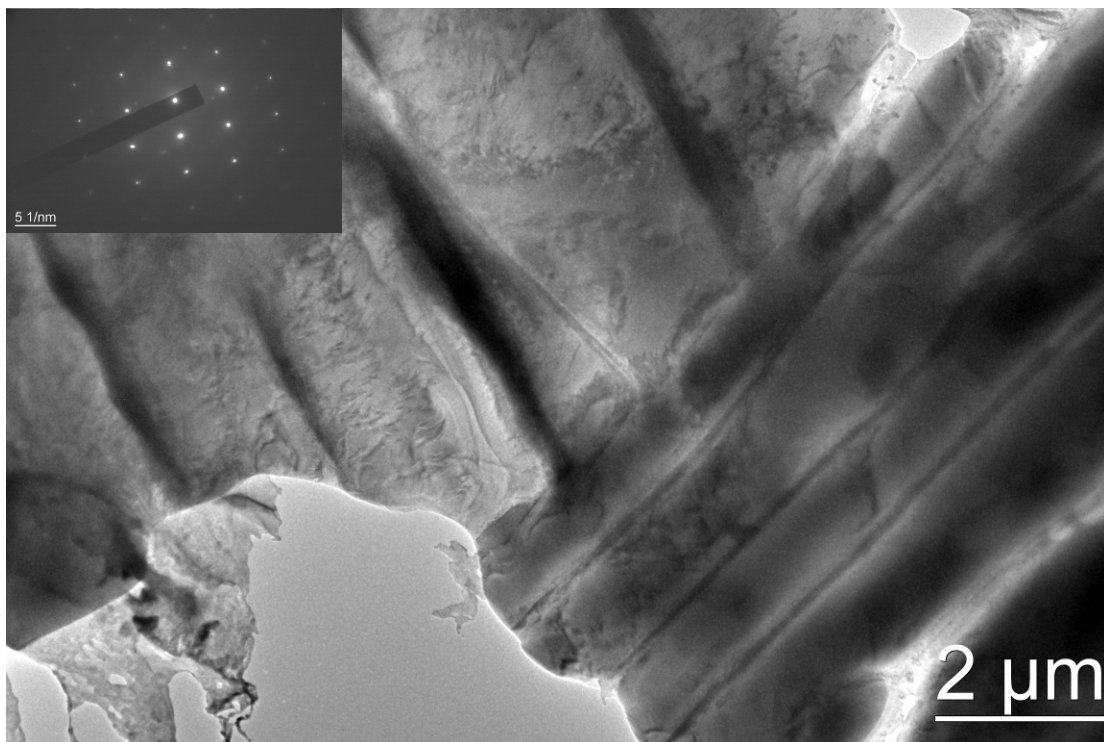
Figure 71. Base metal specimen with defined α and β at room temperature and prior to heating.
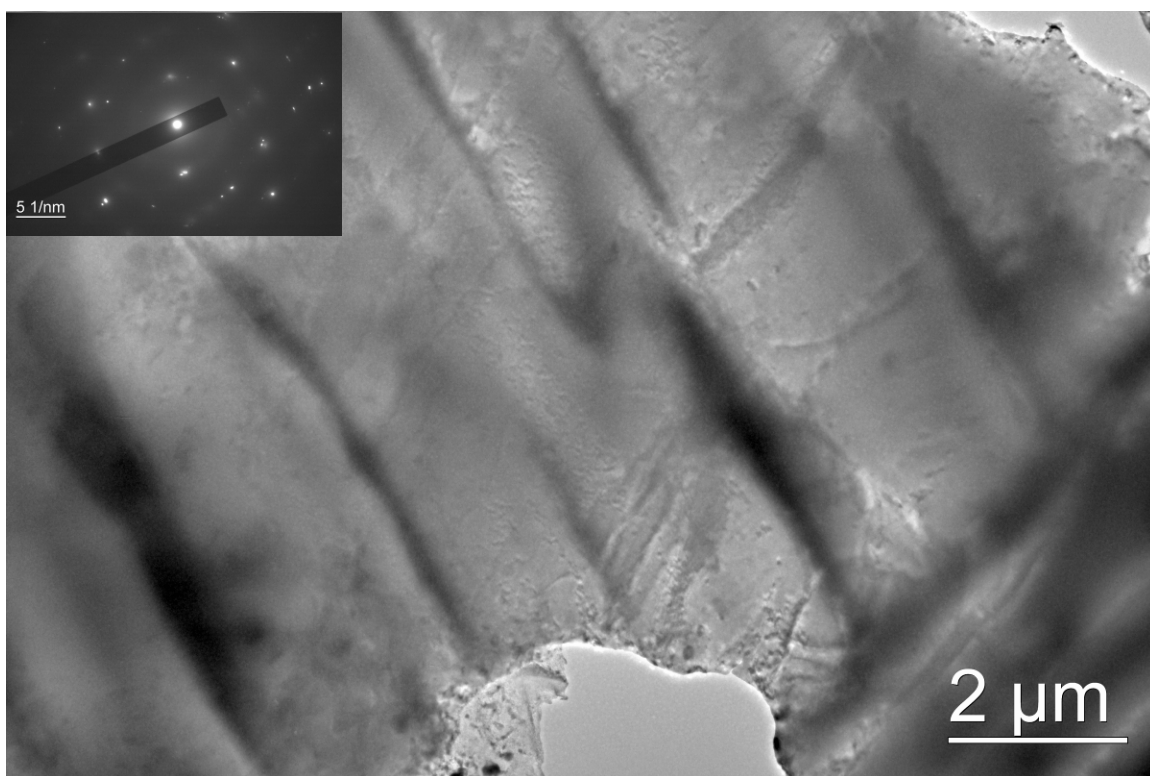
Figure 72. Base metal specimen with defined α and β at 940ºC an still contains the α lath structure.
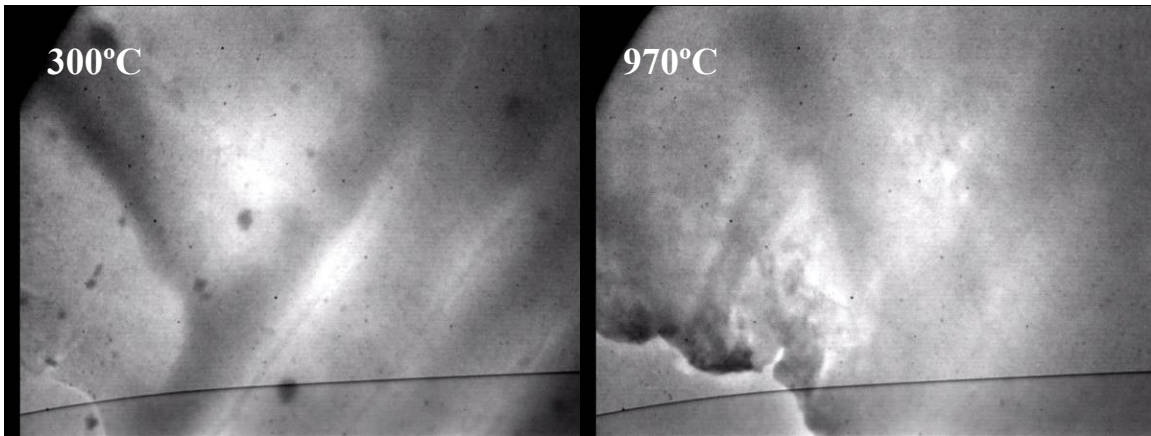
Figure 73. Video still images from heating a base metal sample showing the microstructural change during heating. Transformation initiation began at 949ºC which is close to the expected equilibrium transformation temperature.

An in-situ heating experiment was also performed on a TEM sample prepared from the stir zone. Taken from the center of the stir zone, jet polishing and ion milling resulted in a clearly defined α and β structure as shown in Figure 74. Bend contour bands were identified within the specimen. Upon heating, the specimen experienced thermal expansion shifting the contour bands. The specimen was heated to 300ºC and held at temperature to obtain a starting image and diffraction pattern shown in Figure 75. The structure is a lamellar α-β structure. The specimen was then heated to 1000 ºC at a set rate of 1000ºC/minute. The heating curve with respect to time in seconds is given in Figure 76. The actual heating rate was less than 1000ºC/minute. The video still images Figure 75 show transformation initiating at 450ºC and fully completed within the region by 650ºC within 30 seconds. At peak temperature of 1000ºC the structure is completely transformed and the diffraction pattern shows a (001) BCC diffraction pattern. This result is dramatically different than equilibrium transformation temperatures for as received Ti-5111 discussed above in this section and has not been previously reported in the literature. The significance of this work shows that Ti-5111 friction stir welded material transforms to β at lower than expected temperatures. The

99

severe deformation during the friction stir process and the grain refinement may lead to the lower transformation temperature. This may mean that applying a second deformation process (i.e. a second friction stir weld pass) to this material may lead better material consolidation and load reduction due to the lower transformation temperature within the weld.
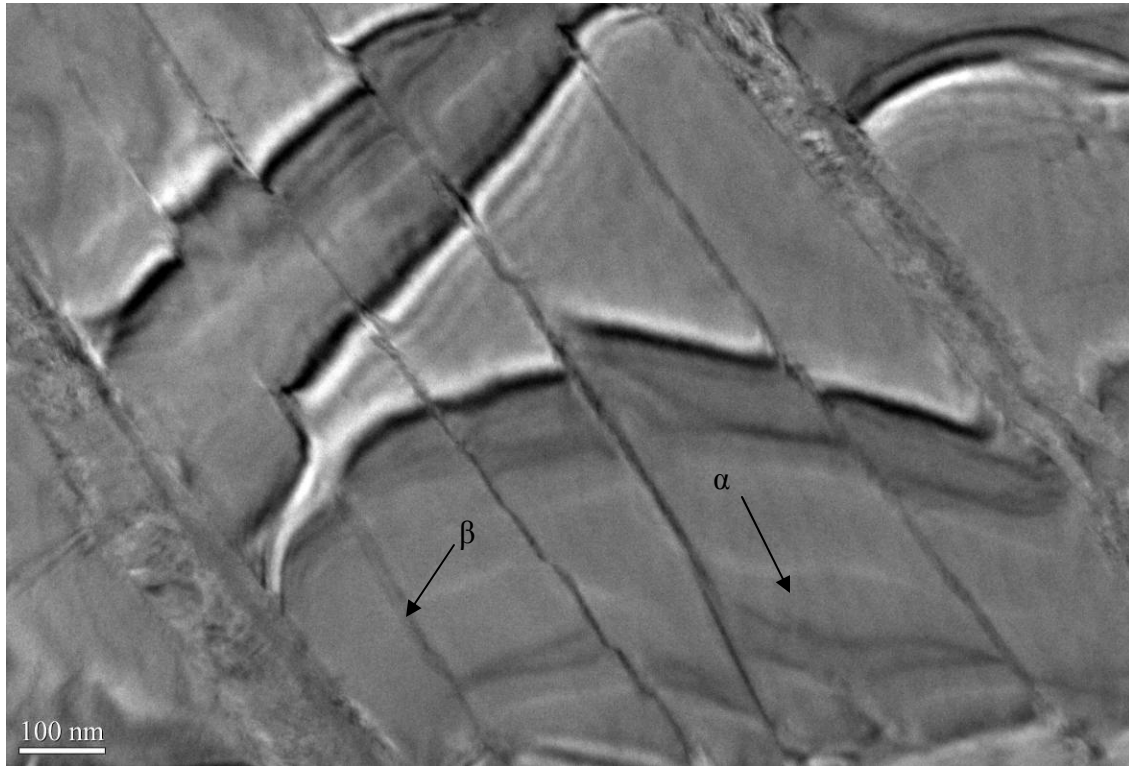
Figure 74. All-stir zone specimen with defined α and β at room temperature and prior to heating.
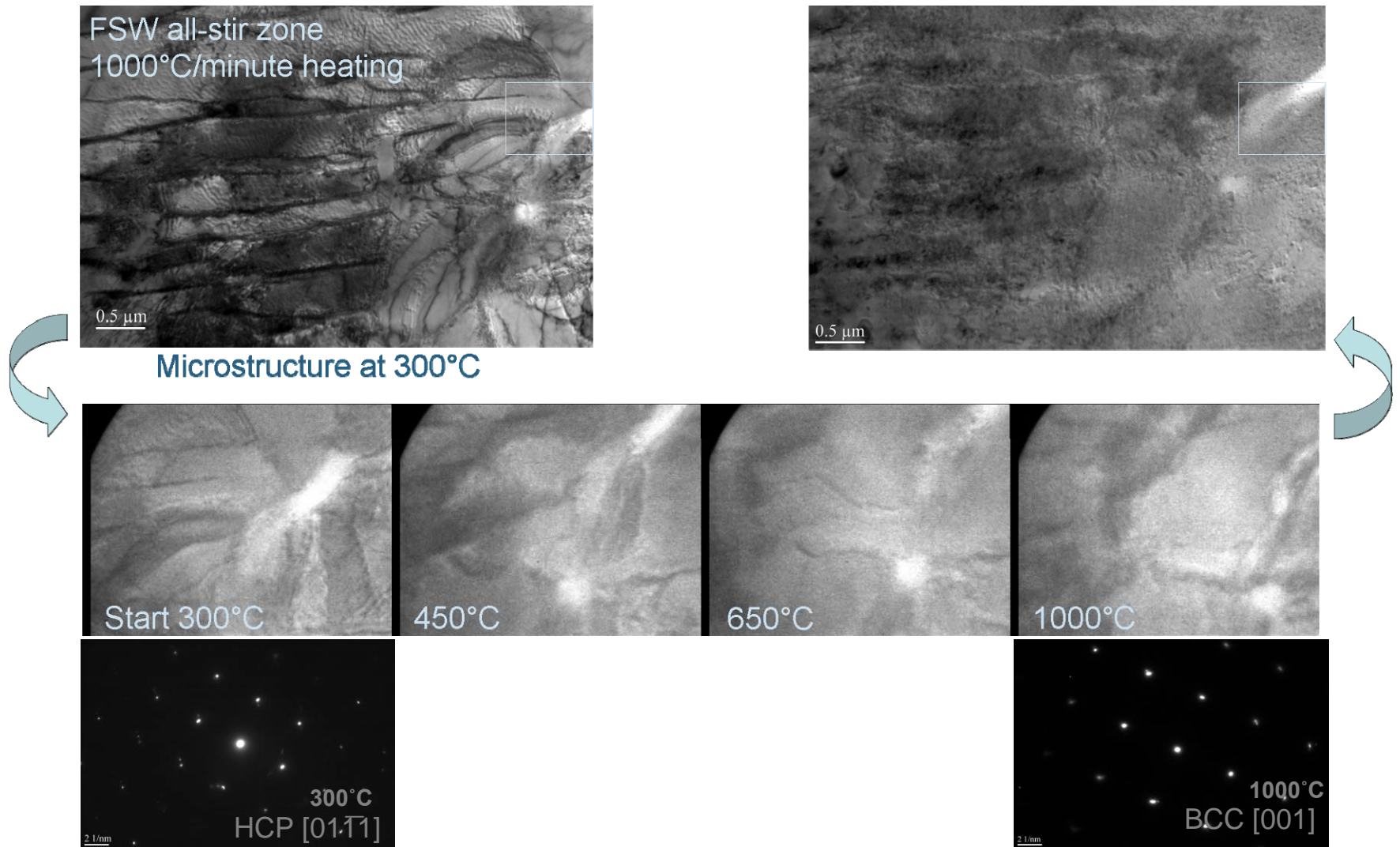
Figure 75. Stills from hot stage TEM video from the stir zone correlated to approximate temperatures from Figure 76. Transformation initiates at 450°C and is fully completed within the region by 650°C. At peak temperature of 1000 °C the structure is completely transformed and the diffraction pattern shows a (001) BCC diffraction pattern. This result is dramatically different than equilibrium transformation temperatures for as received Ti-5111.

Gatan Hot Stage Heating Curve
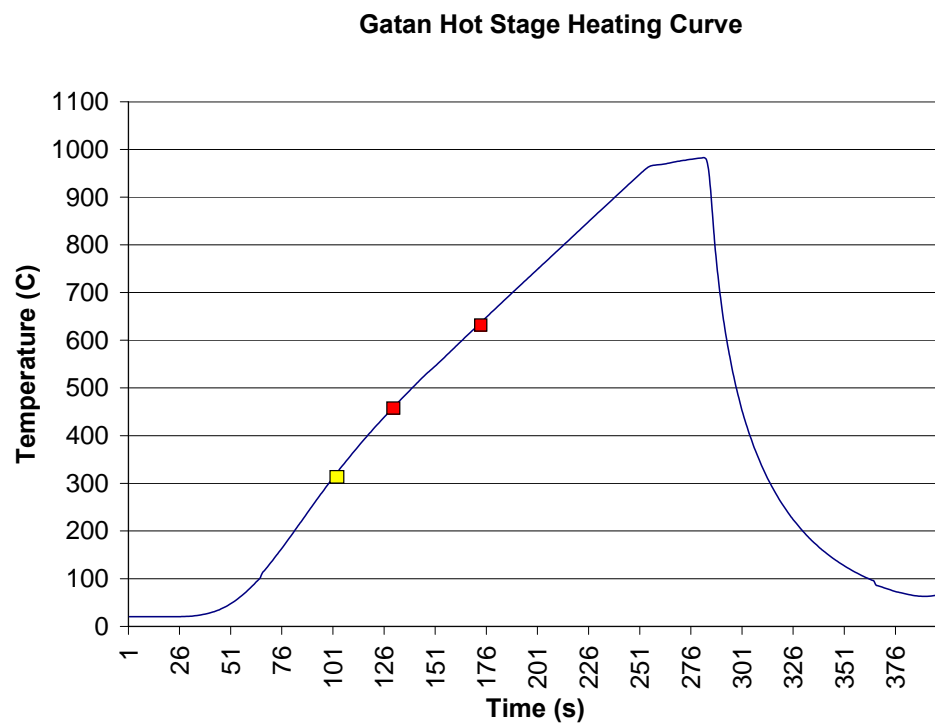
Figure 76. Gatan hot stage heating curve with respect to time for a set heating rate of 1000°C/minute. Yellow box indicates the start of heating. Red boxes indicate points where still video images were taken.

3.2.7 Defect analysis

The presence of macroscopic defects during welding provides a unique opportunity to understand fundamental material characteristics that lead to the formation of the defects. The following section is an in depth examination of defect formation and material flow in 12.7 mm Ti-5111 friction stir welds through the use of microstructural characterization, computed tomography, and texture analysis.

3.2.7.1 Optical microscopy of macroscopic defects

In addition to the optical microscopy presented in Section 3.2.1, further optical microscopy focused on the advancing side defects and the lack of consolidation at the bottom of the stir zone. A schematic of the defect locations is shown in Figure 77. Figure 78 highlights the bottom of the stir zone defect. This worm-hole type defect extends from the lower advancing side edge into the stir zone. After etching to enhance the contrast of the defect structure in the wormhole region, the area near the transition zone appears to have shear layers of material. These layers appear to attempt consolidation within the stir zone. These layers lead to an inconsistent defect shape and size. This may be due to material flow and temperature variations during welding. Flow instabilities have been noted for a range of strains/strain rates within Ti-64 with flow localized bands [Sescharyulu]. Flow localization may also result in the defect formation noted in the 12.7mm weld. The optical metallography of the materials layers give the appearance of being extruded into the defect. This is reminiscent of the "onion ring" formation within aluminum friction stir welds [Mishra 2005].
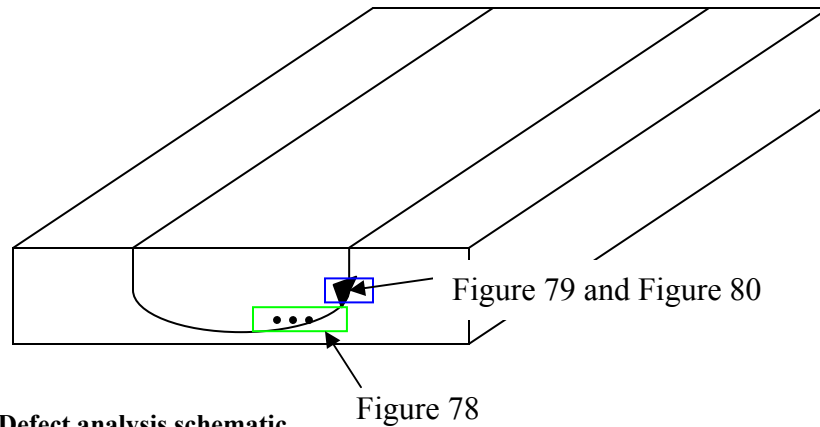
Figure 77. Defect analysis schematic.
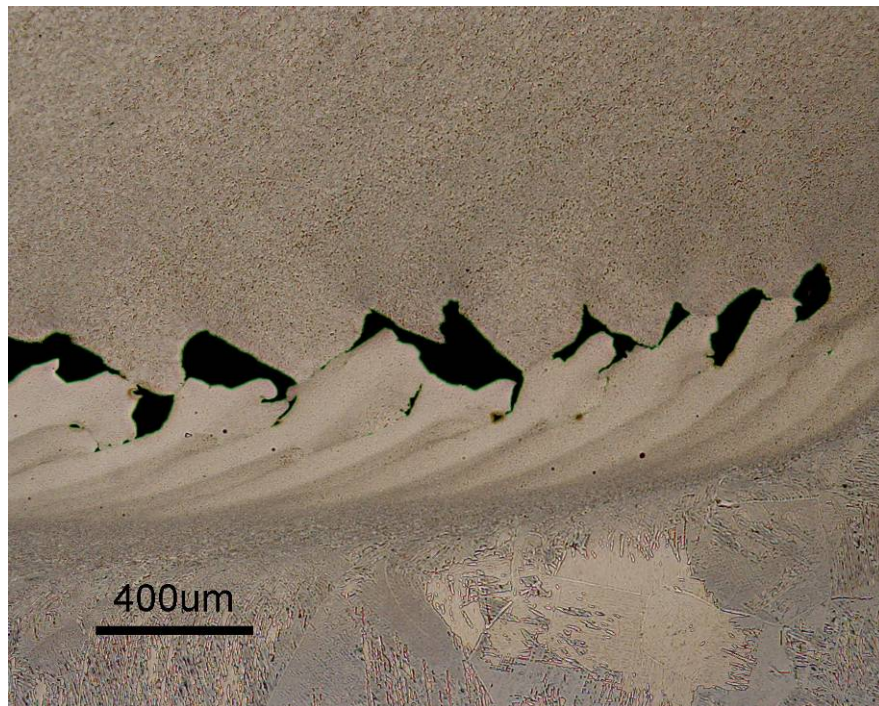
Figure 78. Stir zone bottom wormhole defect within 12.7mm Ti-5111 FSW. The defect extends from the edge of the advancing side into the middle of the stir zone. Defect geometry within this area is inconsistent.

Another large macroscopic defect was observed on the advancing side of the stir zone base metal interface in the region as shown in Figure 79A. Etching of the defect shows the presence of distinct particles throughout the surrounding stir zone. Similar to the wormhole-type defect, this advancing side defect shows evidence of material attempting to

reconsolidate at the edge of the stir zone. In Figure 79D, the material is able to connect with the base metal. Figure 79B and C show the presence of tungsten particles (identified by EDS in the scanning electron microscope) that range in size from 10-40μm. Within the surrounding stir zone above the defect, Figure 79B shows the underlying microstructure of Ti-5111 within the defect. Unlike the center of the stir zone, the grains in this region do not exhibit the same lamellar microstructure. The grains are smaller with a discontinuous grain boundary α. The α laths in Figure 79B are shorter and do not form the typical colony structure. This is in contrast to Figure 79C taken below the advancing side defect. The microstructure in Figure 79C is similar to the center of the stir zone. The presence of tungsten in the center of the image does not appear to affect the colony structure.
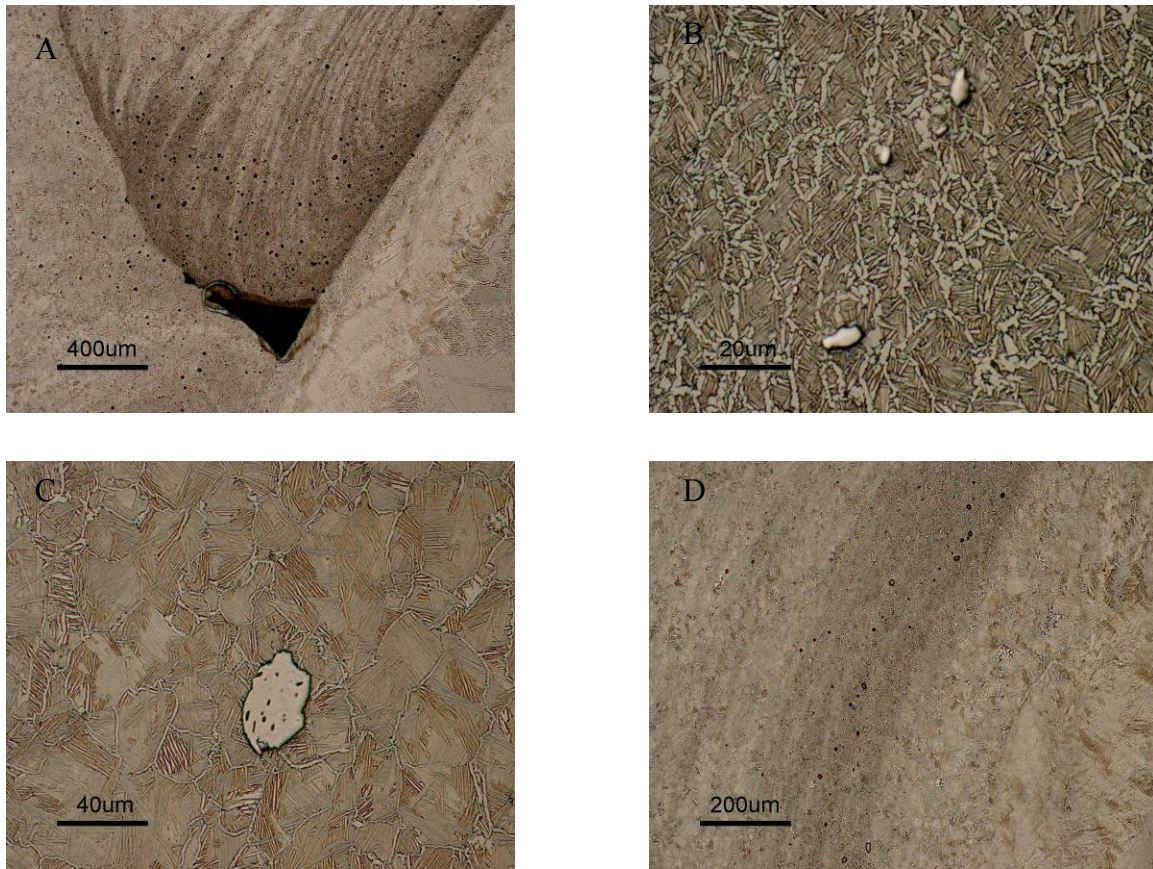
Figure 79. Advancing side defect. A) Low magnification image of the defect B) Tungsten particles within the defect C) Particle within the stir zone D) Material flow lines within the defect

In addition to optical metallography, backscatter electron imaging in the JEOL 6400V at 15kV in Figure 80 highlights the compositional differences within the advancing side defect. This image shows the wide deposition of tungsten around the defect.

Figure 80, which shows the backscatter SEM image — the visible labels are "Stir zone" and "Base metal", with scale marker "100u" and the caption block reading "Title: Ti–5111 FSW backscatter defec   Date: 02–16–2007 Time: 12:32" and "Comment: 100x   Filename: DEFECTBACKSCA" along with "X100 15KV 16mm Spot 5   SS: P3".
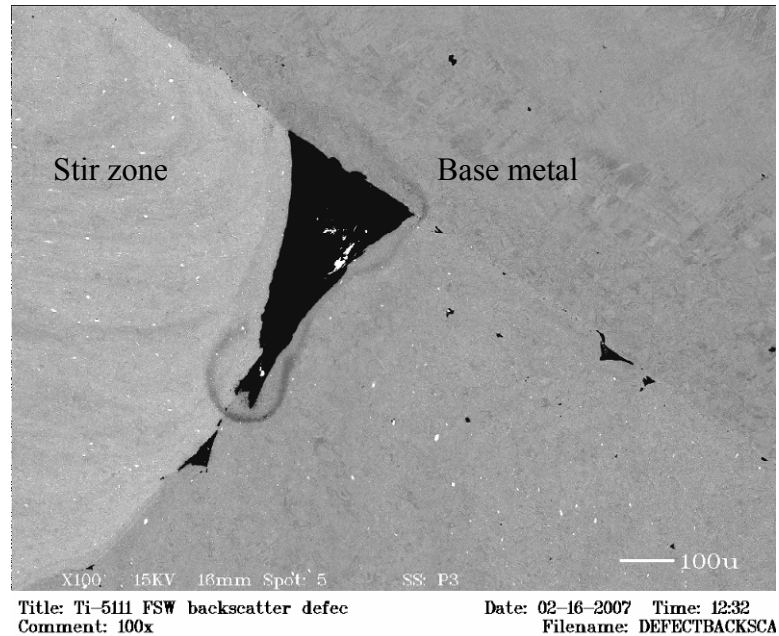
Figure 80. Backscatter SEM image of the defect. Material flow is shown above the defect.

3.2.7.2 Computed Tomography of Defects

A portion of a 12.7mm weld was supplied to the Naval Research Laboratory for a collaborative analysis of the defect formation through the use of computed tomography. Both synchrotron- and tabletop-tomography have been previously utilized to determine void geometries in ferrous and non-ferrous samples. A low speed diamond saw with liquid coolant was used to section a specimen containing the advancing side defect. The specimen dimensions were 10 x 16 x 1.56 mm^3. The specimen was mounted on an aluminum rotation stage using clay. Figure 81 presents a low resolution overview image of the piece showing two defects.

107
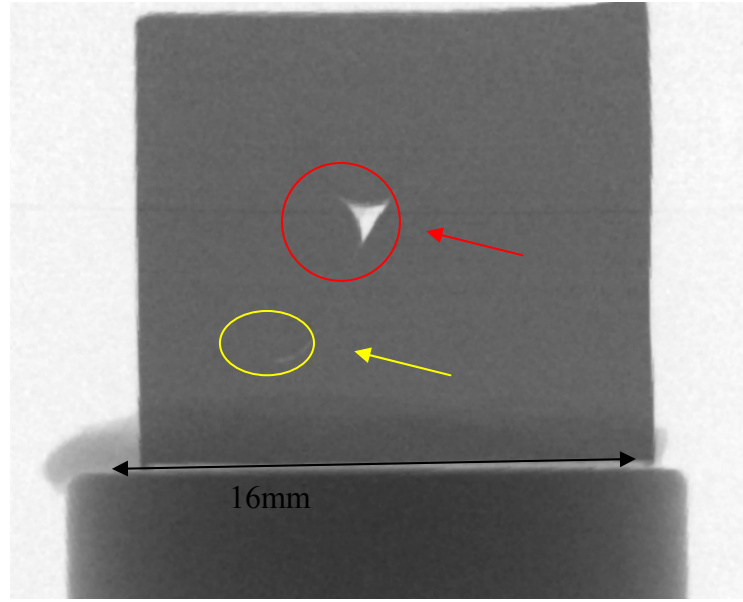
Figure 81. Radiograph (100kV) of a Ti-5111 specimen showing two voided region (arrows) at the interface between the stir zone and the base metal.

All x-ray tomograms were taken using a Skyscan model 1172 tomography system with a 1.3 Megapixel camera at Naval Research Laboratory [Wolk 2010]. Scans were performed using a 100 kV x-ray source with 0.45 degree rotation steps (400 images). Image voxel size was approximately 6.0 microns. Image cone-beam reconstruction was performed using the Skyscan proprietary software. Ring artifact and beam hardening corrections were applied, but only minimal smoothing was applied. The reconstructed images were further manipulated for viewing using two additional software packages. ImageJ was used to stack and crop regions of interest. It was also used to remove some reconstruction and rendering artifacts. OsiriX was used for three dimensional volume renderings (Figure 82). Rendered surfaces of the material were made transparent to reveal the internal void structures. The defects are shown in the rendered images in red.
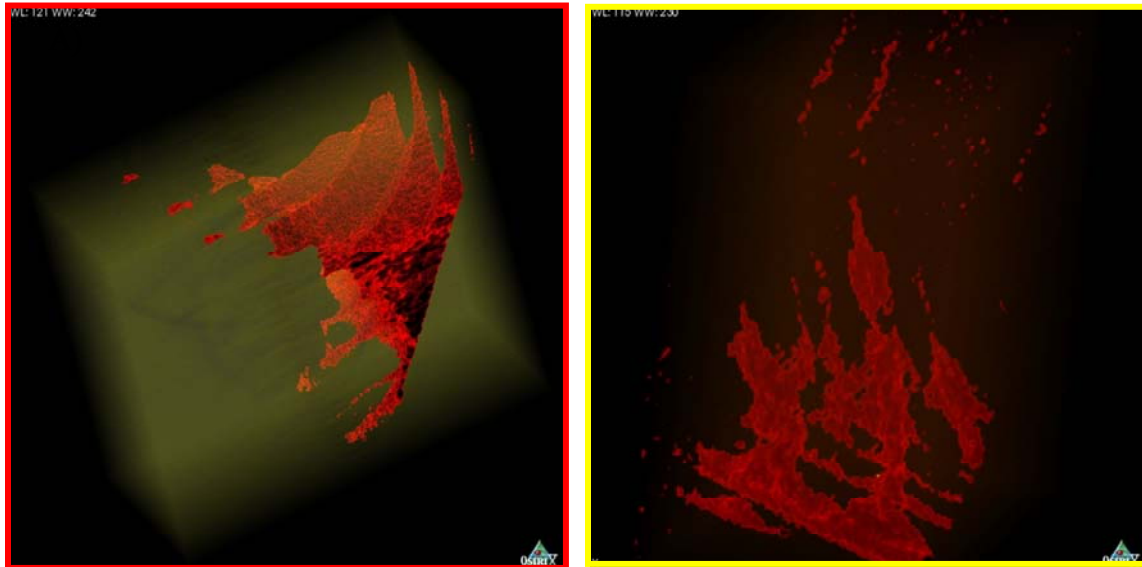
Figure 82. Volume renderings of voids in titanium friction stir welds. The red outlined left image corresponds to the uppermost defect highlighted in red in Figure 81 while the yellow outlined right image corresponds to the lower defect highlighted in yellow. This image is shown sideways to highlight the layers in the defect

A number of interesting features are apparent in the rendered images. Primarily, the lacuna (left image in Figure 82) has definite substructure with at least three bands visible. This resembles thread-like features similar to a screw. However, the friction stir welding tool is featureless. The substructure is most likely due to the shearing of material layers that occurs during the deformation process. The peak-to-peak distance appears to be approximately the same as the forward advance per revolution.

The lower voided region (lower yellow arrow in Figure 81) is rendered in right image in Figure 82. The image shows the complex substructure in the region indicating wormhole type defects that continue through thickness. The defect layer follows the contour of the weld. Figure 83 presents evidence of tool wear (bright spot indicated with the yellow arrow) located in the lower region, as well.

109
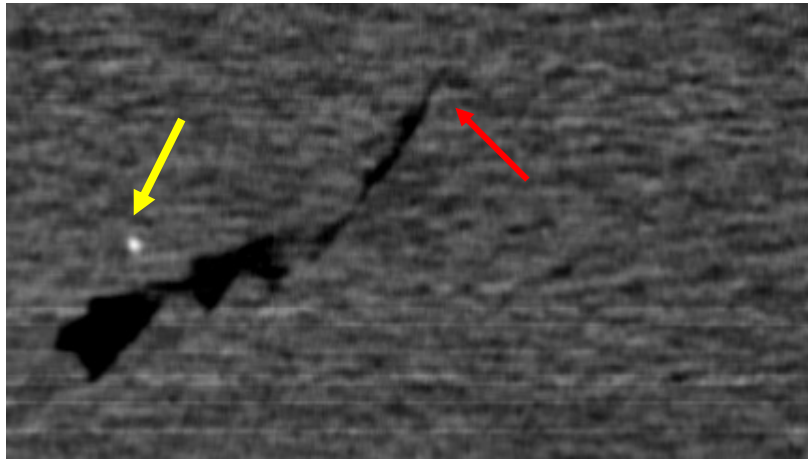
Figure 83. Tool debris (arrow) imaged near the bottom void.

3.2.7.3 Texture in Defect Formation

In conjunction with the x-ray computed tomography, electron backscatter diffraction was performed on areas of interest. On the transverse cross-section in Figure 83, the start of the j-shaped wormhole defect is shown with a red arrow. Electron backscatter diffraction scans of the initiation of the j defect show the deformation surrounding the defect in Figure 84. Large alpha lath structures within the base metal shows a rapid transition to the friction stir processed region. The image quality map in Figure 84A shows a fine grained region surrounding the defect on the base metal and on the friction stir weld. The confidence interval (areas green indicating a CI>0.1 and areas in blue with a CI<0.1) in Figure 84B shows the inability to index the pattern surrounding the defect. This is most likely due to the inability to correctly index the Kikuchi patterns due to the high deformation in this FSW transition region between the base metal and the stir zone. Higher magnification images and analysis in Figure 84C were unable to resolve regions around the defect. It is clear from these regions that the area is highly distorted with significant grain refinement.

110

Examining the substructure banding within the defect shows distinct lath structure formation within each of the bands in Figure 85. Figure 85A shows the image quality map of the region with more refined lath structures at the juncture of the bands. A higher magnification image in Figure 86 shows the highly refined lath size within the ridges. This is most likely due to the rapid cooling caused at the junction of the defect.
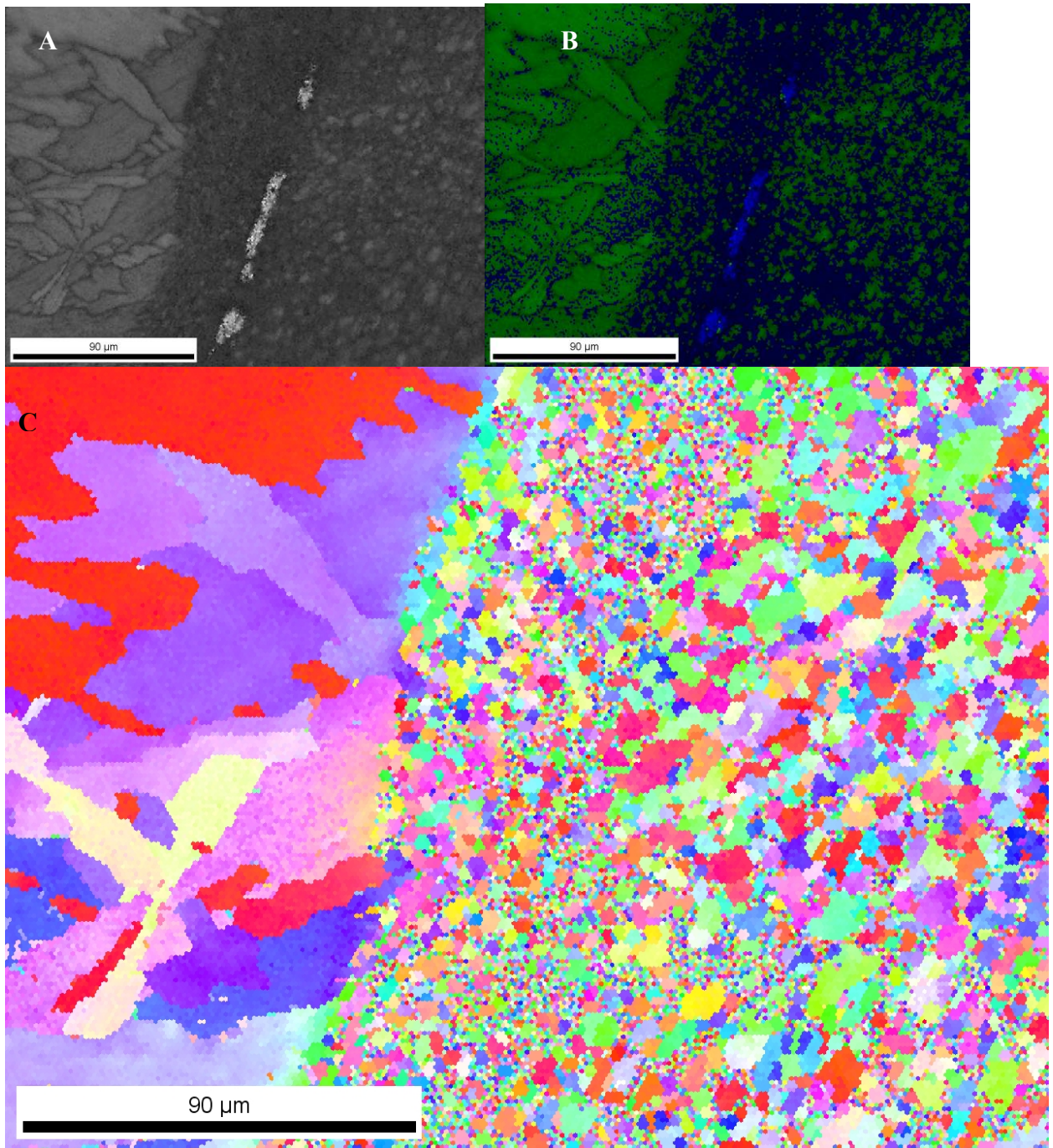
Figure 84. Electron backscatter diffraction of defect marked by the red arrow. A) Image quality B) Confidence interval (CI>0.1) C) Inverse pole figure (IPF)
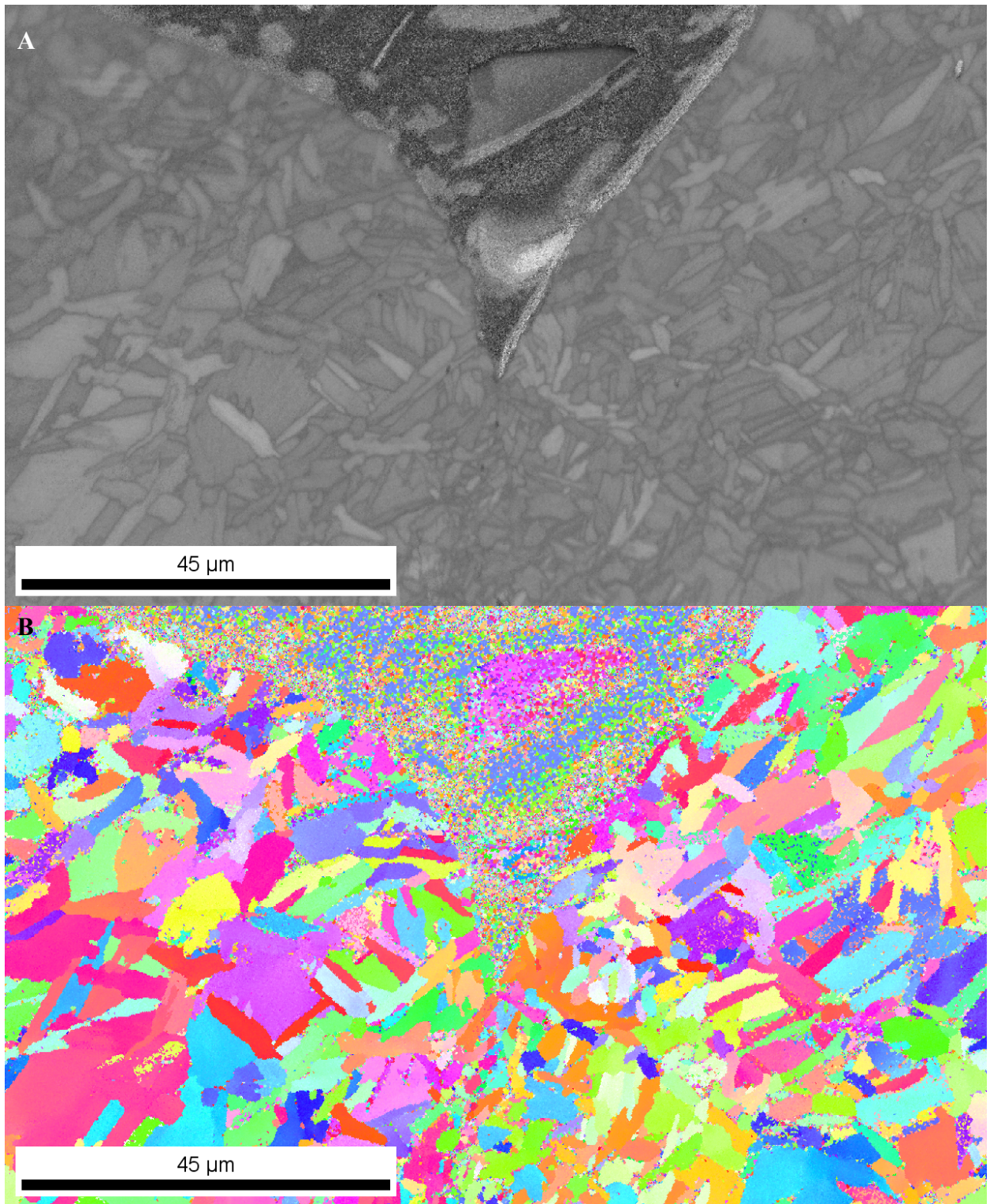
Figure 85. Electron backscatter diffraction image of advancing side defect. A) Image quality map of the intersecting bands. B) Inverse pole figure of intersecting bands within the defect.
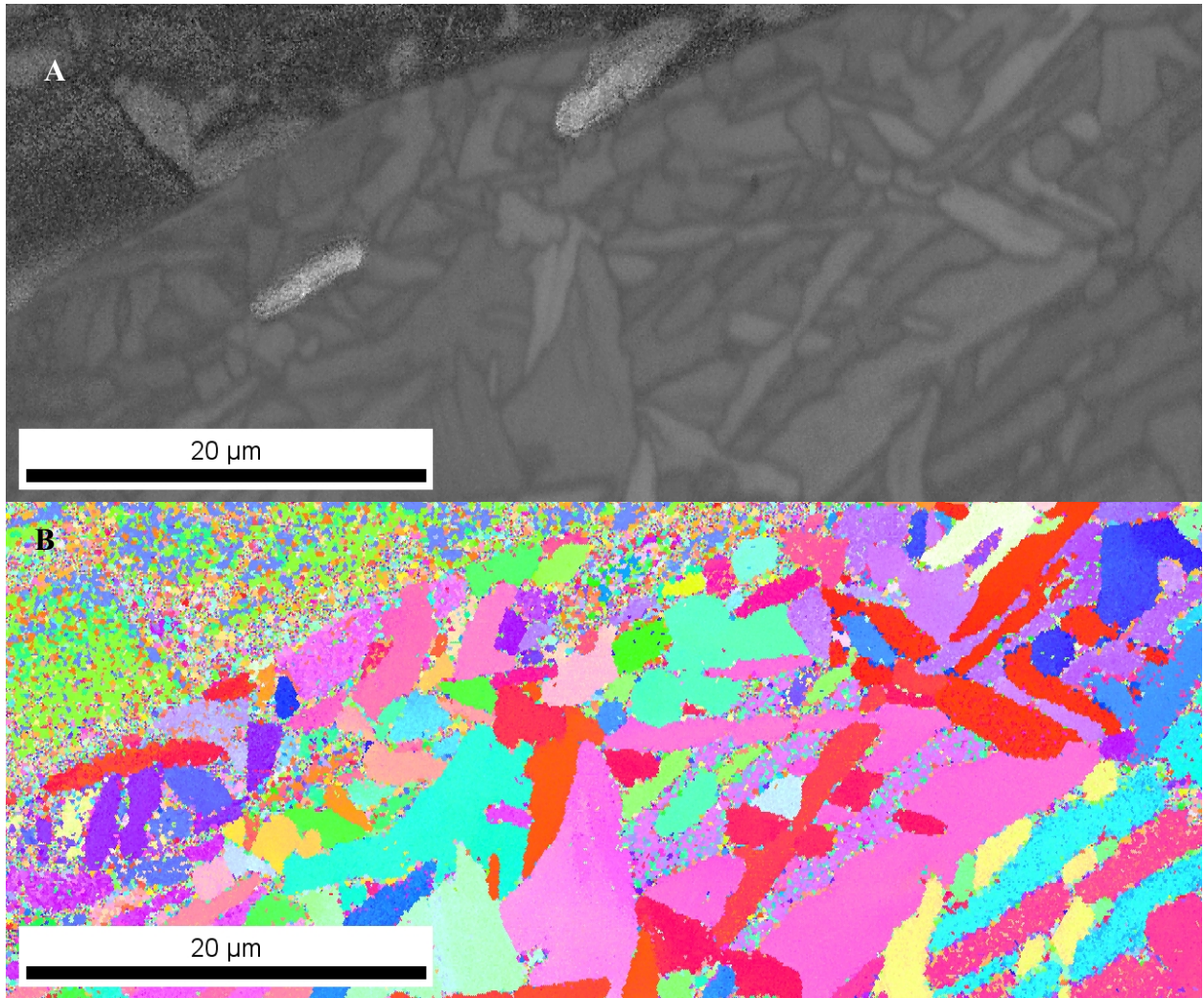
Figure 86. Electron backscatter diffraction pattern of advancing side defect shown in Figure 3. A) Image quality map of an advancing side ridge. B) Inverse pole figure of advancing side ridge

3.3. Summary

The results presented within this chapter show that significant microstructural refinement takes place in the stir zone compared to the base metal for 12.7mm and 6.35mm friction stir welds. All welds show an abrupt transition from the base metal to the stir zone with a narrow transition region. The calculated friction stir weld heat input is in general lower than arc welding heat input. However, for some weld travel speeds the heat input was comparable to that of arc welding. The analysis of the thermal field surrounding the weld shows that

temperatures within the stir zone likely exceeded β transus. This result is in agreement with the fully lamellar microstructures developed in all the welds.   The grain refinement mechanism for these welds shows strengthening of the BCC F fiber component through the transition region before transformation to D_2 shear texture in the stir zone with a rotation of the pole figure by approximately 28.4º about the center of the pole figure.   Transmission electron microscopy results of the base metal and the stir zone shows a similar lath structure with low dislocation density and no lath grain substructure. High resolution TEM shows the difference in atomic structure and broad ledges at the interface between α and β.   This interface does not show evidence of dislocations within the high resolution TEM image. However, more detailed analysis of this interface is necessary to confirm if there are dislocations. In situ TEM of Ti-5111 friction stir welded material shows transformation to the high temperature β phase at significantly lower temperatures compared to the base metal. Defect formation within the friction stir welds were also analyzed through the use of computed tomography and electron backscatter diffraction, showing shear layers of material within the defect.

CHAPTER 4: THERMOMECHANICAL SIMULATIONS OF TI-5111 USING GLEEBLE 1500D

4.1. Introduction

The Gleeble 1500D has successfully been used to simulate the HAZ and TMAZ in friction stir welds of HSLA-65 at NSWCCD with temperature and deformation histories provided by 2-D Cornell Hickory model [Forrest]. The following work describes simulation of distinct regions within the Ti-5111 friction stir weld. Literature on flow stress for hexagonal crystal structures shows that flow stress is highly dependent on temperature. For α- β alloy systems that contain a Widmanstatten or acicular α microstructure after welding, there is a well-defined difference in ductile behavior at low strain rates and high temperature, and brittle behavior at high strain rates and low temperature. Thermo-mechanical processing maps and hot tension tests indicate this is due to a critical stress level [Semiatin][Li]. Compression test results described in the following sections provide critical information about high temperature deformation correlated with microstructural results. These results are correlated to the results obtained from FSW Ti-5111.

4.2. Experimental Procedure

Physical simulations of the Ti-5111 friction stir weld were based on thermocouple data discussed in Section 3.1. Tests were performed using a Gleeble 1500D thermomechanical simulator. The Gleeble uses resistive heating and controlled hydraulics to simulate desired heating and cooling curves as well as controlled deformation [DSI]. The experimental set-up is shown in Figure 87 and is described in Section 2.5. Experiments discussed in this chapter focus on compressive simulations. Thermomechanical simulations of titanium and steel

reported by Rubal and Sinfield utilized a Gleeble torsional unit [Rubal] [Sinfield]. Thermocouple data described in Section 3.1 showed a peak temperature of 800˚C at a distance of 2mm from the edge of the stir zone. Using the thermocouple curves from Section 3.1, a representative thermocouple curve was extrapolated to give peak temperatures of 800˚C, 1000˚C, and 1200˚C. These temperatures were selected to examine the effect of peak temperature on microstructure based on the allotropic transformation temperature at 980˚C. The heating and cooling curves for the heat affected zone, flow stress experiments, quench experiments, and stir zone simulations were specific for each experiment and are described in the following sections. The strain rates for compression specimens ranged from 0.1, 1, and 10/s.
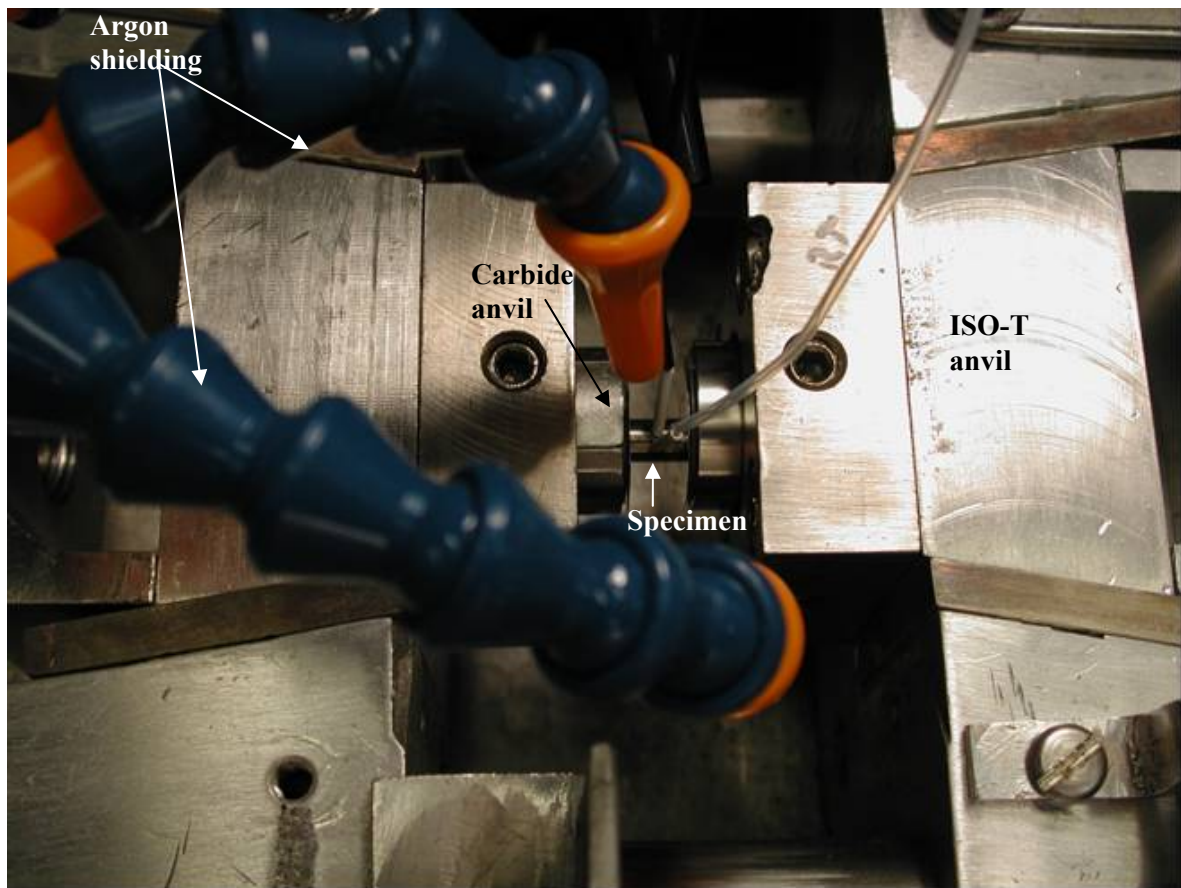
Figure 87. Experimental set-up for the Gleeble 1500D within the testing chamber.

4.3. Results and Discussion

4.3.1 Heat affected zone simulations

Heating curves were generated from actual HAZ weld data and peak temperatures were selected to mimic temperatures below beta transformation, slightly above beta transformation, and well above equilibrium transformation temperatures. Examination of the programmed temperature profile and simulated temperature profile shows a close relationship with the programmed heating curve. However, above peak temperatures of 1000˚C, the specimen cooling curve is unable to maintain the programmed cooling curve (Figure 88). This is due to phase transformation from beta to alpha shown at equilibrium temperatures of 980˚C. The phase change was detected through the use of dilatometry on the specimen upon cooling during the HAZ simulation (Figure 89). The green circle indicates the transformation from α to β on heating at 764˚C. The red circle indicates transformation on cooling from β to the HCP α system at approximately 989 ˚C. The noise during data collection partially obscures phase transformation start and finish temperatures. High magnification images of the center of the thermal specimens (with no strain applied) at 10x shows the presence of Widmenstatten or basketweave formation between alpha lath structures and alpha colonies at 800˚C. This Widmenstatten structure is more apparent at 800˚C compared to 1000˚C and 1200˚C due to the higher cooling rate, preventing extensive growth of the Widmenstatten structure (Figure 90). Higher temperatures show the growth of the prior beta grains and a reduction of grain boundary alpha. A heat tint in air was applied at 400˚C for 3 minutes to color specific phases preferentially [Vander Voort]. Retained β is typically a deep violet to bright blue with α colored a dull golden yellow. Martensite is shown as a yellow with violet blue due to the retained β. Applications of heat tint to

118

metallographic specimens are shown in Figure 91. At 800˚C, the structure has fully lamellar α with retained β in between α laths. Higher temperatures result in increased amount of retained β that appears in clusters. The increased β is expected based on the cooling rates shown in Table 19 from above transformation from 1000˚C to 500˚C for simulated peak temperatures of 1000˚C and 1200˚C.

While this set of experiments provides information on the isolated effects of temperature on the microstructure, the friction stir process influences the microstructure with both temperature and deformation. Thermal effects alone do not mimic the friction stir microstructure in the stir zone or in the transition zone shown in Section 3.2.1.

Table 19. Cooling rates for HAZ Gleeble simulations

Peak Temperature (˚C)	T_{trans}-T_{500} (˚C)	Time (s)	Cooling rate (˚C/s)
1200	500	8.2831	60.36
1000	500	39.1547	12.77
800	300	38.973	7.70

FSW HAZ Simulations
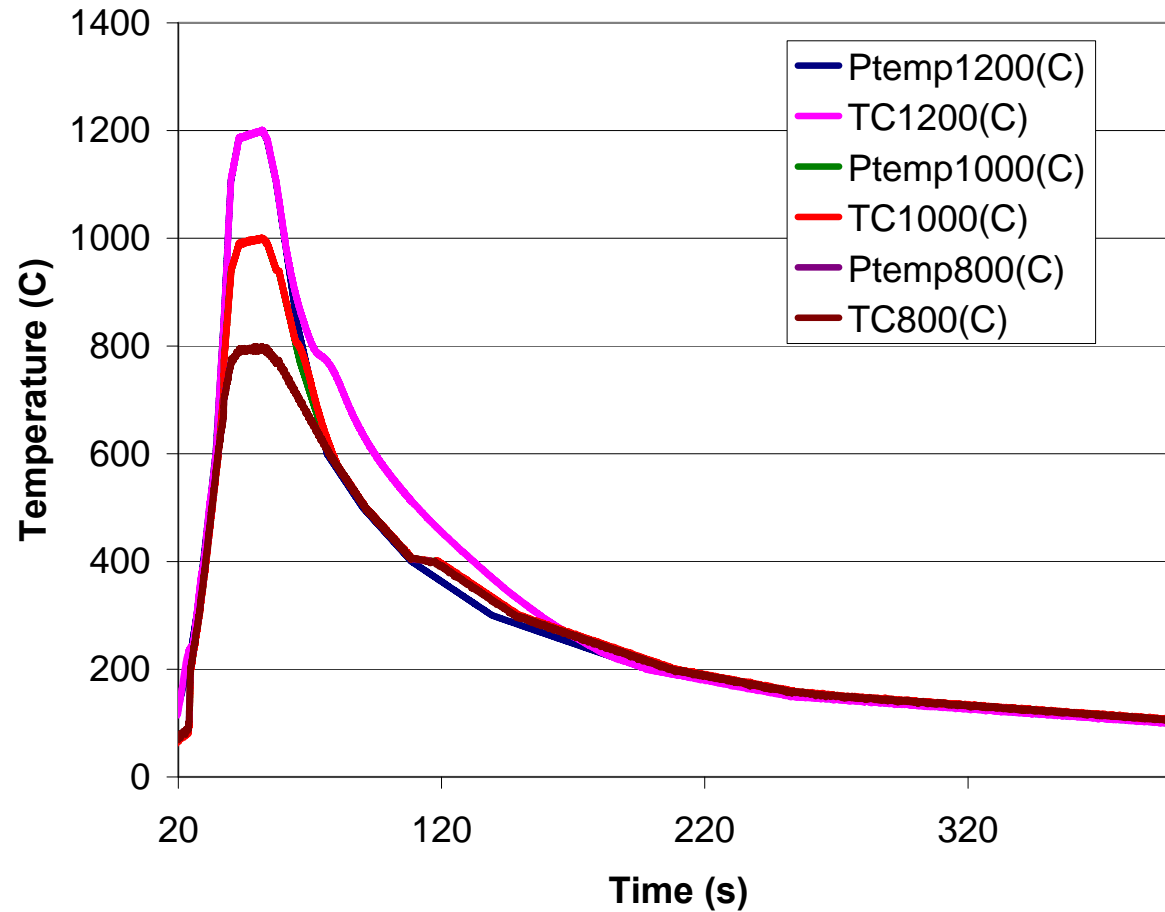
Figure 88. Thermocouple curves for Gleeble simulation. Curves were generated from actual HAZ weld data and the graph shows the program curves and the experimental curves. Examination of the programmed temperature profile and simulated temperature profile shows a close relationship with the programmed heating curve. However, above peak temperatures of 1000°C, the specimen cooling curve is unable to maintain the programmed cooling curve due to phase transformation.
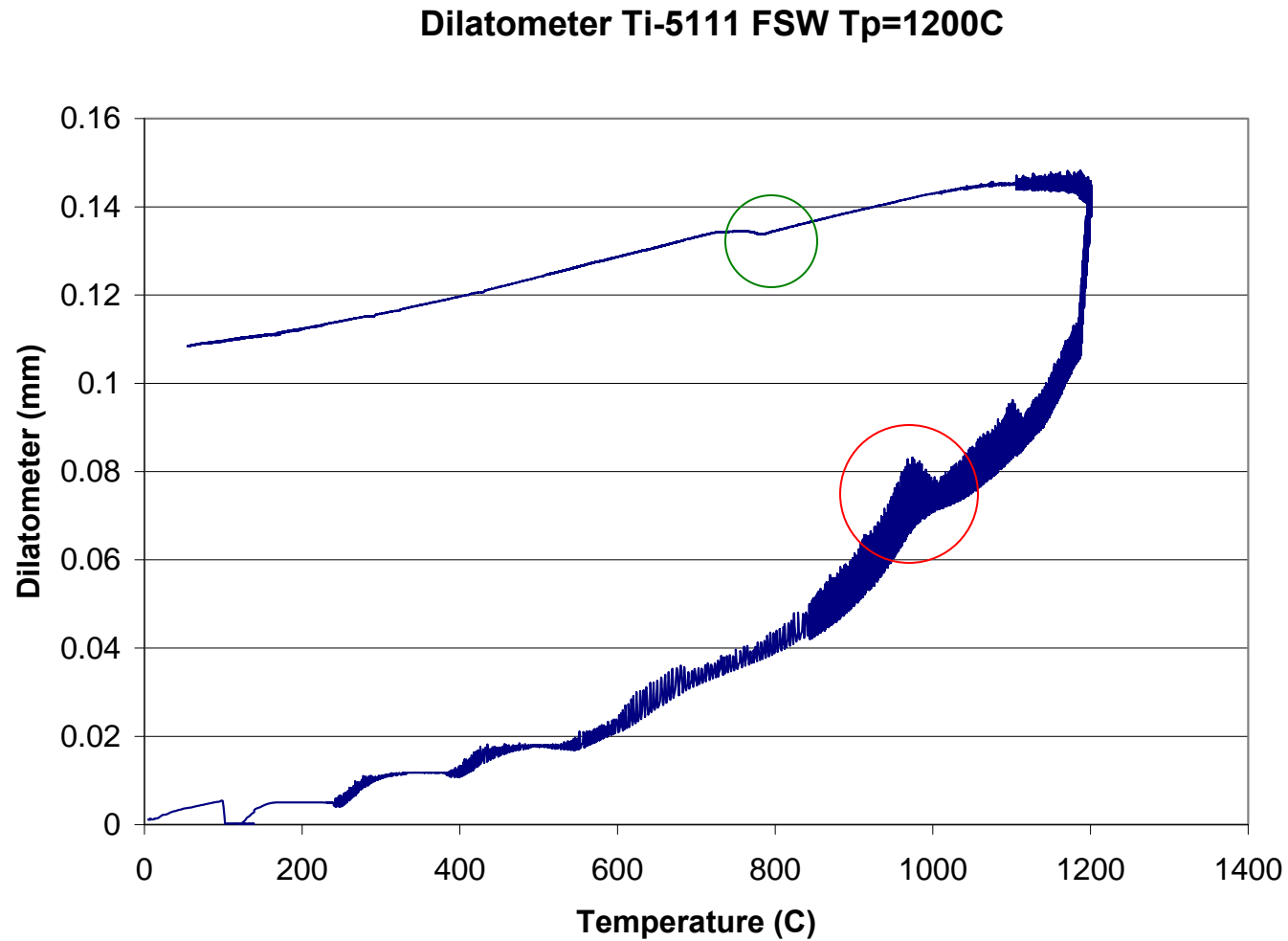
Figure 89. Gleeble dilatometry data from the simulated FSW thermal curve at a peak temperature of 1200C. The red circled indicates the phase transformation detected on cooling. The green circle is the phase transformation on heating.
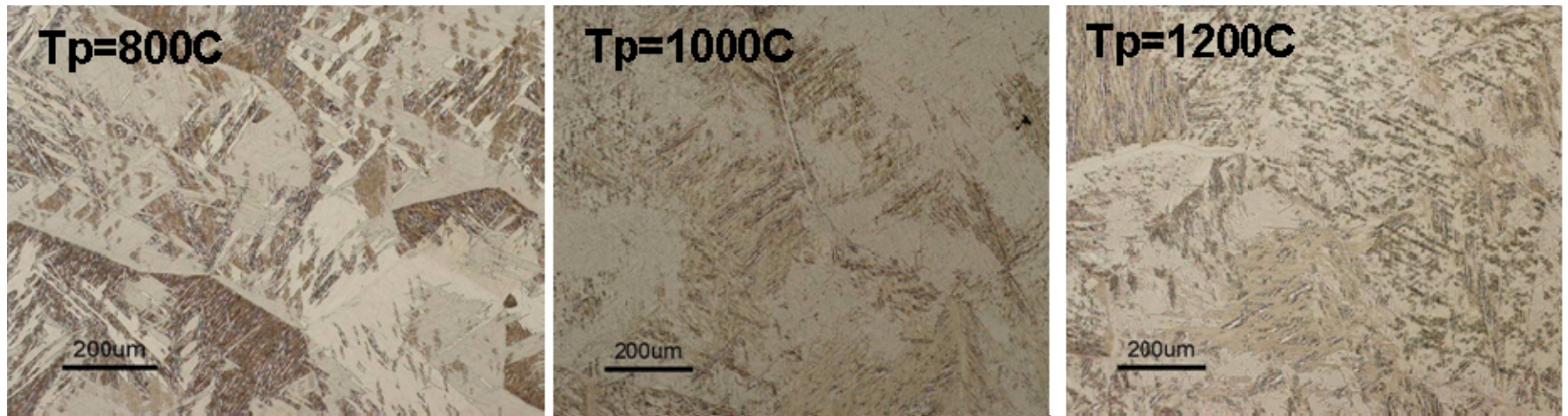
Figure 90. Optical images of simulated specimens with different peak temperatures (Tp) and with no deformation
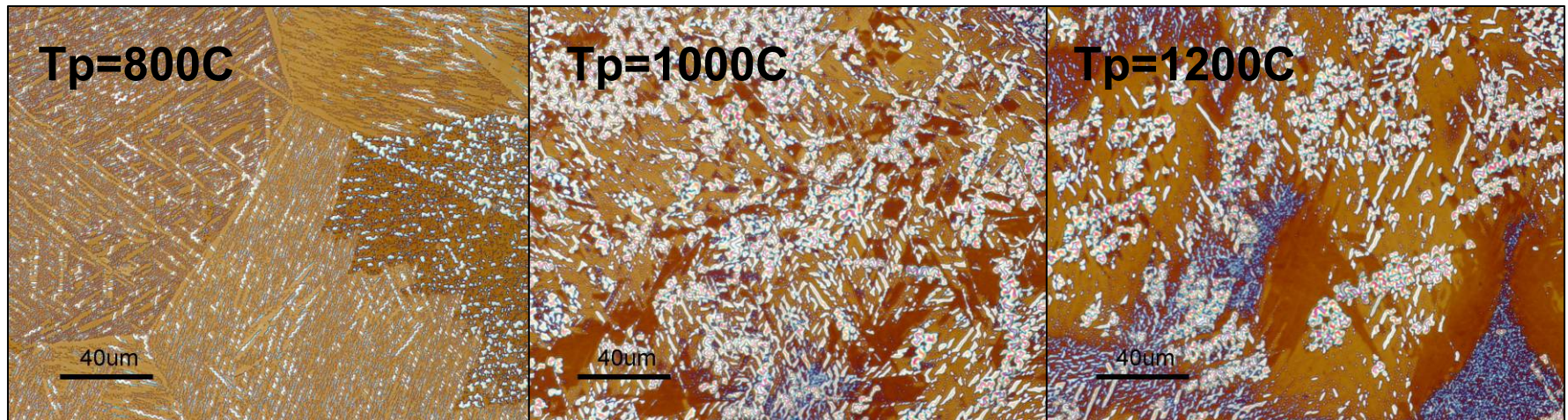
Figure 91. Optical images of simulated specimens with different peak temperatures and no deformation after heat tint application. Images are taken from the same area as Figure 90 at higher magnification. Images show the presence of α' (shown in violet).

4.3.2 DEFORM finite element model for compression testing

The behavior of compression specimens was predicted with modeling trials using DEFORM, a finite element thermal and deformation based modeling software with the assistance of Dr.David Forrest at Naval Surface Warfare Center, Carderock. Compression testing generates a range of strain and strain rates through the transverse cross-section of the test specimen in the compression axis. Without modeling the experiment, calculation of constant strain rate and strain within a given point of the system would be challenging. DEFORM has also been successfully used to calculate strain and strain rates experienced within torsional Gleeble work [Sinfield]. DEFORM computational trials used a combination of thermophysical parameters of Ti-CP and Ti-64 to mimic the flow stress behavior of Ti-5111 and the heat transfer into the Gleeble 1500D system. This modeling work enabled determination of general trends with respect to temperature and strain in the system. Computational trials show a decline in maximum predicted force during compression with increasing test temperature. Additionally, there is an increase in predicted force with increased strain rate. As the test temperature decreases from 1200°C to 800°C, there is an increased thermal effect due to adiabatic heating during compression (Figure 92). In contrast, the effective strain remained constant around 1.0 in the center of the compression specimen with respect to temperature and strain rate (Figure 93). The calculated change in length to maintain a constant strain rate was used for experimental trials described in the next section. Each trial used the precise dimensions of the test specimen for computational analysis.
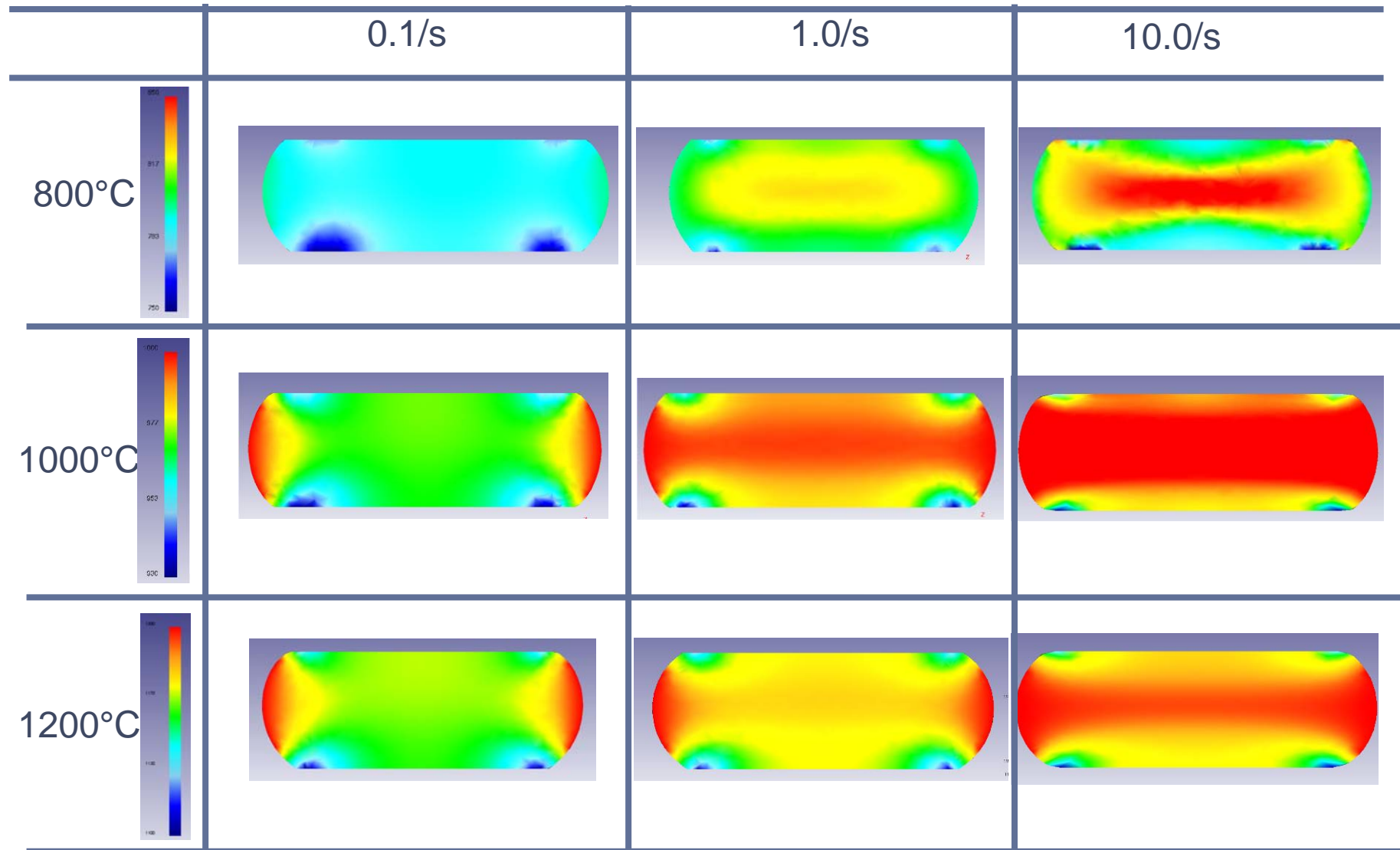
Figure 92. DEFORM compression sections (thermal cross-section) at different strain rates and peak temperatures. As the test temperature decreases from 1200°C to 800°C, there is an increased thermal effect due to adiabatic heating during compression.

	0.1/s	1.0/s	10.0/s
800°C			
1000°C			
1200°C			
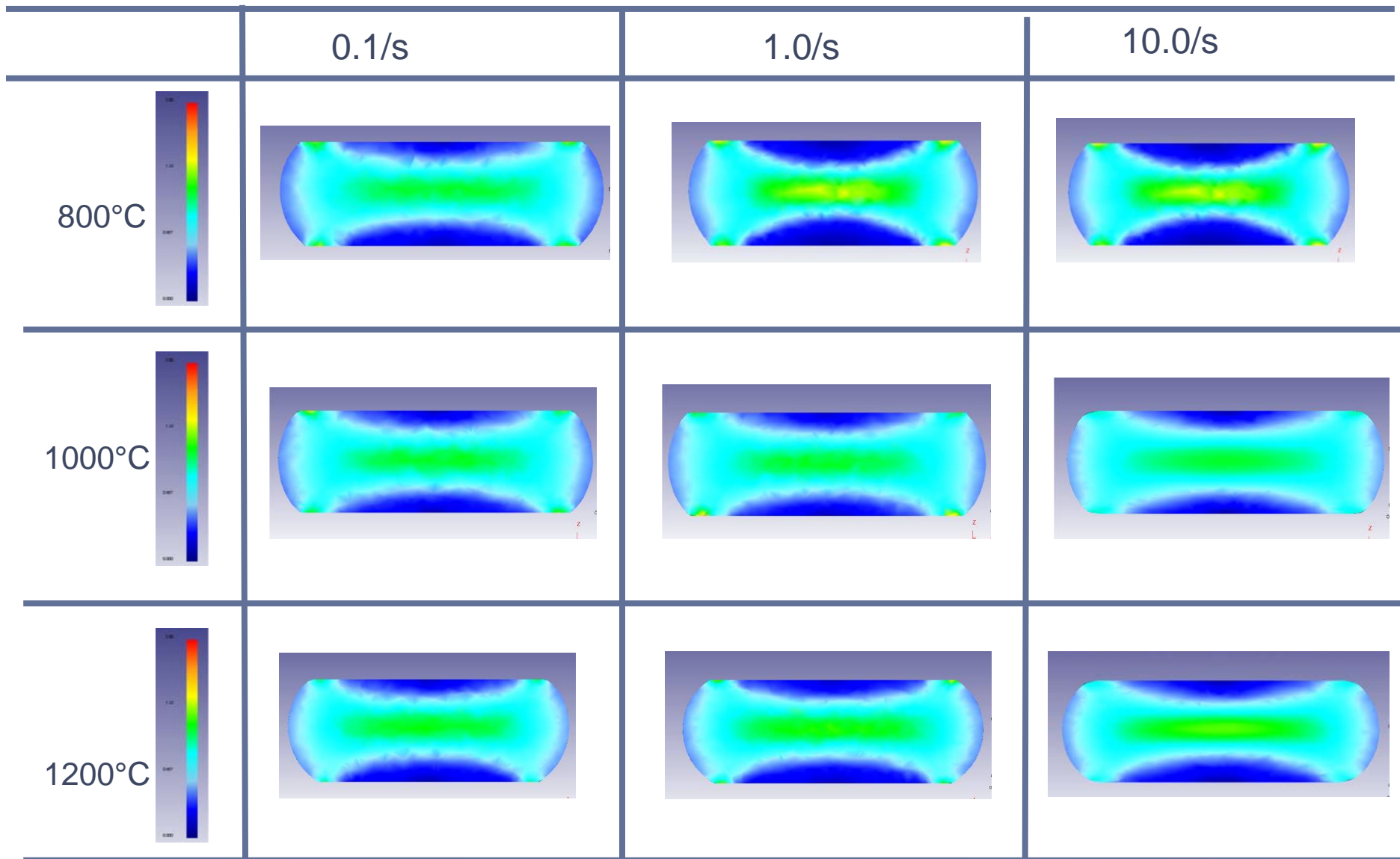
Figure 93. DEFORM compression sections (strain cross-section) at different strain rates and peak temperatures. The effective strain remained constant around 1.0 in the center of the compression specimen with respect to temperature and strain rate.

4.3.3 Influence of α-β transformation temperature on compression forces

Building upon the Gleeble thermal simulations, compression forces for steady state constant strain rate were studied on Ti-5111 at a wide range of constant strain rates to determine thermophysical properties for incorporation into the ISAIAH model [Dawson 2008]. Cylindrical specimens approximately 1.25 x 1.25 cm were prepared using procedures described in Section 2.5. Specimens were heated with a 20˚C/sec heating curve and held at temperature for 90 seconds prior to compression at strain rates of 0.1/s, 1.0/s, and 10.0/s. Specimens were programmed at a cooling rate of 20˚C/sec. The Gleeble program development used DEFORM modeling results to determine compression length (measured through the LGauge) to maintain constant strain rate. All forces were corrected to account for the inherent friction within the Gleeble system at given strain rates. At the peak temperature of 800˚C, the sample is held below transformation to the beta phase resulting in a significant increase in force required for compression. As shown in Figure 94 forces exceeded 5000 kgf at a strain rate of 10/s. The rapid compression at the high strain rate results in signal noise and the sample did not compress fully. The force required for compression at a strain rate of 0.1/s was greater than for a strain rate at 1.0/s. This contradictory result is explained with the underlying microstructure. This increase in force is due to the lower number of available slip systems in the HCP crystal structure below transformation temperature compared to the BCC crystal structure. Compression forces above beta transformation temperatures (1000˚C and 1200˚C) are significantly lower during testing as shown in Figure 95 and Figure 96. Higher strain rates show higher overall forces during compression. Peak forces for each condition are shown in Table 20. Forces for a

strain rate of 10/s at 800˚C are over seven times higher than forces experienced at 1200˚C for the same strain rate.

Flow stress and hot workability for titanium alloys with respect to transformation temperatures has been well documented in the literature. Semiatin *et al* examined the hot workability of α/β titanium alloys [Semiatin]. The authors noted that subtransus hot working resulted in strain induced porosity, such as wedge cracks and cavities. Hot tension tests for Ti-64 resulted in high ductility near β transus and ductility drop due to wedge cracking and intergranular failure [Semiatin]. Hot deformation below β transus for near α alloys show initial work-hardening and then near steady state flow [Weiss]. This flow stress is related to solute strengthening within near α titanium. Processing below β transus for α/near α alloys gives an activation energy for dynamic recovery in the range of 200-360 kJ/mol compared to the activation energy for dynamic recrystallization of 180-220 kJ/mol when processing above β transus [Weiss]. The activation energy obtained during dynamic recrystallization for processing above β transus is close to the self diffusion energy in β [Seshacharyulu]. Sesharcharyulu suggests slow strain rates result in a steady-state type curve due to softening at the same rate of work hardening and is indicative of dynamic recovery, dynamic recrystallization or superplasticity. Weiss similarly suggested a method of dynamic recovery resulting in the steady-state flow stress curves [Weiss].

General trends for compression force relative to position in this thesis are consistent with the reported literature. Analysis of true stress/true strain for flow stress cannot be performed in these tests due to specimen geometry. Flow stress and hot workability tests reported in the

127

literature are typically performed on larger specimens to allow for accurate measurement of cross-sectional area change. Due to the system configuration for compression of 12.5 x 12.5mm cylindrical specimens, we cannot experimentally determine the change in cross-sectional area. Deformation modeling to achieve the experimental forces in compression and the final specimen geometry is recommended to back-calculate flow stress.

Table 20. Peak forces during constant strain rate and temperature compression testing.

Strain rate (s^{-1})	800˚C Peak Force (kgf)	1000˚C Peak Force (kgf)	1200˚C Peak Force (kgf)
0.1	4389.09	843.89	501.95
1.0	2015.25	1533.45	769.20
10.0	5272.71	1287.61	716.39
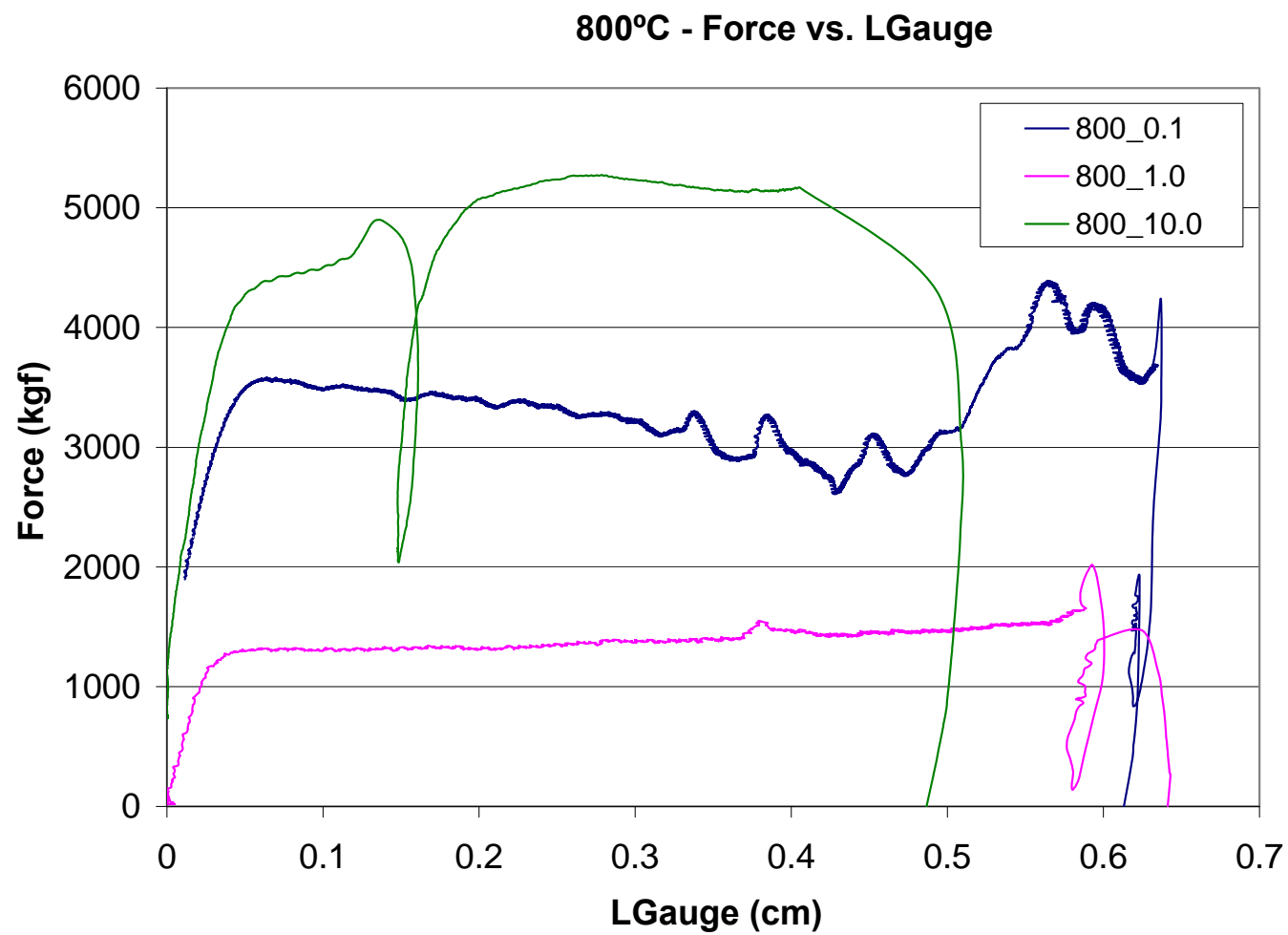
Figure 94. Forces at constant strain rate of 0.1, 1.0, and 10/s at 800°C show an increase in force with respect to increased strain rate.
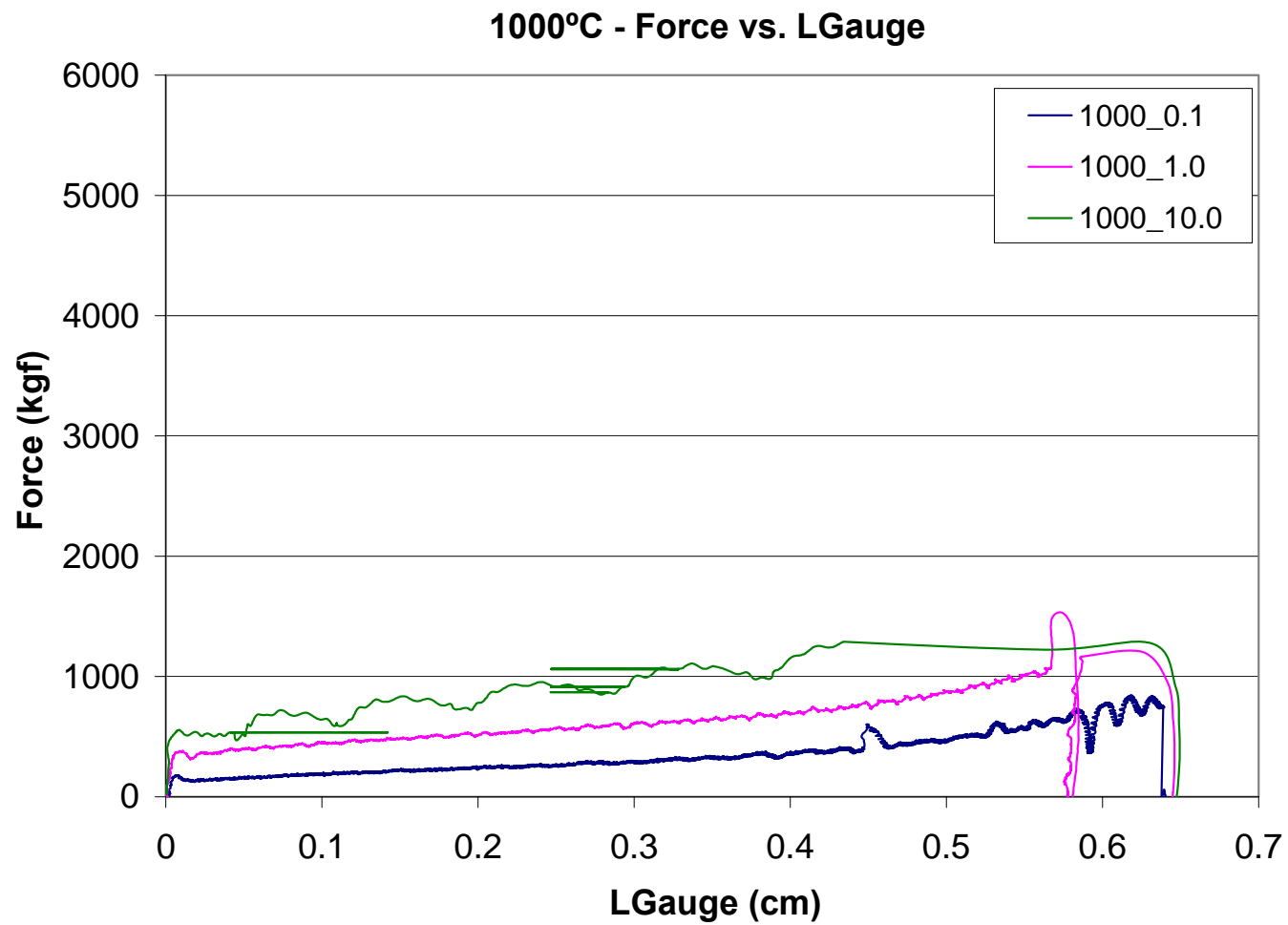
Figure 95. Forces at constant strain rate of 0.1, 1.0, and 10/s at 1000 °C show a dramatic reduction in force compared to 800°C. There is an increased force with respect to increased strain rate.
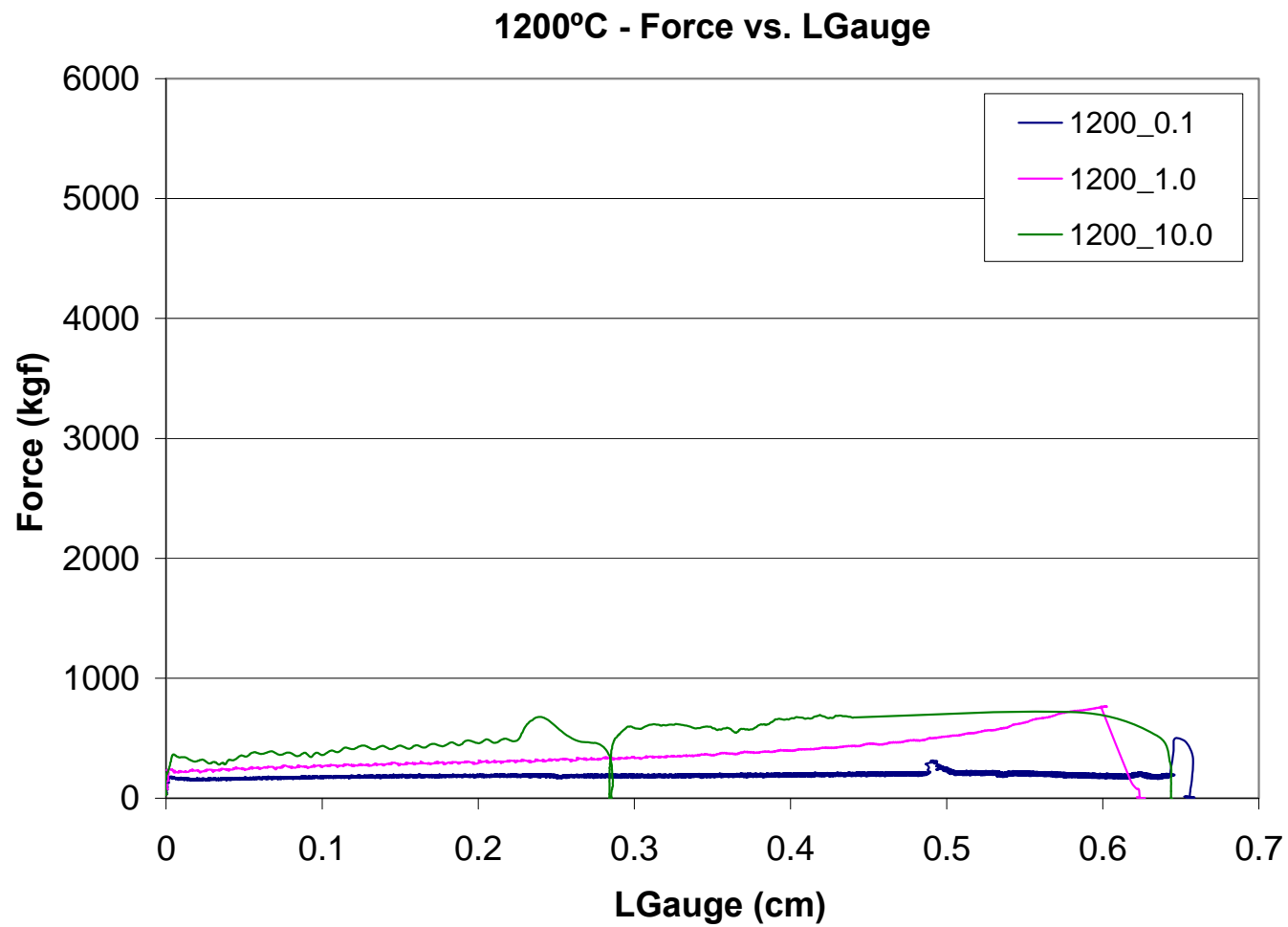
Figure 96. Forces at constant strain rate of 0.1, 1.0, and 10/s at 1200 °C show a dramatic reduction in force compared to 800°C. There is an increased force with respect to increased strain rate.

4.3.3.1 Microstructural comparison of specimens under steady state compression at constant strain rate

Low magnification images of the transverse cross-section along the compression axis of the tested specimens shows a difference in compression test barreling below beta transus for different strain rates (Figure 97 top panel). Test specimens at 800°C did not result in full compression at 10/s strain rate. Compression test specimens for 1000°C and 1200°C show even compression through the sample (Figure 97 middle and bottom panels). Strain and strain rates were calculated from the DEFORM model for the center point of each specimen. Images of high strain region at the center of the specimen show evidence of near alpha transformed microstructures at 1000°C and 1200°C (Figure 98 middle and bottom panel). However, no clear α transformed microstructure is observed at 800°C instead kinking of the α laths is observed at the lower temperature (Figure 98 top panel). The metallography is consistent with the theory of β transformation for reduction in force experienced during compression. Deformation for 1000°C and 1200°C occurs while the microstructure is uniformly in the β phase field. Figure 99 illustrates that at 1000°C and 1200°C for all strain rates, the material shows narrow α lath formation within the alpha colony structure with a Widmenstatten structure. At slower strain rates in this temperature regime, grain boundary α formation is more defined compared to higher strain rates. At 800°C, below β transus, the grain structure undergoes compression for strain rates of 0.1 and 10/s. The α colony structure becomes compressed along the centerline of the test specimen. At higher magnification the α lath structure shows compression and displacement of individual laths when compared to the original base metal as indicated in (Figure 99 top panel) with black arrows. The higher strain rate resulted in increased lath kinking almost perpendicular to the compression axis. The

microstructure in Figure 99 at 800˚C and 1.0/s shows evidence of β phase transformation and deformation in β. This explains the unexpected drop in compression force presented in Section 4.3.3. This unexplained transformation may be due to momentary thermocouple loss and reattachment during compression. The sub-transus lath deformation and kinking is reminiscent of deformation within the transition zone between the base metal and the stir zone shown in Section 3.2.1.

Similar isothermal tests in Ti-64 with a colony microstructure examined the effect of Hall-Petch type strengthening discussed in Section 3.2.6.2 [Semiatin 2001]. This work showed a difference in deformation mode with respect to strain. Sub-transus temperatures and low strain rates (0.0004/s) results in dislocation glide/climb. Higher strain within Semiatin's work resulted in dynamic spheroidization and grain boundary sliding [Semiatin 2001]. The α-β interface strengthening was shown to have an effect on the flow softening behavior and peak stresses [Semiatin 2001] [Picu]. As discussed earlier hot deformation above and below β transus for near α alloys displays dynamic recovery. However, processing above β transus results in recovery within developed subgrain structures [Weiss]. This difference in deformation mode with respect to strain rate may account for the increased force of compression at higher strain rates and low temperature.

Microstrucutral analysis for this experimental set indicates that the behavior of Ti-5111 in isothermal constant strain rate tests show evidence of little variation in hardness properties along the centerline of the specimen despite deformation above and below β transus (Figure 100**Error! Reference source not found.**-Figure 105). Increased strain rate resulted in

higher peak hardness at the center of the specimen. Deformation above transus resulted in lower scatter in the hardness values. The resulting microstructures do not show evidence of dynamic spheroidazation or globularization. The microstructures shown in this work seem to indicate that the mechanisms of dynamic recovery and recrystallization are in agreement with the force compression curves discussed in Section 4.3.3. The hardness values obtained from these tests fall in the range of values measured in the FSW samples for the base metal and the stir   zone.

	0.1/s	1.0/s	10.0/s
800°C			
1000°C			
1200°C			

Figure 97. Transverse cross-sections of constant strain rate specimens (0.1, 1.0,10.0/s) at peak temperatures of 800, 1000, and 1200 C. There is a difference in compression test barreling below beta transus for different strain rates (top panel). Test specimens at 800°C did not result in full compression at 10/s strain rate. Compression test specimens for 1000°C and 1200°C show even compression through the sample (middle and bottom panel)

	0.1/s	1.0/s	10.0/s
800°C			
1000°C			
1200°C			
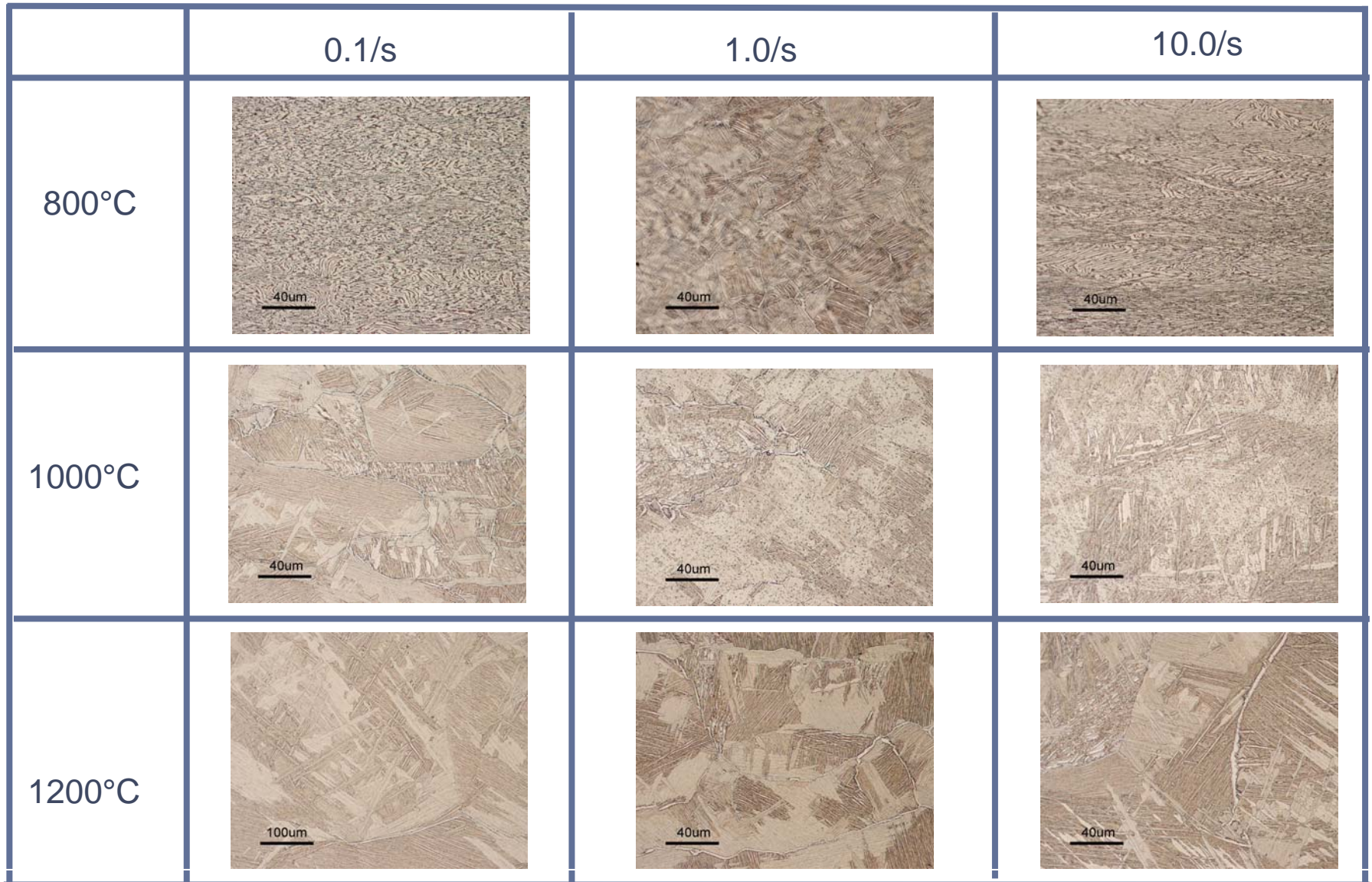
Figure 98. Optical micrographs of the center of constant strain rate specimens (0.1, 1.0,10.0/s) at peak temperatures of 800, 1000, and 1200 C. Images of high strain region at the center of the specimen show evidence of near alpha transformed microstructures at 1000°C and 1200°C (middle and bottom images)
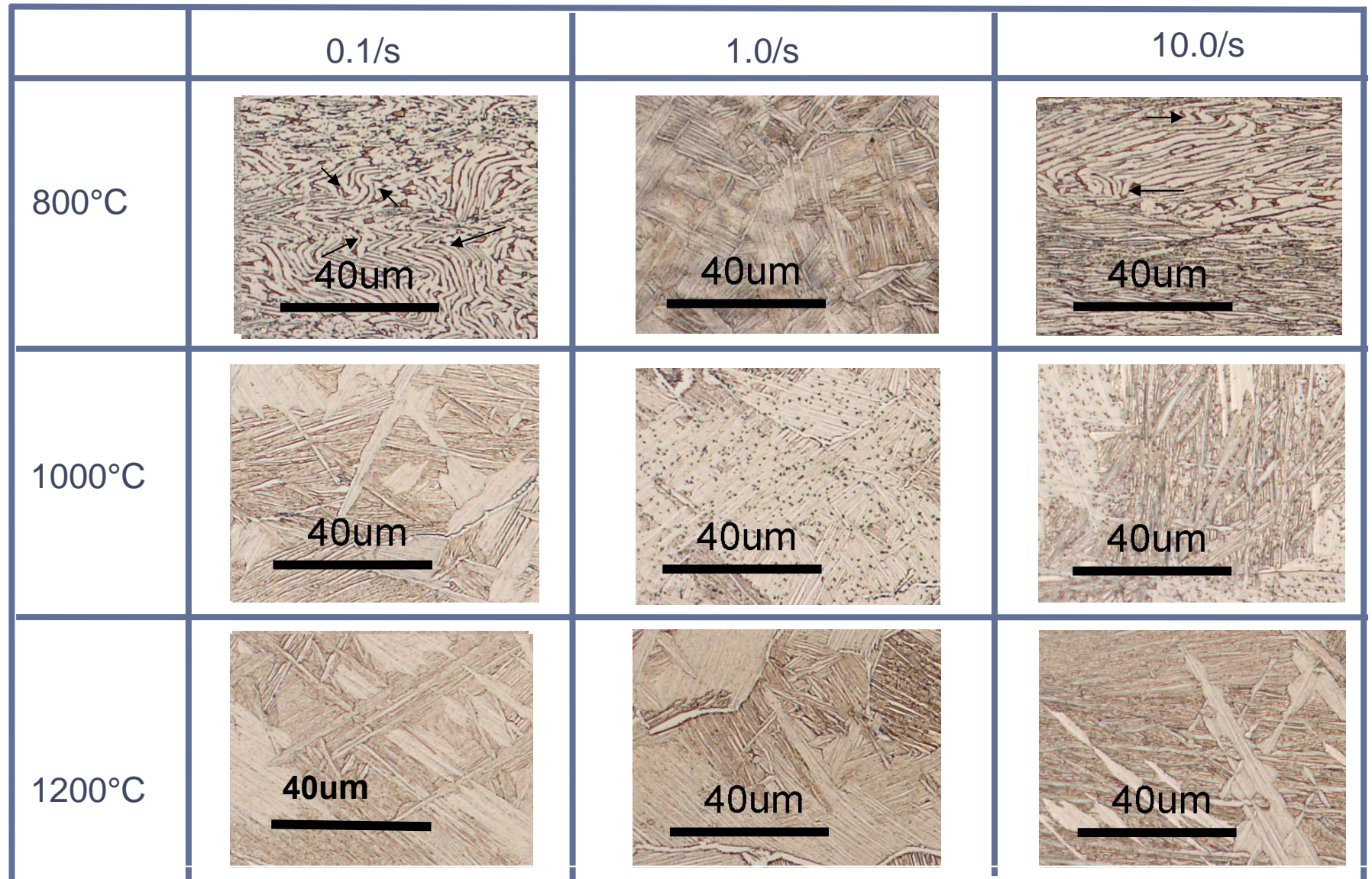
Figure 99. Optical micrographs of the center of constant strain rate specimens (0.1, 1.0,10.0/s) at peak temperatures of 800, 1000, and 1200 C. Arrows show kinking of the α laths below β transus. At 1000˚C and 1200˚C for all strain rates, the material shows narrow α lath formation within the alpha colony structure with a Widmenstatten structure.
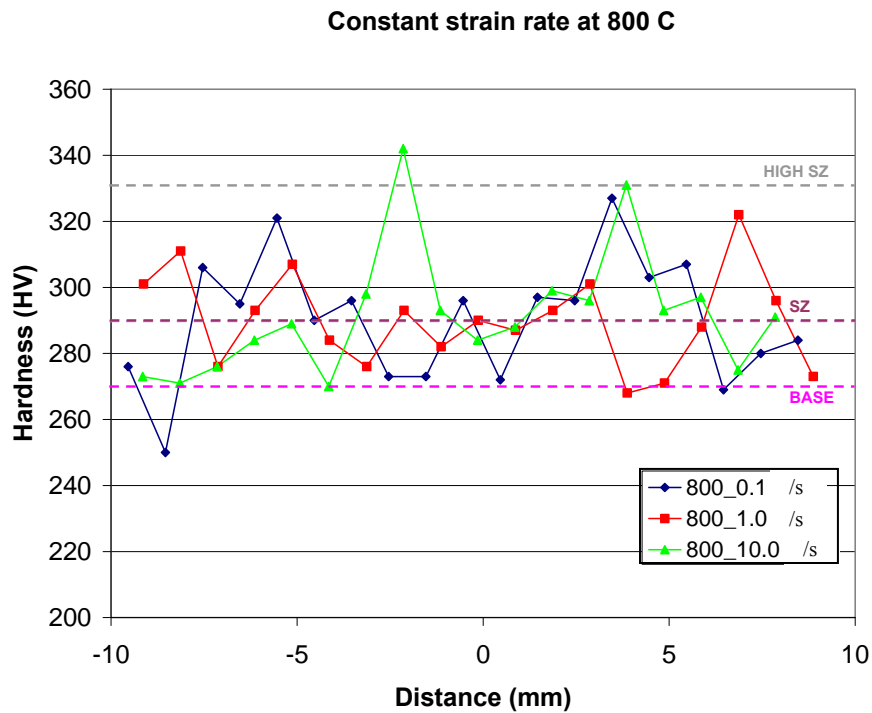
Figure 100. Microhardness traverse along the Gleeble constant strain rate compression specimens at 800ºC. Hardness values fall in the range for FSW and base metal.
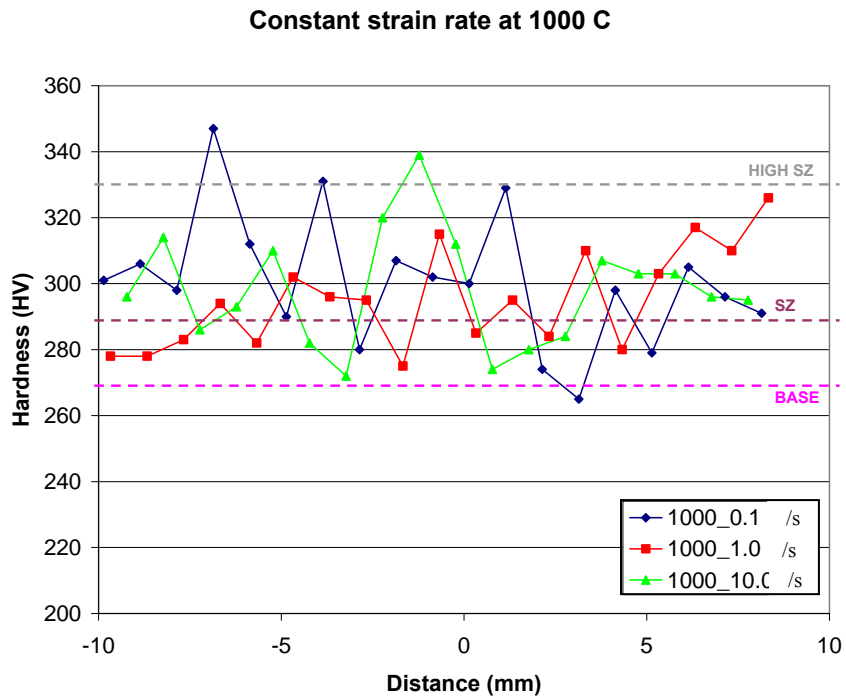
Figure 101. Microhardness traverse along the Gleeble constant strain rate compression specimens at 1000ºC. Hardness values fall in the range for FSW and base metal.

138

Constant strain rate at 1200 C
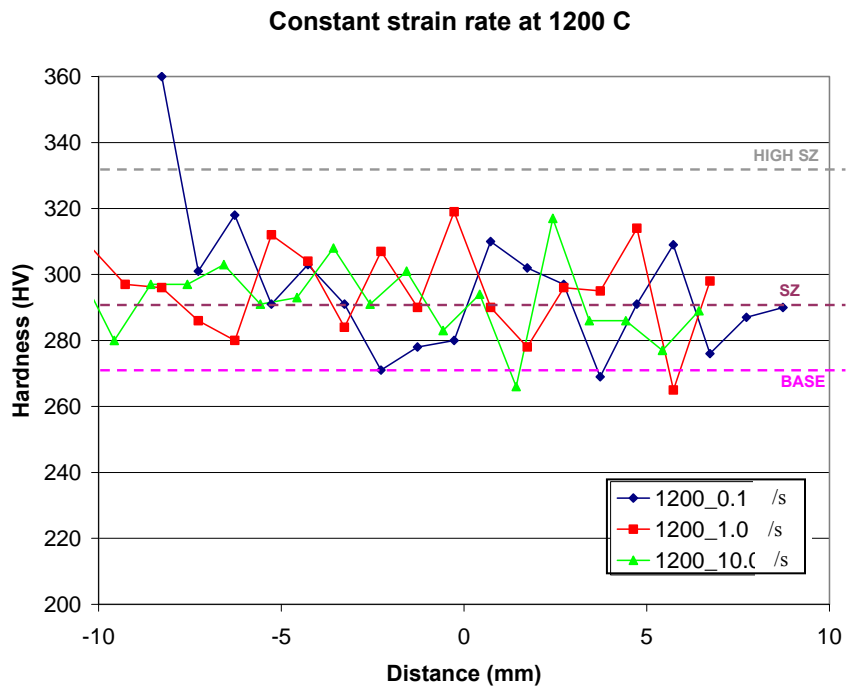
Figure 102. Microhardness traverse along the Gleeble constant strain rate compression specimens at 1200ºC. Hardness values fall in the range for FSW and base metal.

Constant strain rate of 0.1/s
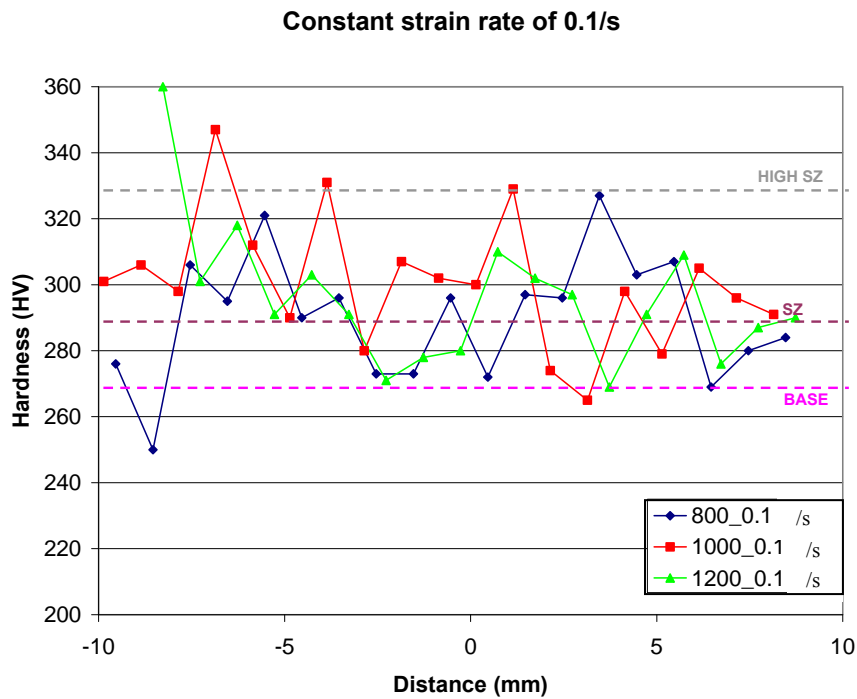
Figure 103. Microhardness traverse along the Gleeble constant strain rate of 0.1/s for different temperatures. Hardness values fall in the range for FSW and base metal.

Constant strain rate of 1.0/s
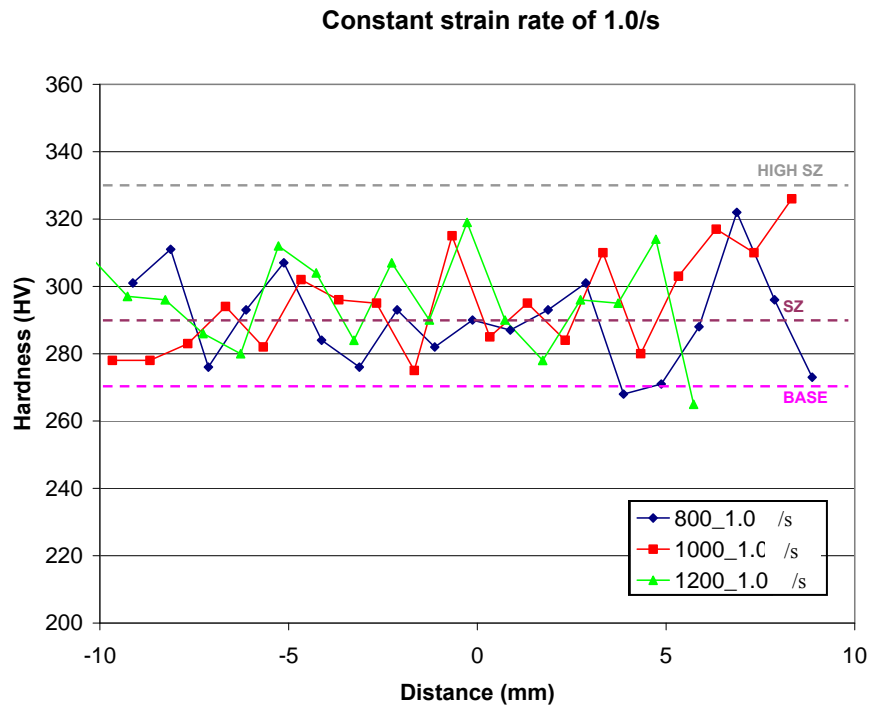
Figure 104. Microhardness traverse along the Gleeble constant strain rate of 1.0/s for different temperatures. Hardness values fall in the range for FSW and base metal.

Constant strain rate of 10.0/s
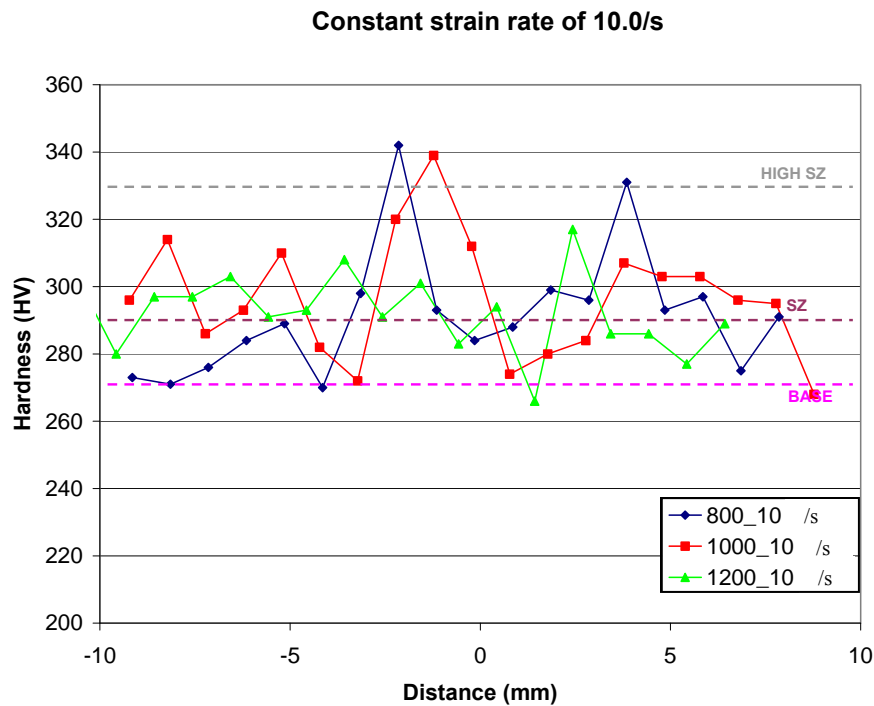
Figure 105. Microhardness traverse along the Gleeble constant strain rate of 10/s for different temperatures. Hardness values fall in the range for FSW and base metal.

140

4.3.3.2 Rapid quenching of thermomechnical simulation flow stress specimens

The Gleeble 1500D controls heating and cooling of a specimen in accordance with a specified thermal cycle through the use of resistive heating and active cooling. The system also has capability to rapidly quench a specimen. However, the supplied quench unit is unable to compress a 1.25cm specimen due to the dimensions of the quench unit. Experiments discussed in this section focus on quenching specimens after compression through the use of a specialized water quench system designed at NSWCCD by Wolk and Shepherdson [Wolk 2009]. The quench system utilized a faucet style design with water flow above and around the specimen. Based on the constant strain rate experiments, quench experiments used 1.0/s strain rate at 800˚C, 1000˚C, and 1200˚C. Specimens used a heating rate of 20˚C/s and were held at peak temperature for 90s prior to compression. Immediately following compression, the specimens were water quenched. Force curves for each specimen with respect to compression length are shown in Figure 106. Force values are similar to experimental values for constant strain rate tests. Unlike the prior 800˚C at 1.0/s test presented in Section 4.3.3, a peak force of 3779.7 kgf was experience during compression testing (Table 21) . This force is significantly higher compared to the force for compression at 1000˚C and 1200˚C and is consistent with the results presented in Section 4.3.3. Optical micrographs at the center of the transverse specimen cross-section along the compression axis are shown in Figure 107. Quenching the specimen after compression at 800˚C shows compression and kinking of α laths (Figure 107 top panel). Isothermal specimens quenched after compression above transus result in the formation of acicular martensite (α') (Figure 107 middle and bottom panel). While the α' transformation obscures grain substructure analysis, it allows for analysis of the deformed prior β grain structure. Grains appear

compressed and flattened with the grain boundaries showing evidence of serration indicative

of grain boundary sliding, similar to experiments performed by Li *et al* in Ti-3Al-5V-5Mo

[Li]. The experiments above β transus do not show evidence of recrystallization.

Table 21. Peak forces for quenched specimens at 1.0/s

Peak Temperature	Peak Force (kgf)
800˚C	3779.7
1000˚C	1193.6
1200˚C	1127.8
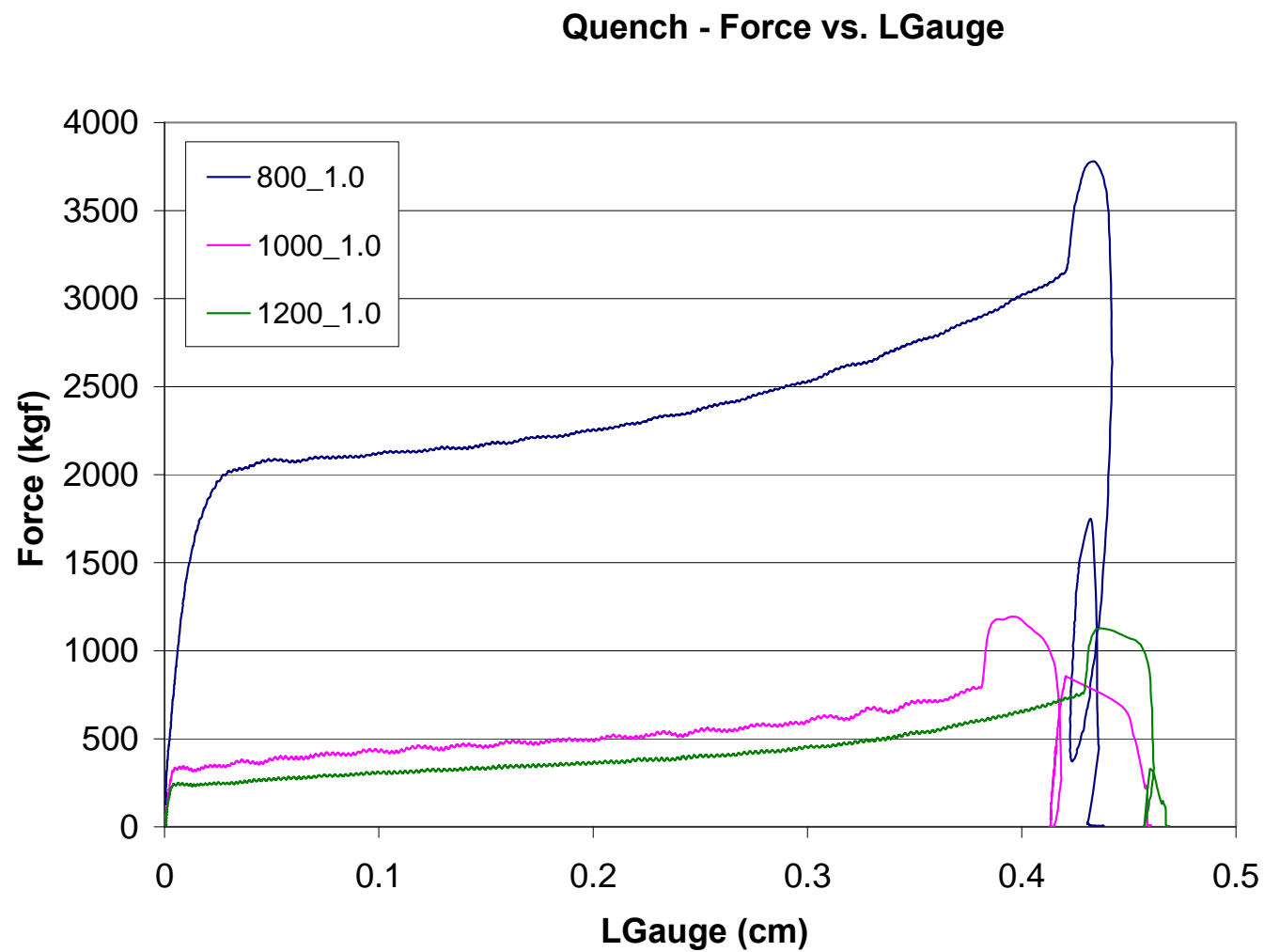
Figure 106. Force curves for water quenched specimens at a constant strain rate of 1.0/s and peak temperatures of 800, 1000, and 1200 C. There is increased force for compression at 800 C.

	20x	50x
800°C	100um	40um
1000°C	100um	40um
1200°C	100um	40um
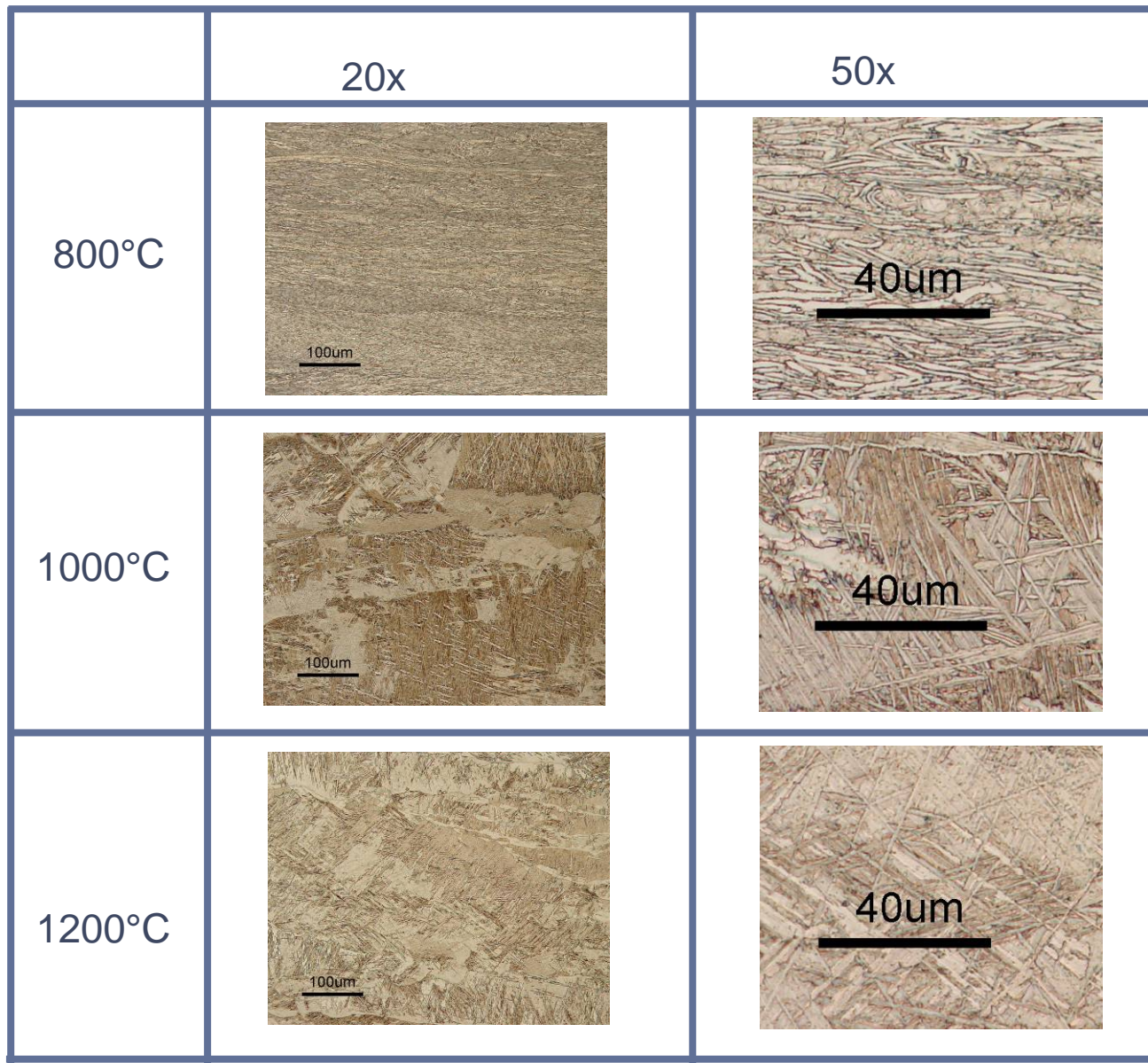
Figure 107. Optical micrographs of quenched specimens represented in Figure 106. Quenching the specimen after compression at 800˚C shows compression and kinking of α laths. Isothermal specimens quenched after compression above transus result in the formation of acicular martensite (α').

4.3.4 Thermomechanical simulations of friction stir welded Ti-5111

Friction stir welding experiences transient thermal effects during deformation. Constant strain rate specimens focus on maintaining a uniform temperature for compression. The compression experiments are intended to isolate deformation effects from thermal effects. Similarly, experiments focusing on applying the thermal conditions of friction stir were designed to decouple deformation effects. By understanding the individual effects of deformation and transient temperature, we can better understand the behavior of the entire system. Following the thermal curves in Figure 88, compression of the cylindrical specimens took place at a designated peak temperatures and strain rates of 1.0 and 10/s. A representative experimental thermal curve for compression is shown in Figure 108 along with the actual FSW temperature variation. Figure 109 and Figure 110 show the measured forces for compressed specimens that underwent thermal curves given in Figure 108 and for strain rates of 1 and 10/s, respectively. Peak forces are given in Table 22 and are lower than the peak forces from the isothermal constant strain rate compression tests. The shape of the compression curves for a strain rate of 10/s appears similar to curves from the constant strain rate tests.

FSW Thermal Curve for 1000 C at 10/s
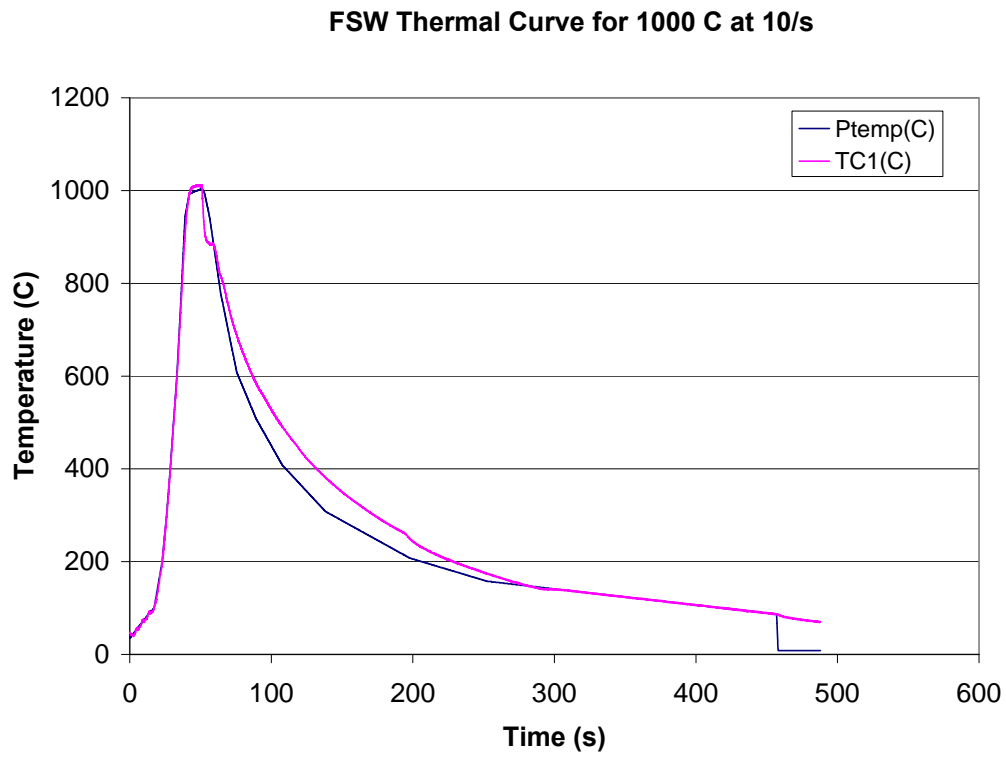
Figure 108. Sample thermal curve for compression based on experimental friction stir welding temperature curve.

Table 22. Peak forces in thermomechanical simulation based on friction stir welding thermal curves.

Strain rate (s⁻¹)	800°C Peak Force (kgf)	1000°C Peak Force (kgf)	1200°C Peak Force (kgf)
1.0	5523.25	1088.85	620.52
10.0	3874.31	576.29	651.85
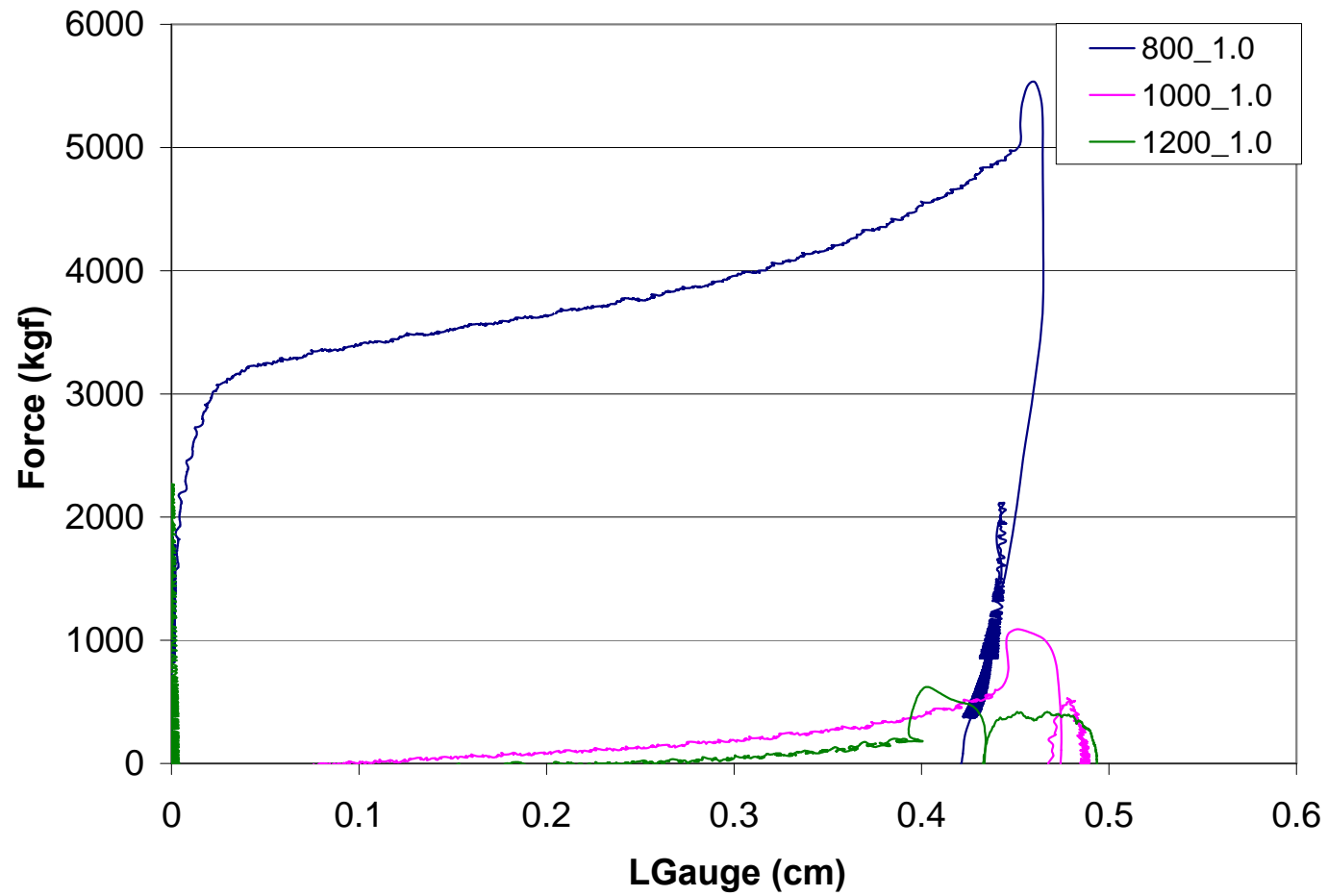
Figure 109. Force curves for FSW thermal cycle specimens at a strain rate of 1.0/s and peak temperatures of 800, 1000, and 1200 C
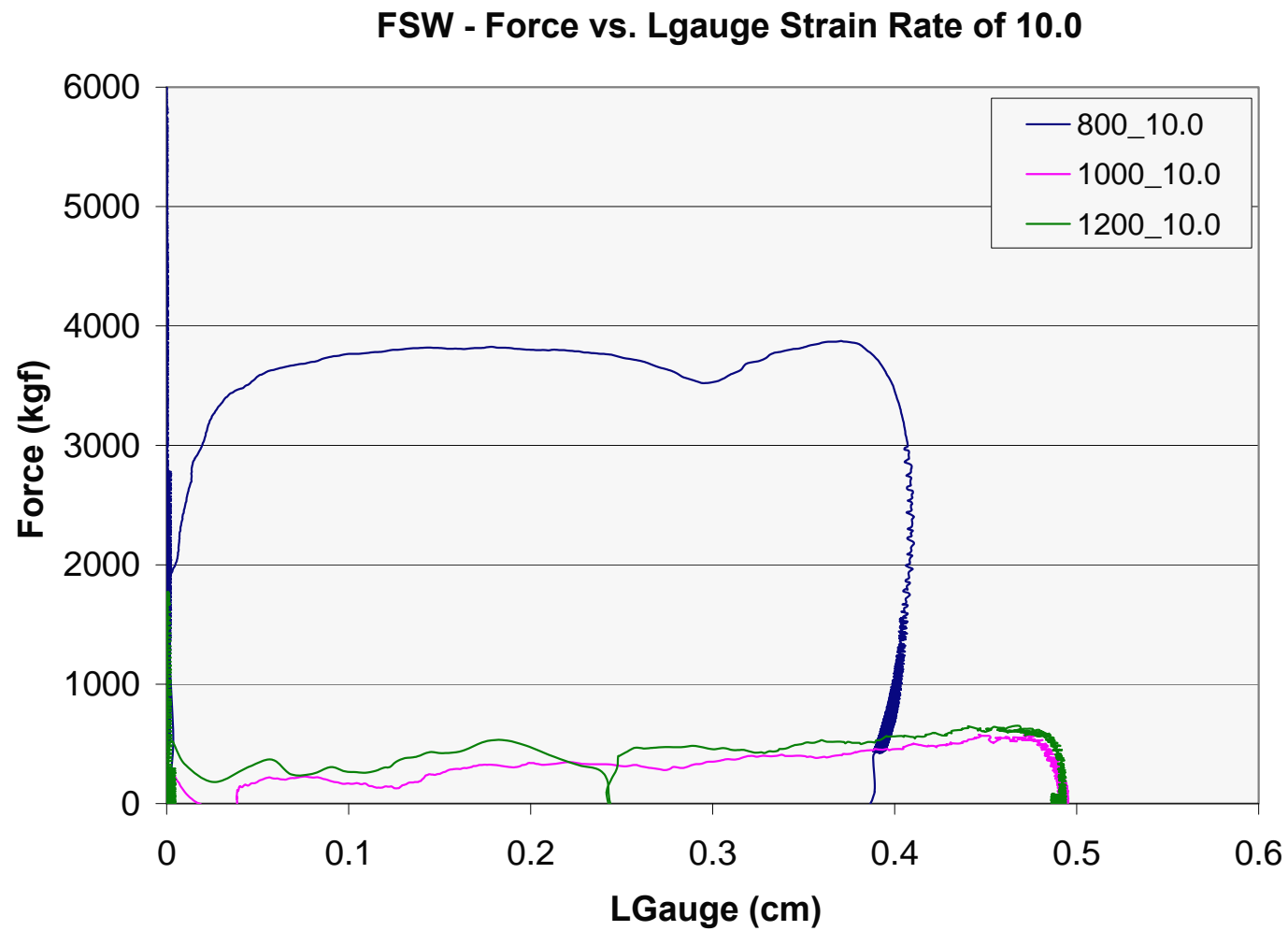
Figure 110. Force curves for FSW thermal cycle specimens at a strain rate of 10/s and peak temperatures of 800, 1000, and 1200 C

Optical micrographs from this set of experiments provide interesting insight into the friction stir welding process and are shown in Figure 111 and Figure 112. Following the same thermal curves as recorded from experimental data, subtransus peak temperature (800ºC) compression results in α lath bending and kinking (see Figure 111 and Figure 112 top panel). This response is consistent with isothermal compression and istothermal compression and quenching. The α lath deformation is not dependant on the thermal cycle, however the amount of lath deformation varies with the strain rate. The effect of peak temperatures and the transient thermal cycle is more apparent above β transus. At 1200ºC, optical micrographs (see Figure 111 and Figure 112 bottom panel) show a fully lamellar structure with increased grain size compared to 1000ºC (see Figure 111 and Figure 112 middle panel). The higher strain rate of 10/s results in smaller grain size compared to 1.0/s. Optical micrographs of deformation above β transus also show evidence of dynamic recrystallization and development of a fully lamellar colony microstructure with a continuous grain boundary α network. The microstructures shown in Figure 111 and Figure 112 are indicative of deformation in the β-phase field [Ma]. Dynamic recrystallization for specimens at 1200ºC and 1000ºC was completed within the β phase field resulting in equiaxed microstructure. A schematic of the microstructure evolution with respect to increasing deformation is shown in Figure 113. The increased grain size in specimens at 1200ºC is due to the longer time spent above β-transus allowing for growth of new β grains. Comparing the microstructures in the FSW thermomechanical compression simulations to the actual 12.7mm weld microstructure shows remarkable agreement at peak temperatures of 1000ºC and a strain rate of 10/s. More detailed microstructural analysis comparing the simulated specimen at peak temperatures of

1000ºC and a strain rate of 10/s to the actual friction stir specimen will be discussed in the following section.
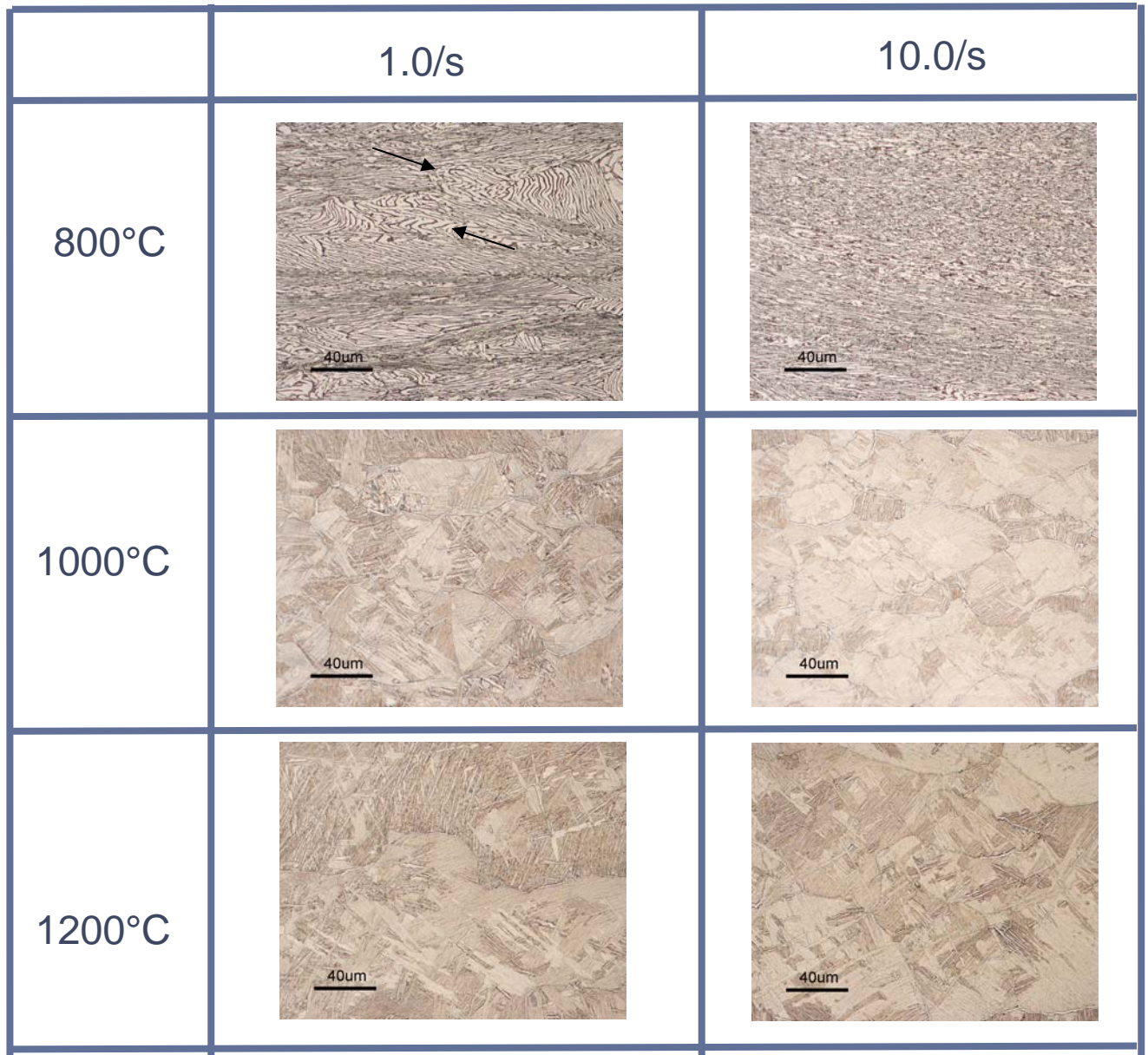
Figure 111. Optical micrographs of the center of compressed specimens using the FSW thermal curve specimens at strain rates of 1.0 and 10.0/s at peak temperatures of 800, 1000, and 1200 C. Arrows show kinking of the α laths below β transus (top panel). Dynamic recrystallization for specimens at 1200ºC and 1000ºC was completed within the β phase field resulting in equiaxed microstructure. There is an increased grain size in specimens at 1200ºC due to the longer time spent above β-transus.

	1.0/s	10.0/s
800°C	40um	40um
1000°C	40um	40um
1200°C	40um	40um
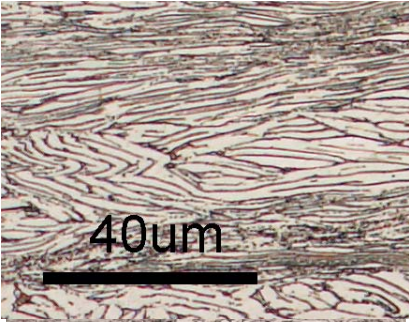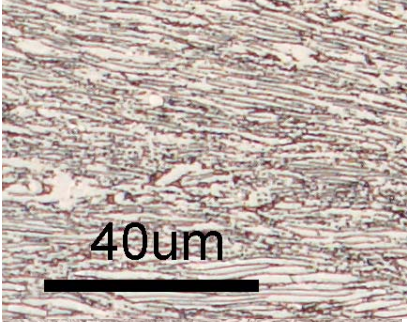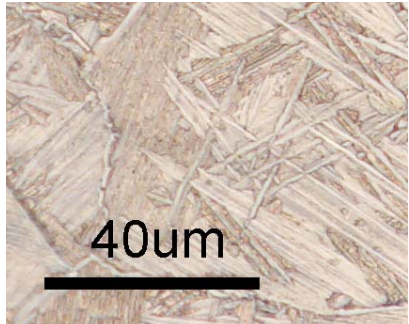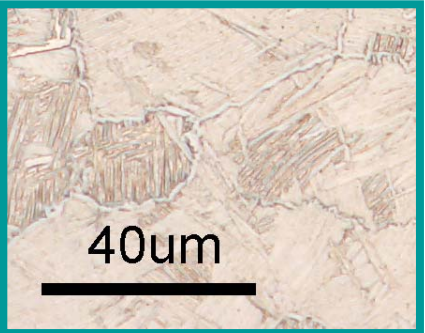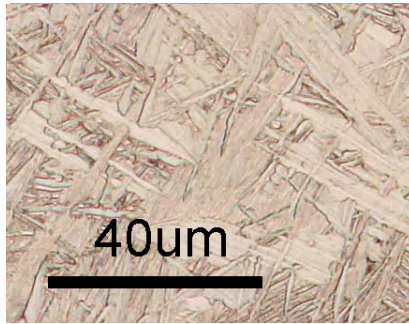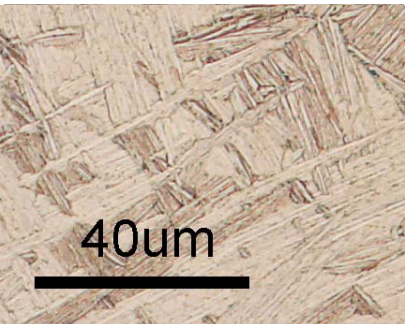
Figure 112. Higher magnification optical micrographs of the center of FSW thermal curve specimens at strain rates of 1.0 and 10.0/s at peak temperatures of 800, 1000, and 1200 C. Subtransus peak temperature (800ºC) compression results in α lath bending and kinking (top panel). Dynamic recrystallization for specimens at 1200ºC and 1000ºC was completed within the β phase field resulting in equiaxed microstructure (middle and bottom panel).
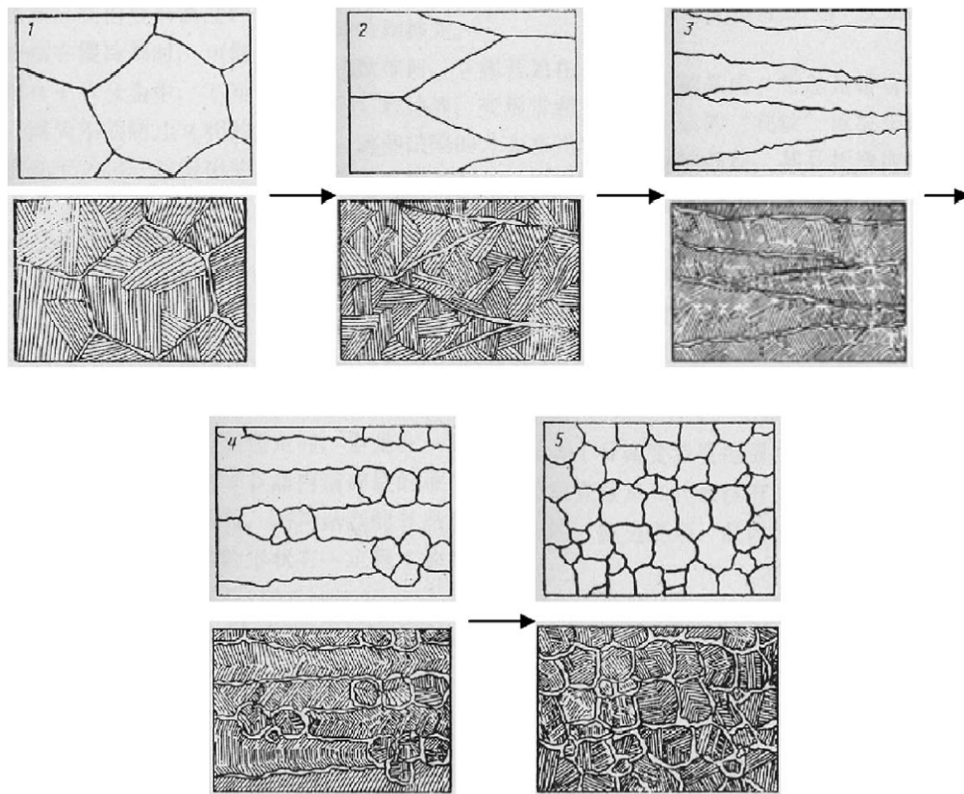
Figure 113. Schematic of the deformation and dynamic recrystallization above the β phase field. Top schematics 1-5 show increasing amounts of deformation. Bottom schematics are the microstructure after cooling to room temperature[Ma].

4.3.4.1 Simulated Strain, Strain Rate, Temperature

A direct optical microscopy comparison of the simulated specimen at a peak temperature of 1000ºC and a strain rate of 10/s to the actual 12.7mm friction stir specimen is shown in Figure 114. This comparison shows similar fully developed lamellar structures of approximately the same grain size and similar α lath width. The grains show the presence of 2-3 α colonies in both the actual weld and the simulated specimen. The grain boundary α in the FSW stir zone is slightly wider than in the Gleeble specimen. Nevertheless, this work provides an estimated strain, strain rate, and peak temperature for friction stir welding of Ti-5111 not previously reported in the literature.

Electron backscatter diffraction was performed on the Gleeble FSW simulation for comparison with the actual FSW sample discussed in Section 3.2.5. Figure 115 shows the image quality map of the center of the specimen as well as the inverse pole figure. The grain boundary misorientation map shows 0.814 fraction of high angle grain boundaries, a similar percentage to that found in the actual weld analysis presented in Section 3.2.5. While the optical microstructures show strong agreement between the simulated and actual specimens, there is a drastic difference in the sterographic projections for (0001) and the $(11\bar{2}0)$ in Figure 116. This difference is due to the inability to simulate the simple shear component of the texture within a compression specimen using the Gleeble simulation. To accurately mimic the texture, a torsional simulation at the estimated temperatures and strain rate is necessary.

Torsional Gleeble simulations have been performed to simulate microstructures in the stir zone and TMAZ for steel welds [Sinfield] as well as for Ti-5111 [Rubal]. The titanium simulations provided a unique challenge due to material properties preventing an accurate strain/strain rate measurement. This work was able to successfully mimic the optical microstructures, but the results were not repeatable due to localized deformation. The localized deformation caused specimen shearing within the deformation gauge length [Rubal]. Rubal recommended further trials with a change in specimen geometry to prevent strain localization during torsion. Combining Rubal's results with the results presented herein would give a powerful analysis tool for simulation of high strain, strain rate, and temperature effects for friction stir welding.

Figure 114. Comparison of the Gleeble FSW thermomechanical simulation at peak temperature of 1000ºC and a strain rate of 10/s (left) with the 12.7mm friction stir weld stir zone (right). The two images show similar grain size and α lath width with 2-3 α colonies/grain.

Figure 115. EBSD analysis of Gleeble FSW thermomechanical simulation at peak temperature of 1000ºC and a strain rate of 10/s. A) Image quality map B) Inverse pole figure C) Image quality map overlaid with grain boundary misorientation map

Figure 116. Pole figures of Gleeble FSW thermomechanical simulation at peak temperatures of 1000ºC and a strain rate of 10/s and of the actual FSW stir zone. There is drastic difference in the sterographic projections for (0001) and the ($1\bar{1}20$).

4.4. Summary

The results presented in this chapter examined the thermal and deformation mechanisms within Ti-5111 through the use of thermomechanical simulation. Experiments were aimed at decoupling the effects of temperature and deformation by applying: the friction stir thermal profile without deformation, isothermal constant strain rate, isothermal constant strain rate with a water quench after deformation, and combining the friction stir thermal profile with constant strain rate. Isothermal constant strain rate tests show evidence of dynamic recrystallization and deformation above β transus when compared with the FSW thermal profile without deformation. Subtransus deformation for all thermomechanical experiments show α lath kinking and bending. Applying the friction stir thermal profile to constant strain rate deformation successfully reproduced the friction stir microstructure at a peak temperature of 1000ºC and a strain rate of 10/s.

CHAPTER 5: CONSTITUTIVE MODELING OF FSW OF TI-5111 AND APPLICATION TO OTHER TITANIUM FRICTION STIR WELDING SYSTEMS

5.1. Introduction

Collaborative efforts in FSW of HSLA-65 have led to the development of mathematical models of the friction stir welding process for naval applications [Forrest]. The ISAIAH Code, a 3-D thermo-mechanical model developed by Cornell University, has transitioned to NSWCCD and is able to provide microstructural development and texture evolution from deformation and recrystallization for regions in a friction stir weld. Additionally, ISAIAH is able to provide strain, strain rate, and thermal data. Recent work by Dawson, *et al* successfully modeled the texture evolution during friction stir welding of 304L stainless steel and compared the results to EBSD measurements of welds [Cho]. Collaborative efforts with Cornell focused on sharing isothermal constant strain rate simulation results combined with actual welding parameters and the tool design to feed into the ISAIAH code.

5.2. Description of ISAIAH model

The ISAIAH model is an Eulerian based three-dimensional model of friction stir welding. ISAIAH was developed from the two-dimensional Cornell Hickory model utilizing constitutive materials modeling assuming isotropic strain hardening with independently characterized limits on the state variables and strain rate dependence on material flow strength. ISAIAH uses a simplified Hart's model for state variables of flow stress [Cho]. The Hart's model contains a plastic component and a viscous component for flow stress [Forrest] [Cho]. The governing equations for the ISAIAH/Hickory model and an in depth description of the simplified Hart's model can be found in Cho *et al* [Cho].

Important aspects of the model are:

- Ability to compute velocity and thermal fields for material flow through the use of viscoplastic constitutive flow models, heat transfer with conduction and convection, and themomechanical coupling[Cho]

- Ability to isolate specific particle streamlines for analysis [Cho]

- Ability to model damage prediction based on void growth within the friction stir welding process [He] [Dawson 2009]

- Ability to apply a decoupled texture evolution model for specific thermomechanical histories. [Cho 2008]

Hickory/ISAIAH has been extensively applied for 304L stainless steel [Cho][Cho 2008] [He] [Dawson 2009]. A comparison of experimental results and model predictions have shown good agreement with the thermal field and estimated weld strength. The model suggests that the stress ahead of the tool is compressive while the stress behind the tool is tensile [Cho]. The three-dimensional model has the ability to examine material flow with respect to tool design. Some material streamlines show the material wrapping around the tool several times or material moving upward through the weld in stainless steel [Cho 2008]. Examination of the texture evolution with the model shows a change in texture with respect to deformation rate and stress [Cho 2008]. More significantly, the damage model for welding within 304L stainless steel with the tapered, or frustum, pin shows defects forming at the advancing side of the pin tool [He].

While this friction stir welding model has been successfully applied for steels, application to titanium alloys is still under development. The work presented in Section 5.3 is preliminary results provided by Dr. Paul Dawson for comparison to experimental data.

5.3. Results and Discussion

5.3.1 Strain, Strain Rate, and Temperature Estimations from ISAIAH Model

ISAIAH, as mentioned before, uses a Eulerian reference frame based on 8000 elements and 20-node bricks. The model uses a fixed mesh with the pin located in the center. In this model the pin does not traverse the length of material, but rather material enters on the left and exits to the right. ISAIAH modeling results for Ti provided by Dr. Dawson used a tapered pin or frustum designed tool based on the actual tool design used for the 12.7mm welding. Initial work examined modeling spindle speeds varied from 100-300 rpm for 12.7mm welds[Dawson 2008]. Figure 117 and Figure 118 show the thermal field distribution for two different rotational rates. The estimated temperatures closest to the tool on the advancing side for both conditions of 100rpm and 300 rpm show peak temperatures of 1200ºC. The slower spindle speed results in a wider temperature distribution beneath the tool shoulder and behind the tool (Figure 117).
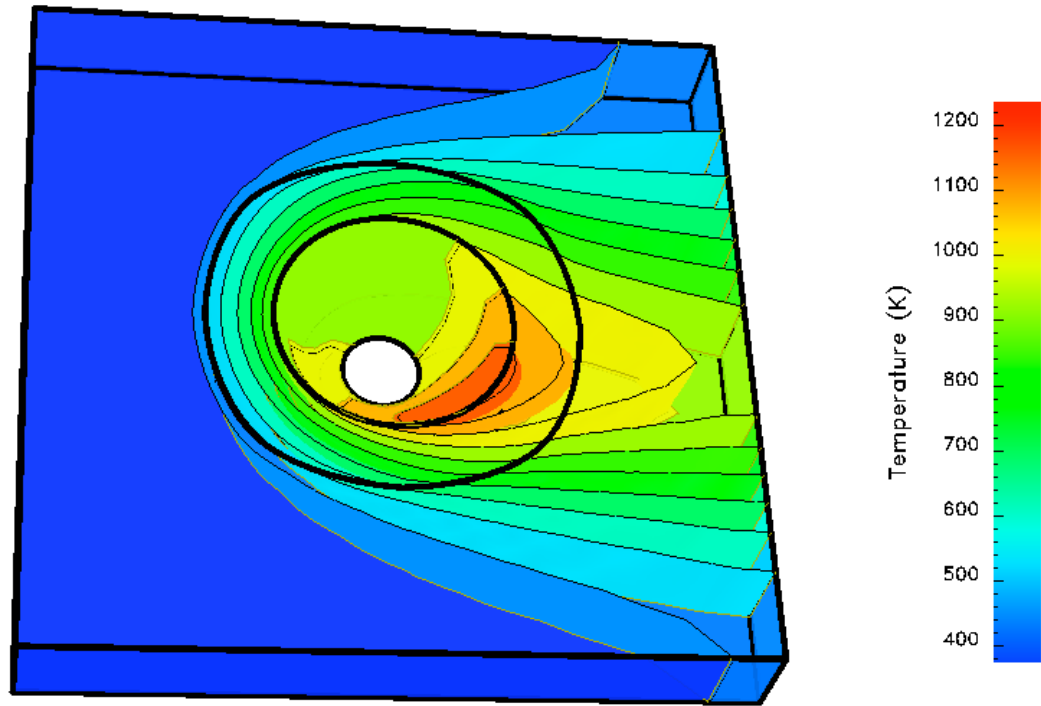
Figure 117. Temperature distribution with lower rotation rate of 100rpm [Dawson 2008]
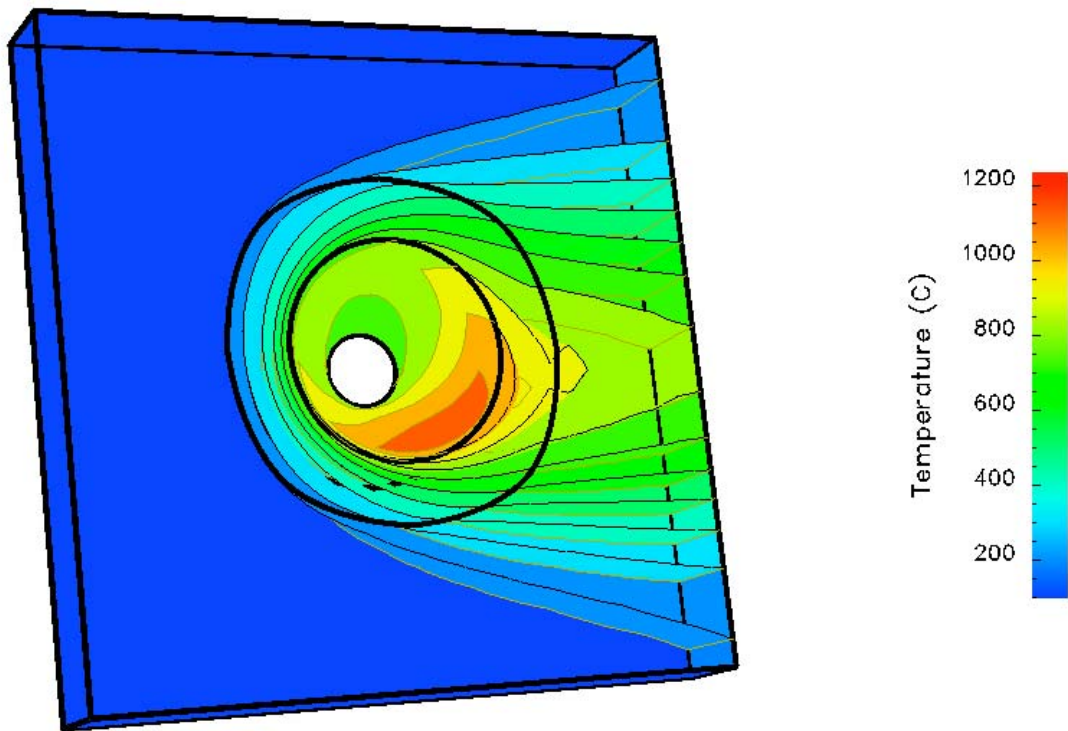
Figure 118. Temperature distribution with higher (300rpm) rotation rate [Dawson 2008]

162

5.3.2 Comparing modeling results with experimental welding

Further analysis based on experimental welding used four individual streamlines from the temperature distribution for both rotational rates [Dawson 2008]. The four streamlines for comparison to experimental welding are:

- advancing side on the edge of the stir zone

- advancing side closest to the tool

- retreating side closest to the tool

- retreating side on the edge of the stir zone

For a lower rotational rate in the simulation, the peak temperature is similar to the experimental weld temperature, however the shape of the thermal curve in the simulation does not reproduce the experimental temperature curve (Figure 119). Earlier chapters discussed the dynamic recrystallization apparent within the friction stir weld; however, the temperatures predicted with the lower rotational speed would not result in recrystallization. The higher rotational rate of 300 rpm (Figure 120), does predict higher temperatures for all model streamlines that would result in recrystallization, but the shape of the thermal curve does not match with the experimental weld thermal curves.

Recent advancements and improvements to the ISAIAH code have focused on implementation of a new material model and advance post-processing of the data. Recent results provided by Dr.Dawson are shown in Figure 121-Figure 124. This set of results examined material flow at the mid-plane of the weld and shows material on the advancing side being pulled around the tool (Figure 121). Peak temperatures with the modified model

are higher and approach 1350 closest to the tool (Figure 122). All temperatures within these streamlines exceed β transus. The shape of the temperature curve is closer to the experimental results but the peak temperatures are higher than expected. As discussed in Section 4.3.4, the cooling curve is very important for the transformation from β to α and current modeling results have not mimicked the experimental temperature curve. Figure 123 shows the effective strain rate with respect to streamlines located along the mid-plane of the weld. Figure 124 shows the peak strains of the streamlines with the highest strain rate of 3.75/s closest to the tool. All streamlines experience some strain within the system. These predicted strain rates are lower than the estimated strain rate based on microstructural development presented in Section 4.3.4. Ongoing modeling efforts continue to show improvements with advancements in the material model to handle allotropic transformation.
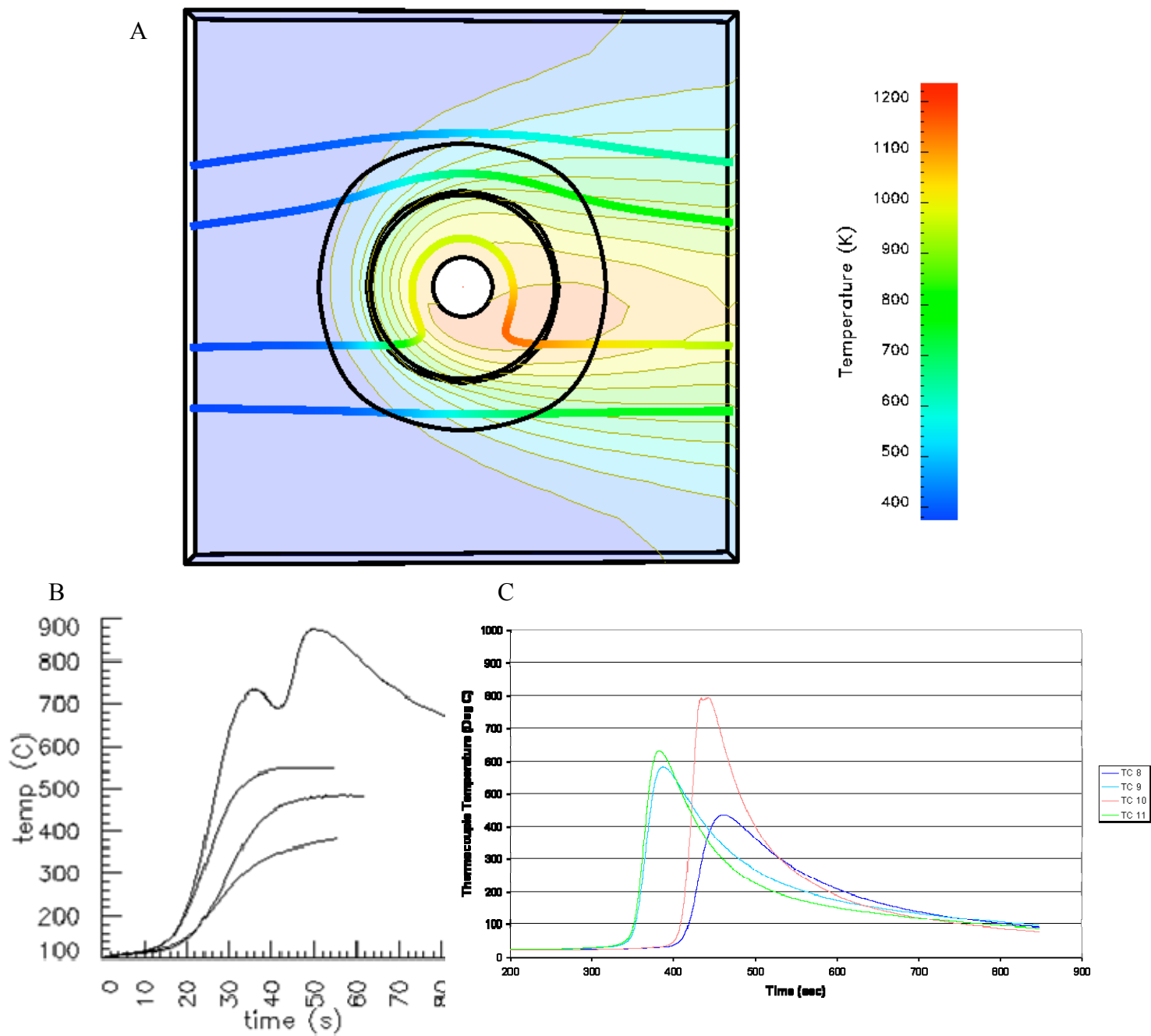
Figure 119. Temperature streamline traces for lower rotational rate of 100rpm A) Streamline with respect to the tool B) Temperature profile with respect to the streamline C) Experimental FSW thermal data at the same respective locations [Dawson 2008]
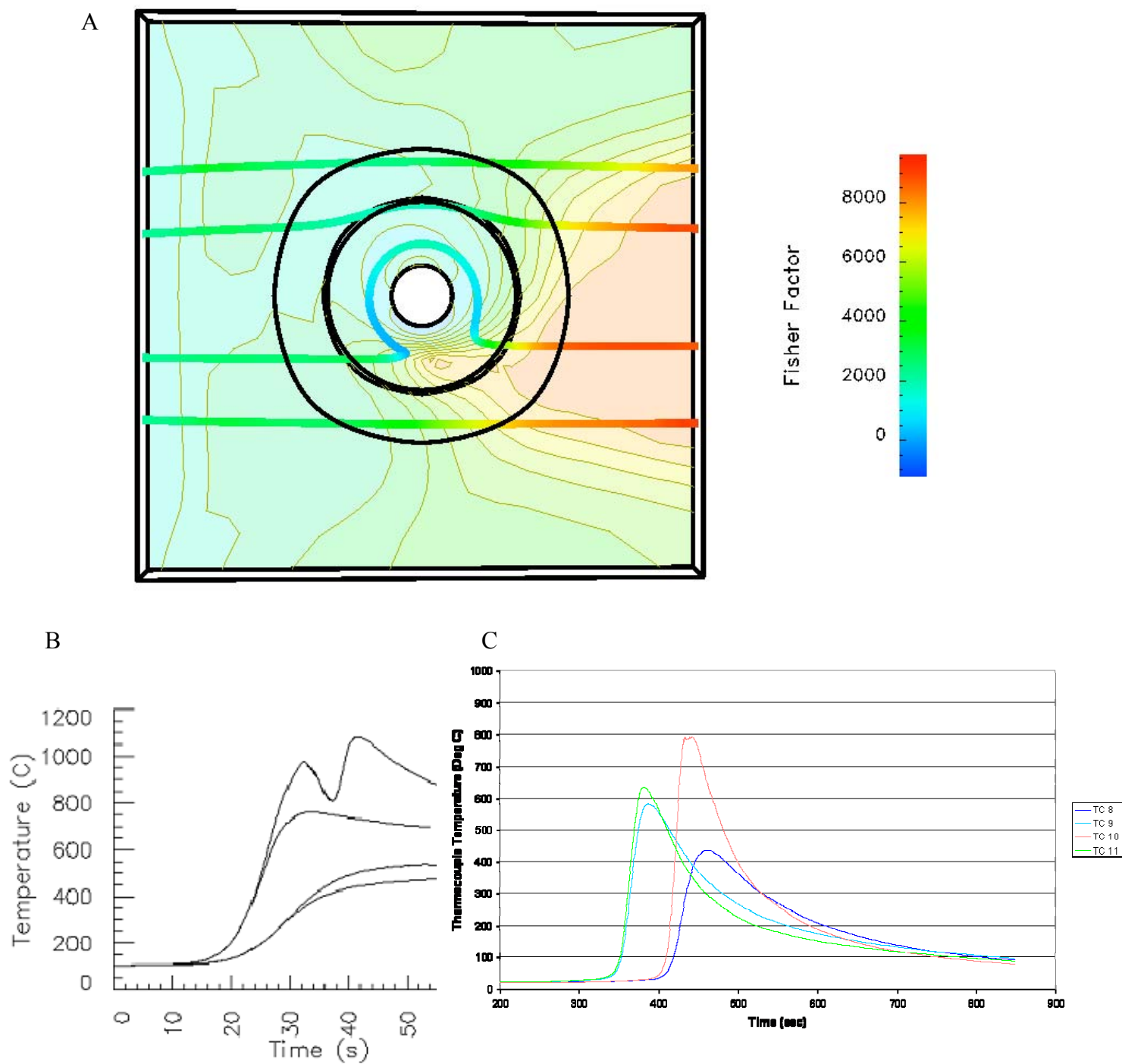
Figure 120. Temperature streamline traces for higher rotational rate 300rpm A) Streamline with respect to the tool B) Temperature profile with respect to the streamline C) Experimental thermal data at the same respective locations [Dawson 2008]
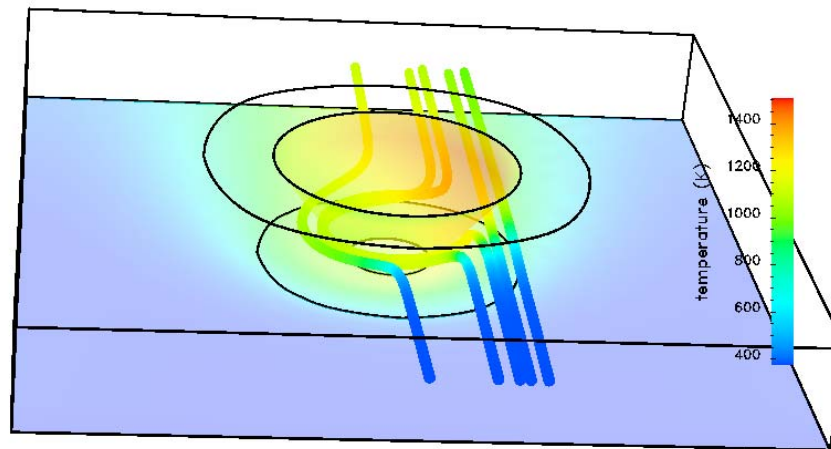
Figure 121. Temperature streamlines with respect to the tool for 12.7mm FSW of Ti-5111 utilizing ISAIAH code advancements [Dawson 2010]
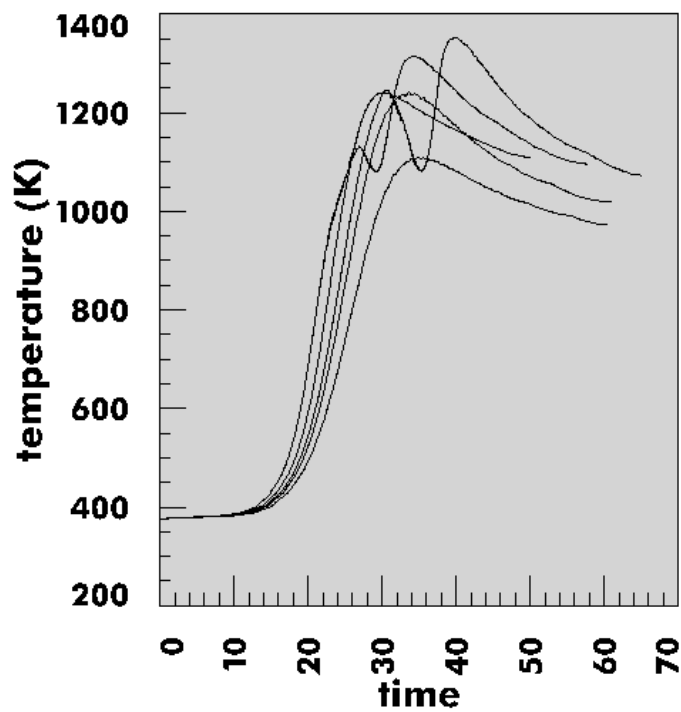
Figure 122. Temperature profile with respect to streamlines in Figure 121 [Dawson 2010]
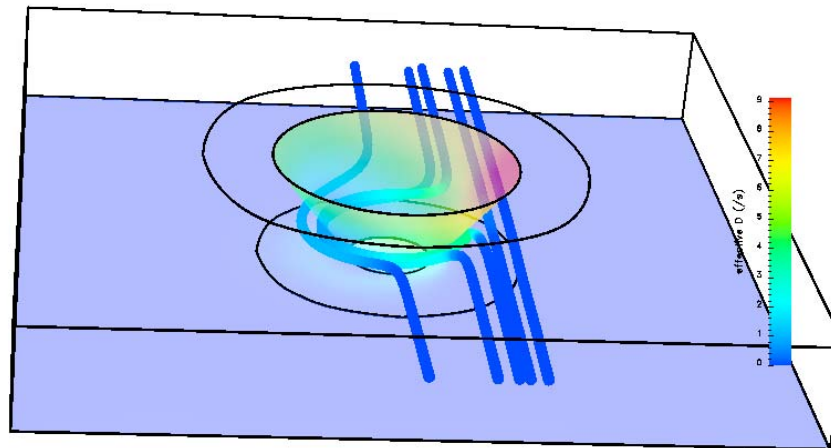
Figure 123. Effective strain rate streamlines with respect to the tool for 12.7mm FSW of Ti-5111 utilizing ISAIAH code advancements [Dawson 2010]
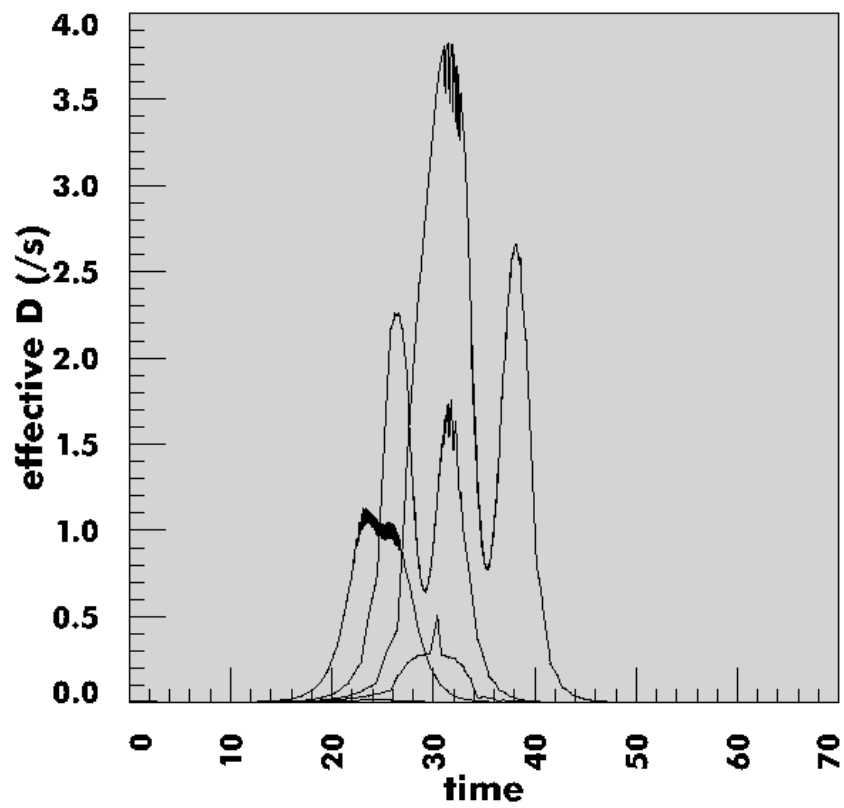
Figure 124. Effective strain rate profile with respect to streamlines in Figure 123 [Dawson 2010]

168

5.4. Summary

ISAIAH model is an Eulerian based three-dimensional model of friction stir welding. ISAIAH has been extensively applied for friction stir welding of 304L stainless steel showing good agreement with the thermal field and estimated weld strength comparisons. Preliminary modeling results for FSW of Ti-5111 shows material on the advancing side being pulled around the tool during welding. All temperatures within these streamlines exceed β transus, but the predicted curves do not match experimental thermal curves. Modeling results also predict a high strain rate of 3.75/s closest to the tool, but all streamlines experience some strain within the system, however the predicted strain rates are lower than the estimated strain rate based on microstructural development observed in this study. Preliminary results show promise for the model when compared to experimental data, however, further efforts with the improved code are necessary to fully explore the potential of modeling friction stir welding of titanium alloys to estimate strain, strain rates, and the thermal field.

CHAPTER 6: CONCLUSIONS AND FUTURE WORK

6.1. Conclusions

This work study examined experimental welds, physical simulation, and constitutive modeling to gain a fundamental understanding of the relationship between processing parameters, microstructure, and mechanical properties of experimental Ti-5111 friction stir welds. Primary deformation and texture mechanisms were determined to further understand the effect of transient temperature and deformation during the friction stir. This work provided a basis for strain, strain rate, and temperature experienced during the friction stir welding process.

The following conclusions can be made regarding the welding parameters and welding temperatures:

- The calculated friction stir weld heat input for FSW is lower than for arc welding but for some weld travel speeds it is comparable to that of arc welding.

- The analysis of the thermal field surrounding the weld shows that temperatures within the stir zone likely exceeded β transus. This result is in agreement with the fully lamellar microstructures developed in all the welds.

With respect to the microstructures developed within the weld the following conclusions can be made:

- Significant microstructural refinement takes place in the stir zone compared to the base metal for 12.7mm and 6.35mm friction stir welds. All welds show an abrupt transition from the base metal to the stir zone with a narrow transition region.

- The grain refinement mechanism for these welds shows strengthening of the BCC F fiber component through the transition region before transformation to D_2 shear texture in the stir zone with a rotation of the pole figure by approximately 28.4° about the center of the pole figure.

- Transmission electron microscopy results of the base metal and the stir zone show a similar lath structure with low dislocation density and no lath grain substructure. High resolution TEM shows the difference in atomic structure between the two phases and broad ledges at the interface of α and β. In situ heating experiments in the TEM of Ti-5111 friction stir welded material show transformation to β at significantly lower temperatures compared to the base metal.

- Computed tomography and electron backscatter diffraction of defect regions show shear layers of material formed within the defect.

The following conclusions can be made from decoupling temperature and deformation in thermomechanical simulations using the Gleeble:

- Applying the friction stir thermal profile without deformation resulted in the presence of Widmenstatten structure at 800˚C. Higher temperatures result in increased amount of retained β that appears in clusters as well as the presence of martensitic α'.

171

- Isothermal constant strain rate tests show evidence of dynamic recrystallization upon deformation above β transus when compared with the FSW thermal profile without deformation. Subtransus deformation for all thermomechanical experiments show α lath kinking and bending.

- Applying the friction stir thermal profile to constant strain rate deformation successfully mimicked the friction stir microstructure at a peak temperature of 1000ºC and a strain rate of 10/s. This microstructure is indicative of dynamic recrystallization.

Lastly, with respect to the constitutive modeling of titanium friction stir welds using the ISAIAH model, the following conclusions can be made:

- Preliminary modeling in Ti-5111 shows that all temperatures within the streamlines exceed β transus, but the predicted curves do not match experimental thermal curves of FSW of Ti-5111.

- High strain rates of 3.75/s are predicted closest to the tool, but all streamlines experience some strain within the system. The strain rates are lower than the estimated strain rate based on microstructural development presented in this thesis.

- Preliminary results show promise for the model when compared to experimental data but requires refinement and application of a more advanced material model to handle the allotropic phase transformation.

6.2. Scientific Contributions

This dissertation resulted in the following scientific contributions:

- Microstructural development in friction stir welding of Ti-5111 occurs through deformation in the β phase field. Rapid cooling after deformation results in microstructural refinement. This microstructural refinement results in increase weld strength.

- Texture evolution of the material is directly affected by the texture found in the BCC β structure. This influences selection of α variants upon phase transformation. This work shows strengthening of the BCC F fiber component through the transition region before transformation to D_2 shear texture in the stir zone with a rotation of the pole figure by approximately 28.4º about the center of the pole figure. This discovery provides a more complete understanding of the texture formation within the friction stir weld.

- The phase transformation of the α-β interface is influenced by grain refinement as shown through in situ TEM results comparing the base metal and the stir zone. In situ TEM of Ti-5111 friction stir welded material shows transformation to β at significantly lower temperatures compared to the base metal due to grain refinement in the friction stir welding process. During heating, the β phase grows from the α-β interface through ledges shown in high resolution TEM. This result has significant implications for traditional metalworking processes because microstructural refinement results in lower transformation temperatures to β allowing for reduction in forging loads.

- Thermomechanical simulations of friction stir welding process show peak temperatures of 1000ºC with a strain rate of 10/s. This provides experimental

evidence of peak temperature and strain through successful replication of the weld microstructure.

6.3. Technological Contributions

This work utilized a number of different techniques and approaches resulting in the following technological contributions:

- Application of in situ heating of TEM foils for high temperature analysis that provides information on material phase transformation

- Development of a friction stir welding simulation tool that allows independent control of strain, strain rate, and temperature. Thermomechanical simulations are able to successfully recreate optical microstructures observed during welding. This will lead to a reduction in experimental weld trials.

- Applications of successful friction stir welding parameters to other titanium alloys.

- Improved friction stir welding three dimensional model for titanium alloys

6.4. Future Work

While this work provided fundamental understanding of the microstructural evolution in titanium friction stir welding, the following suggestions for future work are recommended:

- DEFORM modeling to back-calculate flow stress and determine potential strain hardening and flow softening conditions it recommended.

- Further TEM microscopy of thermomechanical simulation specimens and the relationship to examine the presence of α' in the thermal simulations. High resolution

- As discussed in Section 4.3.4.1 torsional thermomechanical simulation at the experimentally determined strain, strain rate, and thermal profile is recommended to further elucidate the thermomechanical processing path for friction stir welding of Ti-5111.

- To assist in transitioning the technology for use on targeted applications, further mechanical property testing is recommended, in particular fatigue, creep, and fracture toughness are recommended.

- The role of thermomechanical processing above and below β transus is critical for friction stir welding of Ti-5111. Expanding this study to look at the influence of allotropic transformation temperature for friction welding of other α, $\alpha+\beta$, and β alloys is recommended.

- Further efforts with the improved ISAIAH code are necessary to fully explore the potential of modeling friction stir welding of titanium alloys to estimate strain, strain rate, and the thermal field.

REFERENCES

[ASM] Materials Properties Handbook Titanium Alloys. *ASM (1994)*

[ASTM B265] ASTM B265 Specification for Titanium Alloys.

[AWS G2] AWS G2.4 2007. Guide for the fusion welding of titanium and titanium alloys. *American Welding Society (2006)*

[Beausir] B. Beausir, L.S.Toth, K.W.Neale. "Ideal orientations and persistence characteristics of hexagonal close packed crystals in simple shear." *Acta Materialia 55 (2007) 2695-2705.*

[Bruschi] S. Bruschi, S. Poggio, F. Quadrini, and M.E. Tata. "Workability of Ti-6Al-4V alloy at high temperatures and strain rates. *Materials Letters 58 (2004) 3622-3629*

[Cheng] C. Cheng, M.Zupan, J. Wolk. "Mechanical evolution of friction stir-welded Ti-5111 microsamples." *PLASTICITY '10: The Sixteenth International Symposium on Plasticity and its Current Applications. (2010)*

[Cho] J.H. Cho, D.E. Boyce and P.R. Dawson. "Modeling strain hardening and texture evolution in friction stir welding of stainless steel." *Materials Science and Engineering A (2005) 146-163*

[Cho 2008] J.H. Cho and P.R. Dawson. "Modeling texture evolution during friction stir welding of stainless steel with comparison to experiments." *Journal of Engineering Materials and Technology 130 (2008) 011007-1 – 011007-12*

[Dawson 2008] P.R. Dawson, D.E. Boyce, and T. Marin. "Simulations and Experiments on Titanium and Stainless Alloys." *ONR Friction Stir Technologies Review, October 2008.*

[Dawson 2009] P.R. Dawson, D.E. Boyce, and T. Marin. "Simulations and Experiments on Titanium and Stainless Alloys." *ONR Friction Stir Technologies Review, October 2008.*

[Dawson 2010] Private communication with P.R. Dawson, D.E. Boyce Oct 2009-March 2010.

[Dieter] G.E. Dieter. Mechanical Properties of Materials. McGraw-Hill, 1986

[DSI] DSI. "Gleeble 1500D System Product Description and Specifications." *2005*

[Fonda 2007] R.W. Fonda, K.E. Knipling, C.R. Feng, and D.W. Moon. "Microstructural evolution in Ti-5111 friction stir welds." *TMS Annual Meeting Orlando, FL (2007)*

[Fonda 2007b] R.W. Fonda, K.E. Knipling, J.F.Bingert. "Microstructural evolution ahead of the tool in aluminum friction stir welds. *Scripta Materialia 58 (2007) 343-348.*

[Forrest] D. Forrest, J. Nguyen, M. Posada, and J. Deloach. "Simulation of HSLA-65 Friction Stir Welding." *Proceedings of the 7th International Conference on Trends in Welding Research (2006) 279-286*

[Gey 1996] N.Gey, M.Humbert, M.J. Phillippe, and Y.Combres. "Investigation of the α- and β- texture evolution of hot rolled Ti-64 products."*Materials Science and Engineering A219 (1996) 80-88.*

[Gey 1997] N.Gey, M.Humbert, M.J. Phillippe, and Y.Combres. "Modeling the transformation texture of Ti-64 sheets after rolling in the β-field." *Materials Science and Engineering A230 (1997) 68-74.*

[Gey 2002] N.Gey and M.Humbert. "Characterization of the variant selection occurring during the α→β→α phase transformations of a cold rolled titanium sheet." *Acta Materialia 50 (2002) 277-287.*

[He] Y.L. He, P.R. Dawson, D.E. Boyce. "Modeling damage evolution in friction stir welding process." *Journal of engineering materials and technology – transactions of the ASME 130 (2008) 021006-2-021006-10*

[Han] Y.Han and H.Zhuang. "Deformation-induced ambient temperature α-to-β phase transition and nanocrystallization in (α+β) titanium alloy." *Journal of Material Research 24 (2009) 3439-3445*

[Knipling] K.E. Knipling and R.W. Fonda. "Texture development in the stir zone of near-α titanium friction stir welds." *Scripta materialia 60 (2009) 1097-1100*

[Kestel] BJ Kestel. Polishing methods for metallic and ceramic transmission electron microscopy specimens. *Argonne National Laboratory. (1986)*

[Kocks 1998] U.F. Kocks, C.N.Tome and H.R.Wenk. Texture and Anisotropy: Preferred orientations in polycrystals and their effect on materials properties. *Cambridge University Press (1998).*

[Li] L.X. Li, Y. Lou, L.B. Yang, D.S. Peng, and K.P. Rao. "Flow stress behavior and deformation characteristics of Ti-3Al-5V-5Mo compressed at elevated temperatures." *Materials and Design 23 (2002) 451-457*

[Li 2005] S. Li, I.J. Beyerleinb, M.A.M. Bourkea "Texture formation during equal channel angular extrusion of fcc and bcc materials: comparison with simple shear." *Materials Science and Engineering A 394 (2005) 66–77*

[Li and Salamanca-Riba] H.Li and L. Salamanca-Riba. "The concept of high angle wedge polishing and thickness monitoring in TEM sample preparation." *Ultramicroscopy 88 (2001) 171-178*

[Lienert 2001] T.J. Lienert, K.V. Kata, R. Wheeler, and V. Seetharaman. Proceedings of the Joining of Advanced and Specialy Materials III, *ASM International (2001)*

[Lee] W.B. Lee, C.Y. Lee, W.S. Chang, Y.M. Yeon, S.B. Jung. "Microstructural investigation of friction stir welded pure titanium." *Materials Letters 59 (2005) 3315-3318*

[Lutjering] G. Lutjering and JC Williams. Titanium. *Springer (2007)*

[Lutjering] G. Lutjering. "Influence of processing on microstructure and mechanical properties of (α+β) titanium alloys." *Materials Science and Engineering A 243 (1998) 32-45*

[Ma] F.Ma, W.Li, J.Qin, and D. Zhang. "Microstructure evolution of near-α titanium alloys during thermomechanical processing." *Materials Science and Engineering A 416 (2006) 59-65*

[Ma 2008] Z.Y.Ma, A.L. Pilchak, M.C.Juhas, and J.C. Williams. "Microstructural refinement and property enhancement of cast light alloys via friction stir processing." *Scripta Materialia 58 (2008) 361-366.*

[Mironov 2008a] S.Mironov, Y.Zhang, Y.S. Sato, and H. Kokawa. "Development of grain structure in β phase field during friction stir welding to Ti-6Al-4V alloy" *Scripta Materialia 59 (2008) 27-30*

[Mironov 2008b] S.Mironov, Y.Zhang, Y.S. Sato, and H. Kokawa. "Crystallography of transformed β microstructure in friction stir welded to Ti-6Al-4V alloy" *Scripta Materialia 59 (2008) 511-514*

[Mironov 2009] S.Mironov, Y.S. Sato, and H. Kokawa. "Development of grain structure during friction stir welding of pure titanium" *Acta Materialia 57 (2009) 4519-4528*

[Mishra 2005] R.S. Mishra and Z.Y. Ma. "Friction stir welding and processing." *Materials Science and Engineering R. 50 (2005) 1-78*

[Mishra 2007] R.S. Mishra and M.W. Mahoney. Friction Stir Welding and Processing. *ASM (2007)*

[MMADCP] K Klug. Metallic Materials Advanced Development and Certification Project (MMADCP) Task 6: Certification of Titanium Alloy Ti-5111 for Critical Applications. *Naval Metal Working Center. (2006)*

[Neuberger] B. Neuberger. "Dynamics of Near Alpha Titanium Welding." *University of Maryland (2004)*

[Peters] M. Peters, G. Luterjing, G. Ziegler. "Control of microstructure of (α+β) titanium alloys. *Zeitschrift fur Metallkunde 74 (1983) 274-282*

[Picu] R.C. Picu and A. Majorell. "Mechanical behavior of Ti-6Al-4V at high and moderate temperature—Part II: constitutive modeling." *Materials science and Engineering A326 (2002) 306-316*

[Pilchak 2007] A.L. Pilchak, M.C. Juhas, and J.C. Williams. "Observations of tool-workpiece interactions during friction stir processing of Ti-6Al-4V." *Metallurgical and Materials Transactions A 38A (2007) 435-437*

[Pilchak 2009] A.L. Pilchak. "The effect of friction stir processing on the microstructure, mechanical properties, and fracture behavior of investment cast Ti-6Al-4V." *Ohio State University (2009)*

[Ramirez] A.J. Ramirez and M.C. Juhas "Microstructural evolution in Ti-6Al-4V friction stir welds." *Materials Science Forum 426-432 (2003) 2999-3004*

[Reynolds] A.P. Reynolds, E.Hood, and W.Tang. "Texture in friction stir welds of Timetal 21S." *Scripta Materialia 52 (2005) 491-494*

[Rubal] M. Rubal, J. Lippold, and M. Juhas. "Physical simulation of friction stir processed Ti-5111." *Friction Stir Welding and Processing V. Warrendale, TMS (2007) 21-28*

[Savage] M.F. Savage, J. Tatalovich, M. Zupan, K.J. Hemker and M.J. Mills. "Deformation mechanisms and micro-tensile behavior of single colony Ti-6242Si." *Materials Science and Engineering A, 319-321, pp.398-403 (2001)*

[Schwartz] A.J. Schwartz, M. Kumar, and B.L. Adams Electron Backscatter Diffraction in Materials Science. *Kluwer Academic/Plenum Publishers (2000).*

[Sinfield] M.F. Sinfield, J.C. Lippold, and B.T. Alexandrov. "Physical Simulation of Friction Stir Weld Microstructure of a High-Strength, Low Alloy Steel (HSLA-65)." *7th International Friction Stir Welding Symposium Awaji Island Japan (2008)*

[Semiatin] S.L. Semiatin, V. Seetharaman, I. Weiss. "Hot workability of titanium and titanium aluminide alloys—an overview." *Materials Science and Engineering A243 (1998) 1-24*

[Semiatin 1999] S.L. Semiatin, V. Seetharaman, I. Weiss. "Flow behavior and globularization kinetics during hot working of Tii-6Al-4V with a colony alpha structure." *Materials Science and Engineering A263 (1999) 257-271*

[Semiatin 2001] S.L. Semiatin and T.R. Bieler. "The effect of alpha platelet thickness on plastic flow during hot working of Ti-6Al-4V with a transformed microstructure." *Acta materialia 49 (2001) 3565-3673*

[Seshacharyulu] T. Seshacharyulu, S.C. Medeiros, W.G. Frazier, Y.V.R.K Prasad. "Hot working of commercial Ti-6Al-4V with an equiaxed α-β microstructure: materials modeling considerations." *Materials Science and Engineering A284 (2000) 184-194.*

[Suri] S. Suri, C.B. Viswanathan, T. Neeraj, D.H. Hou, and M.J. Mills. "Room temperature deformation and mechanisms of slip transmission in oriented single-colony crystals of an α/β titanium alloy." *Acta Materialia 47(1999) 1019-1034.*

[Thomas] W.M. Thomas, E.D. Nicholas, J.C. Needham, MG Murch, P Templesmith, CJ Dawes, *G.B. Patent Application No. 9125978.8 (1991)*

[Timet] Titanium Metal Corporation: Timetal 5111, Report # TMC-0170.

[TWI] TWI classification. http://www.twi.co.uk/content/fswintro.html

[Vander Voort] G.F. Vander Voort. Metallography, principles and practice. *McGraw-Hill (1984).*

[Wang] S.C. Wang, M. Aindow, M.J. Starink. "Effect of self-accommodation on α/α boundary populations in pure titanium." *Acta Materialia 51 (2003) 2485–2503*

[Welding Handbook] Hobart Institute of Welding Technology. Welding Handbook. Hobart Institute of Welding Technology, 1995.

[Weiss] I. Weiss, and S.L. Semiatin "Thermomechanical processing of alpha titanium alloys-an overview." *Materials Science and Engineering A263 (1999) 243-256.*

[Williams] D.B. Williams and C.B. Carter. Transmission electron microscopy. *Plenum Press (1996).*

[Wolk 2009] J.N. Wolk and W.L. Shepherdson. Unpublished research.

[Wolk 2010] J.N.Wolk, R.Everett, and L. Salmanca-Riba. "Computed Tomography of Ti-5111 friction stir welding." *TMS Annual Meeting Seattle, WA (2010)*

[Yung] W.K. Yung, B.Ralph, W.B. Lee, R. Fenn. "An investigation into welding parameters affecting the tensile properties of titanium welds". *Journal of Materials Processing Technology 63 (1997) 759-764*

[Zeng] L.Zeng and T.R.Bieler. "Effects of working, heat treatment, and aging of microstructural evolution and crystallographic texture of α, α', and α" and β phases in Ti-6Al-4V." *Mataerials Sciene and Engineering A 392 (2005) 403-414.*

[Zhang 2007] Y.Zhang, Y.S. Sato H. Kokawa, S.H. Park, S. Hirano. "Microstructural characteristics and mechanical properties of Ti-6Al-4V friction stir welds." *Materials Science and Engineering A 488 (2008) 25-30*

[Zhang 2008] Y.Zhang, Y.S. Sato H. Kokawa, S.H. Park, S. Hirano. "Stir zone microstructure of commercial purity titanium friction stir welded using pcBN tool." *Materials Science and Engineering A 488 (2008) 25-30*

[Zhou] L.Zhou, H.J. Liu, P.Liu, and Q.W. Liu. "The stir zone microstructure and its formation mechanism in Ti-6Al-4V friction stir welds." *Scripta Materialia 61 (2009) 296-599.*

[Zhou 2010] L.Zhou, H.J. Liu, and Q.W. Liu. "Effect of process parameters on stir zone microstructure in Ti-6Al-4V friction stir welds." *Journal of Materials Science 45 (2010) 39-45.*

[Zupan 1998] M. Zupan and K.J. Hemker. "Tensile/Compressive Properties of Single Crystal Gamma Ti-55.5at%Al." *Metallurgical and Materials Transactions A, 29A, pp.65-71 (1998)*

[Zupan 2001] M. Zupan and K.J. Hemker, "High Temperature Microsample Tensile Testing of γ-TiAl." *Materials Science and Engineering A, 319-321, pp.810-814 (2001)*

[Zupan 2002]M. Zupan and K. J. Hemker. "Application of Fourier analysis to the laser based interferometric strain/displacement gage." *Experimental Mechanics, vol. 42, pp. 214-220, 2002.*